THESE DE DOCTORAT de L'UNIVERSITE PARIS 6

Spécialité :

PHYSIQUE DU SOLIDE

Présentée par Martin Chauvin
pour obtenir le grade de Docteur de l'Université Paris 6

Sujet de la thèse :

Effet Josephson dans les contacts atomiques

Soutenue le 22 Novembre 2005
Devant le jury composé de :

M. Aprili (rapporteur)
R. Combescot (président)
J. C. Cuevas (rapporteur)
C. Schönenberger
V. Shumeiko
C. Urbina (directeur de thèse)
J. M. van Ruitenbeek

Cover

Upper picture: current phase relation (see introduction, Figure 9)

Lower left picture: bending mechanism (see chapter 5, Figure 3)

Lower right picture: suspended aluminum bridge (see chapter 5, Figure 1)

Remerciements

Au moment de conclure ces trois années de recherche passées dans le Groupe Quantronique, je tiens à remercier Jacques Hamman et Eric Vincent de m'avoir accueilli au sein du Service de physique de l'état condensé (SPEC). Merci à Michel Devoret qui, en m'acceptant en stage m'a permis pendant l'été 2001, de faire la connaissance de l'équipe et de m'initier à ses travaux de recherche. Au cours de ce stage, j'ai pu découvrir les techniques de fabrication des échantillons conçus pour les expériences de physique du groupe, en bénéficiant de la patience et de la pédagogie de Denis Vion et de Philippe Joyez. J'y ai aussi découvert que la rigueur n'est pas incompatible avec l'enthousiasme, ni la recherche scientifique avec le bricolage. Quand, à la fin de mon stage, Daniel Estève m' a proposé de reprendre contact avec le groupe si j'envisageais de faire une thèse, je n'ai donc pas hésité longtemps : après mon DEA, je poursuivrai cette expérience courte mais enrichissante tant du point de vue scientifique que du point de vue humain. Et c'est après une année passée à Imperial College à Londres que j'ai pu, grâce à l'efficacité des démarches de Daniel Estève et de Cristián Urbina –que je ne connaissais pas encore car il était aux Etats-Unis lors de mon stage–, obtenir une allocation et rejoindre le groupe Quantronique pour commencer une thèse sur les contacts atomiques.

Il se trouve que c'est précisément Cristián Urbina qui allait diriger ma thèse. Merci beaucoup Cristián pour ces trois années passées à faire de la physique avec toi. Merci pour ton exemple de rigueur, d'exigence et de persévérance. J'ai aussi beaucoup bénéficié de tes qualités pédagogiques qui m'ont permis de trouver peu à peu ma place dans l'ensemble de ce projet sur les contacts atomiques. Merci pour ta disponibilité et la qualité de ton écoute. J'ai beaucoup apprécié les « sessions tableau » que l'on a eues ensemble : j'en repartais toujours enrichi de nombreuses idées et avec l'esprit beaucoup plus clair. Merci, enfin et avant tout, pour tout ce que j'ai appris grâce à toi, sur les sciences et le reste.

Merci Daniel pour ton soutien permanent et la confiance que tu m'as accordée tout au long de ma thèse. Malgré tes multiples occupations, tu as toujours gardé un œil

attentif sur la manipe du sous-sol et tu as toujours trouvé le temps de me faire partager ton expérience. Merci pour toutes les pistes de recherche que tu m'as suggérées. Merci pour cette tape dans le dos qui rassurait pendant les moments difficiles de la thèse, quand les expériences ne marchaient pas toujours bien.

Merci à tous les deux, Daniel et Cristián pour votre efficacité dans la relecture et les corrections du manuscrit de thèse.

Pendant ces années, j'ai eu le plaisir de travailler avec Peter vom Stein, qui m'a initié (lourde tâche !) aux arcanes de la programmation. Grâce à de nombreux et excellents gâteaux, tu as su aussi adoucir les moments difficiles où les expériences finissaient tard sans être toujours concluantes. L'une de tes recettes fait même maintenant partie du patrimoine culinaire Quantronique… Bonne chance dans tes nouvelles activités.

Merci aussi à Maria-Luisa qui a pris le relais après Peter. Merci pour ta bonne humeur et pour ton aide précieuse lorsque je rédigeais ma thèse. Avec Benjamin Huard, vous formiez tous les deux une sacrée équipe au sous-sol sur la manipe courant-phase. Merci de m'avoir fait partager votre gros travail d'analyse de données expérimentales et de simulations numériques.

Grâce à Philippe Joyez, j'ai beaucoup progressé dans la compréhension de la supraconductivité mésoscopique. Merci pour le temps que tu as passé avec moi à discuter des réflexions d'Andreev. Pendant mon stage, tu m'avais aussi consacré beaucoup de ton temps à m'expliquer les machines de dépôt, les techniques du vide, de la cryogénie et la nanofabrication. Merci aussi d'avoir récupéré la Clio dans la descente enneigée de Chamrousse de retour d'un week-end ski !

Merci à Denis Vion. J'ai beaucoup bénéficié de ta pédagogie et de ton aide pour Mathematica et Sonnet. En plus tu étais toujours de bonne humeur. C'était aussi très utile de pouvoir te consulter lors des problèmes pour la fabrication des échantillons. Merci pour ton souci permanent d'expliquer aux autres les choses que tu connais.

Hugues Pothier a toujours été très disponible pour répondre à mes questions diverses. Merci à toi pour ton expertise TestPoint et toutes les bonnes idées pour les mesures lors des manipes PAMAR et courant-phase. J'ai bien apprécié ta confiance juste avant ma soutenance de thèse, lors de mes répétitions ! Merci aussi de m'avoir laissé quelques parts de gâteau pendant les « réunions » en salle café !

Merci à Pief Orfila pour son aide pour les équipements informatiques ainsi que ses conseils sur l'utilisation des machines de nanofabrication. Merci pour toutes tes

astuces qui m'ont, au jour le jour, rendu la vie plus facile dans le labo. Je te remercie aussi pour tes conseils avisés pour ma vieille Peugeot 309.

Merci à Pascal Sénat pour sa patience et son expertise quant à la fabrication des pièces mécaniques nécessaires aux expériences. Merci bien pour ta bonne volonté quand il fallait modifier les petits montages mécaniques quand je n'avais pas pensé à tout du premier coup…

La bonne ambiance du groupe tient aussi à tous les autres thésards et post-docs : Anne Anthore (merci pour tes cours du DEA de Grenoble), Grégoire Ithier, Hélène le Sueur (vivent les pizzas tardives du Guichet, quand la physique nous retenait au labo !), Abdel Aassime, Eddy Collin et Nicolas Boulant.

Je tiens à remercier Marcelo Goffman. C'était vraiment pratique de t'avoir à portée de main pour te poser des questions sur les expériences que Ronald Cron, mon prédécesseur, et toi même aviez faites ensemble. Merci aussi à Roland Lefèvre et Antoine Isambert qui partageaient la salle blanche et les équipements de nanofabrication.

Je tiens aussi à remercier Michel Juignet et Jean-Claude Tac du grand atelier. Merci aussi à Pierre Janvier pour la flexibilité qu'il a pu m'apporter tout au long de la thèse pour les commandes d'hélium que je ne prévoyais pas toujours assez en avance... Merci à Jean-Michel Richomme pour ses conseils techniques lors de mes passages au petit atelier. Merci aussi à Sandrine Thunin pour son accueil chaleureux et son aide précieuse dans les démarches administratives.

Tout au long de ma thèse, j'ai eu le plaisir de collaborer avec Alfredo Levy Yeyati et Juan Carlos Cuevas sur la théorie des expériences. Merci aussi à Raphaël Duprat pour son calcul sur les pas de Shapiro fractionnaires. Je tiens aussi à remercier Norman Birge, Phil Meeson et Joachim Ankerhold pour toutes les discussions instructives que j'ai eues avec eux.

Je suis reconnaissant envers Juan Carlos Cuevas et Marco Aprili d'avoir été rapporteurs, et envers Jan van Ruitenbeek, Christian Schönenberger, Vitaly Shumeiko et Roland Combescot d'avoir accepté de participer au jury.

Enfin, un grand merci à tous ceux qui sont venus me supporter lors de ma soutenance, et notamment à ceux qui savaient par avance qu'ils n'y comprendraient rien !

Table of contents

Introduction: The Josephson effect in superconducting atomic contacts

The Josephson effects are probably one of the most striking signatures of extended quantum coherent states of matter, like superfluids, superconductors, and the more recently achieved atomic Bose-Einstein condensates. Our description of these remarkable systems is based on the use of a single macroscopic wave function to account for the collective quantum state of a very large number of particles. The Josephson effects appear when one creates a weak-link allowing particles to flow between two reservoirs of these quantum systems, thereby establishing phase coherence between the two corresponding macroscopic wave functions.

These effects are named after B. D. Josephson who described them for the case of superconductors in 1962 [1]. He predicted that an electrical current could flow in absence of any voltage and that this supercurrent is driven by the phase difference δ between the two reservoirs. This so-called dc Josephson effect was first experimentally observed in 1963 by Anderson and Rowell [2]. Josephson also predicted that under a constant voltage bias V, ac currents should appear at a frequency $\nu_0 = V/\phi_0$, where $\phi_0 = h/(2e)$ is the flux quantum, the ratio of two fundamental constants of nature. This

second effect, known as the ac Josephon effect, was also first experimentally reported in 1963, by S. Shapiro [3].

Since then, the Josephson effects have also been explored in great detail in superfluids [4] and to some extent in Bose-Einstein condensates [5]. Furthermore, in the field of superconductivity these effects have been observed in fact in a variety of weak-links (tunnel junctions, proximity effect bridges, microbridges, point contacts…) [6, 7, 8], which have lead to numerous applications (radiation detectors, magnetometers, voltage standards…). Nevertheless, it was only in the 1990's [9] that a unifying picture, able to treat on the same footing all the different coupling structures, emerged in the framework of mesoscopic superconductivity.

This modern view of the Josephson effect, which is described in chapter 1, is based on the combination of two important concepts. The first one, coming from the field of mesoscopic physics, states that in a generic coherent structure electrical transport occurs through independent conduction channels [10], characterized by a set of transmission coefficients $\{\tau_i\}$ nicknamed the mesoscopic PIN code [11]. The second one is the concept of Andreev reflection, now regarded as the basic microscopic mechanism at the heart of superconductivity. The combination of these two concepts leads to a picture in which the Josephson coupling through an arbitrary weak-link is determined in each channel by two localized Andreev bound states[1]. The phase dependent energies of these states lie inside the superconducting gap between $-\Delta$ and $+\Delta$ (see Figure 1):

$$E_{\pm}(\delta, \tau) = \pm\Delta\sqrt{1-\tau\sin^2(\delta/2)}$$

The zero temperature Josephson coupling energy $E_J(\delta, \tau)$ for one channel is simply the energy of the Andreev ground state $E_J(\delta, \tau) = E_-(\delta, \tau)$.

[1] This description is valid only in the case where the channel is short compared with the superconducting coherence length ξ_0. If not, a new pair of Andreev state has to be considered each time the length exceeds a multiple of ξ_0.

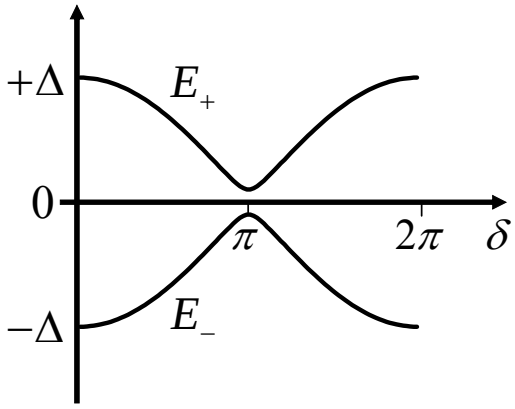

Figure 1: Energy spectra of the two Andreev bound states as a function of the phase difference between two superconducting electrodes connected through a single short channel of transmission $\tau = 0.99$ *.*

The two states carry opposite currents given by:

$$I_{\pm}(\delta, \tau) = \frac{2e}{\hbar}\frac{\partial E_{\pm}(\delta, \tau)}{\partial \delta} = \mp\frac{e\Delta}{2\hbar}\frac{\tau \sin(\delta)}{\sqrt{1-\tau \sin^2(\delta/2)}} \qquad (1)$$

This current-phase relationship for a single channel is the central prediction of the mesoscopic theory of the Josephson effect. It describes the equilibrium properties of the Josephson weak-link under a constant (or more generally adiabatic) phase bias. The net supercurrent flowing in a channel is determined by the imbalance in the populations of the two Andreev bound levels. The critical current of a channel is the maximum supercurrent that can be sustained in absence of any voltage. Beyond this value, a voltage develops across the system, i.e. transport becomes dissipative.

The theory also copes with this out-of-equilibrium situation. Essentially, this dissipative current is carried by multiple Andreev reflection (MAR) processes [12], which were observed as early as in 1963 [13, 14], and which can be understood in terms of a non-adiabatic evolution of the Andreev levels population [15, 16]. In its most fundamental form the theory predicts the time dependence of the current through a single channel of arbitrary transmission at finite voltage bias [15, 17, 18]. Under a constant voltage bias the phase evolves linearly in time following $\delta = 2\pi\nu_0 t$. Because the current phase relation (equation (1)) is non-sinusoidal, ac currents should appear at the Josephson frequency and all its harmonics. In general, the time dependence of the current writes in this case:

$$I(V,t)=\sum_{n=-\infty}^{+\infty} I_n(V)e^{in2\pi\nu_0 t}$$

The dc component $I_0(V)$ contains both the supercurrent at zero voltage and the dissipative current carried through MAR at finite voltage. Actually, it is only very recently that the progressive and continuous transformation of the supercurrent into MAR current as the voltage is increased could be explained by taking into account the effect of an electromagnetic environment in a self-consistent manner [19].

The goal of this thesis work is to explore the validity of this mesoscopic point of view of the Josephson effect. For this purpose, we have performed several experiments on superconducting atomic size contacts, which are fully characterized quantum coherent conductors accommodating just a small number of channels. Because we know how to measure from their current-voltage characteristics their mesoscopic PIN code [20], which can be varied in-situ over a wide range, these contacts allow for a direct comparison between theory and experiment with no adjustable parameters. We report experiments on three different aspects of the Josephson effect:

- The supercurrent peak around zero voltage,
- The ac Josephson currents (Shapiro resonances and photon assisted multiple Andreev reflections),
- The current-phase relationship.

This work completes and extends the one that Ronald Cron, my predecessor in the Quantronics group, carried out in 2001 [21].

The supercurrent peak around zero voltage

How the Josephson effect actually manifests itself in an experiment depends on the way the structure is biased, and on the amplitude of the fluctuations (both thermal and quantum) around the mean bias conditions. In practice one can distinguish the case when a Josephson structure is dissipatively biased using either an external voltage or current source, or when it is inserted in a totally superconducting loop in which case it is phase-biased. During this thesis work we have used all possible bias schemes.

Under dissipative bias, a Josephson atomic contact develops in its current-voltage characteristics a so-called "phase diffusion branch" in which the voltage is actually not zero, albeit small (see Figure 2).

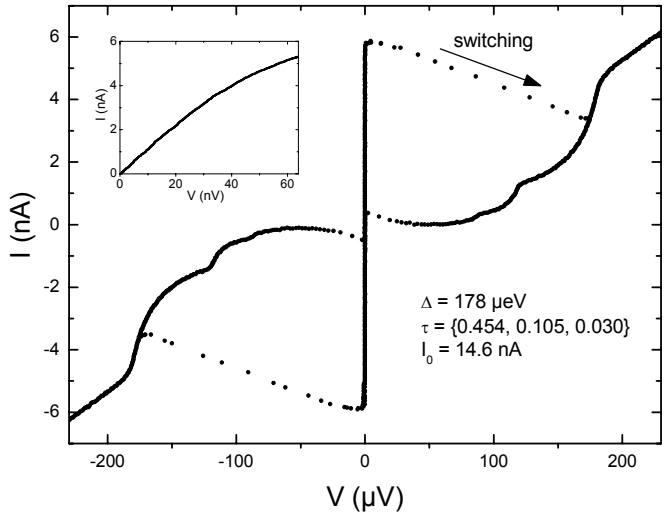

Figure 2: IV characteristic of a contact in a current bias setup. Below a threshold value of the current, the system stays on the phase-diffusion branch at very small voltage (inset). Above this threshold value, the contact switches to a finite voltage state (typically of the order of the superconducting gap Δ/e) determined by the load-line of the setup.

This is due to the fact that for contacts containing only a few channels the Josephson coupling energy is small, and the role of thermal fluctuations is not negligible even at the lowest achieved temperatures.

In a current-bias mode, as the current is increased the contact switches at some point from this branch to a state in which a finite voltage of the order of the superconducting gap Δ/e develops. The current at which the switching occurs is a stochastic variable and its value approaches the critical current at low enough temperature if the contact is embedded in an appropriate electromagnetic environment that damps the fluctuations of the phase at high frequencies [22]. Goffman *et al.* [23] already carried out detailed measurements of this kind in atomic contacts and found a quite good agreement with the predictions of equation (1), but for very highly transmitting channels. It is important to note that the switching instability prevents from observing the negative differential resistance parts of the IV characteristic.

In the voltage-biased experiment reported in chapter 2, we go one step further. A small shunt resistor placed in parallel with the contact prevents the structure from switching and makes it possible to measure the entire supercurrent peak [24], of which the phase diffusion branch is only the positive differential resistance part (see Figure 3).

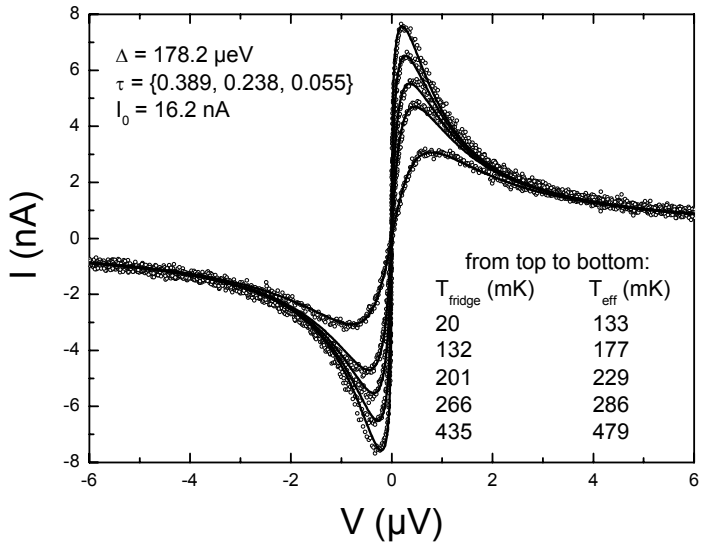

Figure 3: Supercurrent peak for an aluminum atomic contact containing three channels for five values of the refrigerator temperature T_{fridge}. The full lines are the predictions of the theory based on the current-phase relationship, using the independently measured set of transmissions of the contact and parameters of the biasing setup. The temperature T_{eff} of the dissipative elements of the environment was the only adjustable parameter and is higher than the refrigerator temperature due to spurious noise.

The shape of the peak is essentially determined by the electromagnetic environment close to the contact. Its height is determined by the ratio $k_B T / E_J\left(\{\tau\}\right)$ which compares the energy of thermal fluctuations in the bias resistor with the Josephson energy characteristic of the coupling between the two reservoirs.

We show that experimental supercurrent peaks are very well described by a model taking into account the phase dynamics with no other adjustable parameter than the temperature of the environment (the admittance of the electromagnetic environment and the mesoscopic PIN code of the contact are both independently measured). We did not observe with this setup significant deviations from the expected behavior even for the

largest transmissions explored. However, due to spurious noise, the temperature used to fit the data is higher than the actual fridge temperature.

The ac Josephson currents

Shapiro resonances

The experiments reported in chapter 3 aimed at probing not only the dc component $I_0(V)$ of the current but also its ac components. To do so, an external microwave signal of frequency ν_r is applied to the contact. The beatings of this signal with the Josephson currents when their frequencies are commensurate ($q\nu_0 = p\nu_r$, with p, q integer numbers) give rise to resonances on the dc IV characteristic of the contact. These so-called Shapiro resonances are replicas of the supercurrent peak centered at well defined values of the dc voltage, given by:

$$V = \frac{p}{q}\phi_0\nu_r .$$

Cuevas *et al*. [25] have calculated the zero temperature amplitude of these resonances for a channel of arbitrary transmission in the case of an ideal dc voltage-bias. Furthermore, during the course of this thesis work, and motivated by our results, a Fokker-Planck treatment of the dynamics of the phase in a contact under irradiation and embedded in a finite impedance environment was developed by Duprat & Levy Yeyati [26].

We find that on contacts with channels of moderate transmissions (up to $\tau \sim 0.8$), only integer Shapiro resonances ($q = 1$) are visible on the IV characteristics (see Figure 4). This is so because the current phase relation is in this case still very close to the sine function characteristic of tunnel junctions. The predictions of the model of replicas, which coincides exactly with the more rigorous Fokker-Plank treatment in this case, describe the experimental results on a quantitative basis.

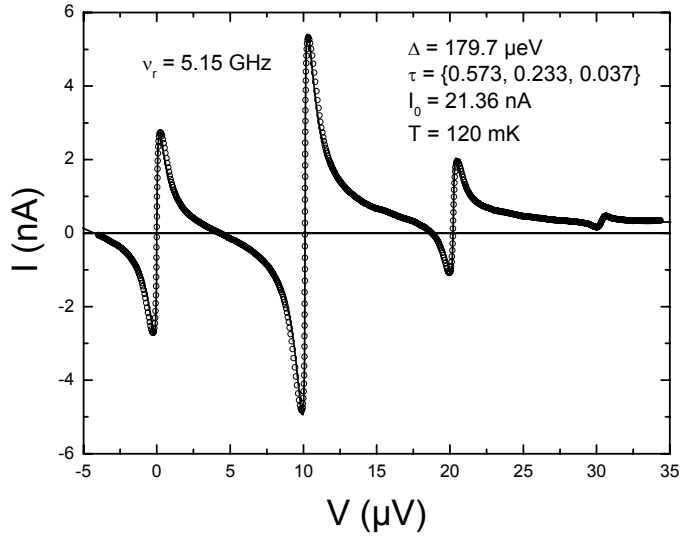

Figure 4: Shapiro resonances for an atomic contact containing only low transmission channels. Only integer resonances are observed. Dots are experimental results at $T_{fridge} = 20$ mK. *The microwave frequency was* $\nu_r = 5.150$ GHz. *The full line is the prediction of the theory by Duprat & Levy Yeyati [26] with no adjustable parameters other than the effective temperature (*$T = 120$ mK*).*

For contacts containing highly transmitting channels, the important qualitative outcome is that, in addition to the well known integer Shapiro resonances, fractional resonances ($q > 1$) also appear (see Figure 5). They are the direct signature of a non-sinusoidal current-phase relation. However, the fractional resonances are very small compared to the integer ones. This is due to the fact that thermal phase fluctuations have a stronger effect on the former than on the latter [26, 27]. If the amplitudes of the integer resonances and of the supercurrent peak correspond to a noise temperature T, then for a fractional resonance p/q the effect of temperature is amplified by a factor q. Moreover, the background itself is deeply modified by the microwaves (see below). Therefore, the IV characteristics are more complex, as the Shapiro resonances superimpose on top of the background current due to MAR which is then sizeable even at very low voltages.

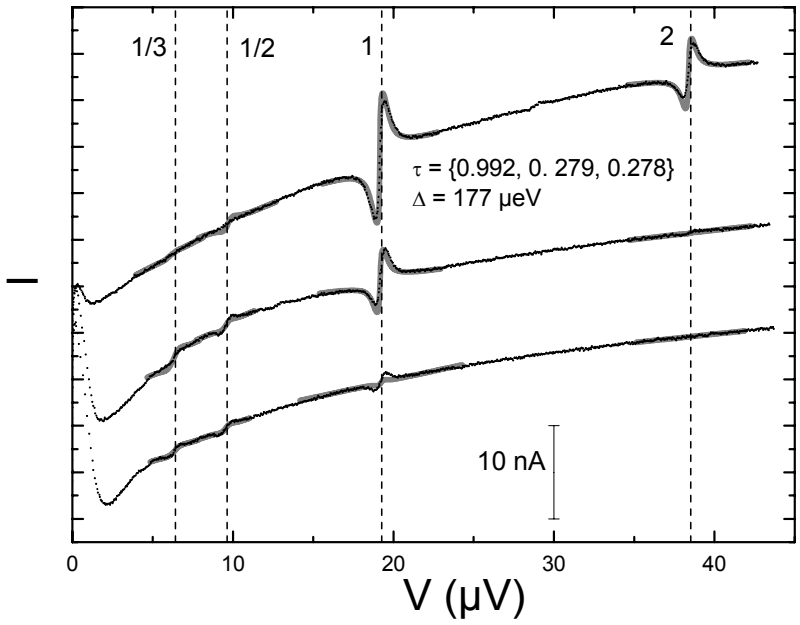

Figure 5: Shapiro resonances for an atomic contact containing a high transmission channel. The external microwave frequency was $\nu_r = 9.3156$ GHz. *Small fractional resonances are observed. Black dotted lines are experimental results. The full grayed lines are the predictions of the theory of replicas with no other adjustable parameter than the temperature.*

Photon assisted multiple Andreev reflections (PAMAR)

As mentioned before, when microwaves are applied to a contact, Shapiro resonances appear on the dc IV characteristic superimposed on the background MAR current. The background itself is also modified by the microwaves due to absorption or stimulated emission of one or several photons during the transfer of electronic charges through MAR processes (see Figure 6). The voltage threshold for the onset of an *m*-photon assisted MAR process of order n is given by:

$$eV = \frac{2\Delta}{n} \pm \frac{mh\nu_r}{n} \qquad (2)$$

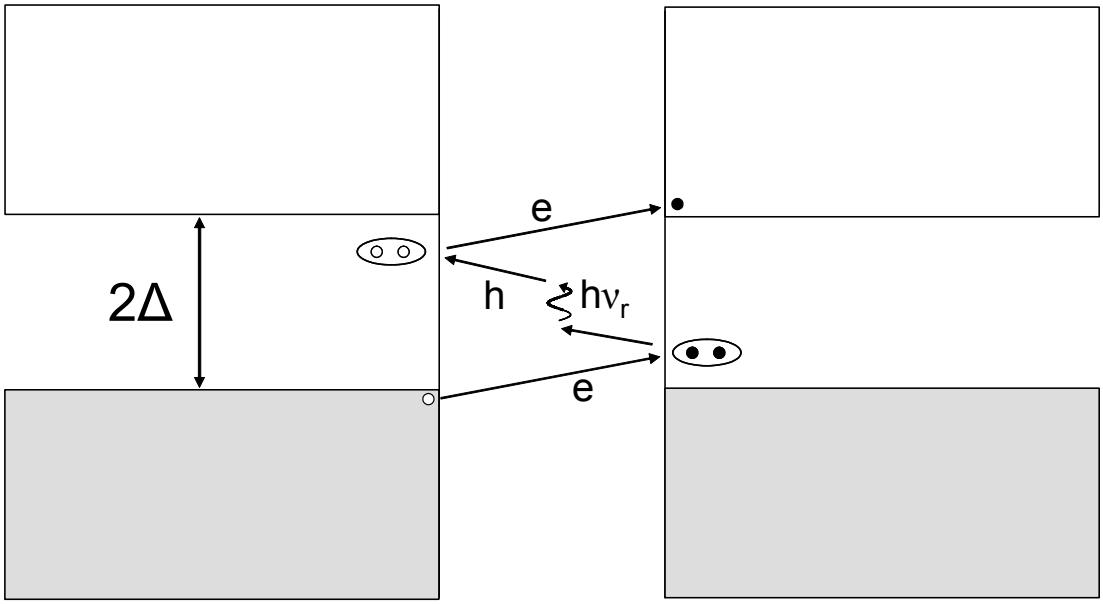

Figure 6: Schematic representation of a one-photon assisted MAR process of order three. The grayed rectangles represent the occupied states in the left and right electrodes which are biased at a constant voltage V. Empty states (white rectangles) are at a distance 2Δ *in energy from the occupied states. This particular MAR process is a three step process, involving an Andreev reflection at each electrode, which transfers all in all three electronic charges from left to right. In the case illustrated here, a photon is absorbed by the hole traveling to the left during the second step, thus lowering the voltage threshold of the full process from* $2\Delta/(3e)$ *to* $(2\Delta - h\nu_r)/(3e)$.

Dayem and Martin [28] already pointed out the effect of microwave on tunneling between two superconductors in an experiment on a Josephson tunnel junction. Tien and Gordon [29] could qualitatively account for this effect with their calculation on multiphoton assisted tunneling. Later on, Gregers-Hansen [30], in an experiment on Dayem microbridges, observed that in presence of microwave the subgap structure developed sidebands at values given by equation (2). But it is only recently that the size of these sidebands could be predicted using, once again, the full microscopic quantum theory [25].

We show on Figure 7 an example of the differential conductance of a voltage-biased contact measured as a function of voltage in presence of microwaves. As shown in chapter 3, we find a semi-quantitative agreement between the experimental results and the predictions of the existing theory [25]. Note however that the latter doesn't include the effect of the finite impedance and finite temperature of the environment.

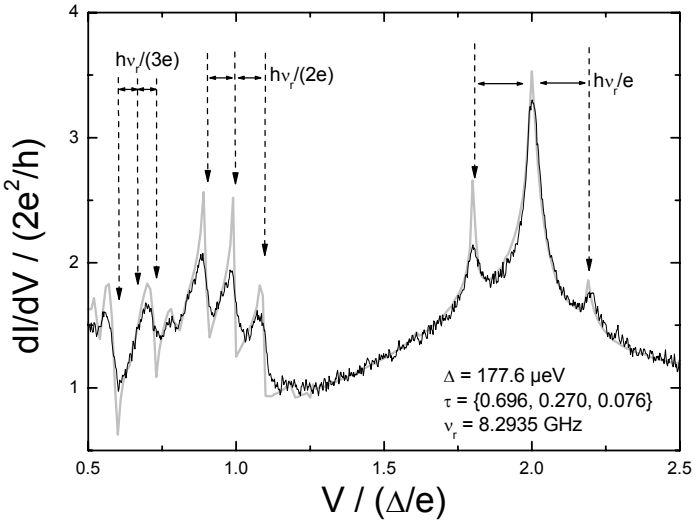

Figure 7: Measured (black line) differential conductance of an atomic contact in presence of microwave irradiation at $\nu_r = 8.2935$ GHz. *The sidebands around* $2\Delta/e$ *correspond to photon assisted tunneling of single electrons from one superconducting electrode to the other. The sidebands around* $2\Delta/(2e)$ *and* $2\Delta/(3e)$ *correspond to photon assisted MAR of order two and three, respectively. The grayed line is the prediction of the theory of photon assisted multiple Andreev reflections (for a perfectly voltage biased contact), in which we have plugged the independently measured transmissions of the contact.*

The current phase relationship

A direct measurement of the equilibrium current phase relationship requires to phase-bias the atomic contact. This can be achieved by placing the contact in a superconducting loop and applying an external magnetic flux. Koops *et al*. [31] carried out such a measurement in Nb atomic contacts. However, the direct comparison with theory was lacking since the transmissions couldn't be measured in this setup. Placing the contact in a superconducting loop makes it difficult, if not impossible, to voltage-bias it in order to extract the mesoscopic PIN code from the IV.

We have designed and implemented an experiment, described in chapter 4, which allows for the two biasing schemes (voltage and phase) to be achieved in the same

setup. In this experiment, the atomic contact is placed in parallel with a large Josephson tunnel junction (see Figure 8), with a critical current I_t^0 one order of magnitude larger than the one of the contact. The contact forms with the tunnel junction a superconducting loop (an atomic contact-SQUID) hence allowing for an almost perfect phase bias. However, if an external bias current I larger than I_t^0 is applied through the device, the tunnel junction acts as a reversible superconducting switch that "opens" electrically the loop. A voltage develops across the parallel setup which allows for the measurement of its IV. As on the other hand the contact can be itself completely open physically, it is possible to calibrate separately the contribution to the dissipative current of the tunnel junction alone.

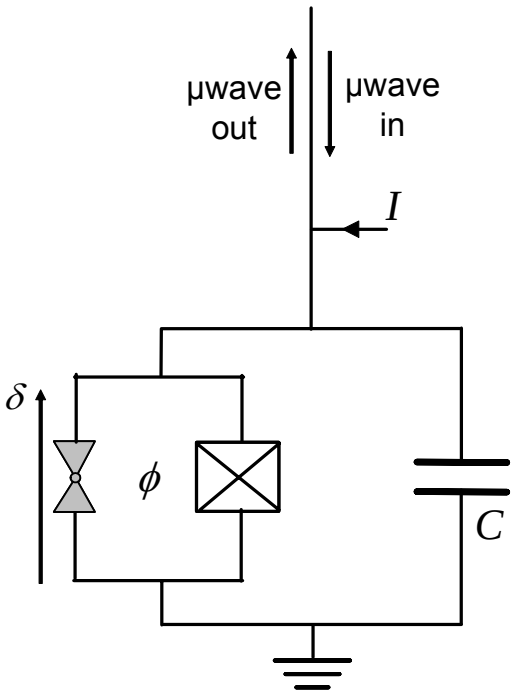

Figure 8: Atomic contact-SQUID setup used for the direct measurement of the current-phase relation of an atomic contact (triangular symbols with central dot). δ is the superconducting phase difference across the atomic contact. The crossed box is a Josephson tunnel junction. An external magnetic flux ϕ is applied to the small superconducting loop connecting the two elements. The external capacitor C forms a resonator with the Josephson inductance of the device. The bias line allows to inject a dc bias I and a microwave excitation, and to recover the microwave signal reflected by the device.

We have used two methods to measure the current-phase relationship of the contacts with this setup. The first one relies on the direct measurement of the switching current

of the atomic contact-SQUID as a function of the external flux, as shown in Figure 9. Essentially, the modulations δI^S with the external flux ϕ of the average total switching current around the switching current of the bare junction correspond to the current-phase relation of the contact. The experimental data are reasonably well described by the theoretical current-phase relation calculated using the independently measured mesoscopic PIN code.

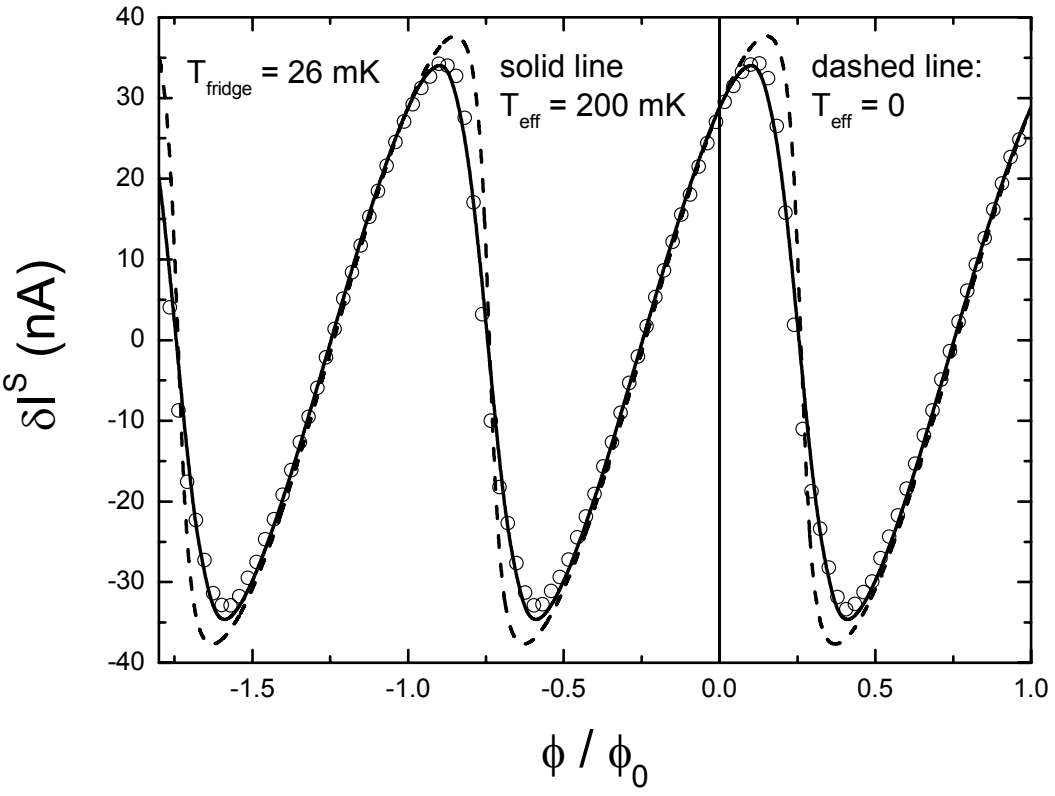

Figure 9: Modulation δI^S of the SQUID mean switching current as a function of the external flux ϕ threading the loop. Dots are experimental results. The measurements were performed at 26 mK. Lines are theoretical predictions calculated from the independently measured mesoscopic pin code of the contact ($\tau = \{0.983\}$). The dashed line is the zero temperature prediction. The solid line is the prediction at an effective noise temperature of 200 mK.

The second method is based on the fact that any Josephson structure behaves as an inductor with an inductance inversely proportional to the first derivative of its current phase relation:

$$L_{-}(\delta) = \frac{\hbar}{2e} \frac{1}{\partial I_{-}(\delta) / \partial \delta}$$

By adding a suitable capacitor in parallel with the atom-SQUID one creates an *LC*-resonator which can be probed near its resonance frequency by a very small external microwave field. The signal reflected by the oscillator carries all the information on the Josephson inductance of the contact and thus on its current-phase relation. As shown for example in Figure 10, the experimental data compare qualitatively quite well with the predictions of the theory for the reflection coefficient R_ν at the frequency ν.

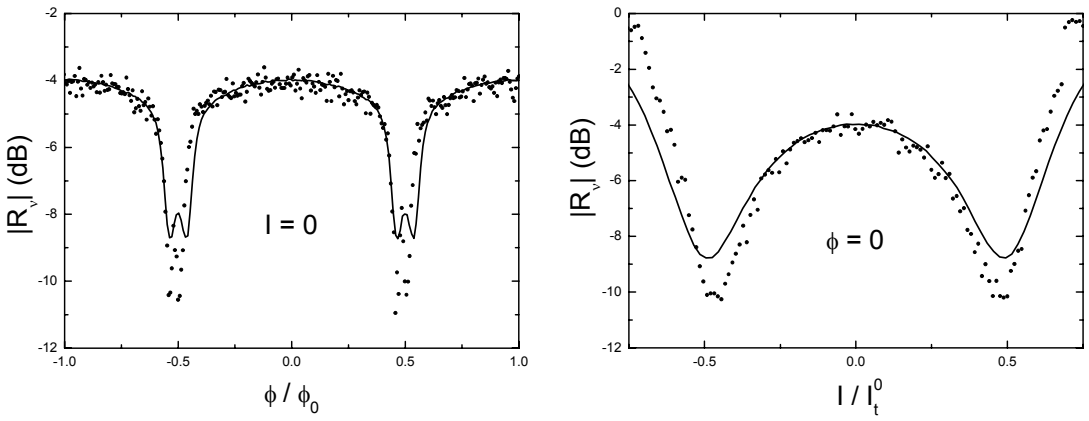

Figure 10: Reflection coefficient measured as a function of the external flux ϕ at $I = 0$ (left panel) and as a function of the bias current I at $\phi = 0$ (right panel). I_t^0 is the critical current of the Josephson tunnel junction. The atomic contact is the same as in Figure 9 ($\tau = \{0.983\}$). Dots are experimental results. The solid line is the zero temperature theoretical prediction calculated from the independently measured mesoscopic pin code of the contact.

To conclude this introduction, we think that the experiments on superconducting atomic contacts described in this thesis illustrate the profound unity behind a variety of transport phenomena observed in superconducting weak links. They firmly support the idea that the basic microscopic transport mechanism behind ac Josephson supercurrents

is Andreev reflection, or more precisely multiple Andreev reflections. During this thesis work we strongly interacted with the theory group formed by Juan Carlos Cuevas (then at Karlsruhe), Alvaro Martín Rodero and Alfredo Levy Yeyati in Madrid, and very often developments on one side motivated new developments on the other one, leading to a deeper understanding of superconducting contacts under different bias conditions. For example, we have now a clear picture on how the supercurrent transforms continuously into the MAR dissipative current at finite voltage. In fact, there is no fundamental difference between the two, as both contributions to the total current can be treated on the same footing within a formalism that takes into account the electromagnetic environment of the contact [19]. We have also put into evidence the richness of the spectrum of the ac currents in highly transmitting junctions, through the detection of both fractional Shapiro resonances and photon assisted MAR. Finally, although the experimental results are still preliminary, our direct measurements of the current-phase relation provide strong support to the picture of transport through Andreev bound levels.

The experiments reported here suffered from several limitations, and there is certainly room for technical improvement in many aspects. First, in all three experiments the effective temperature was larger than expected, indicating that some noise was not completely filtered out, despite our efforts. It should be possible to really cool down the electrons in these devices to the base temperature of the refrigerator. Secondly, a finer tuning of the dissipative elements of the environment should help to get narrower, and thus easier to detect fractional Shapiro resonances. Finally, the microwave reflectometry experiment could benefit from the use of cryogenic amplifiers.

From the physics point of view, several questions remain unanswered. First, is it possible to perform the spectroscopy of Andreev levels? Are the relaxation and dephasing times long enough [32] to perform coherent manipulations within the Andreev doublet of each channel [33, 34]? Second, when the series impedance of the environment becomes larger than what we have implemented here, the classical treatment of the phase dynamics that we have used all along this thesis ceases to be valid and has to be replaced by a quantum description. In this situation, multiple Andreev reflections are subject to dynamical Coulomb blockade [35] and a detailed experimental confirmation of this is still missing [21]. Finally, the description of the Josephson effect in terms of Andreev bound levels is universal, and it would be interesting to explore this physics with quantum point contacts tailored in two-

dimensional electron gases, with superconductivity induced by the proximity effect. In this case the ideal situation of a single channel of tunable transmission can be accessed.

References of the introduction

[1] B. D. Josephson, Phys. Lett. **1**, 251 (1962).

[2] P. W. Anderson and J. M. Rowell, Phys. Rev. Lett. **10**, 230 (1963).

[3] S. Shapiro, Phys. Rev. Lett. **11**, 80 (1963).

[4] O. Avenel and E. Varoquaux Phys. Rev. Lett. **60**, 416-419 (1988); J. C. Davis, R. E. Packard, Rev. Mod. Phys., **74,** 741, (2002).

[5] M. Saba *et al., Science* **307**, 1945 (2005); Cataliotti *et al*. Science **293**, 843 (2001).

[6] K. K. Likharev, Rev. Mod. Phys. **51**, 101 (1979).

[7] A. Barone and G. Paterno, *Physics and Applications of the Josephson Effect* (Wiley, New York, 1982).

[8] A. A. Golubov, M. Yu. Kupriyanov, and E. Il'ichev, Rev. Mod. Phys. **76**, 411 (2004).

[9] F. W. J. Hekking, G. Schön, and D. V. Averin, Proceedings of the NATO Advanced Research Workshop on Mesoscopic Superconductivity (1994).

[10] R. Landauer, IBM J. Res. Dev. **1**, 223 (1957); Philos. Mag. **21**, 863 (1970).

[11] R. Cron *et al*., Phys. Rev. Lett. **86**, 4104 (2001).

[12] T .M. Klapwijk, G. E. Blonder, M. Tinkham, Physica B **109 & 110**, 1657 (1982).

[13] B. N. Taylor and E. Burstein, Phys. Rev. Lett. **10**, 14 (1963).

[14] C. J. Adkins, Rev. Mod. Phys. **36**, 211 (1964).

[15] D. Averin and A. Bardas, Phys. Rev. Lett. **75**, 1831 (1995).

[16] E. N. Bratus' *et al.*, Phys. Rev. B **55**, 12666 (1997).

[17] J. C. Cuevas, A. Martín-Rodero, and A. Levy Yeyati, Phys. Rev. B **54**, 7366 (1996).

[18] E. N. Bratus', V. S. Shumeiko, and G. Wendin, Phys. Rev. Lett. **74**, 2110 (1995).

[19] A. L. Yeyati *et al.*, in preparation.

[20] E. Scheer *et al.*, Phys. Rev. Lett. **78**, 3535 (1997).

[21] R. Cron, *Atomic Contacts: a Test-Bed for Mesoscopic Physics*, Ph.D. thesis, Université Paris 6 (2001);

http://www-drecam.cea.fr/drecam/spec/Pres/Quantro/Qsite/archives/theses/RCronThesis.pdf.

[22] P. Joyez *et al.*, J. Supercond. **12**, 757 (1999).

[23] M. F. Goffman *et al*., Phys. Rev. Lett. **85**, 170 (2000).

[24] A. Steinbach *et al.*, Phys. Rev. Lett. **87**, 137003 (2001).

[25] J. C. Cuevas *et al*., Phys. Rev. Lett. **88**, (2002).

[26] R. Duprat and A. Levy Yeyati, Phys. Rev. B **71**, 054510 (2005).

[27] E. Ben-Jacob and D. J. Bergman, Phys. Rev. A **29**, 2021 (1984).

[28] A. H. Dayem and R. J. Martin, Phys. Rev. Lett. **8**, 246 (1962).

[29] P. K. Tien and J. P. Gordon, Phys. Rev. **129**, 647 (1963).

[30] P. E. Gregers-Hansen *et al*., Phys. Rev. Lett. **31**, 524 (1973).

[31] M. C. Koops, G. V. van Duyneveldt, and R. de Bruyn Ouboter, Phys. Rev. Lett. **77**, 2542 (1996).

[32] M. A. Despósito and A. Levy Yeyati, Phys. Rev. B **64**, 140511 (2001).

[33] A. Zazunov *et al.*, Phys. Rev. Lett. **90**, 087003 (2003).

[34] A. Zazunov, V. S. Shumeiko, and G. Wendin, Phys. Rev. B **71**, 214505 (2005).

[35] A. Levy Yeyati, J. C. Cuevas, and A. Martín-Rodero, Phys. Rev. Lett. **95**, 056804 (2005).

Chapter 1: Mesoscopic superconductivity

As pointed out in the introduction, the goal of this thesis work is to explore the validity of the modern description of the Josephson effects that emerged in the 1990's in the general framework of mesoscopic physics. This description is based on two cornerstone concepts. On the one hand, the idea of conductance channels, central to the Landauer scattering picture of coherent transport. On the other hand, the idea of Andreev reflection, central to superconducting transport. This chapter will therefore be devoted to a presentation of these two concepts and of their combination, which leads to a unifying picture of electronic transport in Josephson weak links.

1 Scattering formalism of transport

The idea behind this formalism introduced by Landauer [1] in 1957 is that an electronic transport experiment through a coherent device can be viewed as a scattering problem for electronic waves. Electrons[1] are injected from reservoirs into the propagating states of ideal leads. The coherent conductor acts as a scattering center, where the electrons can either be reflected or transmitted (see Figure 1).

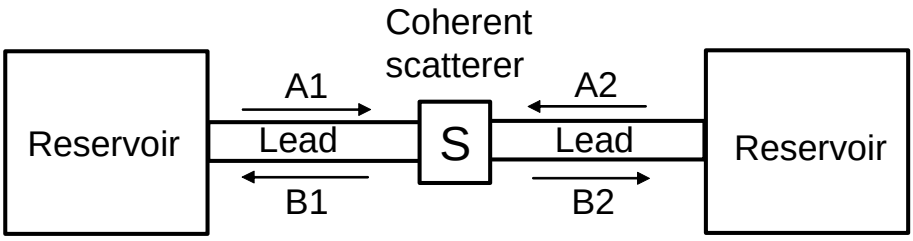

Figure 1: Schematic representation of the electronic transport through a quantum coherent conductor. Electrons from the reservoirs propagating through the leads are fed onto the coherent scatterer. They can be either back-scattered (reflected) or forward-scattered (transmitted) with a probability depending on the microscopic details of the scatterer.

The reservoirs are supposed to be perfect "black-bodies" which absorb all electrons incoming on them. The leads, which confine laterally the electrons, can be viewed as

[1] For the sake of simplicity, we consider here a fluid of non-interacting electrons. But the arguments apply to more general quasiparticles.

electron “waveguides” along which only a finite number of modes can propagate. The number of modes scales like $k_F^2 A$, where A is the cross section of the leads and k_F the Fermi wave vector of the electrons in the material.

The scattering matrix $\underline{\underline{S}}$ relates the amplitudes of the incoming modes to those of the outgoing ones on both sides of the coherent scatterer:

$$\begin{pmatrix} B_1 \\ B_2 \end{pmatrix} = \underline{\underline{S}} \begin{pmatrix} A_1 \\ A_2 \end{pmatrix},$$

$$\underline{\underline{S}} = \begin{pmatrix} \underline{\underline{s_{11}}} & \underline{\underline{s_{12}}} \\ \underline{\underline{s_{21}}} & \underline{\underline{s_{22}}} \end{pmatrix}$$

The off diagonal blocks describe the transmission of the electronic waves and the diagonal ones represent their reflection. The $\underline{\underline{S}}$ matrix verifies $\underline{\underline{S}}^{\dagger}\underline{\underline{S}} = \underline{\underline{S}}\underline{\underline{S}}^{\dagger} = 1$ because of particle conservation.

It is possible to change the basis of the propagating states in the leads to reduce the scattering problem to independent conduction channels. These are simply the eigenmodes of the scattering problem. In this new basis, the scattering matrix writes:

$$\underline{\underline{S'}} = \begin{pmatrix} -i\underline{\underline{r}} & \underline{\underline{t}} \\ \underline{\underline{t}} & -i\underline{\underline{r}} \end{pmatrix},$$

where $\underline{\underline{r}}$ and $\underline{\underline{t}}$ are real, positive and diagonal matrices. The coefficients of the matrices $\underline{\underline{r}}$ and $\underline{\underline{t}}$ are the reflection and transmission probability amplitudes of the independent conduction channels. They carry all the information necessary to describe the electronic properties of the conductor.

For example, the conductance G of a quantum coherent conductor can be simply expressed in terms of the coefficients of the matrix $\underline{\underline{t}}$ as:

$$G = G_0 \mathrm{Tr}\left\{\underline{\underline{t}}^{\dagger}\underline{\underline{t}}\right\} = G_0 \sum_i \tau_i \ ,$$

where $G_0 = 2e^2/h \approx 77\ \mu\text{S} \approx (12.927\ \text{k}\Omega)^{-1}$ is the conductance quantum, and the $\tau_i = |t_i|^2$ are the eigenvalues of the $\underline{\underline{t}}^{\dagger}\underline{\underline{t}}$ matrix, or transmission probabilities.

This is the famous Landauer formula. In this formula, the coefficients t_i are supposed to be energy independent. This assumption is justified in the experiments presented here, where the maximum voltage applied across the atomic contacts is of the order of 1 meV and the Fermi energy for aluminum is 11.7 eV.

Since the late 1980's, many experiments have been carried out that support the validity of this scattering formalism. Different physical properties have been measured in various kinds of mesoscopic conductors and structures.

In seminal experiments, B. J. van Wees *et al.* [2], and D. A. Wharam *et al.* [3] showed that in point contacts tailored in a two-dimensional electron gas, the conductance changes in steps of $2e^2/h$ as conduction channels open one by one when the width of the contact is increased with an electrostatic gate. This is due to the quantization of transverse electronic modes in the contact region.

Measuring the subgap structure on the IV characteristic of superconducting single atom contacts Scheer *et al.* [4] devised a method to obtain the ensemble of the transmission probabilities $\{\tau_i\}$. Because most of the transport properties depend in fact only on these probabilities, the ensemble $\{\tau_i\}$ has been nicknamed the mesoscopic pin code of the contact. Later on, using this method, Scheer *et al.* [5] showed that the number of channels in a one-atom contact is determined by the number of valence orbitals of the atom at the constriction.

The scattering formalism can also account for the fluctuations of the current through a quantum coherent conductor. Of course, at finite temperature noise arises because the occupation number of the states in the reservoirs fluctuate. But even at zero temperature, i.e. in absence of fluctuations in these occupation numbers, the current in the leads fluctuates due to the stochastic nature of the scattering events in the conductor. Obviously, the zero temperature noise should vanish in the vanishing transmission limit because in this case the conductor is an open circuit. It should also vanish for perfect transmission since no scattering events occur in this case. At low frequency, the spectral density of the current fluctuations through a quantum coherent conductor with a mesoscopic pin code $\{\tau_1, ..., \tau_N\}$ is given by [6, 7]:

$$S_I\left(V,\, T,\, \{\tau_1,\, ...,\, \tau_N\}\right) = 2eV\coth\left(\frac{eV}{2k_BT}\right)G_0\sum_{i=1}^{N}\tau_i\left(1-\tau_i\right) + 4k_BTG_0\sum_{i=1}^{N}\tau_i^{\,2} \quad (1)$$

where V is the voltage across the conductor and T the temperature.

When $\frac{eV}{k_BT} \ll 1$, (1) simply rewrites:

$$S_I\left(\{\tau_1,\, ...,\, \tau_N\}\right) = 4k_BTG_0\sum_{i=1}^{N}\tau_i = 4k_BTG\,.$$

This is the spectral density of the Johnson-Nyquist noise.

In the opposite limit, $\frac{eV}{k_BT} \gg 1$, the spectral density is given by:

$$S_I\left(V,\, T,\, \{\tau_1,\, ...,\, \tau_N\}\right) = 2eI\left(1-\sum_{i=1}^{N}\tau_i^{\,2}\Big/\sum_{i=1}^{N}\tau_i\right).$$

This is shot noise, although reduced from its Poissonian limit $2eI$ by the Fano factor $F\left(\{\tau_1,\, ...,\, \tau_N\}\right) = 2eI\left(1-\sum_{i=1}^{N}\tau_i^{\,2}\Big/\sum_{i=1}^{N}\tau_i\right)$. This fact was beautifully demonstrated in the mid 1990's by Reznikov *et al.* [8] and by A. Kumar *et al.* [9] on 2D quantum point contacts. Later on, Cron *et al.* [10] measured this noise reduction in normal multichannel atomic contacts and found a quantitative agreement with the theoretical predictions when the independently measured transmissions were plugged in (1).

The thermopower of atomic-size metallic contacts is another physical quantity that has been investigated. B. Ludolph and J. M. van Ruitenbeek [11] found good agreement with the calculation achieved by E. N. Bogachek *et al*. in 1996 [12] within the framework of the scattering formalism and in the linear response approximation.

It is important to note that, if the noise and the conductance are entirely determined by just the mesoscopic pin code of the conductor, other physical quantities can also depend on the coefficient of the $\underline{\underline{r}}$ matrix. This is the case for example for the tensile force of a one-atom contact when it is stretched [13, 14]. Indeed the mechanical stability comes from electrons delocalized between the two sides of the one-atom constriction. In this sense, conduction channels can be seen as metallic bonds whose strength depends on

the interference of right and left moving electrons at the constriction. Therefore, the full information on the phase of the $\underline{\underline{S}}$ matrix coefficients is necessary.

In conclusion, the scattering formalism is a powerful framework to describe transport properties of mesoscopic structures. To describe transport in structures involving superconductors, one needs to add just the concept of Andreev reflection, that we describe in the next paragraph.

2 Andreev reflection - Bogoliubov de Gennes equations

The most general theory of superconductivity, able to deal with inhomogeneous systems (disordered superconductors, structures involving normal-superconductor interfaces…), is based on the so-called Bogoliubov de Gennes equations.

In the electron-hole representation the superconducting hamiltonian $\hat{H}_S$ writes [15]:

$$\hat{H}_S = \sum_k \xi_k \left(c_k^\dagger c_k - b_k^\dagger b_k \right) - \Delta c_k^\dagger b_k - \Delta^* b_k^\dagger c_k$$

where $c_k^\dagger$ and c_k are the creation and annihilation operators of the normal state electron quasiparticles with spin up, and $b_k^\dagger$ and b_k are those for holes with spin down. The energies of the normal state quasiparticles are ξ_k for the electrons and $-\xi_k$ for the holes of same wavevector *k*. The effective electron-electron interaction responsible for superconductivity corresponds to the electron and hole states of the same wave vector (and opposite energies $\pm\xi_k$ with respect to the chemical potential) being coupled through the pairing potential Δ. Within this framework, the superconducting quasiparticles are coherent superpositions of a normal state electron of spin up and its time-reversed counterpart, i.e. a hole of spin down.

The Bogoliubov de Gennes equations express this physics in a form that allows to deal with inhomogeneous structures. They consist in two coupled Schrödinger equations for the two-component wavefunction of the quasiparticles. In one dimension, they write:

$$\begin{pmatrix} H_N(x) & \Delta(x) \\ \Delta^*(x) & -H_N^*(x) \end{pmatrix} \begin{pmatrix} u(x) \\ v(x) \end{pmatrix} = E \begin{pmatrix} u(x) \\ v(x) \end{pmatrix} \qquad (2)$$

where $H_N(x) = -\frac{\hbar^2}{2m}\frac{d^2}{dx^2} + U(x) - \mu$ is the normal state hamiltonian, $U(x)$ is the potential seen by the electrons, and μ is the chemical potential. Δ is the complex superconducting order parameter that couples the two components of the vector $\begin{pmatrix} u(x) \\ v(x) \end{pmatrix}$ describing the quasiparticle. The solutions of equation (2) can be chosen so that the upper component of the vector represents the "electron" amplitude of the quasiparticle, and the lower component its "hole" amplitude. In what follows we will assume free electrons and no magnetic field, so that $U(x) = 0$ and $H_N = H_N^*$. One searches for solutions of the Bogoliubov de Gennes equations of the general form:

$$\begin{cases} \begin{pmatrix} u(x) \\ v(x) \end{pmatrix} = \begin{pmatrix} u_0 \\ v_0 \end{pmatrix} e^{ikx} \\ \Delta(x) = |\Delta| e^{i\phi(x)} \end{cases}.$$

where ϕ is the space dependent phase of the local order parameter The solutions can be classified in two types. There are electron-like $\begin{pmatrix} u^e(x) \\ v^e(x) \end{pmatrix} = \begin{pmatrix} u_0^e \\ v_0^e \end{pmatrix} e^{\pm ik_e x}$, or hole-like quasiparticles $\begin{pmatrix} u^h(x) \\ v^h(x) \end{pmatrix} = \begin{pmatrix} u_0^h \\ v_0^h \end{pmatrix} e^{\pm ik_h x}$, in the sense that this is what they describe when $\Delta \to 0$, or when $|E| \gg |\Delta|$.

There are no propagating solutions for $|E| < \Delta$ and the density of states $n(E)$ (see Figure 2) develops a gap and a divergence at the gap edges:

$$n(E) = \begin{cases} n_F \dfrac{|E|/|\Delta|}{\sqrt{(E/|\Delta|)^2 - 1}} & |E| \geq |\Delta| \\ 0 & |E| < |\Delta| \end{cases},$$

n_F being the density of states at the Fermi energy in the normal metal.

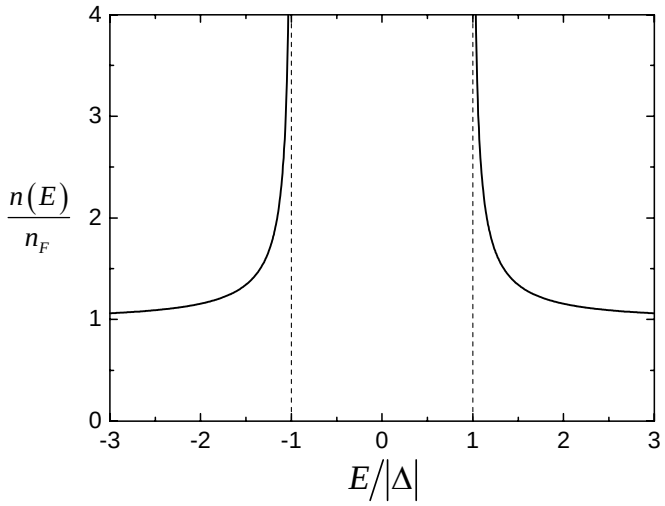

Figure 2: Density of states in a BCS superconducting metal around the Fermi energy ($E=0$). We recall that in the experiments, we are probing energies only a few millielectronvolts away from the Fermi energy. n_F is the density of states at the Fermi energy in the normal metal.

For each energy $|E| \geq \Delta$ there are four solutions (electron-like and hole like quasiparticles in both propagation directions) with wave-vectors satisfying the dispersion relations:

$$k_e(E) = \frac{1}{\hbar}\sqrt{2m\left(\mu + \mathrm{sgn}(E)\sqrt{E^2 - |\Delta|^2}\right)},$$

$$k_h(E) = \frac{1}{\hbar}\sqrt{2m\left(\mu - \mathrm{sgn}(E)\sqrt{E^2 - |\Delta|^2}\right)}.$$

The eigenvectors for the electron-like quasiparticles correspond to:

$$\frac{v_0^e}{u_0^e} = \frac{1}{|\Delta| e^{i\phi}}\left(E - \mathrm{sgn}(E)\sqrt{E^2 - |\Delta|^2}\right),$$

and those for the hole-like quasiparticles are given by:

$$\frac{v_0^h}{u_0^h} = \frac{1}{|\Delta| e^{i\phi}}\left(E + \mathrm{sgn}(E)\sqrt{E^2 - |\Delta|^2}\right).$$

The superconducting quasiparticles are superpositions of electron and hole normal quasiparticles and the charge they carry varies continuously between $\pm e$ (for $|E| \gg |\Delta|$) and zero at $|E| = |\Delta|$. In the limits $\Delta \to 0$ or $|E| \gg |\Delta|$, one recovers the normal state quasiparticles:

electrons $\begin{pmatrix} u_0^e \\ v_0^e \end{pmatrix} \to \begin{pmatrix} 1 \\ 0 \end{pmatrix}$, and holes $\begin{pmatrix} u_0^h \\ v_0^h \end{pmatrix} \to \begin{pmatrix} 0 \\ 1 \end{pmatrix}$.

We now turn into the discussion of Andreev reflection, the key concept to understand the electronic transport in structures involving one or several superconducting electrodes. Let us consider a normal-superconductor interface[2] as depicted in Figure 3.

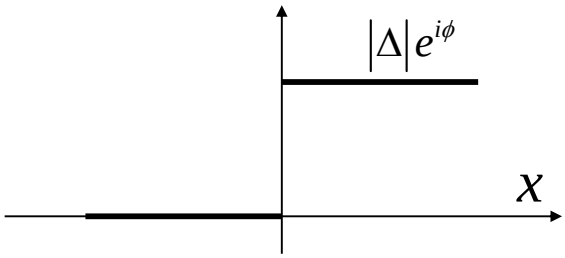

Figure 3: Profile of the superconducting order parameter at a NS interface. Taking a step function means neglecting the proximity effect.

When an electron incident from the normal electrode impinges on the superconducting one, it can of course be fully reflected (i.e. as an electron) therefore not contributing to the current. But it can also be reflected as a hole with a probability $a(E, \phi)$ in what is called an Andreev reflection process [16]. More precisely it is reflected at the order parameter discontinuity, generating an electron-like quasiparticle in the superconductor propagating in the same direction, and a hole in the normal electrode propagating in the opposite direction [17]. The wavefunction describing the situation in the normal side is:

[2] It is important to note that although Andreev reflection is usually associated in the literature almost exclusively with what happens at the interface between a normal metal and a superconductor, it is in fact the microscopic mechanism at the heart of superconductivity responsible for the coupling of the electrons and holes dynamics.

$$\begin{pmatrix}1\\0\end{pmatrix}e^{+ik_e^N x}+a(E,\phi)\begin{pmatrix}0\\1\end{pmatrix}e^{+ik_h^N x}.$$

The upperscript N in the wave vectors in the normal region denotes the fact that we have let $\Delta \to 0$ in the general expression for the wavevectors. At the interface ($x=0$), this must match the wavefunction of the superconducting electron-like quasiparticle, and thus:

$$\begin{pmatrix}1\\0\end{pmatrix}+a(E,\phi)\begin{pmatrix}0\\1\end{pmatrix}=\begin{pmatrix}u_0^e\\v_0^e\end{pmatrix},$$

from which one finds the probability amplitude $a(E,\phi)=\frac{v_0^e}{u_0^e}$ to Andreev reflect an electron into a hole:

$$a(E,\phi)=\frac{1}{|\Delta|e^{i\phi}}\left(E-\mathrm{sgn}(E)\sqrt{E^2-|\Delta|^2}\right)$$

We have taken by convention:

$$\sqrt{E^2-|\Delta|^2}=i\,\mathrm{sgn}(E)\sqrt{|\Delta|^2-E^2}\ \text{ if } |E|<|\Delta|.$$

We can then rewrite the Andreev reflection amplitude as:

$$a(E,\phi)=\begin{cases}\dfrac{1}{|\Delta|e^{i\phi}}\left(E-\mathrm{sgn}(E)\sqrt{E^2-|\Delta|^2}\right) & |E|>|\Delta|\\ \dfrac{1}{|\Delta|e^{i\phi}}\left(E-i\sqrt{|\Delta|^2-E^2}\right) & |E|<|\Delta|\end{cases}$$

The Andreev reflection amplitude of a hole into an electron is simply given by $a(E,-\phi)$. The variations with energy of the Andreev reflection amplitude are plotted in Figure 4. As the energy varies from $-\infty$ to $+\infty$, $a(E,\phi)$ runs over a half-circle in

the complex plane. For an electron impinging with an energy inside the gap ($|E| < |\Delta|$), the modulus of $a(E, \phi)$ is unity, i.e. Andreev reflection is complete.

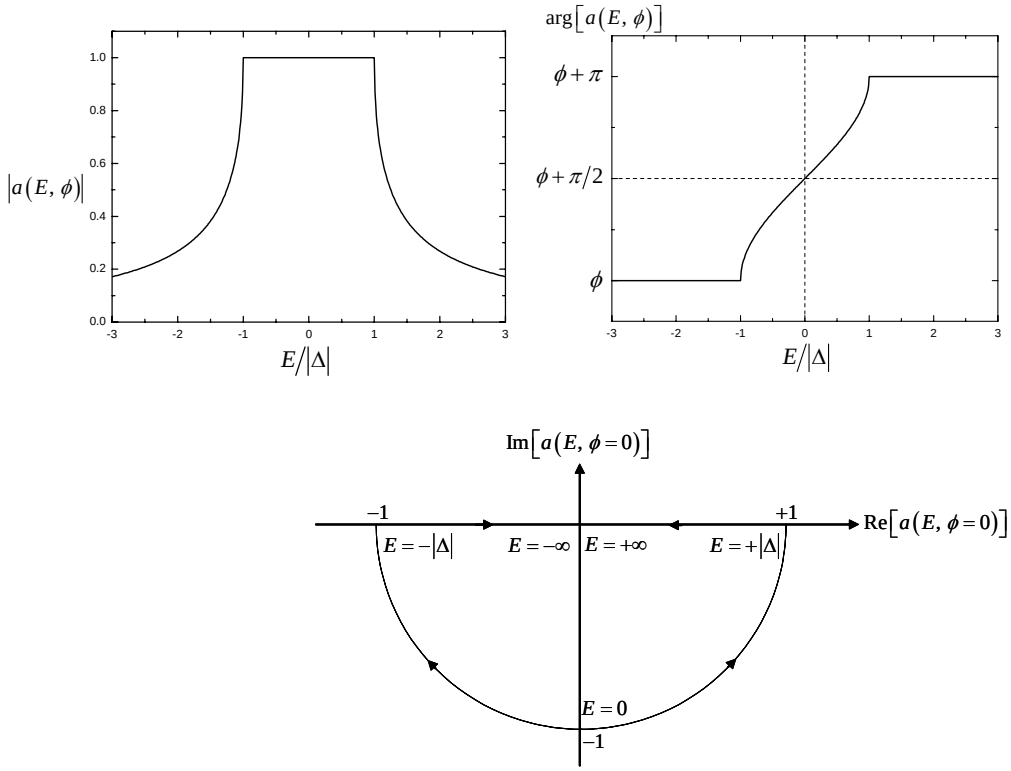

Figure 4: Modulus (top-left) and phase (top-right) of the Andreev reflection probability amplitude as a function of the quasiparticle energy in units of $|\Delta|$. Bottom: polar representation of the Andreev reflection probability amplitude for $\phi = 0$. ϕ is the phase of the superconducting complex order parameter.

We can now introduce this concept of Andreev reflection within the scattering theory of transport.

3 Andreev bound states – current-phase relation – Josephson inductance

We consider the simple situation of two superconducting reservoirs weakly coupled through a single short conduction channel of arbitrary transmission. In this

context, weakly coupled means that a phase difference can be sustained between both sides. Short means smaller than the superconducting coherence length, so that it is possible to have quasiparticle states which probe both sides, and therefore can sense the two different phases.

To describe the transport properties of this structure we need to account for two different scattering mechanisms. On the one hand the scattering due to the finite reflection probability of the channel. On the other hand, Andreev reflections due to the superconducting phase mismatch. Although these processes actually take place in the same region, it is convenient to assume they arise separately. For this purpose, we consider between the superconducting reservoirs a region where the pairing potential is zero, in other words we suppose that the connecting channel is normal, as depicted in Figure 5. As a consequence Andreev reflections occur at the two resulting fictitious NS interfaces, and normal scattering in the conduction channel, which has been divided into two parts, 1 and 2 on each side of the scaterrer for the purposes of section 3.2. Eventually, the length of this fictitious normal region can be taken to be zero.

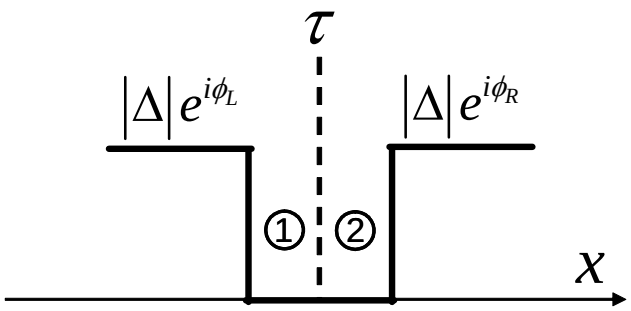

Figure 5: Schematic representation of a SNS structure used to model two superconducting reservoirs connected through a single conduction channel of arbitrary transmission τ.

The normal scattering in the conduction channel is described by the 2×2 matrix:

$$\underline{\underline{S}} = \begin{pmatrix} -ir & t \\ t & -ir \end{pmatrix}$$

When a phase difference $\delta = \phi_R - \phi_L$ is applied between the two superconductors, the electrons (and holes) reflected at both interfaces interfere, producing, like in a Fabry-Perot, two resonant states known as Andreev bound states.

Locally, the density of states of the continuum is also modified [18], and the singularities at $\pm\Delta$ disappear. Instead, two Andreev levels with energies $E_{\pm}(\delta)$ appear inside the gap (see Figure 6). At the interface between the two superconductors, the expression for the density of states of the continuum is:

$$\frac{n(E)}{n_F} = \frac{1}{2}\frac{|E|}{|\Delta|}\sqrt{\left(E/|\Delta|\right)^2 - 1}\,\frac{1+\sqrt{1-\tau}}{\left(E/|\Delta|\right)^2 - 1 + \tau\sin^2(\delta/2)} \qquad \left(|E|/|\Delta| \geq 1\right) \qquad (3)$$

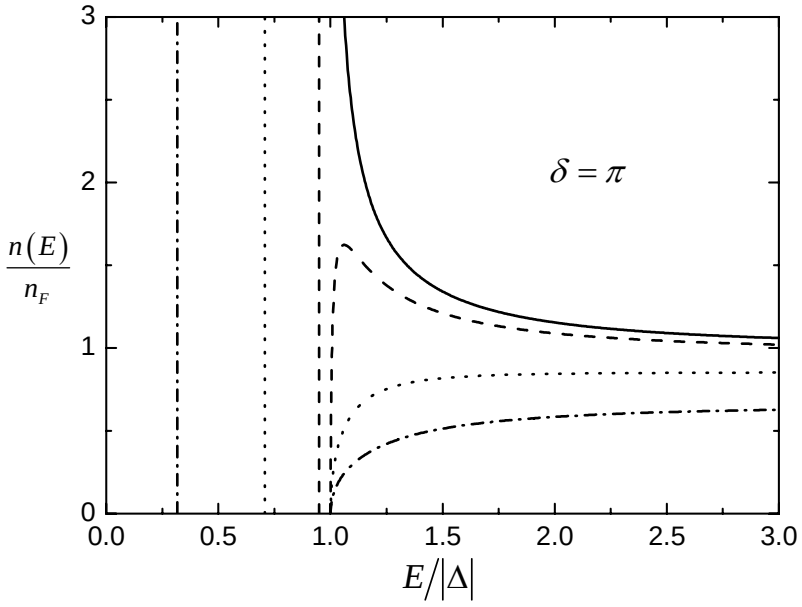

Figure 6: Local density of states at the constriction for four different values of the transmission: $\tau = 0$ (solid line), $\tau = 0.1$(dashed line), $\tau = 0.5$ (dotted line), $\tau = 0.9$ (dashed-dotted line). The case $\tau = 0$ corresponds to having two uncoupled superconductors and one therefore recovers the previously calculated BCS density of states. The vertical lines corresponds to the Andreev levels of energy E_+. The curves have been sketched for a phase difference $\delta = \pi$ across the weak link. For clarity only the energy range $E > 0$ is represented. The local density of states for $E < 0$ is obtained by symmetry with respect to the $E = 0$ vertical line.

3.1 Ballistic limit

In the ballistic limit ($\tau = 1$), no backscattering occurs in the conduction channels. Any incoming wave is perfectly transmitted.

A right moving electron (see Figure 7) with an energy inside the gap ($|E| < |\Delta|$) is Andreev reflected with probability one by the right superconductor into a left moving hole, leaving a charge $2e$ in the right superconductor. The left moving hole is Andreev reflected back by the left superconductor into a right moving electron, taking a charge $2e$ from the left superconductor. During one of these cycles a Cooper pair is transferred from the left to the right superconductor. The electron acquires a phase shift $\arg\left[a\left(E, \phi_R\right)\right]$ at the reflection on the right superconductor and $\arg\left[a\left(E, -\phi_L\right)\right]$ on the left one. Of course, a similar situation arises for left moving electrons. In a short weak link (i.e. of length much smaller than the superconducting coherence length), one can neglect the phase acquired by the electrons and the holes while they propagate in the normal region.

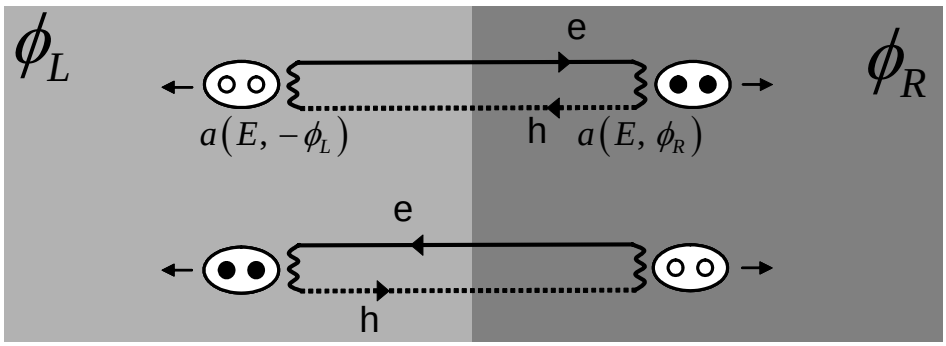

Figure 7: Schematic representation of the Cooper pair transfer process by the ballistic Andreev bound states.

Constructive interferences will therefore occur if:

$$\arg\left[a\left(E, \phi_R\right)\right] + \arg\left[a\left(E, -\phi_L\right)\right] = 0\left[\mathrm{mod}\, 2\pi\right].$$

Expliciting the phase shifts as:

$$\arg\left[a\left(E, \phi_R\right)\right] = -\phi_R + \arctan\left(-\frac{\sqrt{|\Delta|^2 - E^2}}{E}\right),$$

$$\arg\left[a\left(E, -\phi_L\right)\right] = \phi_L + \arctan\left(-\frac{\sqrt{|\Delta|^2 - E^2}}{E}\right),$$

one gets for the resonance condition:

$$2\arctan\left(-\frac{\sqrt{|\Delta|^2 - E^2}}{E}\right) - \delta = 0,$$

which leads to the appearance of two ballistic Andreev bound states with phase dependent energies located inside the gap:

$$E_{\rightleftarrows}(\delta) = \mp|\Delta|\cos\left(\frac{\delta}{2}\right)\mathrm{sgn}\left[\sin\left(\frac{\delta}{2}\right)\right]$$

Figure 8 shows the 2π periodic energies of these two states, which cross at $\delta = \pi$.

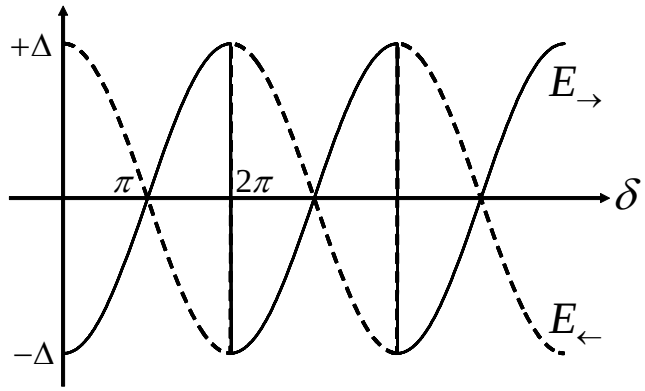

Figure 8: Energy of the two ballistic Andreev bound states as a function of the phase.

These two states carry opposite currents (see Figure 9) given by the current-phase relationship:

$$I_{\rightleftarrows}(\delta) = \frac{1}{\varphi_0}\frac{\partial E_{\rightleftarrows}}{\partial \delta} = \pm 2\frac{e|\Delta|}{2\hbar}\left|\sin\left(\frac{\delta}{2}\right)\right|, \text{ where } \varphi_0 = \frac{\hbar}{2e}.$$

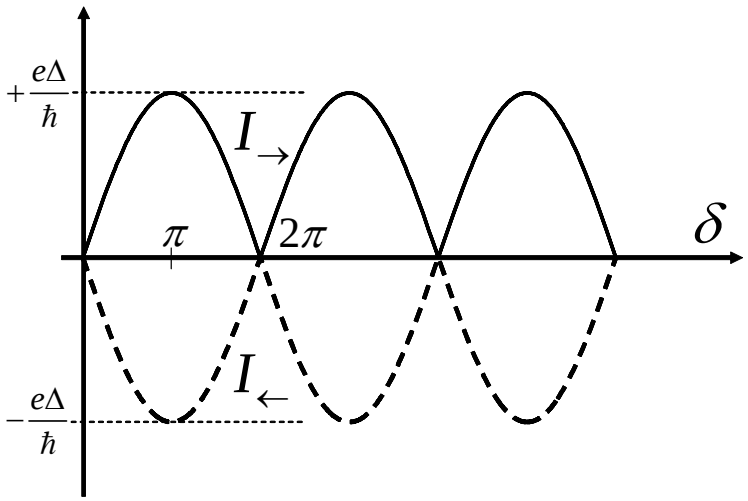

Figure 9: Current carried by the two Andreev bound states of a ballistic channel.

3.2 Conduction channel of arbitrary transmission

In this case, in which there is a finite backscattering probability in the normal region, a right moving electron (or hole) can be reflected back into a left moving electron (or hole) (see Figure 10). This couples the two ballistic Andreev bound states, and results in the opening of a gap in the Andreev spectrum at the crossing at $\delta = \pi$.

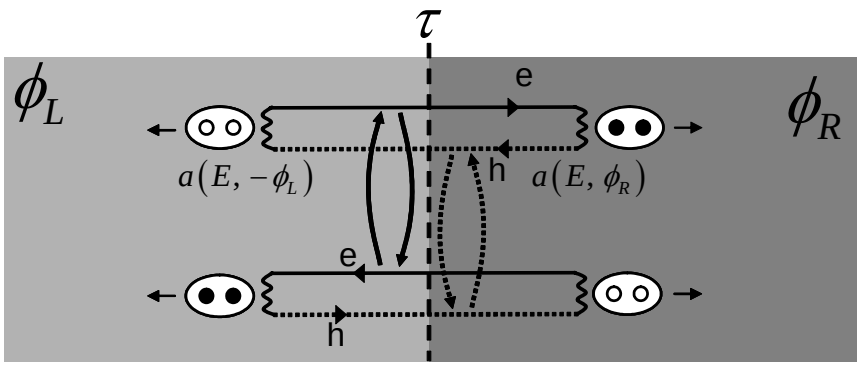

Figure 10: Schematic representation of the Cooper pair transfer process by the Andreev bound states in a channel with a transmission $\tau < 1$. The normal reflection process couples the two ballistic Andreev bound states resulting in the opening of a gap in their energy spectrum.

The wavefunctions on each side of the scattering center in the conduction channel (see Figure 5) can be written as:

$$\psi_1(x) = A_1^e \begin{pmatrix} 1 \\ 0 \end{pmatrix} e^{+ik_e^N x} + B_1^e \begin{pmatrix} 1 \\ 0 \end{pmatrix} e^{-ik_e^N x} + A_1^h \begin{pmatrix} 0 \\ 1 \end{pmatrix} e^{-ik_h^N x} + B_1^h \begin{pmatrix} 0 \\ 1 \end{pmatrix} e^{+ik_h^N x}$$

$$\psi_2(x) = A_2^e \begin{pmatrix} 1 \\ 0 \end{pmatrix} e^{-ik_e^N x} + B_2^e \begin{pmatrix} 1 \\ 0 \end{pmatrix} e^{+ik_e^N x} + A_2^h \begin{pmatrix} 0 \\ 1 \end{pmatrix} e^{+ik_h^N x} + B_2^h \begin{pmatrix} 0 \\ 1 \end{pmatrix} e^{-ik_h^N x}$$

The coefficients in front of the electron (or hole) wave functions are related by the scattering matrix as follows:

$$\begin{pmatrix} B_1^e \\ B_2^e \end{pmatrix} = \underline{\underline{S}} \begin{pmatrix} A_1^e \\ A_2^e \end{pmatrix} \tag{4}$$

and:

$$\begin{pmatrix} B_1^h \\ B_2^h \end{pmatrix} = \underline{\underline{S}}^* \begin{pmatrix} A_1^h \\ A_2^h \end{pmatrix} \tag{5}$$

And the electron and hole coefficients are related by the Andreev reflection amplitude matrix.

At the right interface:

$$\begin{pmatrix} A_2^h \\ A_2^e \end{pmatrix} = \begin{pmatrix} a(E, \phi_R) & 0 \\ 0 & a(E, -\phi_R) \end{pmatrix} \begin{pmatrix} B_2^e \\ B_2^h \end{pmatrix} \tag{6}$$

and at the left interface:

$$\begin{pmatrix} A_1^h \\ A_1^e \end{pmatrix} = \begin{pmatrix} a(E, \phi_L) & 0 \\ 0 & a(E, -\phi_L) \end{pmatrix} \begin{pmatrix} B_1^e \\ B_1^h \end{pmatrix} \tag{7}$$

One can combine equations (4), (5), (6) and (7) to obtain the following equation:

$$\underline{\underline{M}} \begin{pmatrix} A_1^e \\ A_2^e \end{pmatrix} = \begin{pmatrix} A_1^e \\ A_2^e \end{pmatrix},$$

with $\underline{\underline{M}} = \begin{pmatrix} a(E, -\phi_L) & 0 \\ 0 & a(E, -\phi_R) \end{pmatrix} \underline{\underline{S}}^* \begin{pmatrix} a(E, \phi_L) & 0 \\ 0 & a(E, \phi_R) \end{pmatrix} \underline{\underline{S}}$.

This has a non zero solution if

$$\det\left(\underline{\underline{M}}-\underline{\underline{I}}\right)=1-2\gamma\left(E\right)^2\left(1-t^2+t^2\cos\left(\delta\right)\right)+\gamma\left(E\right)^4=0\,,$$

where $\underline{\underline{I}}$ is the 2×2 identity matrix and $\gamma\left(E\right)=\dfrac{E-i\sqrt{\left|\Delta\right|^2-E^2}}{\left|\Delta\right|}$.

This leads to the energy of the two Andreev bound states (see Figure 11),

$$E_{\pm}=\pm\left|\Delta\right|\sqrt{1-\tau\sin^2\left(\delta/2\right)}\,,$$

where $\tau=t^2$.

The energy spectra of the two Andreev bound states for a single channel of arbitrary transmission are the central prediction of this mesoscopic theory of the Josephson effects.

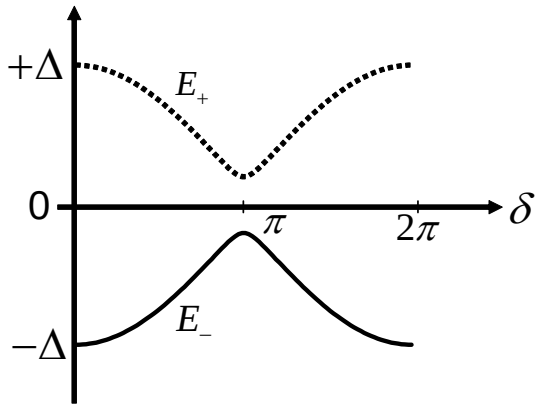

Figure 11: Energy of the two Andreev bound states as a function of the phase in a channel of transmission $\tau=0.99$.

As shown in Figure 12, these two Andreev bound states still carry opposite currents, given by the generalized current-phase relation:

$$I_{\pm}\left(\delta\right)=\frac{1}{\varphi_0}\frac{\partial E_{\pm}}{\partial\delta}=\mp\frac{e\left|\Delta\right|}{2\hbar}\frac{\tau\sin\left(\delta\right)}{\sqrt{1-\tau\sin^2\left(\delta/2\right)}}\qquad(8)$$

Since the conduction channels are independent, the current-phase relation of any weak-link can be calculated from equation (8) by adding up the contribution of the different channels (if the mesoscopic PIN code $\{\tau_1, ..., \tau_N\}$ of the structure is known).

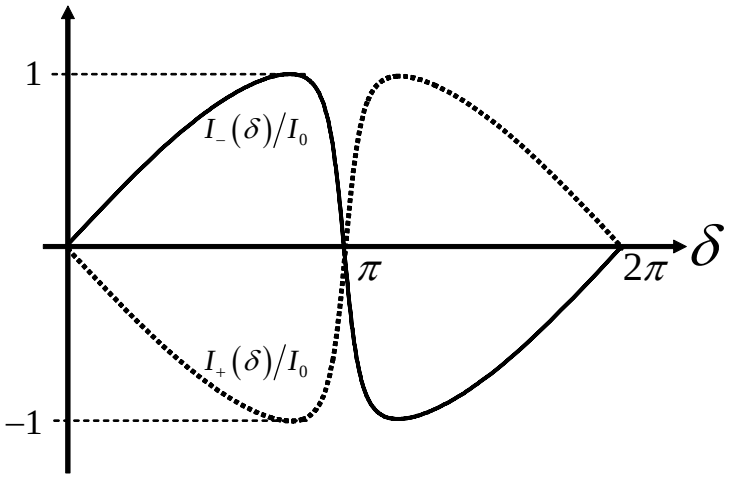

Figure 12: Current carried by the two Andreev bound states of a channel of transmission $\tau = 0.99$. *The two curves have been normalized by* I_0, *the maximum of* $I_\pm(\delta)$.

3.3 Josephson inductance

In section 3.1 and 3.2, we have derived an expression for the phase driven supercurrent in a single channel of arbitrary transmission. This current, which is a physical quantity amenable to measurement (see chapter 4) is proportional to the phase derivative of the Andreev bound state energy.

Another quantity amenable to measurement and carrying some information on the spectrum of the Andreev bound state is the Josephson inductance. The two constitutive relations of a Josephson weak link are the current phase relation and the second Josephson relation, stating that the voltage across it is proportional to the time derivative of the phase:

$$\begin{cases} I = I_{\pm}(\delta, \tau) \\ V = \varphi_0 \dot{\delta} \end{cases}$$

Combining these two relations leads to:

$$V = \frac{\varphi_0}{dI_{\pm}(\delta, \tau)/d\delta} \frac{dI_{\pm}}{dt}.$$

The voltage across the Jospehson weak link is proportional to the time derivative of the current flowing through it. This defines the non linear Josephson inductance:

$$L_{\pm}(\delta, \tau) = \frac{\varphi_0}{dI_{\pm}(\delta, \tau)/d\delta} = \frac{{\varphi_0}^2}{d^2 E_{\pm}(\delta, \tau)/d\delta^2}$$

In chapter 4, microwave reflectometry experiments aiming to probe the Josephson inductance of an atomic contact are presented.

4 Multiple Andreev reflections

In the previous paragraph we calculated the supercurrent through a single channel Josephson weak-link when it is phase biased. However, it is also possible to calculate within this picture of Andreev levels what happens when the system is voltage biased. The basic microscopic charge transfer mechanism in this case was identified in 1982 by Blonder *et al*. [17], who calculated the dissipative current within a semi-classical approach. In the mid 1990's a complete quantum description was achieved by several groups [19, 20, 21]. Following D. Averin and A. Bardas [19], we will sketch, in what follows, the fully quantum scattering formalism developed to calculate the time dependent currents when a voltage V is applied through a single channel weak-link of arbitrary transmission.

Under a voltage bias V, electrons and holes gain or lose an energy eV when they propagate through the conduction channel, i.e. transport becomes inelastic. As a consequence Andreev bound states cannot exist any longer. Instead, a quasiparticle

entering from one of the reservoirs will give rise to a scattering state containing all possible quasiparticle states with energies $E+2neV$, where n is an integer. The components of the wavefunction of this scattering state have different time dependencies giving rise to a time dependent current. This is the so-called ac Josephson effect.

More precisely, a quasiparticle of energy E coming from the left superconductor (see Figure 13) is injected as an electron in the normal region with a probability amplitude $J(E)=\sqrt{1-|a(E,0)|^2}$. In the normal region an infinite series of Andreev reflection is generated. They occur at energies $E+2neV$ ($n\in\mathbb{N}$) on the left interface and at energies $E+(2n+1)eV$ ($n\in\mathbb{N}$) on the right interface. This infinite series is called multiple Andreev reflections (MAR) and is the fundamental process that carries the current when a voltage is applied across a Josephson weak link.

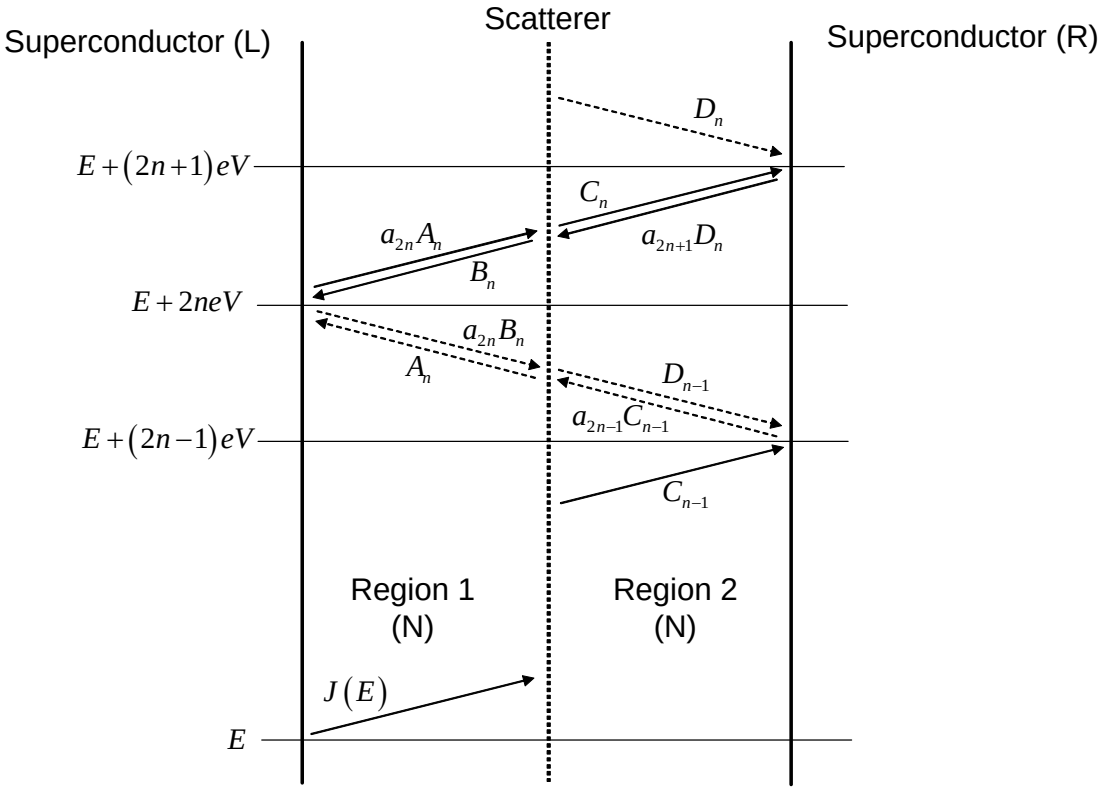

Figure 13: Multiple Andreev reflections in a channel connecting two superconducting reservoirs. Dashed arrows represent holes. Solid arrows represent electrons. The vertical dotted line schematically represents the scattering center. In this figure the chemical potential of both reservoirs are kept at the same level, independently of the bias. The voltage dependence is taken into account through the kinetic energy gained by the electrons and the holes from the electrical field localized in the channel.

In the two normal regions, the electron and hole wave functions can be written as a sum of different components shifted by the quantity $2eV$. In region 1, the wave function writes:

$$\psi_1(x) = \begin{pmatrix} \sum_{n\in\mathbb{N}} \left[\left(a_{2n} A_n + J(E)\delta_{n0} \right) e^{ik_e^N x} + B_n e^{-ik_e^N x} \right] e^{-i(E+2neV)t/\hbar} \\ \sum_{n\in\mathbb{N}} \left[A_n e^{ik_h^N x} + a_{2n} B_n e^{-ik_h^N x} \right] e^{-i(E+2neV)t/\hbar} \end{pmatrix},$$

A_n (B_n) are respectively the probability amplitude associated with a left moving hole (electron) of energy $E+2neV$, and $a_k = a(E+keV, 0)$. δ_{n0} is the Kronecker symbol, defined as: $\delta_{n0} = \begin{cases} 1 \text{ if } n=0 \\ 0 \text{ if } n\neq 0 \end{cases}$

Similarly, the wave function in region 2 is:

$$\psi_2(x) = \begin{pmatrix} \sum_{n\in\mathbb{N}} \left[C_n e^{ik_e^N x} + a_{2n+1} D_n e^{-ik_e^N x} \right] e^{-i(E+(2n+1)eV)t/\hbar} \\ \sum_{n\in\mathbb{N}} \left[a_{2n+1} C_n e^{ik_h^N x} + D_n e^{-ik_h^N x} \right] e^{-i(E+(2n+1)eV)t/\hbar} \end{pmatrix}$$

where C_n (D_n) are respectively the probability amplitude associated with a right moving electron (hole) of energy $E+(2n+1)eV$.

The coefficients in regions 1 and 2 are not independent, as they are related through the scattering matrix. For the electrons, this relation writes [19]:

$$\begin{pmatrix} B_n \\ C_n \end{pmatrix} = \underline{\underline{S}} \begin{pmatrix} a_{2n} A_n + J(E)\delta_{n0} \\ a_{2n+1} D_n \end{pmatrix},$$

and for the electrons:

$$\begin{pmatrix} A_n \\ D_{n-1} \end{pmatrix} = \underline{\underline{S}}^* \begin{pmatrix} a_{2n} B_n \\ a_{2n-1} C_{n-1} \end{pmatrix}$$

The coefficients C_n and D_n can be expressed in terms of A_n and B_n, which can themselves be calculated from a recurrence relation.

The current is then expressed as [19]:

$$I(V,t) = \sum_{k=-\infty}^{+\infty} I_k(V) e^{ik\omega_0 t} \tag{9}$$

where $\omega_0 = 2eV/\hbar$ is the Josephson frequency and:

$$I_k = \frac{2e^2}{h} \times$$
$$\left\{ eV\delta_{k0} - \int dE \tanh\left(\frac{E}{2k_B T}\right)\left[J(E)\left(a_{2k}A_k^* + a_{-2k}A_{-k}\right) + \sum_n \left(1 + a_{2n}a_{2(n+k)}^*\right)\left(A_n A_{n+k}^* - B_n B_{n+k}^*\right)\right]\right\}$$

The current oscillates at all the harmonics of the Josephson frequency. The dc component of the current leads to the highly non linear dc IV characteristics from which the mesoscopic pin code of the contact can be extracted [4].

Let us conclude this section by saying that in 1996, J. C. Cuevas *et al.* [21] developed a different formalism to calculate the components of the current in a voltage biased single channel contact. Their calculation is based on a tight-binding model Hamiltonian that describes the charge transfer through the weak link, and uses non-equilibrium Keldysh Green functions to calculate the current. This formalism is more general than the scattering formalism developed by Averin and Bardas because it allows in principle to include all type of scattering mechanisms which can modify the electronic distribution (electron-electron interactions, impurities, etc…) [22]. For example, it can handle inhomogeneous or disordered systems. In these specific cases, it is indeed very difficult if not impossible to compute the wave functions which are the input of the scattering formalism. For example, the case S-N(diffusive)-S is a situation where the scattering formalism cannot account for the spatial variations of the superconducting correlations in the normal diffusive wire [23]. Of course, this new approach contains all the results predicted by the scattering formalism.

5 From the supercurrent to MAR

In the previous sections the non-dissipative and the dissipative currents in a single channel weak-link were described on separate grounds, in the sense that different and contradictory bias conditions were assumed. On one hand the supercurrent is calculated by assuming a perfect phase bias, and on the other hand the MAR current is evaluated assuming a perfectly voltage biased contact. The issue we address in this paragraph is the link between these two dichotomic approaches. More detailed discussions of this point can be found in [19, 21].

The MAR current, which is driven by the voltage, is simply the dc component of expression (9), i.e. the time average of the ac Josephson currents. Figure 14 shows the IV characteristic of a single channel contact for different values of the transmission, calculated using a code developed by J. C. Cuevas [21].

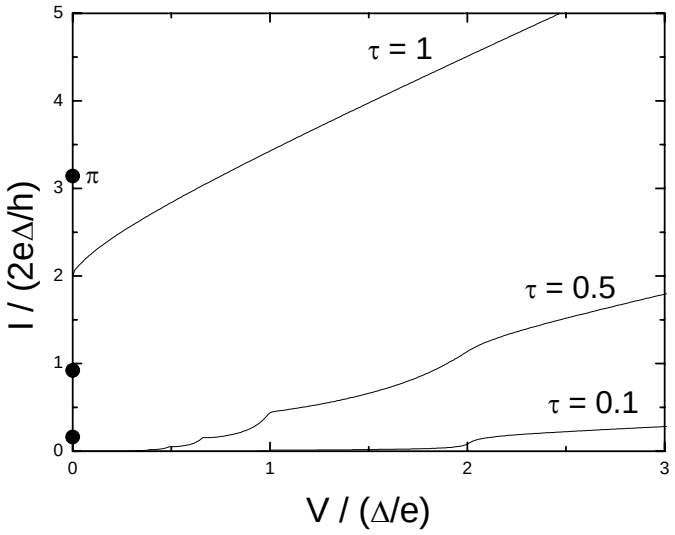

Figure 14: MAR current (lines) and critical current (dots) in channels of various transmissions under perfect voltage bias V .

In the $V \to 0$ limit, the number of MAR processes contributing to the current grows indefinetly, but each step of the MAR ladder (Figure 13) gets smaller and smaller. Eventually, at exactly zero voltage, the infinite series of MAR gives rise to the two Andreev bound states shown on Figure 8 and Figure 11. These two states are responsible for the supercurrent which is driven now by the superconducting phase

difference. The solid dots at zero voltage in Figure 14 represent the maximum supercurrent that the channel can sustain without any voltage, i.e. its critical current I_0, obtained for a phase of $\pi/2$ in the tunnel limit. At zero voltage, the channel can in fact accommodate any current in the interval $[-I_0, I_0]$, the actual value being determined by the static superconducting phase difference δ across the contact, according to equation (8).

Under a constant voltage *V* the phase acquires a dynamics $\dot{\delta} = V/\varphi_0$. As the phase is swept across π, this dynamics can induce Landau-Zener transitions from the lower to the upper Andreev bound level as shown in Figure 15. These non-adiabatic transitions are responsible for the crossover from supercurrent to MAR current.

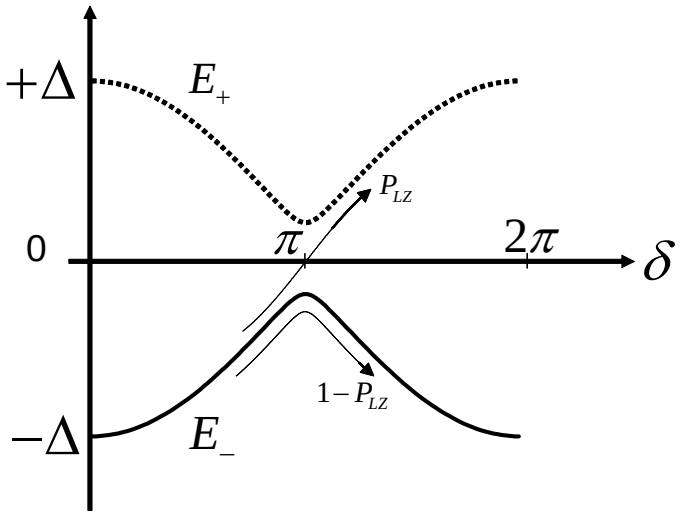

Figure 15: Landau-Zener transitions between the two Andreev bound states (in a channel of transmission 0.99), as the phase is swept at high speed across the Andreev gap ($2\Delta\sqrt{1-\tau}$) at $\delta = \pi$.

When the superconducting phase difference δ is swept through the value π, the system can either follow the lower level (adiabatic limit) or jump to the upper level (diabatic limit). This problem is well known as the standard level crossing problem, ubiquitous in physics and chemistry. The probability to go from the lower to the upper level when the parameter is driven at constant velocity was calculated independently by Landau and Zener in the 1930's [24]:

$$P_{LZ} = \exp\left[-\pi^2 \frac{\left(\nu_a\right)_{lc}^{\ 2}}{\left(\frac{\partial \nu_b}{\partial t}\right)_{lc}} \right] \qquad (10)$$

where ν_a (ν_b) is the transition frequency between the two adiabatic (ballistic) levels (see sections 3.1 and 3.2). The subscript lc indicates values taken at the level crossing.

$$\left(\nu_a\right)_{lc} = \frac{2\Delta}{h}\sqrt{1-\tau}$$

$$\left(\frac{\partial \nu_b}{\partial t}\right)_{lc} = \left(\frac{\partial \nu_b}{\partial \delta}\right)_{lc} \frac{d\delta}{dt} = \frac{\Delta}{h}\frac{V}{\varphi_0}$$

In our specific case equation (10) rewrites as:

$$P_{LZ} = \exp\left[-\pi \frac{\Delta}{eV}\left(1-\tau\right) \right]$$

As the transmission of the channel increases, the Andreev gap at $\delta = \pi$ shrinks and the transition probability increases.

It is possible to understand the MAR current as Landau-Zener transitions between the two stationary Andreev bound states [19, 25] in the limit[3] $\pi \frac{\Delta}{eV}\left(1-\tau\right) > 1$. At finite voltage, the current flowing through the channel can be expressed as a sum of two terms. If the system follows the adiabatic limit (probability $1-P_{LZ}$), the current is given by $\frac{1}{\varphi_0}\left(\frac{\partial E_-}{\partial \delta}\right)_{\delta = V/\varphi_0 t + \delta_0}$. Whereas if the system follows the diabatic limit (probability P_{LZ}), the current is given by $\frac{1}{\varphi_0}\left(\frac{\partial E_\rightarrow}{\partial \delta}\right)_{\delta = V/\varphi_0 t + \delta_0}$ We can therefore write the current as:

$$I\left(V, t\right) \approx \left(1-P_{LZ}\left(V\right)\right)\frac{1}{\varphi_0}\left(\frac{\partial E_-}{\partial \delta}\right)_{\delta = V/\varphi_0 t + \delta_0} + P_{LZ}\left(V\right)\frac{1}{\varphi_0}\left(\frac{\partial E_\rightarrow}{\partial \delta}\right)_{\delta = V/\varphi_0 t + \delta_0} \qquad (11)$$

[3] Ultimately, i.e. for $\pi \frac{\Delta}{eV}\left(1-\tau\right) \gg 1$, this corresponds to the adiabatic limit ($P_{LZ} = 0$).

Because the current phase relation of the lower Andreev level E_- is an odd function of the phase, the first term of equation (11) is an odd function of time, which can therefore be expanded into a sine Fourier series, and which averages out to zero in time. However, the current phase relation of the ballistic level $E_\rightarrow$ is an even function of the phase. The second term of equation (11) is therefore an even function of time, with a non zero average, and can be expanded into a cosine Fourier series. Therefore, the dc current at finite voltage writes:

$$I(V) \approx P_{LZ}(V) \frac{1}{\varphi_0} \left\langle \frac{\partial E_\rightarrow}{\partial \delta} \right\rangle_{\delta \in [0,\, 2\pi]} = \frac{4}{\pi} \frac{e\Delta}{2\hbar} \exp\left[-\pi \frac{\Delta}{eV} (1-\tau) \right] \qquad (12)$$

Figure 16 compares the predictions of this approximate expression with the predictions of the full theory of MAR in the limit $\pi \frac{\Delta}{eV}(1-\tau) > 1$. The good agreement between the two approaches indicates that, within this limit, the MAR current can be viewed as resulting from the Landau-Zener transitions between the stationary Andreev bound states. Equation (11) shows that when the voltage is progressively increased from zero, the MAR current (second term) increases while the supercurrent (first term) decreases. Equation (11) brings out some insight on equation (9). The sine terms in the current expansion of the time dependent current come from the adiabatic dynamics of the system on the lower Andreev level, whereas the cosine terms are the signature of Landau-Zener transitions between the two levels.

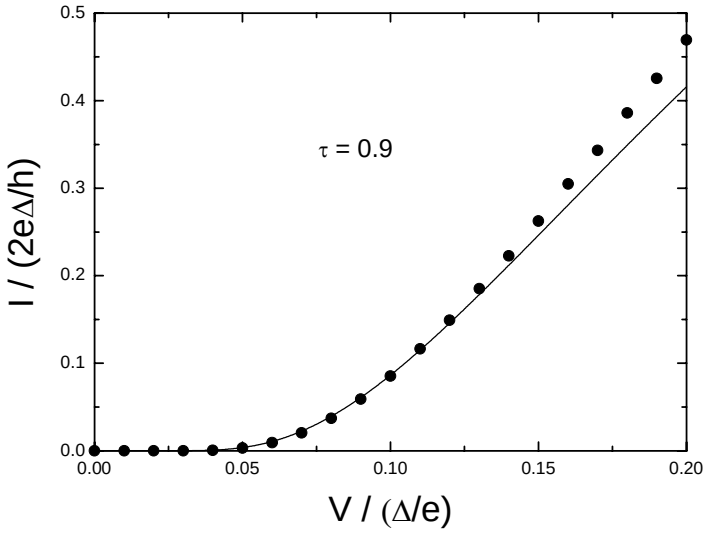

Figure 16: Solid line: prediction of equation (12) for the current arising at low voltages from Landau-Zener transitions between the two Andreev bound levels of a $\tau = 0.9$ *channel. Dots: full microscopic calculation of MAR current.*

The discussion sketched here has the merit to point out that there is no fundamental difference between the supercurrent at zero voltage and the MAR current at finite voltage despite the dichotomy in their description. They both arise from the same basic microscopic mechanism.

We will see in chapter 2 that in practice, the contact is never perfectly voltage biased. The finite impedance of a realistic setup imposes voltage and therefore phase fluctuations which lead to a smooth transition from an essentially non dissipative transport regime to an essentially dissipative one. The voltage range in which this smooth transition happens depends on the environment. There is a voltage range in which supercurrent and MAR current contributions completely mix one with each other. Of course, this is only noticeable for highly transmitting channels where the MAR current is sizeable at very low voltages. In weakly transmitting channels, as the Landau-Zener probability is vanishingly small at small voltages, there is no overlap of the supercurrent and the MAR current contributions.

References of chapter 1

[1] R. Landauer, IBM J. Res. Dev. **1**, 223 (1957); Philos. Mag. **21**, 863 (1970).

[2] B. J. van Wees *et al.*, Phys. Rev. Lett. **60**, 848 (1988).

[3] D. A. Wharam *et al.*, J. Phys. C **21**, L209 (1988).

[4] E. Scheer *et al.*, Phys. Rev. Lett. **78**, 3535 (1997).

[5] E. Scheer, N. Agraït, J.C. Cuevas, A. Levy-Yeyati, B. Ludolph, A. Martín-Rodero, G. Rubio Bollinger, J.M. van Ruitenbeek, C. Urbina, *The signature of chemical valence in the electrical conduction through a single-atom contact,* Nature **394**,154 (1998).

[6] T. Martin and R. Landauer, Phys. Rev. B **45**, 1742 (1992).

[7] M. Büttiker, Phys. Rev. B **46**, 12485 (1992).

[8] M. Reznikov *et al.*, Phys. Rev. Lett. **75**, 3340 (1995).

[9] A. Kumar *et al.*, Phys. Rev. Lett. **76**, 2778 (1996).

[10] R. Cron *et al.*, Phys. Rev. Lett. **86**, 4104 (2001).

[11] B. Ludolph and J. M. van Ruitenbeek, Phys. Rev. B **59**, 12290 (1999).

[12] E. N. Bogachek, A. G. Scherbakov and Uzi Landman, Phys. Rev. B **54**, 11094 (1996).

[13] F. Kassubek, C. A. Stafford and Hermann Grabert, Phys. Rev. B **59**, 7560 (1999).

[14] G. Rubio, N. Agraït and S. Vieira, Phys. Rev. Lett. **76**, 2302 (1996).

[15] R. Cron, *Atomic Contacts: a Test-Bed for Mesoscopic Physics*, Ph.D. thesis, Université Paris 6 (2001).
http://www-drecam.cea.fr/drecam/spec/Pres/Quantro/Qsite/archives/theses/RCronThesis.pdf.

[16] A. F. Andreev, Zh. Eksp. Teor.Fiz. **46**, 1823 (1964) translated in Sov. Phys. JETP **19**, 1228 (1964).

[17] G. E. Blonder, M. Tinkham, and T. M. Klapwijk, Phys. Rev. B **25**, 4515 (1982).

[18] A. L. Yeyati, private communication.

[19] D. Averin and A. Bardas, Phys. Rev. Lett. **75**, 1831 (1995).

[20] E. N. Bratus', V. S. Shumeiko, and G. Wendin, Phys. Rev. Lett. **74**, 2110 (1995).

[21] J. C. Cuevas, A. Martín-Rodero, and A. Levy Yeyati, Phys. Rev. B **54**, 7366 (1996).

[22] A. L. Yeyati, private communication.

[23] J. C. Cuevas, private communication.

[24] L. D. Landau, Phys. Z. Sow. **2**, 46 (1932); C. Zener, Proc. R. Soc. London, Ser A **137**, 696 (1932).

[25] E. N. Bratus' *et al.*, Phys. Rev. B **55**, 12666 (1997).

Chapter 2: The supercurrent peak

In this chapter we report experiments on the dc current flowing in voltage and current biased atomic contacts. The current-voltage characteristics strongly depend in these situations on the fluctuations imposed on the superconducting phase by the electromagnetic environment of the contact, and we discuss this physics in detail. We report measurements on contacts with transmissions up to the ballistic limit and compare the experimental results with the theoretical predictions. In particular we show the crossover from the supercurrent to the dissipative current arising from multiple Andreev reflections.

We first present some theoretical elements on the supercurrent in phase biased Josephson weak links at finite temperature.

1 Current-phase relation of a Josephson weak link at finite temperature

When a Josephson weak link is phase biased, the voltage across it is perfectly zero, according to the second Josephson relation $V = \varphi_0 \dot{\delta}$. However, current can still flow through the structure if an imbalance in the population of the current carrying Andreev bound levels exists.

The goal of this paragraph is to establish how much current can flow in a phase biased single channel at thermal equilibrium. Thermalization occurs through relaxation processes between the two Andreev bound states. The relaxation by phonons has been addressed in [1, 2]. The relaxation of the upper state by the emission of photons in the environment, already pointed out by Goffman *et al.* [3] has been described in detail by M. A. Despósito and A. Levy Yeyati in [4]. The relaxation by the exchange of quasiparticles with states in the bulk superconductors has been described in [5, 6]. None of these processes is very efficient except at some specific values of the phase: at $\delta = 0, 2\pi$ for the exchange of quasiparticles with the continuum and at $\delta = \pi$ for the emission of photons in the environment. The coupling to the phonons is never very efficient.

Considering the fermionic nature of the Andreev bound states, there are four different ways of occupying a pair of them. They are summarized in Table 1. Note that the total

number of superconducting quasiparticles occupying the two Andreev levels is not fixed and is either zero, one or two.

Occupation number of the lower Andreev level	Occupation number of the upper Andreev level	Total energy of the configuration	Current carried in the configuration
0	0	0	0
1	0	E_-	I_-
0	1	E_+	I_+
1	1	$E_- + E_+ = 0$	$I_- + I_+ = 0$

Table 1: The four different configurations for occupying a pair of Andreev bound states. Each line in the table corresponds to a given configuration.

The partition function Ξ writes:

$$\Xi = 2 + e^{-\beta E_-(\delta,\tau)} + e^{-\beta E_+(\delta,\tau)},$$

where $\begin{cases} \beta = 1/(k_B T) \\ E_\pm(\delta,\tau) = \pm\Delta\sqrt{1-\tau\sin^2\left(\frac{\delta}{2}\right)} \end{cases}$.

At equilibrium, the current through the channel thus writes:

$$\overline{I(\delta,\tau,T)} = \frac{1}{\Xi}\left[0 + e^{-\beta E_-(\delta,\tau)} I_-(\delta,\tau) + e^{-\beta E_+(\delta,\tau)} I_+(\delta,\tau) + 0\right]$$

with $I_\pm(\delta,\tau) = \frac{1}{\varphi_0}\frac{\partial E_\pm(\delta,\tau)}{\partial\delta} = \mp\frac{e\Delta}{2\hbar}\frac{\tau\sin(\delta)}{\sqrt{1-\tau\sin^2\left(\frac{\delta}{2}\right)}}$.

The current phase relation of the Andreev ground state $I_-(\delta,\tau)$ is plotted on Figure 1 for different values of the channel transmission.

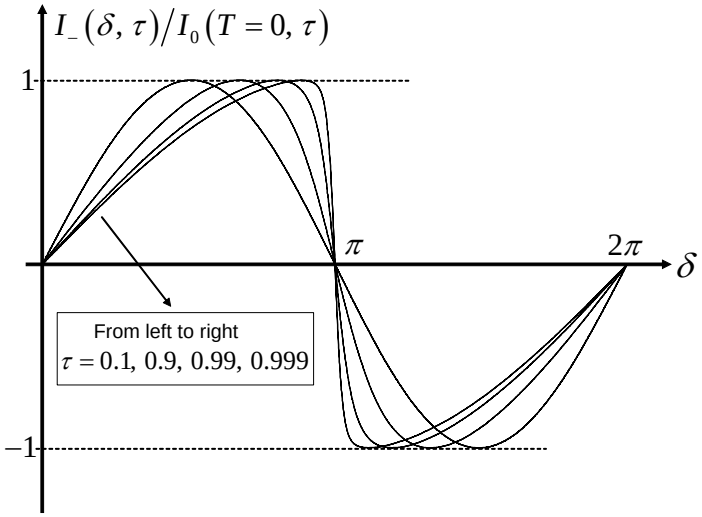

Figure 1: Current phase relation of the Andreev ground state for different transmissions ($\tau = 0.1, 0.9, 0.99, 0.999$) of the channel. The current phase relations have been normalized to their respective zero temperature critical currents $I_0(T=0, \tau)$ (see below).

Given the fact that $E_- = -E_+$ and $I_+ = -I_-$, the finite temperature[1] current phase relation simply rewrites:

$$\overline{I(\delta, \tau, T)} = \frac{e\Delta}{2\hbar} \frac{\tau \sin(\delta)}{\sqrt{1-\tau \sin^2\left(\frac{\delta}{2}\right)}} \tanh\left[\frac{\beta E_+(\delta, \tau)}{2}\right] \qquad (1)$$

The critical current is $I_0(T, \tau) = \max_{\delta}\left\{\overline{I(\delta, \tau, T)}\right\}$ which at zero temperature reduces to (see Figure 2):

$$I_0(T=0, \tau) = \frac{e\Delta}{\hbar}\left(1-\sqrt{1-\tau}\right).$$

[1] For simplicity, we don't consider here the temperature dependence of the superconducting gap. This is valid for temperatures well below the critical temperature.

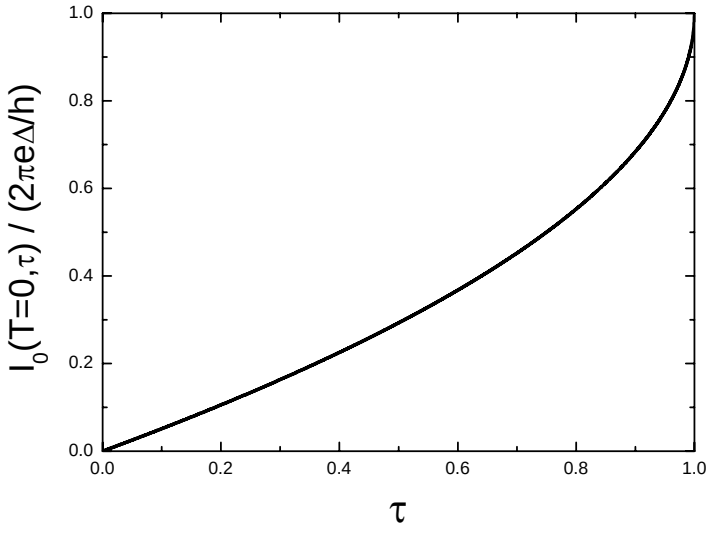

Figure 2: Transmission dependence of the critical current of a single channel contact at zero temperature.

For a contact with N channels, the generalization is straightforward. The contribution of the different channels simply sum up:

$$I\left(\delta, \{\tau\}\right) = \sum_{i=1}^{N}\left[n_{+}^{i} I_{+}\left(\delta, \tau_i\right) + n_{-}^{i} I_{-}\left(\delta, \tau_i\right)\right]$$

where n_{+}^{i} and n_{-}^{i} are respectively the occupation numbers of the upper and lower Andreev bound state in the *i*-th channel. Because the channels are independent, at thermal equilibrium, we have:

$$\overline{n_{\pm}^{i}} = \frac{e^{-\beta E_{\pm}(\delta, \tau_i)}}{\Xi_i},$$

with the partition function $\Xi_i = 2 + e^{-\beta E_{-}(\delta, \tau_i)} + e^{-\beta E_{+}(\delta, \tau_i)}$.

The total thermal equilibrium current phase relation is then:

$$\overline{I\left(\delta, \{\tau\}, T\right)} = \sum_{i=1}^{N}\left[\overline{n_+^i} I_+\left(\delta, \tau_i\right) + \overline{n_-^i} I_-\left(\delta, \tau_i\right)\right]$$

$$= \frac{e\Delta}{2\hbar}\sum_{i=1}^{N}\left\{\frac{\tau_i \sin\left(\delta\right)}{\sqrt{1-\tau_i \sin^2\left(\frac{\delta}{2}\right)}} \tanh\left[\frac{\beta E_+\left(\delta, \tau_i\right)}{2}\right]\right\} \qquad (2)$$

There is no simple analytical formula for the critical current in the general case. The calculation has to be performed numerically.

Nevertheless, a simple formula can be found for the temperature dependence of the critical current in the tunnel limit. This result was first established by Ambegaokar and Baratoff in 1963 [7, 8]. A tunnel junction is a quantum coherent conductor containing only channels of very small transmission.

Rewriting equation (2) with $\tau_i \ll 1$ leads to:

$$\overline{I\left(\delta, \{\tau\}, T\right)} = \left(\frac{e\Delta}{2\hbar}\sum_{i=1}^{N}\tau_i\right)\tanh\left[\frac{\beta\Delta}{2}\right]\sin\left(\delta\right).$$

Hence the well known result:

$$I_0\left(T\right) = \frac{\pi\Delta G_N}{2e}\tanh\left[\frac{\beta\Delta}{2}\right],$$

where $G_N = \frac{2e^2}{h}\sum_{i=1}^{N}\tau_i$ is the normal state conductance of the tunnel junction.

For a channel of perfect transmission, the two Andreev bound states cross each other at $\delta = \pi$ (see Figure 3), and their energies are:

$$\begin{cases} E_{\rightleftarrows}\left(\delta\right) = \mp\Delta\cos\left(\frac{\delta}{2}\right),\ \delta \in \left[0,\ 2\pi\right] \\ E_{\rightleftarrows}\left(\delta + 2\pi\right) = E_{\rightleftarrows}\left(\delta\right) \end{cases}$$

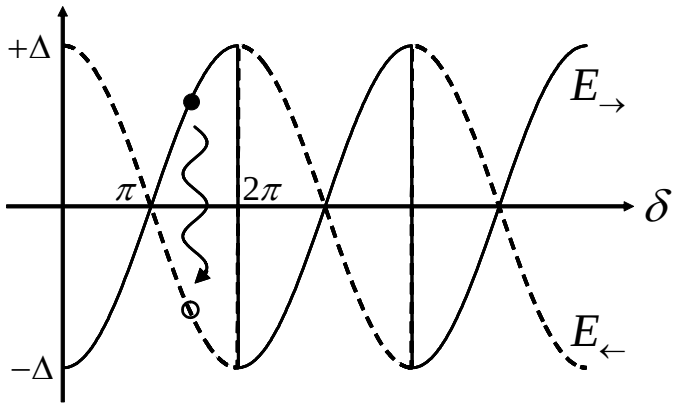

Figure 3: Phase dependence of the energy of the ballistic Andreev bound states. The wiggly line represents relaxation processes from the upper Andreev level.

Therefore, the current carried by the ballistic bound states writes:

$$I_{\rightleftarrows}(\delta) = \pm 2\frac{e\Delta}{2\hbar}\left|\sin\left(\frac{\delta}{2}\right)\right|.$$

Whatever the phase, the Andreev level of energy $E_{\rightarrow}$ carry the positive current $I_{\rightarrow}$; the level of energy $E_{\leftarrow}$ carry the opposite current $I_{\leftarrow}$, as shown on Figure 4.

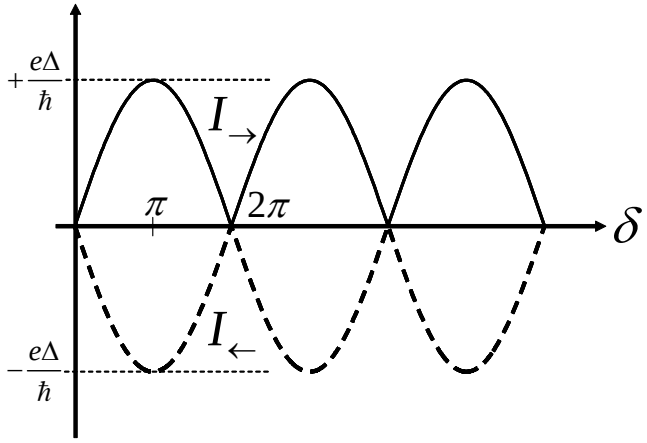

Figure 4: Phase dependence of the current carried by the two ballistic Andreev bound states.

The case of transmission perfectly one is singular because $I_{\rightleftarrows}(\delta)$ have a non zero phase average. Nevertheless, this singularity disappears if relaxation processes between the two ballistic bound states (see Figure 3) occur at a fast enough rate for the thermal

equilibrium to be reached at each value of the phase. In this case, the equilibrium current phase relation $\overline{I(\delta,\ \tau=1,\ T)}$ is simply given by equation (1), letting $\tau \to 1^{-}$:

$$\overline{I(\delta,\ \tau=1,\ T)} = \overline{I(\delta,\ \tau\to 1^{-},\ T)} = \frac{e\Delta}{2\hbar}\frac{\sin(\delta)}{\left|\cos\left(\frac{\delta}{2}\right)\right|}\tanh\left[\frac{\left|\Delta\cos\left(\frac{\delta}{2}\right)\right|}{2k_B T}\right]$$

In the zero temperature limit, this simply rewrites:

$$\overline{I(\delta,\ \tau=1,\ T\to 0)} = I_{-}(\delta,\ \tau\to 1^{-}) = \frac{e\Delta}{2\hbar}\frac{\sin(\delta)}{\left|\cos\left(\frac{\delta}{2}\right)\right|}$$

The low temperature ($T \to 0$) equilibrium current phase relation of a single channel contact of transmission 1 is represented on Figure 5.

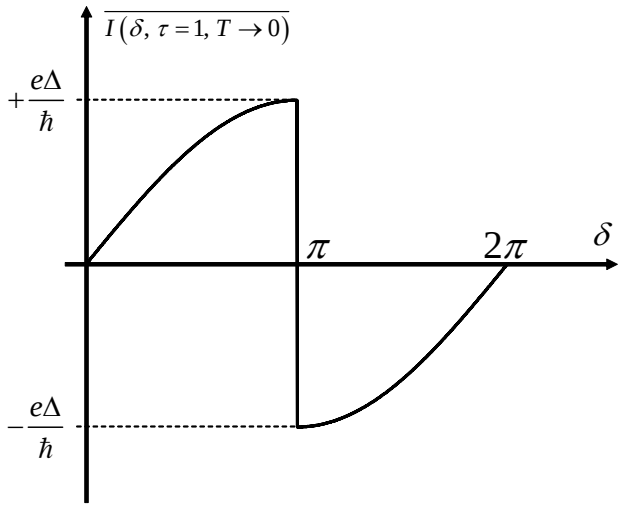

Figure 5: Low temperature ($T \to 0$) equilibrium current-phase relation of a single channel contact of transmission one.

2 Phase dynamics in a purely ohmic environment

In the previous paragraph, we assumed the Josephson weak link to be phase biased. However, in the experiments carried out on the supercurrent, the contacts were embedded in an electromagnetic environment to measure their *IV* characteristics. In such a setup, the phase is a dynamical variable that experiences both thermal and quantum fluctuations. If the phase fluctuations are too large, then the supercurrent is averaged out. Therefore, to measure a maximum supercurrent close to the critical current, it is necessary to damp the fluctuations of the phase. For this purpose, the contact has to be embedded in an on-chip dissipative electromagnetic environment.

Let us start by describing the simplest dissipative electromagnetic environment. It consists of a resistor in parallel with the Josephson weak link. Actually, the Josephson weak link itself consists of the parallel combination of two elements: a pure Josephson element and an intrinsic capacitor (the geometric capacitance of the two superconducting electrodes that form the weak link). This is the well known resistively and capacitively shunted junction (RCSJ) model (see Figure 6). We will start by describing the phase dynamics in this circuit.

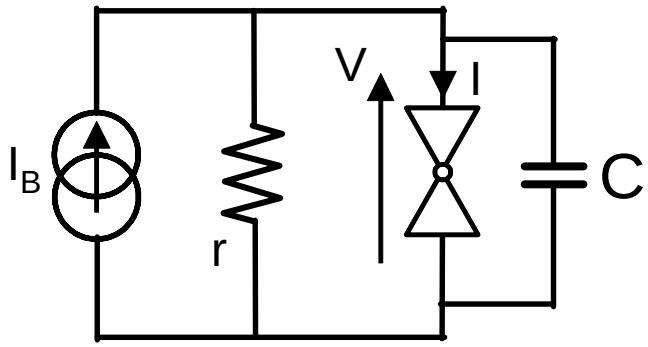

Figure 6: Electromagnetic environment of the RCSJ model.

The Kirchhoff laws for this circuit writes

$$I_B = \frac{V}{r} + i_n(t) + I(\delta) + C\frac{dV}{dt} \qquad (3)$$

where i_n is the Johnson Nyquist current noise associated with the resistor r. i_n is Gaussian white noise characterized by: $\langle i_n(t)\rangle = 0$ and $\langle i_n(t) i_n(t')\rangle = \frac{2k_B T}{r}\delta(t-t')$.

In equation (3), the phase is treated as a classical variable that doesn't experience quantum fluctuations. Only phase fluctuations due to thermal noise of the resistor are taken into account. In the circuit presented on Figure 6, the condition for the phase to be classical is [9]:

$$\frac{\beta E_C}{\pi\rho} \ll 1 \tag{4}$$

with $\beta = \frac{1}{k_B T}$, $E_C = \frac{2e^2}{C}$ the charging energy and $\rho = \frac{r}{R_Q}$, where $R_Q = \frac{h}{4e^2}$ is the resistance quantum. In the following, we will assume a classical behavior for the phase.

Using the second Josephson relation $V = \varphi_0 \dot{\delta}$, one obtains the equation governing the dynamics of the phase in this circuit:

$$C\varphi_0{}^2 \ddot{\delta} + \frac{\varphi_0{}^2}{r}\dot{\delta} + \varphi_0 i_n(t) + \varphi_0\left(I(\delta) - I_0 s\right) = 0 \tag{5}$$

where $s = \frac{I_B}{I_0}$ and $I_0 = \underset{\delta}{\mathrm{Max}}\{I(\delta)\}$.

The dynamics of the phase is therefore equivalent to the Brownian motion of a particle of mass m in a potential $U(\delta)$, submitted to a random force $f(t)$ with a friction coefficient λ, according to the following replacing rules:

$$\begin{cases} m = C\varphi_0{}^2 \\ U(\delta) = \varphi_0\left(\int_0^{\delta} I(x)dx - I_0 s\delta\right) = E_J(\delta) - I_0\varphi_0 s\delta \\ f(t) = -\varphi_0 i_n(t) \\ \lambda = \frac{\varphi_0{}^2}{r} \end{cases}$$

$U(\delta)$ is the so-called tilted washboard potential, represented on Figure 7 for two single channel contacts of different transmissions. $E_J(\delta)$ corresponds to the Josephson coupling energy already defined in the introduction. In the following, the notation "E_J" will refer just to the maximum of this coupling ($E_J = I_0\varphi_0$), and will not contain its phase dependence.

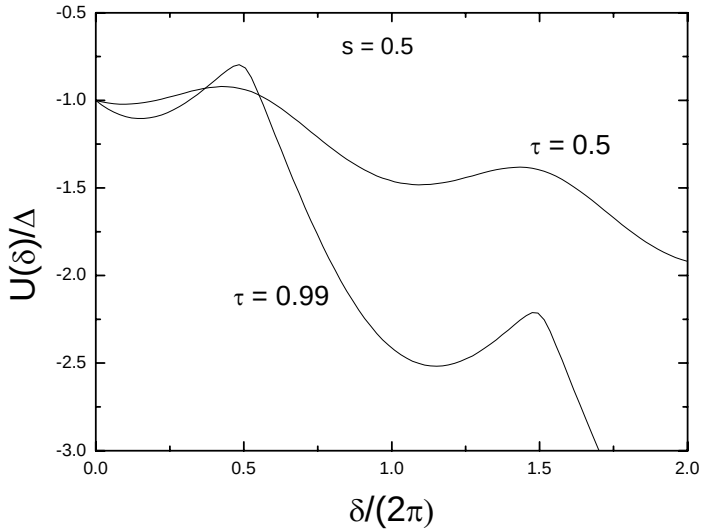

Figure 7: Tilted washboard potential for two single channel contacts of transmission 0.5 and 0.99. The parameter s has been set to 0.5 in both these plots. Only the ground Andreev level is assumed to be occupied.

For small transmissions, $U(\delta)$ is close to the tilted cosine function of the tunnel junction. For transmissions close to unity, the shape of the potential is strongly modified.

The particle can oscillate around a minimum of the potential well. These oscillations are called plasma oscillations. From equation (5), we can determine the frequency of the free oscillations of the fictitious particle in the potential well around $\delta = 0$ for $s = 0$. In the limit of small oscillations, i.e. for $\delta \ll 1$, $\frac{I(\delta)}{I_0} \approx \alpha\delta$, where α depends on the current-phase relation of the contact. For a Josephson tunnel junction, $I(\delta) = I_0 \sin(\delta)$

and $\alpha = 1$. For a single channel contact of arbitrary transmission τ, $\alpha = \frac{\tau}{2\left(1-\sqrt{1-\tau}\right)}$.

In absence of tilt ($s = 0$), the plasma frequency thus simply writes[2]:

$$\nu_p\left(s=0,\,\alpha\right) = \frac{1}{2\pi}\sqrt{\frac{\alpha I_0}{\varphi_0 C}}$$

As an example, the plasma frequency for a single channel contact of transmission 0.7 is 34.2 GHz (assuming a typical geometric capacitance $C = 1$ fF between the two superconducting electrodes).

In fact, as the potential is highly anharmonic, the oscillation frequency decreases with amplitude. A Josephson weak link can therefore be considered as a non-linear inductor. To calculate the Josephson inductance at any given value of the phase δ, one goes back to the two fundamental Josephson relations:

$$\begin{cases} I = I\left(\delta\right) \\ V = \varphi_0 \dot{\delta} \end{cases}$$

Combining these two relations leads to:

$$V = \frac{\varphi_0}{dI\left(\delta\right)/d\delta}\frac{dI}{dt}.$$

The voltage across the Josephson weak link is proportional to the time derivative of the current flowing through it. This defines the non linear Josephson inductance:

$$L\left(\delta\right) = \frac{\varphi_0}{dI\left(\delta\right)/d\delta}.$$

---

[2] When the washboard potential is tilted $s \neq 0$, the plasma frequency of a Josephson tunnel junction ($\alpha = 1$) can be expressed as:

$\nu_p\left(s,\,\alpha=1\right) = \nu_p\left(s=0,\,\alpha=1\right)\left(1-s^2\right)^{1/4} \approx \nu_p\left(s=0,\,\alpha=1\right)\left[2\left(1-s\right)\right]^{1/4}$. The oscillations become slower when the bias current increases because the potential becomes smoother.

Two dynamical regimes can be distinguished depending on whether the plasma oscillations are underdamped or overdamped. The oscillations are overdamped if the characteristic damping time is shorter than the period of the oscillations: $rC \ll \sqrt{\frac{\varphi_0 C}{I_0}}$.

This condition can be expressed as:

$$\frac{r^2 C I_0}{\varphi_0} \ll 1.$$

The quantity $r^2 C I_0 / \varphi_0$ is the so-called McCumber Stewart parameter [10, 11].

In the following, we will focus on the overdamped regime, since in this case, the dynamics of the phase is exactly solvable. In the overdamped limit, the inertial term of equation (5) can be neglected. Therefore the equation of motion rewrites:

$$\lambda \dot{\delta} - f(t) + \frac{dU(\delta)}{d\delta} = 0 \qquad (6)$$

An analytical solution can be found for the mean voltage $\langle V \rangle = \varphi_0 \langle \dot{\delta} \rangle$ across the Josephson element and current $\langle I \rangle = I_0 \langle \sin(\delta) \rangle$ flowing through it. This solution was first established in 1968 by Ivanchenko and Zil'berman [12] for a tunnel junction. Their result was recovered by Ambegaokar and Halperin [13, 14] who developed a more general approach able to treat arbitrary potentials $U(\delta)$. In particular, their approach enables us to treat the case of a weak link containing channels of arbitrary transmissions.

2.1 The Ivanchenko Zil'Berman solution

Ivanchenko & Zil'berman calculated the dc IV characteristic of a tunnel junction solving the Fokker-Planck[3] equation (7) associated with the Langevin equation (6).

[3] In the specific case of a Langevin equation in the overdamped regime, the Fokker-Planck equation is called a Smoluchowski equation.

$$\frac{\partial W}{\partial t} = \frac{1}{\lambda}\frac{\partial}{\partial \delta}\left[\left(\frac{\partial U}{\partial \delta}\right)W + k_B T \frac{\partial W}{\partial \delta}\right]$$
$$\frac{\lambda}{E_J}\frac{\partial W}{\partial t} = \beta E_J \frac{\partial^2 W}{\partial \delta^2} + \cos(\delta)W + \left[\sin(\delta) - s\right]\frac{\partial W}{\partial \delta} \qquad (7)$$

where W is the probability density to find the phase in the interval $[\delta, \delta + d\delta]$ at time t when at $t = t_0$, the phase was δ_0.

Then, it is useful to take the Fourier transform of W:

$$x_n(t) = \int_{-\infty}^{+\infty} e^{in\delta} W(\delta, t) d\delta$$

In terms of x_n, the Josephson current is then:

$$I = I_0 \lim_{t\to\infty} \int_{-\infty}^{+\infty} \sin(\delta) W(\delta, t) d\delta = I_0 \frac{x_1(\infty) - x_{-1}(\infty)}{2i}$$

W is real therefore $x_n = x_{-n}^{*}$ and $I = I_0 \operatorname{Im}\{x_1(\infty)\}$.

The x_n verify the equation:

$$\frac{\lambda}{E_J}\frac{\partial x_n}{\partial t} = -n\left[(\beta E_J n - is)x_n + \frac{x_{n+1} - x_{n-1}}{2}\right]$$

In the limit $t \to \infty$, the system reaches a steady state, i.e. $\frac{\partial x_n}{\partial t} = 0$. The x_n verify the recurrence relation $2(\beta E_J n - is)x_n(\infty) = x_{n+1}(\infty) - x_{n-1}(\infty)$ which is similar to the recurrence relation verified by the modified Bessel function of the first kind:

$$2\eta I_\eta(z) = z\left[I_{\eta-1}(z) - I_{\eta+1}(z)\right]$$

W is normalized, as a consequence $x_0 = 1$ and:

$$x_1(\infty) = \frac{I_{1-is\beta E_J}(\beta E_J)}{I_{-is\beta E_J}(\beta E_J)}$$

Finally:

$I(I_B) = I_0 f_{IZ}\left(\frac{I_B}{I_0}, \frac{E_J}{k_B T}\right)$, where $f_{IZ}(x, y) = \operatorname{Im}\left[\frac{I_{1-ixy}(y)}{I_{-ixy}(y)}\right]$.

The voltage through the junction is then calculated using the relation $V = r\left(I_B - I\left(I_B\right)\right)$.

At zero temperature, this can be simplified as:

$$I(V) = \begin{cases} I_B & 0 \le I_B \le I_0 \quad ; \quad V = 0 \\ \dfrac{V}{r}\left(\sqrt{1+\left(\dfrac{rI_0}{V}\right)^2} - 1\right) & \quad ; \quad V \neq 0 \end{cases}$$

IV characteristics of a tunnel junction at different temperatures are plotted on Figure 8 in reduced units. The natural units are I_0 for the current scale and rI_0 for the voltage scale. The supercurrent branch at $V = 0$ of the phase biased weak link broadens to form a supercurrent peak centered around zero voltage when it is placed in an electromagnetic circuit.

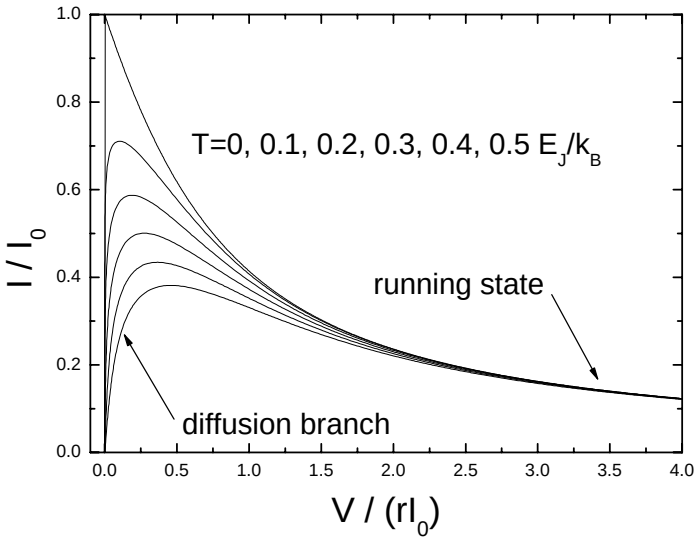

Figure 8: IV characteristic of a tunnel junction at different temperatures calculated using the Ivanchenko Zil'Berman result.

The shape of the supercurrent peak calculated by Ivanchenko and Zil'berman can be understood by means of a qualitative analysis. The dynamics of the phase in this potential depends on the value of s compared to 1 (see Figure 9 and Figure 10).

At zero temperature, as long as $0 < s < 1$, the particle sits in a minimum of the potential.

Therefore the average voltage across the junction is perfectly zero if one assumes a perfectly classical behavior for the phase. Actually, the phase can oscillate even at zero temperature because of zero point fluctuations.

When s reaches and goes beyond the value 1, the washboard potential has no minima any longer. Therefore the particle starts to run away in the potential at a constant velocity fixed by the dissipation in the resistor. A voltage appears across the junction.

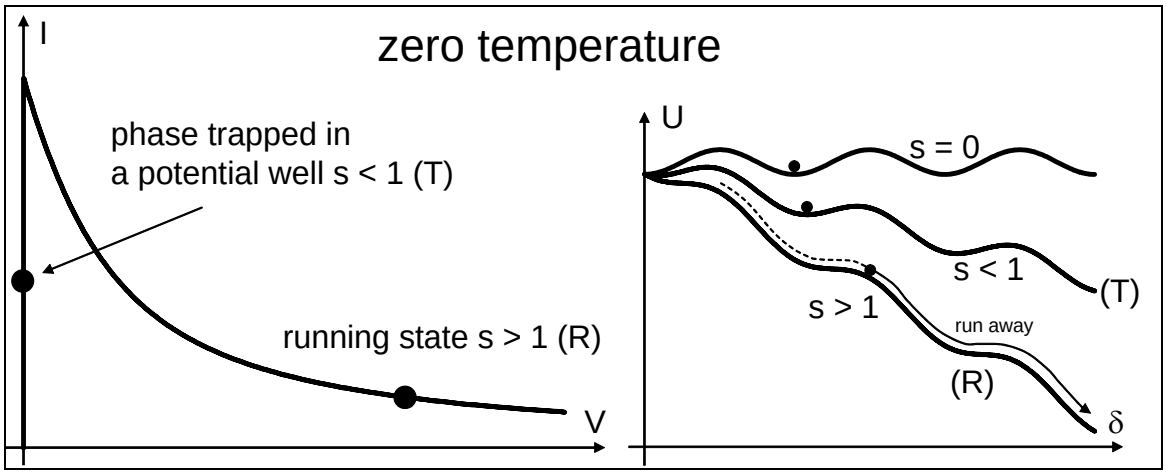

Figure 9: Pictorial illustration of the phase dynamics at $T = 0$. As long as s < 1, the particle sits in a minimum of the potential well and the voltage across the junction is zero. For s > 1, the particle starts to run away in the potential and a finite voltage develops across the junction.

At finite temperature, the situation is more complex. Indeed, even for $0 < s < 1$, the particle can be activated out of a potential minimum. But if the dissipation is large enough, it can be retrapped in the next one, from where it is activated once again and so on. In this case, the motion of the particle in the potential is diffusive, and the average velocity $\langle \dot{\delta} \rangle$ is small but non zero: a small voltage appears across the junction.

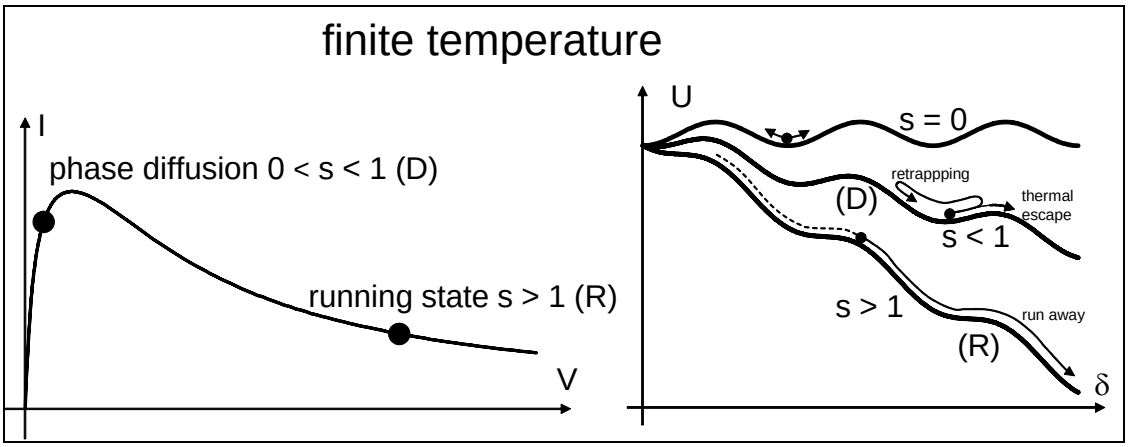

Figure 10: Pictorial illustration of the phase dynamics at finite temperature. At s = 0, the particle oscillates in a minimum of the potential well. When s is increased, the particle has a diffusive motion in the potential: it is successively activated out of a minimum of the well and retrapped, resulting in a small voltage across the junction. For larger s, the particle runs away in the potential and a large voltage develops across the junction.

2.2 The Ambegaokar Halperin method

Ambeagaokar & Halperin proposed a slightly different approach, which can deal with any type of current-phase relation. They start from the very same Smoluchowski equation (equation (7)):

$$\frac{\partial W}{\partial t} = \frac{1}{\lambda}\frac{\partial}{\partial \delta}\left[\left(\frac{\partial U}{\partial \delta}\right)W + k_B T \frac{\partial W}{\partial \delta}\right] = -\frac{\partial J}{\partial \delta}$$

where $J = -\frac{1}{\lambda}\left[\left(\frac{\partial U}{\partial \delta}\right)W + k_B T \frac{\partial W}{\partial \delta}\right]$ is the probability current. It is worth noticing that $\frac{\partial W}{\partial t} = -\frac{\partial J}{\partial \delta}$ is a continuity equation, where the current is the sum of two terms. The first one describes the deterministic evolution of W whereas the second one describes its diffusive evolution due to the random force.

In steady state, W is time independent. As a consequence, J doesn't depend on δ. Therefore it is easy to find a solution for W in terms of J. For periodic boundary conditions ($W(\delta=0)=W(\delta=2\pi)$), this solution writes [13, 14, 15]:

$$W(\delta)=\frac{J\lambda}{k_BT}\frac{S(\delta)}{S(2\pi)-S(0)}\left[S(0)\int_0^{\delta}\frac{dx}{S(x)}+S(2\pi)\int_{\delta}^{2\pi}\frac{dx}{S(x)}\right],$$

with $S(\delta)=\exp\left[-\frac{U(\delta)}{k_BT}\right]$.

For an atomic contact with N channels, $U(\delta)$ writes (considering only the ground Andreev state of each channel to be occupied):

$$U(\delta)=-E_J\left(\frac{\Delta}{E_J}\sum_{i=1}^{N}\sqrt{1-\tau_i\sin^2\left(\frac{\delta}{2}\right)}+s\delta\right)$$

Therefore:

$$W(\delta)=\beta J\lambda\frac{S(\delta)}{\exp(2\pi s\beta E_J)-1}\left[\int_0^{\delta}\frac{dx}{S(x)}+\exp(2\pi s\beta E_J)\int_{\delta}^{2\pi}\frac{dx}{S(x)}\right]$$

Using the normalization condition $\int_0^{2\pi}W(\delta)d\delta=1$, one finds:

$$J=\frac{\exp(2\pi s\beta E_J)-1}{\beta\lambda\int_0^{2\pi}S(\delta)\left[\int_0^{\delta}\frac{dx}{S(x)}+\exp(2\pi s\beta E_J)\int_{\delta}^{2\pi}\frac{dx}{S(x)}\right]d\delta},$$

It is possible to express the average phase velocity, and thus the mean voltage across the contact, in terms of the probability current.

From equation (6), the time averaged phase velocity defined by $\langle\dot{\delta}\rangle=\lim_{D\to\infty}\left\{\frac{1}{D}\int_0^{D}\dot{\delta}(t)dt\right\}$ in the stationary limit is given by:

$$\langle\dot{\delta}\rangle=\frac{1}{\lambda}\left\langle f(t)-\frac{dU(\delta)}{d\delta}\right\rangle=\frac{1}{\lambda}\left\langle\frac{dU(\delta)}{d\delta}\right\rangle,$$

because $\langle f(t)\rangle=0$.

Therefore $\langle\dot{\delta}\rangle=\frac{1}{\lambda}\int_0^{2\pi}\frac{dU(\delta)}{d\delta}W(\delta)d\delta=\int_0^{2\pi}\left(J-\frac{k_BT}{\lambda}\frac{dW(\delta)}{d\delta}\right)d\delta=2\pi J$, because J doesn't depend on the phase and $W(\delta=0)=W(\delta=2\pi)$.

Thus the dc voltage across the contact simply writes as:

$$V = \varphi_0 \left\langle \dot{\delta} \right\rangle = \varphi_0 2\pi J$$

Hence:

$$V = \frac{2\pi r I_0}{\beta E_J} \frac{\exp\left(2\pi s \beta E_J\right) - 1}{\int_0^{2\pi} S(\delta) \left[\int_0^{\delta} \frac{dx}{S(x)} + \exp\left(2\pi s \beta E_J\right) \int_{\delta}^{2\pi} \frac{dx}{S(x)} \right] d\delta}.$$

And the current simply writes: $I = sI_0 - V/r = I_B - V/r$.

This calculation by Ambegaokar and Halperin reproduces the Ivanchenko Zil'berman result in the tunnel limit. It doesn't provide us with an analytical result but it applies to any potential $U(\delta)$.

It appears that the shape of the supercurrent peak is only slightly dependent on the transmission of the channel, as shown on Figure 11.

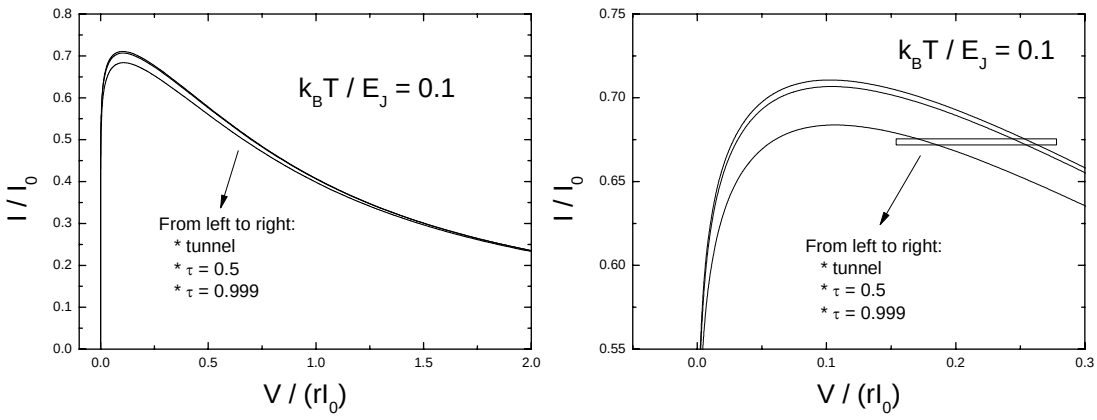

Figure 11: Calculated supercurrent peaks for single channel contacts of various transmissions. The right panel is a zoom around the maximum of the peaks.

The curves presented here have been in fact calculated using a code developed by A. L. Yeyati & R. Duprat (see section III. of [16]).

Only for transmissions very close to unity, i.e. in the ballistic limit, the shape of the peak starts to depart from the Ivanchenko Zil'berman result for tunnel junctions (see

Figure 11). Therefore the shape of the supercurrent peak is not a good tool, having a large discriminating power, to extract the current phase relation of the weak link. In chapter 3 and specially chapter 4, we present other techniques to really measure the current-phase relation of an atomic contact.

Anyhow, it is worth noticing here that the Ambegaokar Halperin calculation does not describe the reality correctly for highly transmitting channels. Indeed, this calculation assumes that the system stays in the lower Andreev bound state by taking the adiabatic current phase relation to be valid even at finite voltages. But at finite voltages, the phase acquires a dynamics which can induce Landau-Zener transitions to the upper Andreev level when the phase δ is swept through $\delta = \pi$ (see chapter 1). This happens only in highly transmitting channels, when the Andreev gap between the two levels is small enough for the Landau-Zener probability to be sizeable. Therefore, the measured IV characteristics at low voltage look very different from the IV calculated within this simple adiabatic formalism because in highly transmitting channels, the current due to MAR processes start at voltages within the width of the supercurrent peak. In this voltage range, the supercurrent and MAR current interfere to build up the total current, as described in paragraph 2.3.
Thermal fluctuations in the contact electrodes [17] also change the occupation numbers of the Andreev bound states. This effect, addressed in [18, 19] for contacts containing only ballistic channels is not included in our theoretical analysis. This simplification is justified for contacts with channels of not too high transmission, however the effect should become sizeable for high enough transmissions.

2.3 From the supercurrent to MAR

In chapter 1, we showed that Landau-Zener transitions between the two Andreev bound states were responsible for the MAR current at finite voltages. A. L. Yeyati [20] has extended Cuevas *et al.* [21] calculation, which corresponds to the perfect voltage bias case, to account for the electromagnetic environment of the contact. Within this new approach, both the supercurrent peak and the MAR current can be obtained at once for a Josephson weak link embedded in an ohmic environment (see Figure 12). In

particular, it can account for the IV characteristic at small voltages, when both MAR current and supercurrent mix in highly transmitting channels. This calculation is based on a selfconsistent method and goes as follows for each value of the bias current I_B:

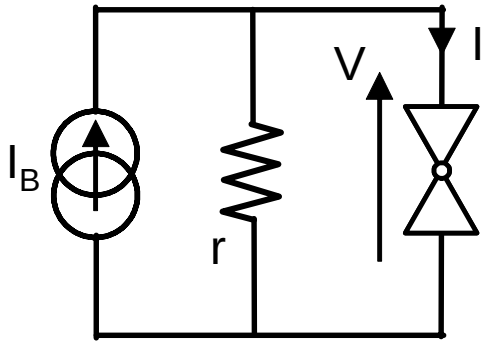

Figure 12: Atomic contact embedded in an ohmic environement r.

1) A guess dc voltage V is chosen.
2) All the harmonics (sines and cosines components) of the current (see chapter 1) are calculated at the voltage V using the MAR formalism for a perfect voltage bias [21]. They define an "effective", voltage dependent, current-phase relation.
3) This effective current phase relation is plugged in the Smoluchovski equation (7) to take into account the effect of the fluctuations in the resistor. A new dc voltage V is obtained from the resolution of the Smoluchovski equation, as well as the corresponding dc current $I = I_B - V/r$.
4) Steps 2 and 3 are iterated until the value of the voltage V has converged.

Each point on the IV curve is calculated in the same way by sweeping the bias current I_B. The outcome of this selfconsistent calculation is presented on Figure 13. The MAR and supercurrent contributions don't add up independently but rather interfere to build up the full IV curve.

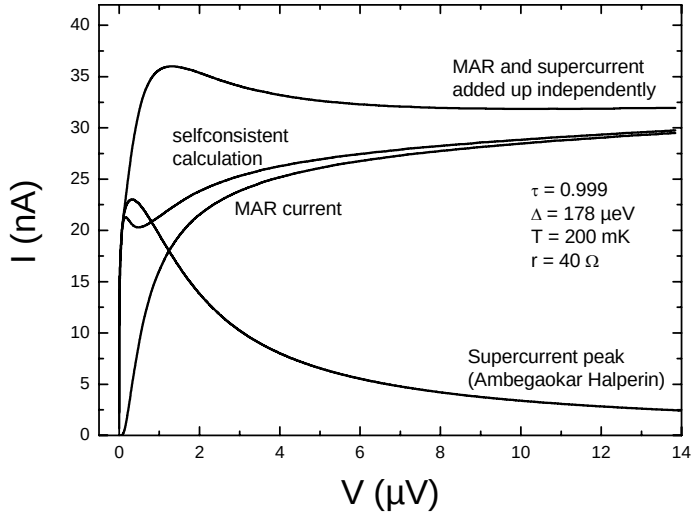

Figure 13: Comparison of the adiabatic calculation (Ambegaokar Halperin) with the self consistent approach for a channel of transmission 0.999.

It is worth looking at the case of transmission very close to unity to clearly understand the effect of the Landau-Zener transitions on the magnitude of the supercurrent peak. Figure 14 shows the *IV* curve calculated at finite temperature for a single channel of transmission 0.9999.

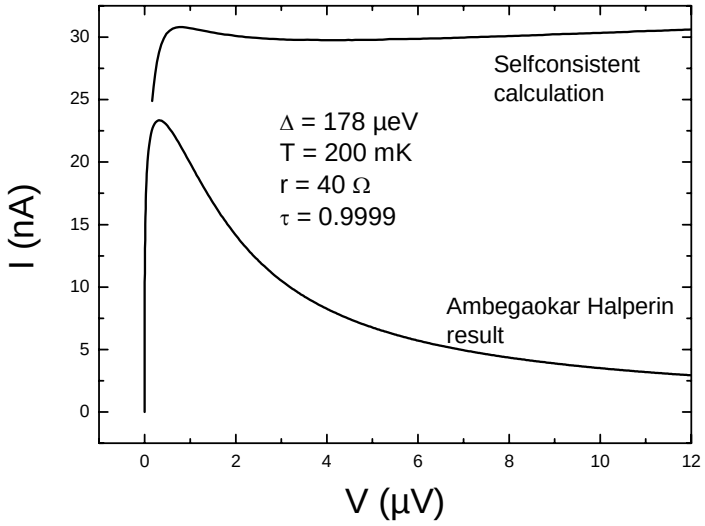

Figure 14: IV curve at small voltages for an almost ballistic channel. The predictions of the adiabatic Ambegaokar Halperin calculation and of the selfconsistent calculation are displayed.

The IV curves on Figure 14 clearly exhibit the fact that Landau-Zener transitions[4] enhance the magnitude of the supercurrent peak in almost ballistic channels.

This statement can easily be understood by means of a handwaving argument. As the ballistic Andreev bound state always carry a positive current (see Figure 15), it is clear that thermal fluctuations of the phase will have a smaller effect on the maximum of the supercurrent peak than for contacts with transmission smaller than 1 where phase fluctuations can wash out completely the supercurrent.

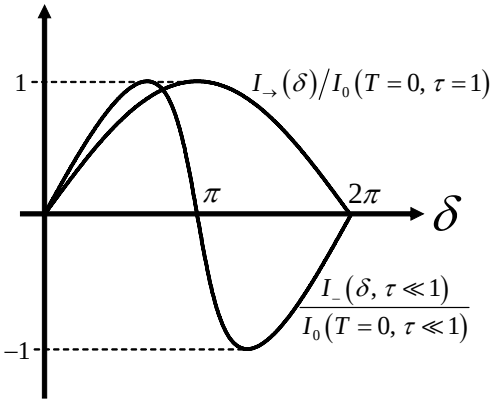

Figure 15: The current phase relations have been normalized by their respective zero temperature critical currents (see section 1). The ballistic bound state $E_{\rightarrow}$ always carry the positive current $I_{\rightarrow}(\delta)$. Fluctuations of the phase have therefore a smaller impact than in a channel with a current phase relation with zero average.

[4] We recall that the Landau-Zener probability is given by $P_{LZ} = \exp\left[-\pi \frac{\Delta}{eV}(1-\tau)\right]$. For channels with very high transmissions, the Landau-Zener probability becomes sizeable even for a slow velocity of the phase. At the maximum of the supercurrent peak of Figure 14, the voltage is $V = 0.76$ μV. Therefore the Landau Zener probability is $P_{LZ} \approx 0.93$.

2.4 Temperature dependence of the maximum of the supercurrent peak

We have calculated the maximum of the supercurrent peak at different temperatures using the self consistent calculation developed by A. L. Yeyati and presented in section 2.3. The results are shown on Figure 16.

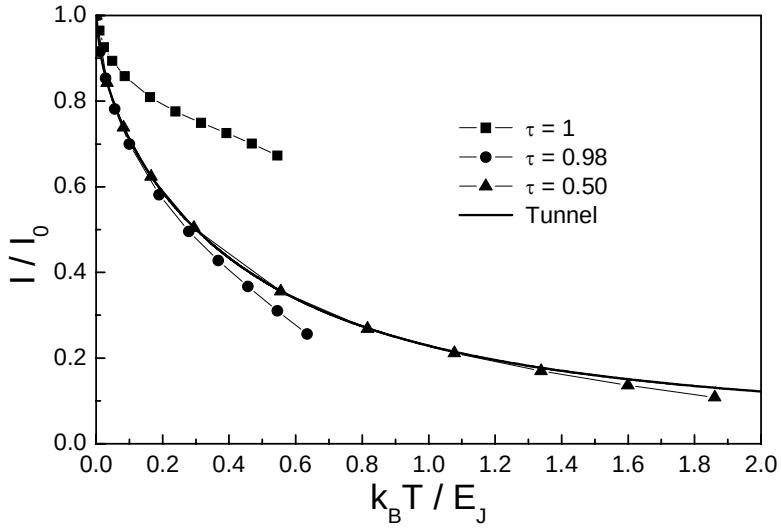

Figure 16: Calculated temperature dependence of the maximum of the supercurrent peak for channels of different transmissions.

The effect of fluctuations on the maximum of the supercurrent peak in a ballistic (or almost ballistic) channel is smaller than on a channel with intermediate transmission. The fundamental reason is the fact that the ballistic current phase relationship has a non zero phase average.

3 Phase dynamics in a frequency dependent electromagnetic environment

In section 2, the atomic contact was embedded in an purely ohmic environment. The resistor played two roles: first to voltage bias the contact at zero frequency, and provide damping for the high frequency phase fluctuations, so as to observe a well developed supercurrent peak.

In practice, it is very hard to implement a purely ohmic environment. Indeed, the characteristic frequency of the oscillating Josephson currents is in the GHz frequency range. Therefore, the dissipative elements have to be small and they have to be fabricated on-chip, very close to the junction to avoid parasitic capacitances and inductances. However, some power is dissipated in the resistors and heats them up. It is thus necessary that the resistors have a large enough volume for the electrons to release their energy in the phonon bath. These conflicting requirements on the size of the resistors impose to find a compromise when designing the environment, as explained in detail in chapter 5. The best environment that we have designed to fulfill these requirements is sketched on Figure 17a. The basic idea is to split the resistance providing the dissipation in two parts: the dissipation for the dc voltage bias takes place in a macroscopic resistor R. The ac dissipation for the damping of the phase fluctuations is ensured by the on-chip resistors r, close to the junction. In chapter 5, we show that seen from the junction, the electric circuit of Figure 17a is very well approximated by the simpler electric circuit depicted on Figure 17b. The phase dynamics will therefore be studied in this simpler circuit.

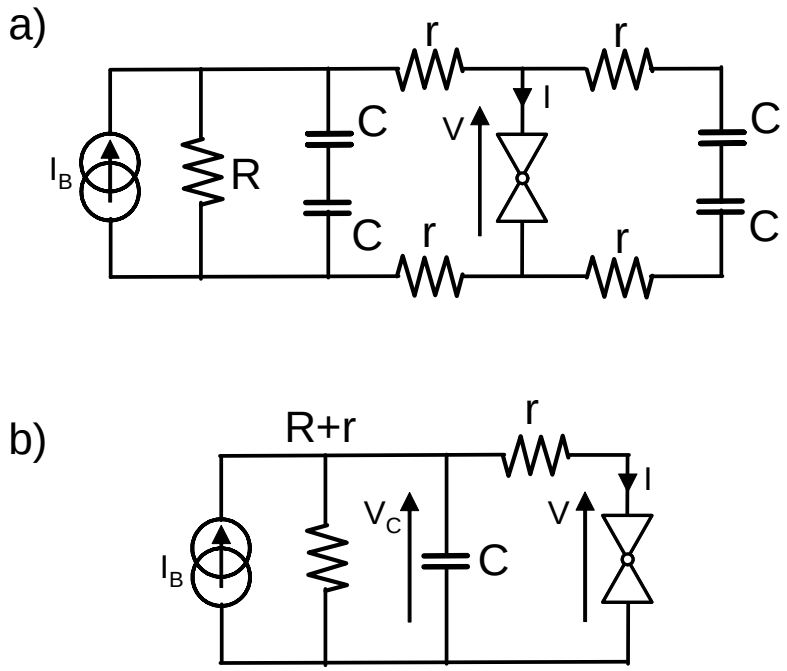

Figure 17: a) Actual electromagnetic environment implemented in the experiments. The conductors between the two capacitors of each branch correspond to the metallic substrate which provides the ground potential. b) Simplified electromagnetic environment seen by the contact.

The electrical equations (Kirchhoff law and second Josephson relation) of the circuit (see Figure 17) write:

$$\begin{cases} I_B = \dfrac{V_C}{R+r} + i_n^{R+r}(t) + I(\delta) + C\dfrac{dV_C}{dt} \\ \varphi_0 \dot{\delta} = V_C - r\left(I(\delta) + i_n^r(t)\right) \end{cases}$$

where i_n^x ($x = r,\ R+r$) is the current noise associated with each one of the resistor. This is Gaussian white noise characterized by $\left\langle i_n^x(t) \right\rangle = 0$ and $\left\langle i_n^x(t) i_n^x(t') \right\rangle = \dfrac{2k_B T}{x}\delta(t-t')$. We assume here that the two resistors are thermalized at the same temperature T. This set of coupled differential equations can be solved by numerical integration. Nevertheless, it is by far more efficient to first derive a Fokker-Planck equation and proceed with the numerics afterwards. The Fokker-Planck equation establishes the time evolution for the probability density $W(\delta, V_C, t)$ of finding, at time t, a phase

difference in the interval $[\delta, \delta + d\delta]$ and a voltage across the capacitor in the interval $[V_C, V_C + dV_C]$.

R. Duprat & A. L. Yeyati derived the Fokker Planck equation associated with this set of coupled differential equations (Section V of [16]). The Fokker-Planck equation writes[5]:

$$\frac{\partial W}{\partial t} = -\frac{\partial}{\partial \delta}\left[\frac{V_C - rI(\delta)}{\varphi_0}W\right] - \frac{\partial}{\partial V_C}\left[\frac{(R+r)(I_B - I(\delta)) - V_C}{(R+r)C}W\right] + \frac{k_B T}{(R+r)C^2}\frac{\partial^2 W}{\partial {V_C}^2} + \frac{r k_B T}{{\varphi_0}^2}\frac{\partial^2 W}{\partial \delta^2} \quad (8)$$

The details of the resolution of equation (8) are presented in [16].

As shown on Figure 18, the effect of the capacitance is essentially to modify the width of the peak but not its amplitude. If the shunt capacitor is large enough, then the environment seen from the junction is essentially a single resistor r. Therefore the Fokker-Planck calculation reproduces the Ivanchenko Zil'berman result. But if the capacitors are smaller, then the frequency dependence of the environment comes into play and deviations from the Ivanchenko Zil'berman result can be observed on the IV's (see Figure 18). This theory allows also to treat weak links with several channels of arbitrary transmissions[6].

A simpler approach (single frequency model) has been investigated to describe the shape of the supercurrent peak of a Josephson weak link embedded in a non-ohmic environment. This approach is based on the crude approximation that at a given voltage V, only Josephson currents at the frequency $\omega_J = V/\varphi_0$ oscillate in the weak link. Therefore, at each value of the dc voltage V on the IV characteristic, the dissipation R of the purely ohmic case is replaced by $\mathrm{Re}[Z(\omega_J)]$ for a contact in an environment

[5] Here, we have set the oscillating drive of [16] to zero.

[6] On Figure 18, the IV curves have been calculated for a tunnel junction to allow comparison with the Ivanchenko Zil'berman result.

of impedance $Z(\omega)$. However, as seen in Figure 18, the predictions of this crude model are not in good agreement with the full calculation (see dotted line on Figure 18).

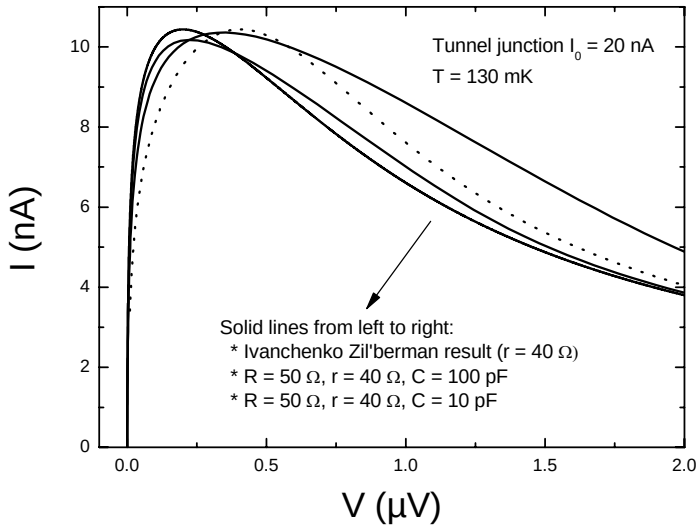

Figure 18: IV characteristics of a tunnel junction embedded in a $r+\left((r+R)//C\right)$ *environment for different values of the capacitor* C *(The "+" symbolizes the series combination of two elements, whereas the "//" represents the parallel combination.). The dotted line is the prediction of the single frequency model for* $C = 10$ pF.

4 Observation of the supercurrent peak

In this paragraph we present experimental results on the supercurrent peak of atomic contacts measured in two different biasing schemes: the atomic contact was either voltage biased or current biased. Goffmann *et al.* [3] already measured the supercurrent peak of a current biased contact. In their setup, it was only possible to measure the diffusion branch because the part of the supercurrent peak with negative slope was unstable. In our experiments, we go one step beyond by voltage biasing the contacts. This allows the measurement of the full supercurrent peak. A detailed analysis of the conditions for voltage biasing the contact and damping the fluctuations of the phase can be found in chapter 5.

We measured the supercurrent peaks of aluminum atomic contacts containing channels of different transmissions at various temperatures. Figure 19 shows a schematic representation of the setup. The detailed wiring can be found in chapter 5.

A current source I_B shunted by a resistor $R \approx 50\ \Omega$ provides the atomic contact with a voltage bias. The four resistances $r \approx 40\ \Omega$ fabricated on chip, close to the junction provide the necessary dissipation at high frequency to damp the phase fluctuations.

The current I through the atomic contact is measured by monitoring the voltage drop across a resistor r. The voltage V across the contact is directly measured.

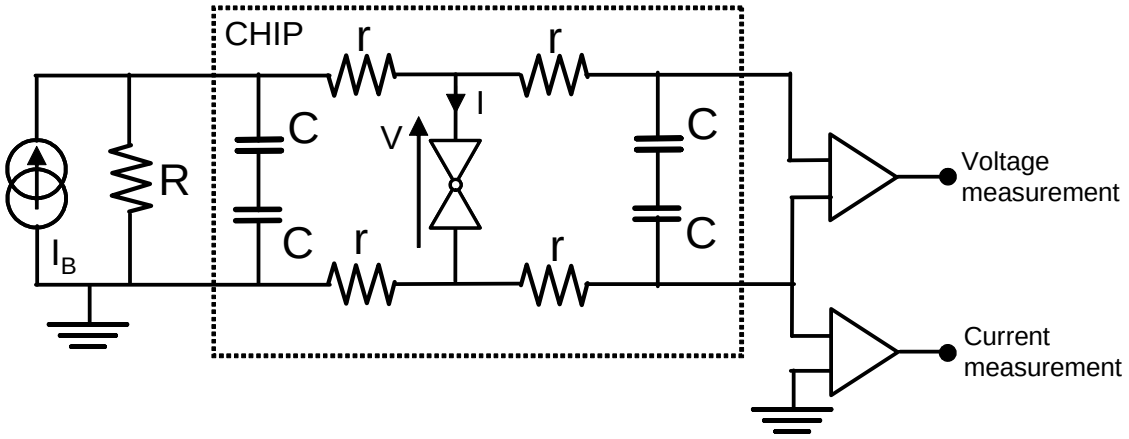

Figure 19: Schematic representation of the experimental setup used for measuring the supercurrent peak.

For each contact, the transmissions and the superconducting gap of the aluminum contact were fitted using the procedure described in chapter 5. The parameters of the electromagnetic environment have been measured independently (see Table 2 and Figure 19).

The value of the capacitors ($C = 92$ pF) was deduced from the surface of the connecting pads and from the value of the polyimide dielectric constant and thickness. All these contacts were obtained on the same sample. The values of the resistors are slightly different for the different contacts because the experimental setup had to be warmed up at room temperature at some point between two runs. The values

$\{R = 50.3\ \Omega,\ r = 39.4\ \Omega\}$ were the values before the warming up and the values $\{R = 50.2\ \Omega,\ r = 40.5\ \Omega\}$ were the values after.

Contact #	Pin code	Superconducting gap (μeV)	Critical current (nA)	$R\ (\Omega)$	$r\ (\Omega)$
1	{0.398, 0.215, 0.067}	177.5	16.07	50.2	40.5
2	{0.603, 0.110, 0.061}	179.0	19.87	50.3	39.4
3	{0.677, 0.391, 0.201, 0.2, 0.2}	178.0	41.76	50.2	40.5
4	{0.995, 0.372, 0.174, 0.022}	179.3	49.89	50.3	39.4
5	{0.389, 0.238, 0.055}	178.2	16.18	50.2	40.5

Table 2: Characteristics of the five contacts used in the experiments. All the contacts were obtained on the same sample.

4.1 Contacts with not too high transmissions

The supercurrent peaks of contacts #1 and #2 containing channels of intermediate transmissions have first been fitted with the Ivanchenko Zil'berman result for a Josephson tunnel junction of same critical current embedded in a resistive environment r. The only adjustable parameter was the temperature of the resistor r. The experimental data and the corresponding Ivanchenko Zil'berman fits are shown on Figure 20 and Figure 21.

The theory describes the experimental results quite well, however, the width of the experimental supercurrent peak is slightly larger than predicted by the Ivanchenko Zil'berman result. This is an effect of the actual environment which is not a simple resistor but rather the $r + \left((r + R) // C\right)$ combination[7]. The dynamics of the phase in this

[7] The "+" symbolizes the series combination of two elements, whereas the "//" represents the parallel combination.

more complex environment can be accounted for by the theory presented in paragraph 3. This calculation also includes the non tunnel nature of the Josephson weak link. The predictions of this full theory are compared to the experimental data on Figure 22 and Figure 23, in a smaller window centered on zero voltage to enhance the differences with the Ivanchenko Zil'berman fits of Figure 20 and Figure 21. Once again, the only adjustable parameter was the temperature T of the two resistors r and R. The width of the peak is better accounted for by including the effects of the non ohmic environment. The noise temperatures extracted from the full calculation are very close to the values obtained from the fits to the Ivanchenko Zil'berman predictions.

Nevertheless, the effective noise temperatures are much higher than the fridge temperature at which the experiments were performed. We attribute this to spurious noise from the measurement and biasing lines, at intermediate frequencies, that we could not eliminate despite filtering. The effective noise temperatures found from the fits are summarized in Table 3.

Contact # Mesoscopic pin code	Effective noise temperature (Ivanchenko Zil'berman) (mK)	Effective noise temperature (full calculation) (mK)
#1 {0.398, 0.215, 0.067}	162	155
#2 {0.603, 0.110, 0.061}	88	80

Table 3: Summary of the fitted effective temperatures for the contacts 1 and 2.

The description of the supercurrent peak of contacts #1 and #2 is rather straightforward. Indeed, the contribution of the supercurrent and of the MAR current don't overlap since the transmissions of the contact are small. The onset of the MAR current occurs at voltages where the tail of the supercurrent peak doesn't contribute any longer. The adiabatic theory presented in paragraph 3 is therefore sufficient to account for the results on these two contacts. This is not the case for contacts containing highly transmitting channels.

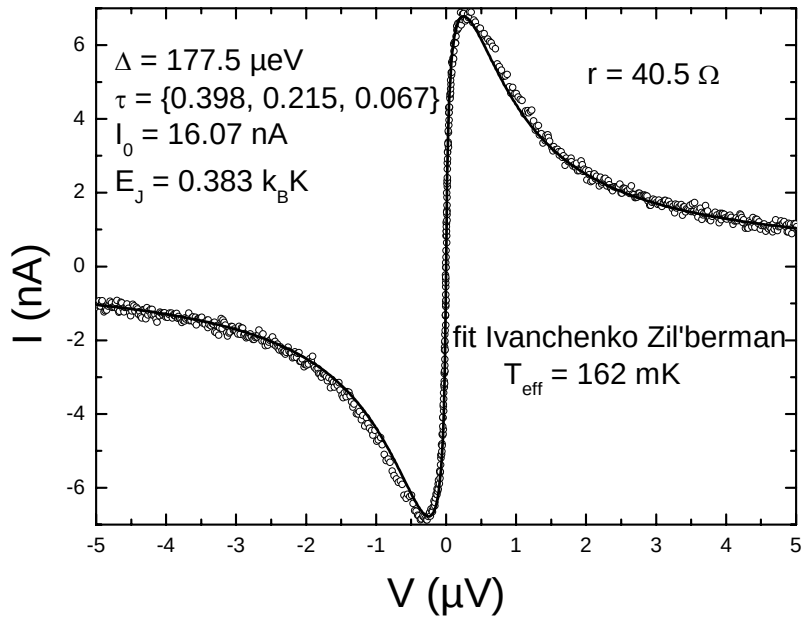

Figure 20: Supercurrent peak of contact #1. The solid line is the fit with the Ivanchenko Zil'berman result, $T_{eff} = 162$ mK. The actual fridge temperature was 20 mK.

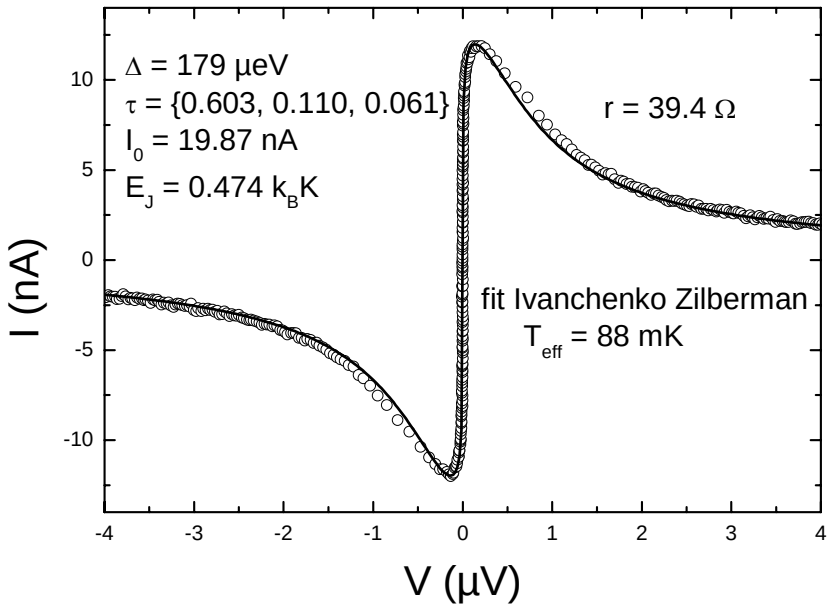

Figure 21: . Supercurrent peak of contact #2. The solid line is the fit with the Ivanchenko Zil'berman result, $T_{eff} = 88$ mK. The actual fridge temperature was 20 mK.

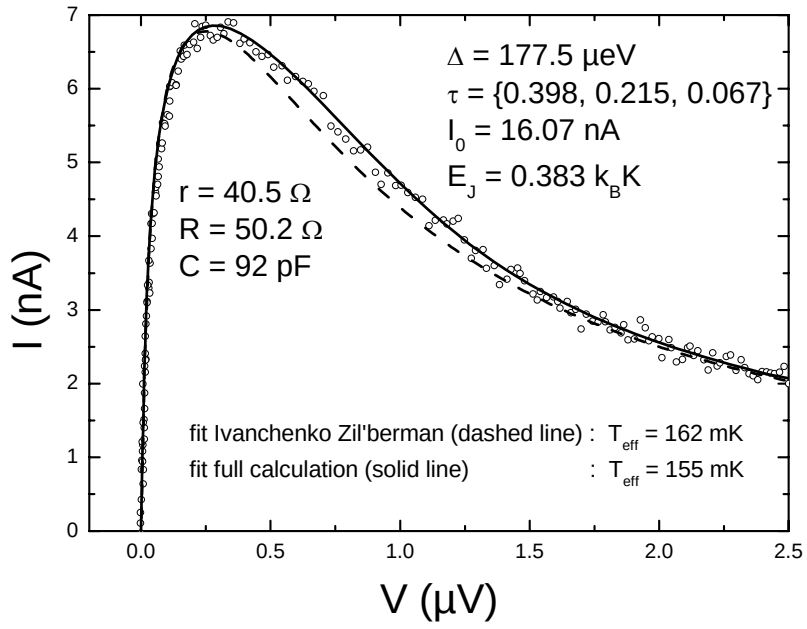

Figure 22: Supercurrent peak of contact #1. The solid line is the prediction of the full calculation, $T_{eff} = 155$ mK. Dashed line: fit with the Ivanchenko Zil'Berman result. The actual fridge temperature was 20 mK.

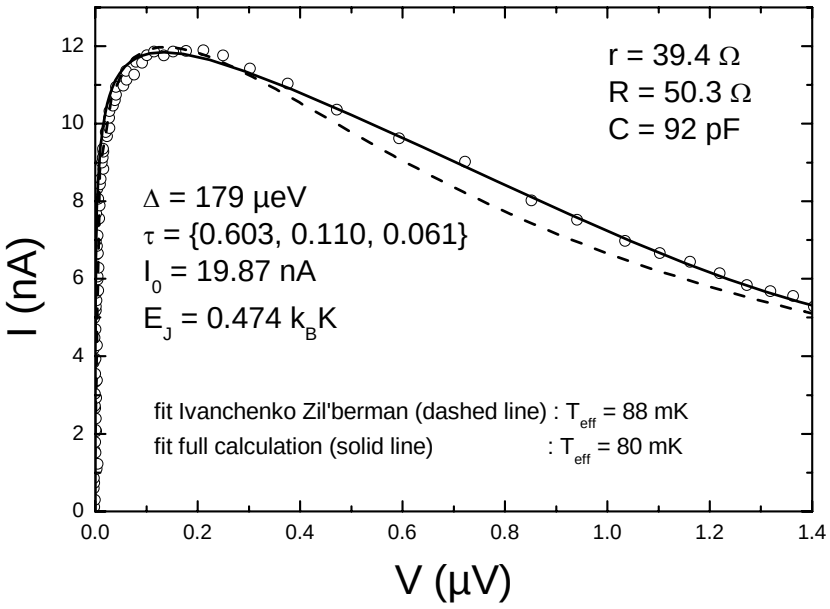

Figure 23: Supercurrent peak of contact #2. The solid line is the prediction of the full calculation, $T_{eff} = 80$ mK. Dashed line: fit with the Ivanchenko Zil'Berman result. The actual fridge temperature was 20 mK.

4.2 From the supercurrent to MAR – contacts with well transmitting channels

The MAR contribution to the dc current is not included in the adiabatic calculation of paragraph 3.

In section 2.3, we presented a selfconsistent theory developed by A. L. Yeyati which treats the supercurrent and the MAR current on the same footing. Within this new approach, it is possible to calculate the full IV curve of a contact containing several channels of arbitrary transmissions and embedded in an ohmic environment.
In particular, the transition from essentially non dissipative transport (supercurrent) at small voltage to dissipative transport (MAR current) at finite voltage can be accounted for. This progressive transformation from the supercurrent into MAR current at higher voltages is shown on Figure 24 for contact #3 ($\tau = \{0.677, 0.391, 0.201, 0.2, 0.2\}$). For this particular contact, the crossover occurs at a voltage around 50 µV.

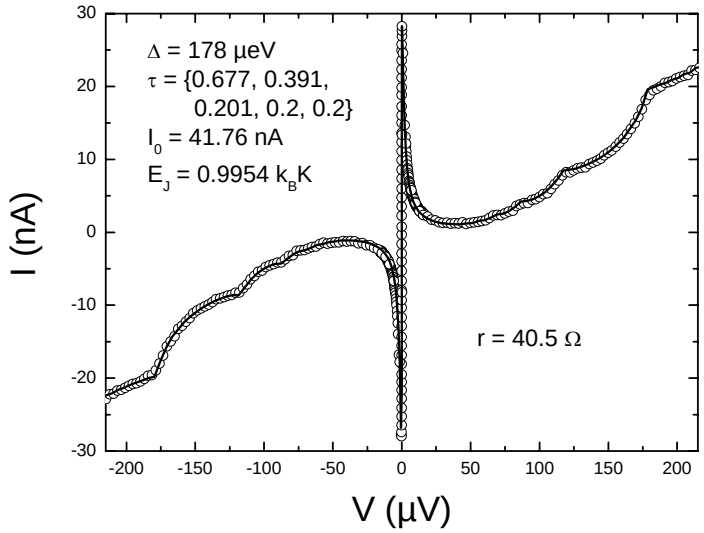

Figure 24: contact #3 ($\tau = \{0.677, 0.391, 0.201, 0.2, 0.2\}$). Smooth transition from the supercurrent around zero voltage to the MAR current at finite voltage. Comparison between the experiment (dots) and the selfconsistent calculation (solid line) of section 2.3. The only adjustable parameter in the theory was the effective noise temperature of the resistor r: $T_{eff} = 125$ mK.

In contacts containing highly transmitting channels, the MAR and supercurrent contributions don't add up independently but rather interfere to build up the full *IV* curve at low voltages, as shown on Figure 25, on which the measured low voltage *IV* of contact #4 ($\tau = \{0.995, 0.372, 0.174, 0.022\}$) and the predictions of the selfconsistent calculation are compared.

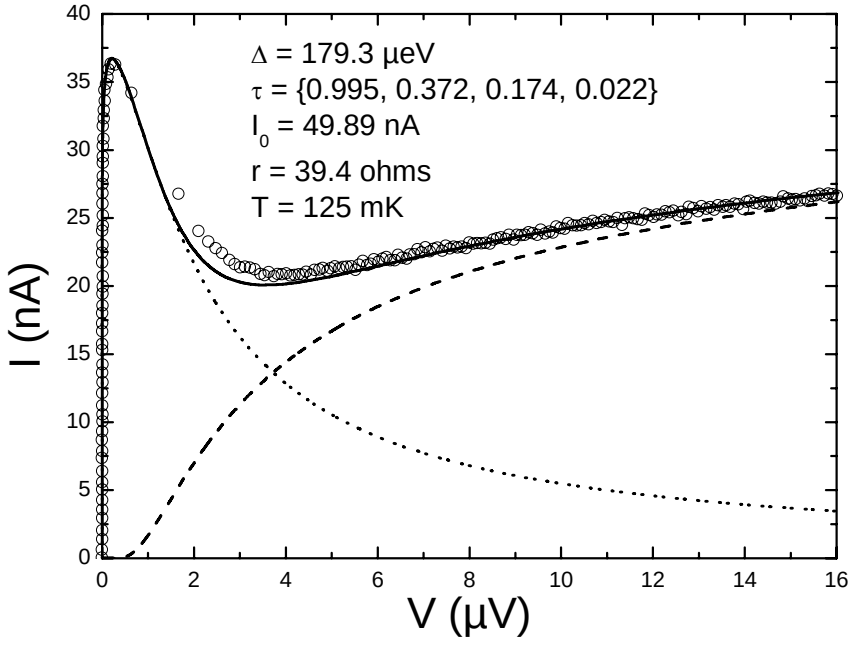

Figure 25: Supercurrent peak of contact #4 (containing a highly transmitting channel). Open circles are experimental data. The solid line is the prediction of the selfconsistent calculation. The MAR current (dashed line) starts to be sizeable at a voltage within the width of the supercurrent peak. The dotted line is the prediction, at 125 mK, of the adiabatic calculation for the supercurrent peak.

The theory describes quite well the experimental results. We attribute the small discrepancy to the purely ohmic environment assumed for the calculation. The actual electromagnetic environment is not a simple resistor r but, as already mentioned, rather the $r + \left(\left(r + R \right) // C \right)$ combination (see Table 2).

4.3 Temperature dependence of the maximum of the supercurrent peak

Detailed temperature studies of the maximum of the supercurrent peak have been carried out on contact #4 ($\tau = \{0.995, 0.372, 0.174, 0.022\}$) and on contact #5 ($\tau = \{0.389, 0.238, 0.055\}$). We first present the results obtained for contact #5 on Figure 26 and Figure 27. Figure 26 presents several supercurrent peaks measured at different temperatures and the corresponding fits with the Ivanchenko Zil'berman result.

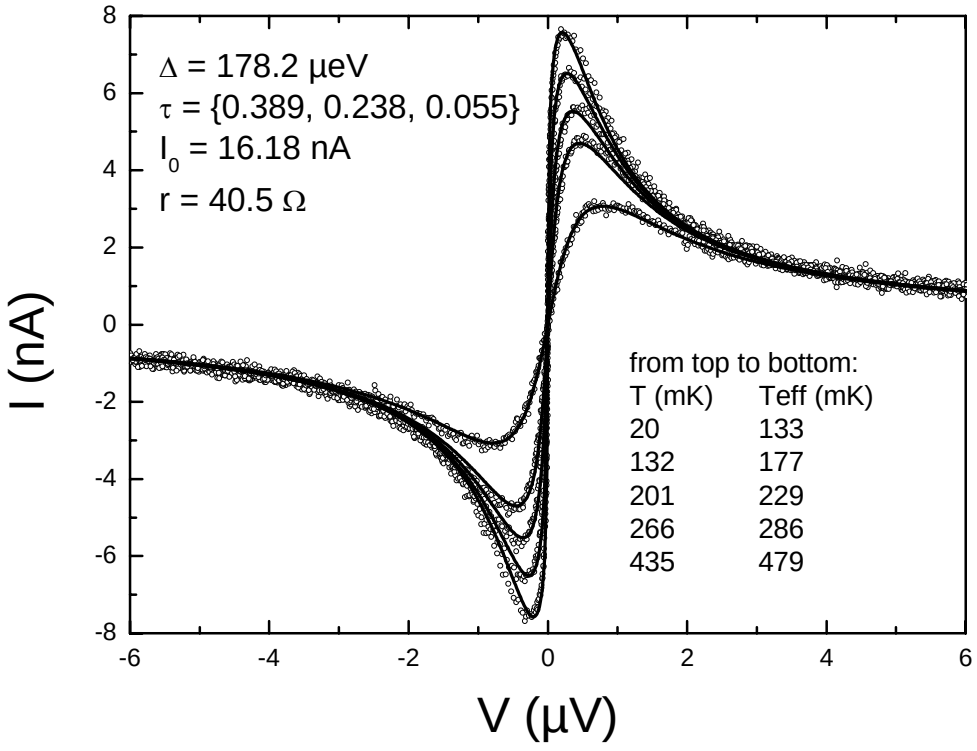

Figure 26: Supercurrent peaks of contact #5 and corresponding fits with the Ivanchenko Zil'berman result at different temperatures. The fridge temperature T and the corresponding fit temperature T_{eff} are indicated on the graph for each curve.

On Figure 27 we have plotted the maximum of the supercurrent peak (notation "$I_{\max}$") as a function of the fridge temperature in reduced units. At high enough temperatures, the experimental points are well described by the theory of paragraph 3. However at low temperatures, the current saturates at $I_{\max}/I_0 = 0.47$, which corresponds to an effective noise temperature $T_{eff} \approx 135$ mK. This is due to spurious noise incoming on the atomic contact.

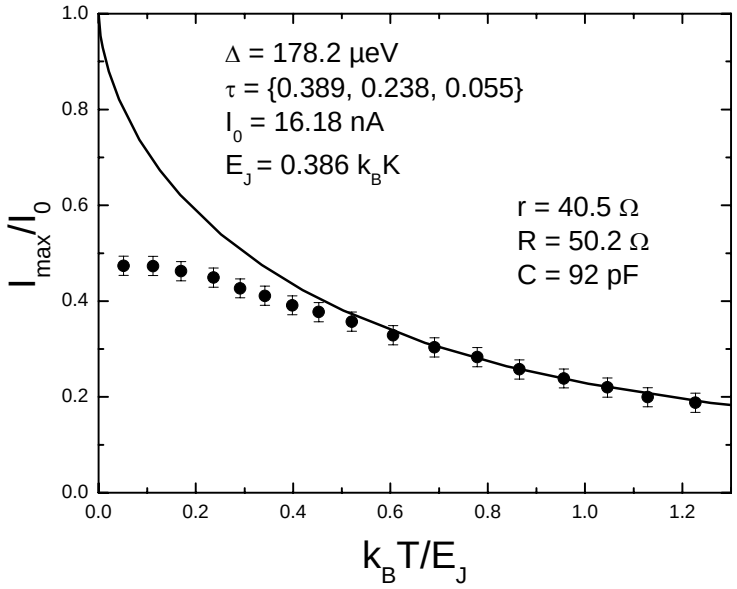

Figure 27: Temperature dependence of the maximum of the supercurrent peak of contact #5. Closed circles are experimental data. The solid line is the prediction of the adiabatic theory of paragraph 3.

Figure 28 shows the temperature dependence of the maximum of the supercurrent peak for contact #4 which contains a highly transmitting channel.

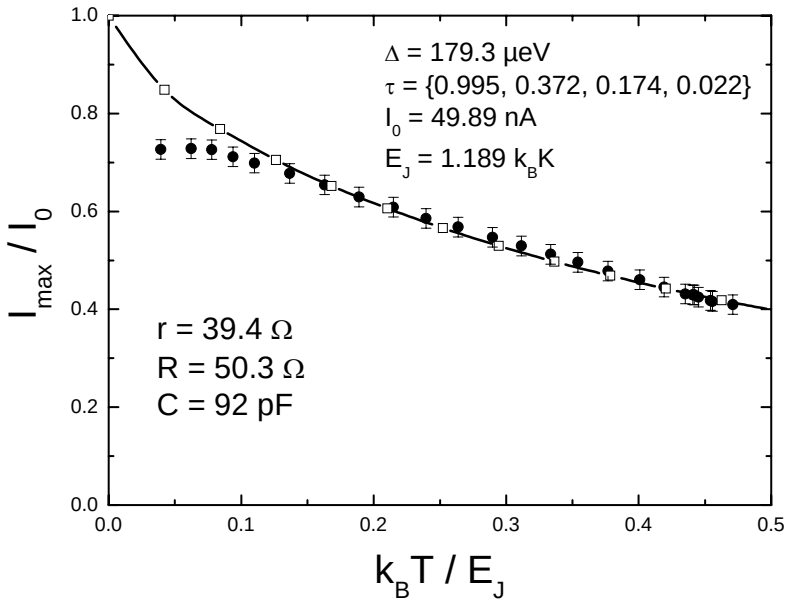

Figure 28: Temperature dependence of the maximum of the supercurrent peak of contact 4. Closed circles are experimental data. The open squares are the prediction of the adiabatic theory of paragraph 3 (the line is just a guide for the eye).

We don't observe deviations from the adiabatic theory on the maximum of the supercurrent peak for contact 4. The Landau-Zener probability to jump from the lower to the upper level is still too small to play a role as described in paragraph 2.3. For this contact, we have indeed checked that the predictions of A. L. Yeyati's selfconsistent theory for the temperature dependence of the maximum of the supercurrent peak (section 2.3) are indistinguishable from those of the adiabatic theory.

4.4 Diffusion branch and switching

The same temperature studies have been performed on current biased contacts. The experimental setup for the measurement of the switching current is similar to the setup for measuring the full supercurrent peak. The only difference is that the atomic contact is no longer shunted at dc by a resistor R. The contact is current biased by a voltage source V_B in series with a large bias resistor R_B, as shown on Figure 29. The detailed wiring can be found in the appendix of this chapter.

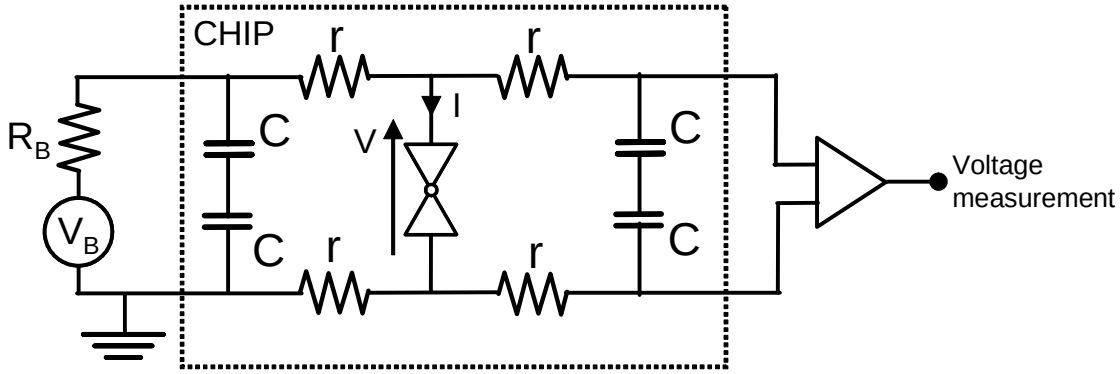

Figure 29: Experimental setup for the current bias mode.

In this setup, only the diffusion branch can be measured and not the full supercurrent peak. Indeed, when the current in the contact approaches the maximum of the supercurrent peak that would be measured in a voltage bias setup, then the system switches to the dissipative branch at larger voltages. We present a typical *IV* characteristic displaying switching on Figure 30. In the experiments, the maximum value of the current that the contact can sustain at zero voltage, called the switching current, was measured. A detailed analysis of the switching process can be found in R. Cron's Ph.D. thesis [22] and in [23]. In the latter, P. Joyez *et al.* showed that for a contact embedded in the dissipative environment of Figure 29, the mean value of the switching current is very close to the maximum of the supercurrent peak that would be measured in a voltage bias setup.

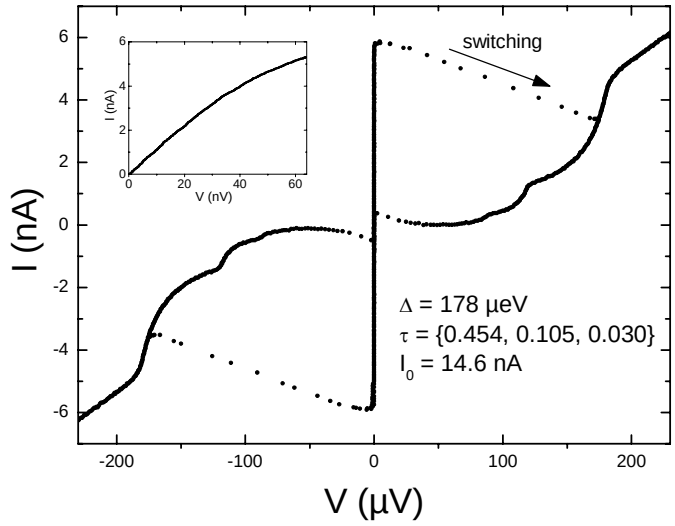

Figure 30: Typical IV characteristic of an atomic contact measured in a current bias setup. When increasing the bias current, a threshold value is reached: The system switches from the diffusion branch (inset) at very small voltages to a state with a voltage of the order of Δ / e.

The measurement of the switching current I_S goes as follows (see Figure 31). A current ramp of both polarities is applied through the contact with a voltage source V_B in series with a large bias resistor R_B. Two timers (Fluke PM6680B & Philips PM 6680) measure the elapsed time between the center of the ramp and the switching event characterized by the sudden onset of a voltage across the contact. Both polarities ($I > 0$ and $I < 0$) were measured to compensate for offsets in the biasing line. The start signal is the TTL synchronization signal of the voltage source. The stop signal is the voltage across the contact after amplification. The wiring of the timers is schematically represented on Figure 31. The switching current is obtained from the two times t_S^1 ($I > 0$) and t_S^2 ($I < 0$) measured by the timers and from the slew rate $\alpha = \left(1/R_B\right) dV_B/dt$ of the current ramp as: $I_S = \alpha\left(t_S^1 + t_S^2\right)/2$. About 10^4 switching events were recorded to have a good accuracy on the mean value of the switching current. Typical values for the ramp parameters were 2 kHz for the frequency and $\alpha = 7.7$ mA.s^{-1}.

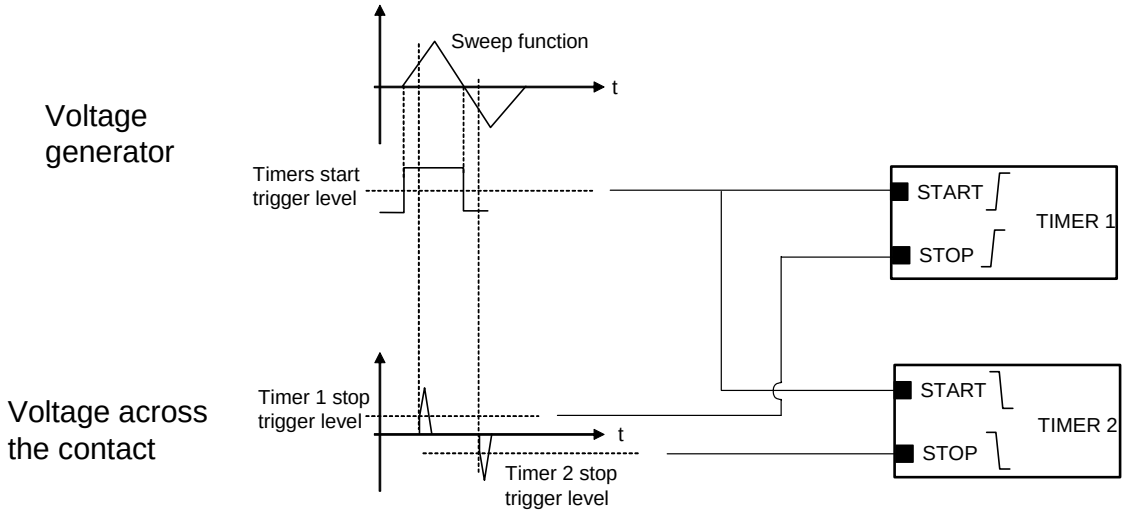

Figure 31: Schematic representation of the setup for measuring the switching current.

Experimental results obtained for the mean switching current are compared to the theoretical predictions, calculated with the Ambegaokar and Halperin method, for the maximum of the supercurrent peak at finite temperature. Figure 32 and Figure 33 show the temperature dependence of the mean switching current in two different contacts. The resistor r (see Figure 29) has been calibrated independently and its value is indicated on each graph.

Results on a contact containing channels with intermediate transmissions are presented on Figure 32.

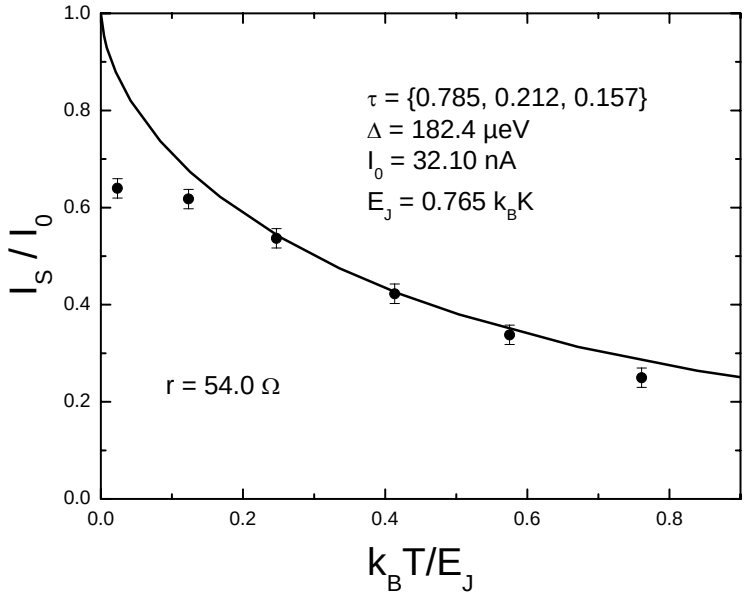

Figure 32: Temperature dependence of the mean switching current I_S in a contact containing channels of intermediate transmissions. Closed circles are experimental data. The line is the theoretical prediction of Ambegaokar and Halperin adiabatic calculation.

The theory describes the experiment quite well but for the lowest and highest temperatures. Figure 32 shows that the switching current saturates at the lowest temperatures, like the maximum of the supercurrent peak (section 4.3.) due, once again, to spurious noise incoming on the atomic contact. The experimental point at the highest temperature lies beneath the theoretical predictions because the reduction of the superconducting gap with temperature was not included in the theory.

Figure 33 displays the results obtained on a contact containing a highly transmitting channel. With the set of transmissions we have measured for this contact, we show that the experimental data cannot be explained neither by the adiabatic theory nor by the selfconsistent calculation[8]. At high temperature, the experimental data lie indeed above the theoretical prediction.

[8] For the set of transmissions that we have extracted from the *IV* characteristic of the contact, we have checked that both theories give exactly the same result.

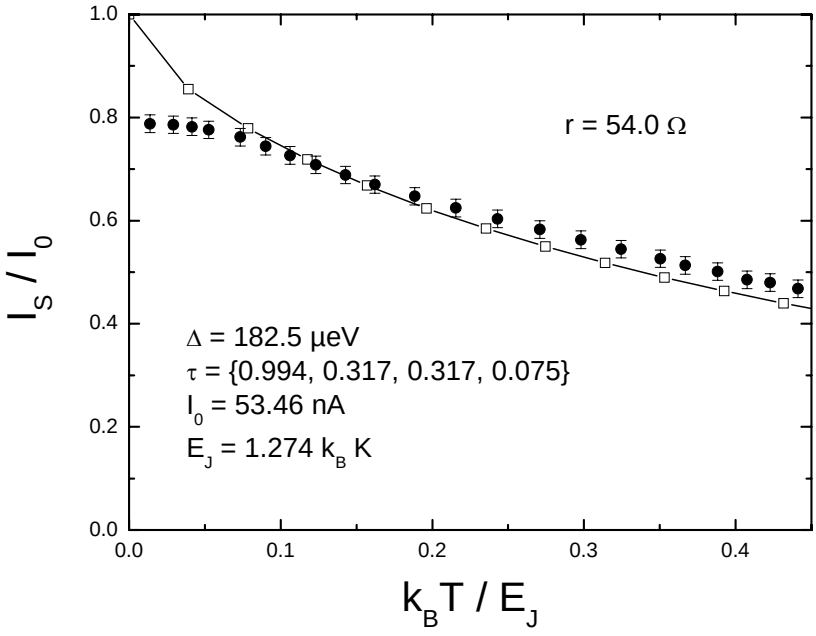

Figure 33: Temperature dependence of the switching current in a contact with a highly transmitting channel. The solid dots are experimental data. The open squares are the theoretical prediction of the Ambegaokar and Halperin adiabatic calculation. (The line is just a guide for the eyes.)

It is worth recalling here that during R. Cron's Ph.D. work [22] Goffman *et al.* [3] already observed that in contacts containing highly transmitting channels, the theory could not account for the excess switching current measured at high temperatures. At that time, this effect was already attributed to Landau-Zener transitions from the lower to the upper level. However, the Landau-Zener probability corresponding to the transmissions fitted from the *IV* 's was found to be too small to account for these experimental results. Therefore, a full understanding of the temperature dependence of the switching current was lacking.

Both in their and our experiments, we attribute the discrepancy with the theory to a wrong determination of the transmissions of the contact. For current biased contacts, the fit underestimates the actual value of the transmission of the almost ballistic channel. Indeed, as switching occurs for current biased contacts, the very low voltage part of the *IV* characteristic is not amenable to measurement. And the crucial information on highly transmitting channels is concentrated in this region. It is the *IV* at low voltages

that can make the difference between a 0.999 channel and a 0.9999 channel, the current at a large voltage being almost identical for these two transmissions.

We now think that both Cron's and our result could be explained within the self consistent theory of A. L. Yeyati by simply increasing the transmission of the most transmitting channel of the contacts.

5 Appendix

The detailed wiring of the experiment on the measurement of the diffusion branch in current biased atomic contacts is presented on Figure 34. The details on the different lines, filters, amplifiers and voltage source can be found in the section 3 of chapter 5.

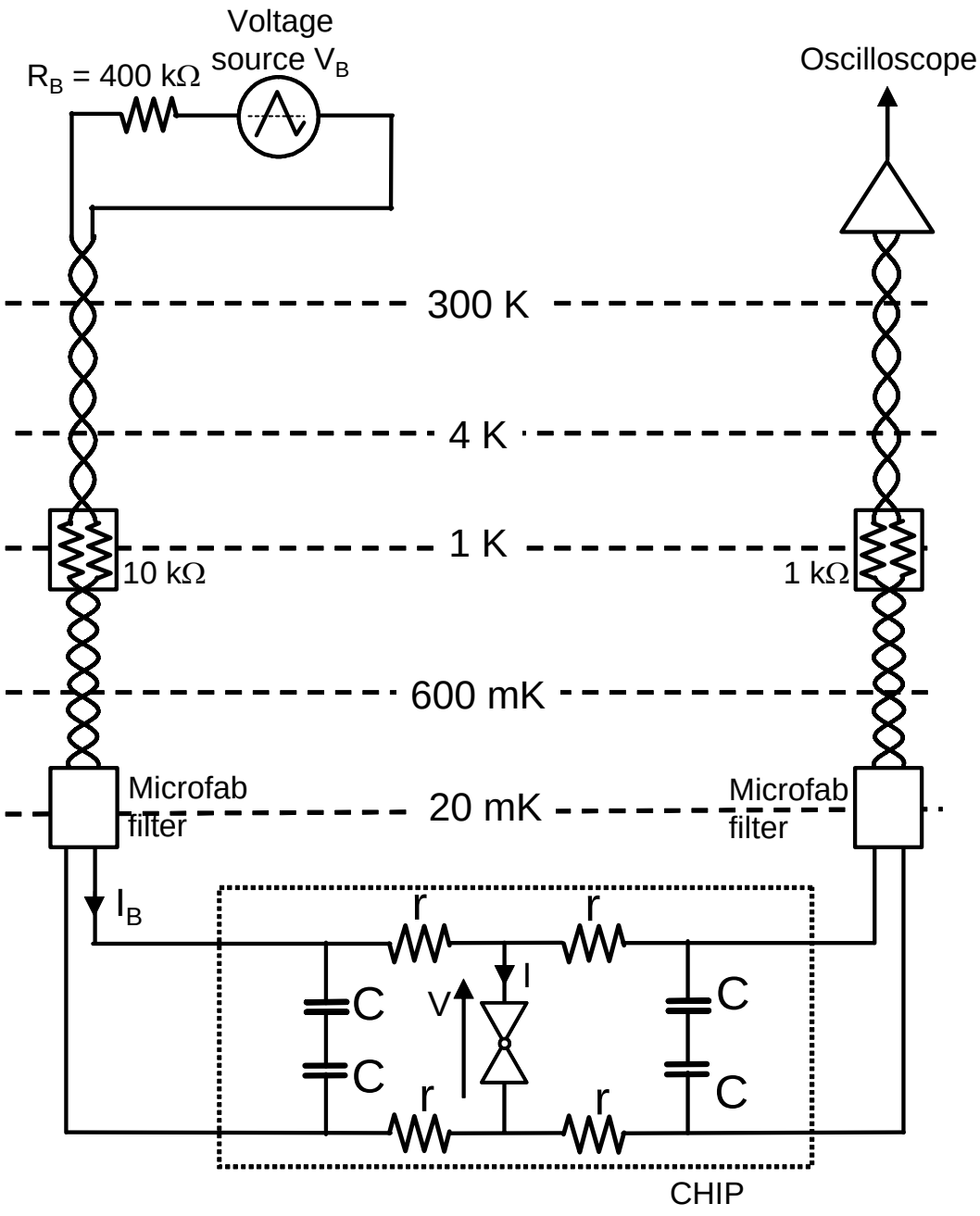

Figure 34: Detailed wiring of the experiment for measuring the diffusion branch of current biased atomic contacts.

References of chapter 2

[1] D. A. Ivanov and M. V. Feigel'man, JETP Lett. **68**, 890 (1998).

[2] A. Zazunov *et al.*, Phys. Rev. B **71**, 214505 (2005).

[3] M. F. Goffman *et al.*, Phys. Rev. Lett. **85**, 170 (2000).

[4] M. A. Despósito and A. Levy Yeyati, Phys. Rev. B **64**, 140511 (2001).

[5] L. Y. Gorelik *et al.*, Phys. Rev. Lett. **81**, 2538 (1998).

[6] N. I. Lundin, Phys. Rev. B **61**, 9101 (2000).

[7] V. Ambegaokar and A. Baratoff, Phys. Rev. Lett. **10**, 486 (1963).

[8] V. Ambegaokar and A. Baratoff, Phys. Rev. Lett. **11**, 104 (1963).

[9] J. Ankerhold, Quantum phase diffusion and charging effects in overdamped Josephson junctions, Europhys. Lett. **67**, 280 (2004).

[10] D. E. McCumber, J. Appl. Phys. **39**, 3113 (1968).

[11] W. C. Stewart, Appl. Phys. Lett. **22**, 277 (1968).

[12] Yu. M. Ivanchenko and L. A. Zil'berman, Zh. Eksp. Teor. Fiz. **55**, 2395 (1968) translated in Sov. Phys. JETP **28**, 1272 (1969).

[13] V. Ambegaokar and B. I. Halperin, Phys. Rev. Lett. **22**, 1364 (1969).

[14] V. Ambegaokar and B. I. Halperin, Phys. Rev. Lett. **23**, 274 (1969).

[15] H. Risken, *The Fokker-Planck Equation* (Springer-Verlag, Berlin, 1984).

[16] R. Duprat and A. L. Yeyati, Phys. Rev. B **71**, 054510 (2005).

[17] D. Averin and H. T. Imam, Phys. Rev. Lett. **76**, 3814 (1996).

[18] D. V. Averin, A. Bardas, and H. T. Imam, Phys. Rev. B **58**, 11165 (1998).

[19] D. V. Averin, Physica B **227**, 241 (1996).

[20] A. L. Yeyati, private communication.

[21] J. C. Cuevas, A. Martín-Rodero, and A. Levy Yeyati, Phys. Rev. B **54**, 7366 (1996).

[22] R. Cron, *Atomic Contacts: a Test-Bed for Mesoscopic Physics*, Ph.D. thesis, Université Paris 6 (2001);
http://www-drecam.cea.fr/drecam/spec/Pres/Quantro/Qsite/archives/theses/RCronThesis.pdf.

[23] P. Joyez, D. Vion, M. Götz, M. Devoret, and D. Esteve, J. Supercond. **12**, 757 (1999).

Chapter 3: AC Josephson currents: Shapiro resonances and photon assisted multiple Andreev reflections

1 Introduction

When a constant voltage is applied across a superconducting weak link, the phase acquires a linear time dependence, which gives rise to oscillating Josephson currents in the structure. This is the ac Josephson effect. This chapter is devoted to the study of these alternating currents and their relation to the current phase relationship.

In particular, this chapter will deal with the interplay of these alternating Josephson currents with an external microwave signal. This interplay gives rise to a twofold modification of the dc current flowing through the weak link:

- Replica of the supercurrent peak will appear at well definite values of the dc voltage on the IV characteristic. These replica are the so-called Shapiro resonances, which can be understood as beatings between the Josephson currents and the external microwave.

- The MAR current on which the Shapiro resonances superimpose will itself be modified in presence of microwave. This modification of the MAR current is referred to as photon assisted multiple Andreev reflections (PAMAR) current. The fundamental processes responsible for this PAMAR current are the absorption and stimulated emission of one ore several microwave photons during the transfer of multiple electronic charges across the Josephson weak link.

1.1 Shapiro resonances in the adiabatic limit

This paragraph aims to give some insight and a qualitative understanding of Shapiro resonances. The current phase relation for a single channel contact of arbitrary transmission τ at zero temperature is an odd function of the phase δ which can be decomposed in a sine Fourier series:

$$I_{-}(\delta,\tau)=\frac{e\Delta}{2\hbar}\frac{\tau\sin(\delta)}{\sqrt{1-\tau\sin^2\left(\frac{\delta}{2}\right)}}=\sum_{n=1}^{+\infty}I_n^{\sin}(\tau)\sin(n\delta)$$

When applying a constant bias voltage V across a Josephson weak link (Figure 1), the phase evolves linearly in time following the second Josephson relation, i.e. $\delta(t)=\delta_0+\omega_0 t$, where $\omega_0=2eV/\hbar$ is the Josephson frequency. In the adiabatic approximation, we suppose that the system stays always in the ground Andreev level, i.e. the dynamics of the phase does not induce transitions to the excited level.

By plugging the linear time dependence of the phase in the current phase relation, one obtains the time dependent Josephson currents (see equation (1)) which oscillate at all the harmonics of the Josephson frequency and which average out in time to zero.

$$I(V,t)=\sum_{n=1}^{+\infty}I_n^{\sin}\sin\left(n\left(\delta_0+\omega_0 t\right)\right) \qquad (1)$$

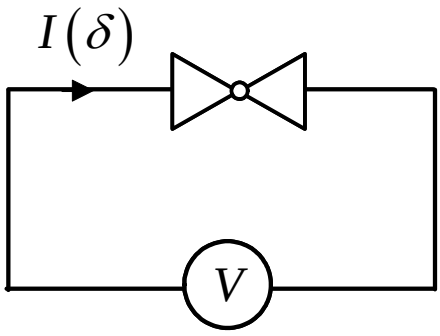

Figure 1: Atomic contact (double triangle symbol) with a perfect voltage bias V.

In tunnel junctions, because the zero voltage current phase relation is purely sinusoidal, the ac currents flowing in the junction under constant voltage bias are also sinusoidal at the Josephson frequency $\omega_0=2eV/\hbar$. In weak links containing channels of arbitrary transmission, the current phase relation departs from the sine function. As a consequence, ac currents oscillate not only at the Josephson frequency but also at all its harmonics. The spectrum of the ac currents is therefore a fingerprint of the current phase relation of the Josephson weak link. The ac Josephson currents were first directly

observed by I. K. Yanson, V. M. Svistunov, and I. M. Dmitrenko [1], I. Giaever [2], and D. N. Langenberg *et al.* [3, 4]. These currents have frequencies lying in the microwave domain. Indeed, the Josephson frequency ν_0 corresponding to a bias voltage V is $\nu_0 = 2eV/h$. A voltage of ~ 2.07 μV corresponds to a Josephson frequency of ~ 1 GHz.

In our experiments, the ac Josephson currents are not directly measured. They are revealed by applying an external microwave $A\cos(\omega_r t)$ on the contact in addition to the dc voltage bias V. The voltage across the contact is then $v(t) = V + A\cos(\omega_r t)$ (see Figure 2).

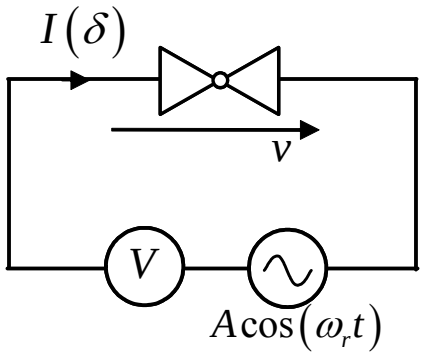

Figure 2: Atomic contact (double triangle symbol) perfectly voltage biased by a dc source V and a microwave source.

In addition to its linear time dependence, the phase acquires an oscillating part:

$$\delta(t) = \delta_0 + \frac{V}{\varphi_0}t + 2\alpha\sin(\omega_r t),$$

where $\alpha = \frac{eA}{\hbar\omega_r}$; and the current phase relation is no longer swept at a constant velocity:

$$I(V, t) = \sum_{n=1}^{+\infty} I_n^{\sin}\sin\left(n\left(\delta_0 + \omega_0 t + 2\alpha\sin(\omega_r t)\right)\right) \qquad (2)$$

Depending on the initial phase difference δ_0, the time averaged current flowing in the junction can be either negative or positive, as shown on Figure 3.

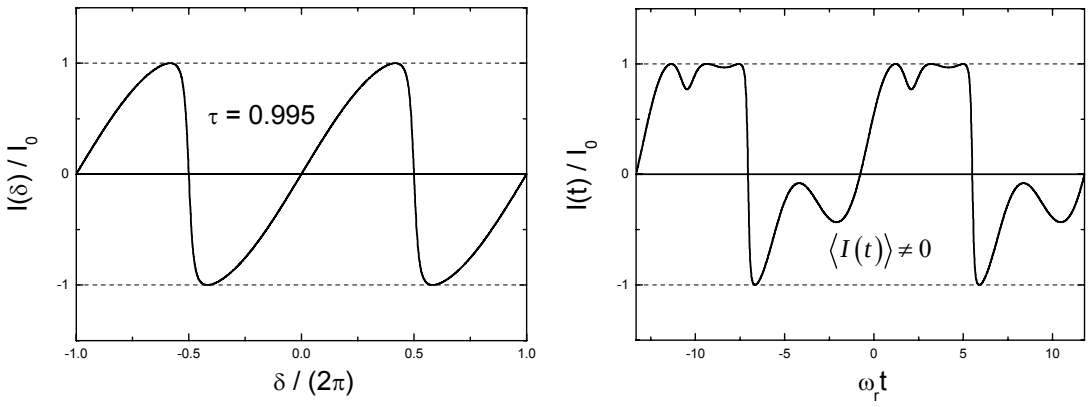

Figure 3: Shapiro resonances result from beatings between the external microwave and the oscillating Josephson currents. Illustration for the ½ Shapiro resonance on a $\tau = 0.995$ *channel. The dc current depends on the initial phase* δ_0*. On the graph, we have taken* $\alpha = 0.5$ *and the value of* δ_0 *which maximizes* $\langle I(t) \rangle$*.*

This extra dc current resulting from the beatings between the Josephson ac currents and the external microwave will appear on the IV characteristic at well defined values of the voltage (see Figure 4). The condition for the beating to appear is:

$$q\omega_0 = p\omega_r ,$$

which expresses that the frequencies of the Josephson currents have to be commensurate with the external microwave frequency. The voltage values at which the resonances appear are then:

$$V = \frac{p}{q}\frac{\hbar}{2e}\omega_r .$$

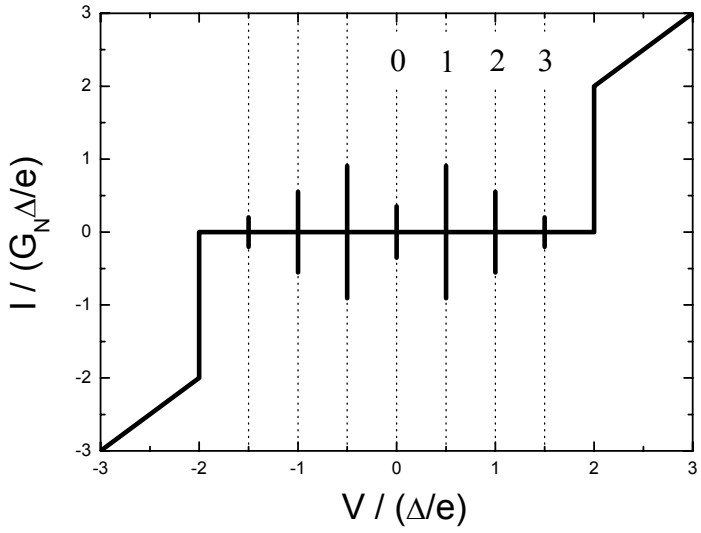

Figure 4: Integer Shapiro resonances $p/q = 1, 2, 3$ *and supercurrent peak* $p/q = 0$ *in a tunnel junction (*$\alpha = 1$ *and* $\omega_r = \Delta/\hbar$*).* G_N *is the normal state conductance of the tunnel junction.*

These resonances were first observed in 1963 on a Josephson tunnel junction by S. Shapiro [5]. They are historically called Shapiro steps because they were first observed in current biased junction. Their exact shape depends in fact on the biasing setup.
In Josephson weak links with well transmitting channels, fractional Shapiro resonances ($q > 1$) should appear in addition to the well known integer resonances of tunnel junctions. Fractional resonances are thus the signature of a non sinusoidal current phase relation.

1.2 Effect of Landau-Zener transitions

In the general case, the time dependence of the phase can't just be taken into account within a simple adiabatic approximation like in equations (1) and (2). Indeed, the dynamics of the phase can induce Landau-Zener transitions [6] between the two Andreev bound states of the conduction channel. In this non-adiabatic situation, the total current can be decomposed in a Fourier series, as shown in chapter 1. At a voltage V the current oscillates at all the harmonics of the Josephson frequency $\omega_0 = 2eV/\hbar$:

$$I(V,t)=\sum_{n=-\infty}^{+\infty} I_n(V)e^{in(\delta_0+\omega_0 t)} \qquad (3)$$

This Fourier expansion can always be rewritten on the basis of sines and cosines, which, in the adiabatic limit, reduces to equation (1). We saw in chapter 1 that the sine components of equation (3) arise from the adiabatic evolution of the system on the lower Andreev level, whereas the cosine components originate in Landau-Zener transitions between the two levels and result in the MAR current at finite voltage. When a microwave is applied on the contact, the sine terms contribute only to the Shapiro resonances whereas the cosine terms are also responsible for the onset of the PAMAR current. The PAMAR current on which the Shapiro resonances superimpose can be seen as a modulation of the MAR current by the external microwave.

Actually, the microwave itself modifies the dynamics of the phase in the general case and the formalism leading to equation (3) needs to be extended to account for an oscillatory part of the voltage bias. J. C. Cuevas *et al.* [7] have calculated the time dependent Josephson currents in a single channel of arbitrary transmission, perfectly voltage biased by a dc voltage source on which a microwave voltage is superimposed ($v(t)=V+A\cos(\omega_r t)$). They have calculated the IV characteristics of single channel contacts of various transmissions and show the dependence of both Shapiro resonance amplitudes and PAMAR current on the microwave parameters.

To conclude this section, it is worth defining the range of validity of the adiabatic approximation. To ensure the adiabatic approximation is valid, the Landau-Zener probability has to be small: $P_{LZ}\ll 1$. In presence of microwave, the Landau-Zener probability writes:

$$P_{LZ}=\exp\left[-\pi\frac{\Delta}{e\left(V+A\cos\left(\omega_r t_{lc}\right)\right)}\left(1-\tau\right)\right] \qquad (4)$$

where $\left(V + A\cos\left(\omega_r t_{lc}\right)\right)/\varphi_0$ is the instantaneous phase velocity at the level crossing. The time t_{lc} is solution of the equation $\delta\left(t_{lc}\right) = \pi \Leftrightarrow \delta_0 + \frac{V}{\varphi_0} t_{lc} + \frac{A}{\varphi_0 \omega_r} \sin\left(\omega_r t_{lc}\right) = \pi$. The condition of small Landau-Zener probability simply rewrites:

$$\frac{e(V + A)}{1 - \tau} < \pi\Delta .$$

For aluminum contacts ($\Delta \approx 180\ \mu\text{eV}$), with an external microwave frequency $\nu_r = 10$ GHz, this condition holds up to the second Shapiro resonance provided $\alpha = eA/\left(h\nu_r\right) < 2$ and $\tau < 0.78$.

2 Shapiro resonances within the adiabatic approximation

In this section, we calculate the amplitudes of the Shapiro resonances assuming that the system doesn't experience any Landau-Zener transitions to the upper Andreev level, i.e. that the adiabatic approximation is valid.

2.1 Perfect voltage bias

We first consider the ideal case of a Josephson weak link under perfect voltage bias. This ideal limit is never achieved in reality because of the unavoidable fluctuations in the electric circuit in which it is embedded. However, this is a good starting point and the effect of fluctuations will be addressed later on.

For a contact with a perfect voltage bias consisting of an oscillating part superimposed on a dc value: $v\left(t\right) = V + A\cos\left(\omega_r t\right)$, the time evolution of the phase writes:

$$\delta\left(t\right) = \delta_0 + \frac{V}{\varphi_0} t + 2\alpha \sin\left(\omega_r t\right),$$

where $\alpha = \frac{eA}{\hbar\omega_r}$.

The ground Andreev state current-phase relation of a *N*-channel structure writes as:

$$I\left(\delta, \{\tau\}\right) = \frac{e\Delta}{2\hbar}\sum_{i=1}^{N} I_{-}\left(\delta, \tau_i\right),$$

$I\left(\delta, \{\tau\}\right)$ is an odd and periodic function of the phase. It can be expanded in a Fourier series as:

$$I\left(\delta, \{\tau\}\right) = \sum_{m=1}^{\infty} I_m^{\sin}\left(\{\tau\}\right)\sin\left(m\delta\right),$$

where $I_m^{\sin}\left(\{\tau\}\right) = \sum_{i=1}^{N} I_m^{\sin}\left(\tau_i\right)$.

The first Fourier coefficients $I_m^{\sin}\left(\tau\right)$ entering the sine expansion are plotted versus the transmission on Figure 5.

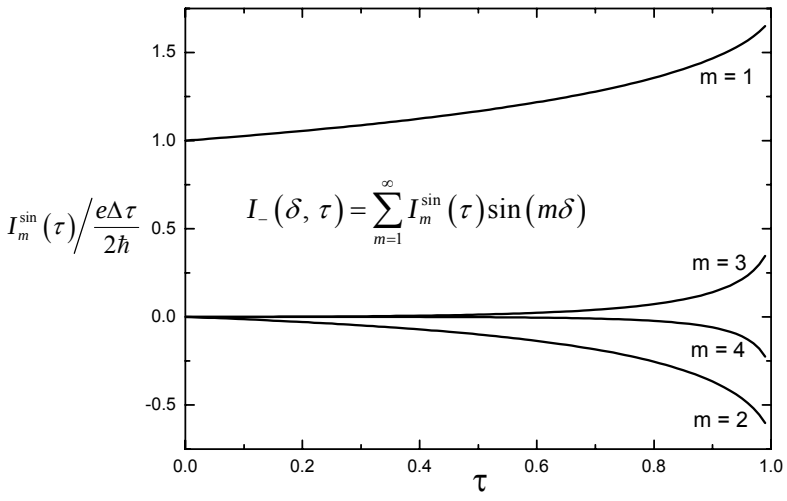

Figure 5: Fourier coefficients of the single channel current phase relation as a function of the channel transmission.

The adiabatic approximation means that one can directly plug the temporal evolution of the phase into the ground state current phase relation to obtain the time dependence of the Josephson currents:

$$I\left(t,\{\tau\}\right)=\sum_{m=1}^{\infty}I_m^{\sin}\left(\{\tau\}\right)\sin\left[m\left(\delta_0+\frac{V}{\varphi_0}t+2\alpha\sin\left(\omega_r t\right)\right)\right]$$

In terms of Bessel functions, this last expression can be expanded as:

$$\begin{aligned}I\left(t,\{\tau\}\right)=\sum_{m\geq 1}I_m^{\sin}\left(\{\tau\}\right)\Big\{&\sin\left(m\theta\right)J_0\left(2m\alpha\right)+\sum_{k\geq 1}\sin\left(m\theta+k\theta_r\right)J_k\left(2m\alpha\right)\\&+\sum_{k\geq 1}\left(-1\right)^k\sin\left(m\theta-k\theta_r\right)J_k\left(2m\alpha\right)\Big\}\end{aligned}\qquad(5)$$

where $\theta\left(t\right)=\delta_0+\frac{V}{\varphi_0}t$ and $\theta_r\left(t\right)=\omega_r t$.

Let's now calculate the dc current across the junction by time averaging equation (5). The time average is different from zero only for the three following sets of values of the applied dc voltage V:

$V=0$: $\quad\left\langle I\left(t,\{\tau\}\right)\right\rangle_{V=0}=\sum_{m\geq 1}I_m^{\sin}\left(\{\tau\}\right)J_0\left(2m\alpha\right)\sin\left(m\delta_0\right)$

$V=\frac{k}{m}\varphi_0\omega_r$: $\quad\left\langle I\left(t,\{\tau\}\right)\right\rangle_{V=\frac{k}{m}\varphi_0\omega_r}=\sum_{n\geq 1}I_{n\times m}^{\sin}\left(\{\tau\}\right)J_{n\times k}\left(2nm\alpha\right)\left(-1\right)^{n\times k}\sin\left(nm\delta_0\right)$

$V=-\frac{k}{m}\varphi_0\omega_r$: $\quad\left\langle I\left(t,\{\tau\}\right)\right\rangle_{V=-\frac{k}{m}\varphi_0\omega_r}=\sum_{n\geq 1}I_{n\times m}^{\sin}\left(\{\tau\}\right)J_{n\times k}\left(2nm\alpha\right)\sin\left(nm\delta_0\right)$

The first condition corresponds to the supercurrent whose amplitude is affected by the microwaves. The two other conditions define the positions of the Shapiro resonances. If the quantities $m\omega_0$ and $k\omega_r$ are commensurate, then multiples of $m\omega_0$ will also be commensurate with the same multiples of $k\omega_r$. An infinity of Josephson ac components thus contribute to the same resonance. In the expressions for the voltages at which the resonances appear, k/m must be irreducible fractions because the different contributions to a same beating are taken into account by the summation over the index

n. The amplitude $S_{k/m}$ of the Shapiro resonances are calculated by taking the maximum over the initial phase δ_0 of the three above expressions:

$$S_{0,\pm k/m}\left(\{\tau\}\right) = \max_{\delta_0}\left[\left\langle I\left(t, \{\tau\}\right)\right\rangle_V\right] \tag{6}$$

with $V = 0, \pm\frac{k}{m}\varphi_0\omega_r$

In practice, this maximization has to be performed numerically in the general case. Figure 6 shows the transmission dependence of the amplitudes of three Shapiro resonances in a single channel contact. Figure 7 shows the dependence of the amplitudes for a channel of transmission 0.8 as a function of the microwave parameter α.

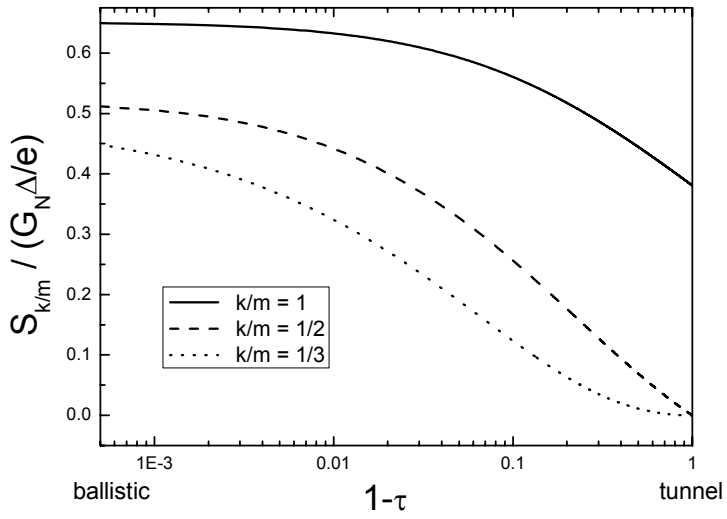

Figure 6: Amplitude of the Shapiro resonances $k/m = 1, 1/2, 1/3$ as a function of the channel transmission, calculated within the adiabatic approximation for $\alpha = 0.25$. Note the horizontal axis: data are plotted as a function of the reflection coefficient $(1-\tau)$ on a logarithmic scale to highlight the high transmissions. $G_N = \left(2e^2/h\right)\tau$ is the normal state conductance of the channel.

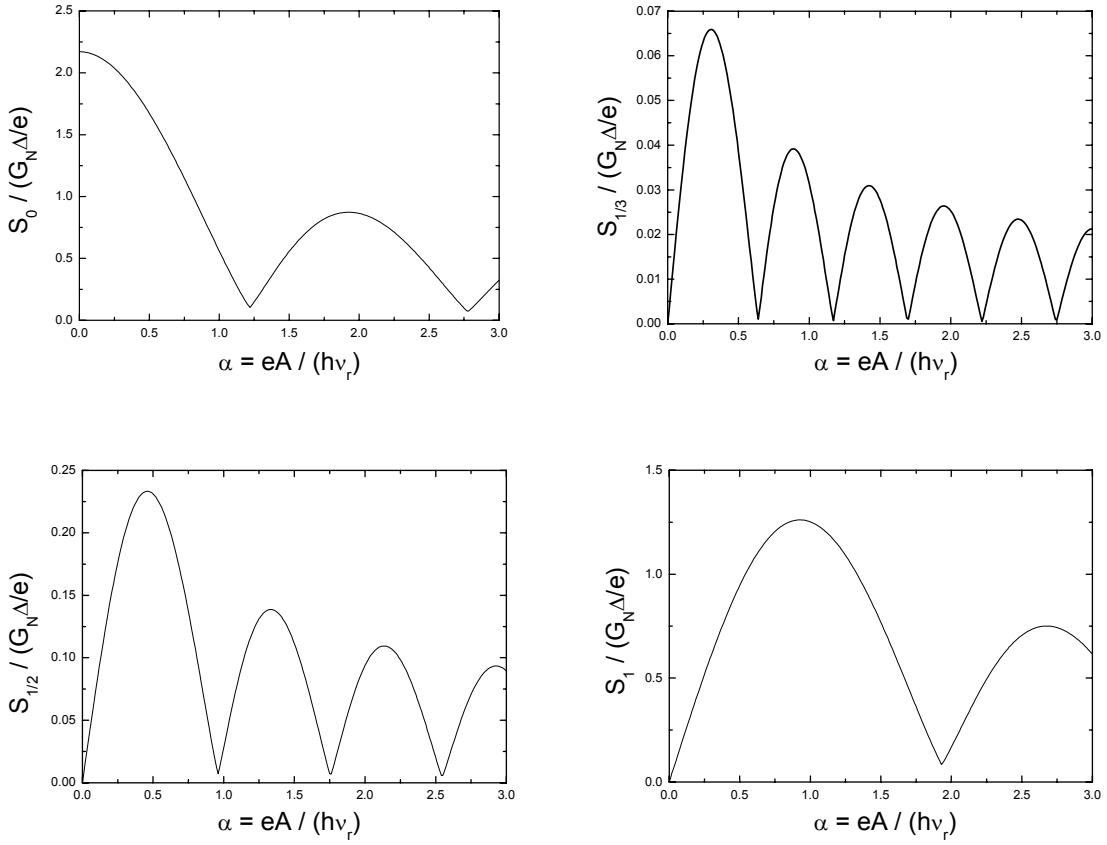

Figure 7: Amplitude of the supercurrent and Shapiro resonances $k/m = 1, 1/2, 1/3$ *for a single channel contact of transmission 0.8 as a function of the microwave parameter* α *, within the adiabatic approximation.*

In the tunnel case, $\tau_i \ll 1$. Hence, $I_{m=1}^{\sin} = I_0$ (the critical current of the Josephson tunnel junction) and $I_{m>1}^{\sin} = 0$. Simplified expressions can be obtained for the amplitudes of the Shapiro resonances:

$$S_0\left(\{\tau \ll 1\}\right) = I_0 J_0\left(2\alpha\right) \tag{7}$$

$$S_{\pm k/m}\left(\{\tau \ll 1\}\right) = \begin{cases} I_0 J_k\left(2\alpha\right) & m = 1 \\ 0 & m > 1 \end{cases} \tag{8}$$

In Josephson tunnel junctions, Shapiro resonances only occur at voltages corresponding to integer multiples of the Josephson frequency. They are the well-known integer Shapiro resonances.

However, for junctions of arbitrary transmission, Shapiro resonances also appear on the IV at fractional multiples of the Josephson voltage $\varphi_0\omega_r$. Fractional Shapiro resonances are the signature of a non sinusoidal current phase relation (see Figure 6 and Figure 7). On Figure 7 it is worth noticing that the α-dependence of the Shapiro resonance amplitudes deviates from the simple Bessel functions observed in the tunnel case (equations (7) and (8)). In particular, the minima of the arches don't necessarily go to zero.

2.2 Effect of the environment: imperfect voltage bias

In reality, a Josephson weak link can never be perfectly voltage biased because the finite impedance of the biasing circuit imposes fluctuations. To observe well developed beatings, the weak link must therefore be embedded in a dissipative environment in order to damp the fluctuations of the phase. Otherwise, the supercurrrent is washed out. In this section, the effect of the fluctuations on the beatings is analyzed in detail. In particular, we show that in presence of an environment, a Shapiro resonance doesn't appear as a singular vertical branch[1] (resp. current step) on the IV characteristic, like in the perfectly voltage (resp. current) biased case, but it rather acquires a peaked shape with a finite width (see Figure 8).

[1] Note the vertical current branches on Figure 4: the Josephson junction was assumed to be perfectly voltage biased.

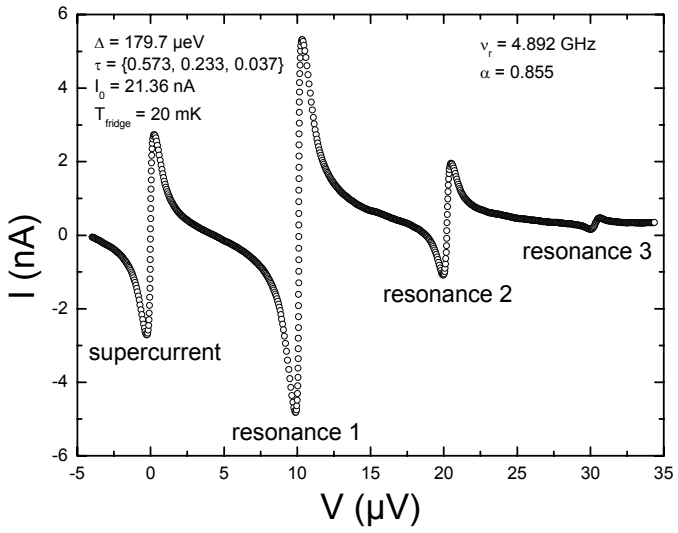

Figure 8: Integer Shapiro resonances measured on a contact with mesoscopic pin code $\tau = \{0.573,\ 0.233,\ 0.037\}$. *The resonances don't appear as vertical branches on the IV characteristic. The imperfect voltage bias and the fluctuations in the electromagnetic environment lead to a peaked shape of the resonances.*

2.2.1 Shapiro resonances as replicas of the supercurrent peak: mapping approach

Figure 9 shows the simplest realistic circuit in which a Josephson weak link can be integrated: The electromagnetic environment of the contact is a simple resistor r, inducing fluctuations of the dc voltage bias V_B because of the Johnson Nyquist noise represented by a voltage source $e_n(t)$. In this paragraph, we show that Shapiro resonances can be described as replicas of the supercurrent peak.

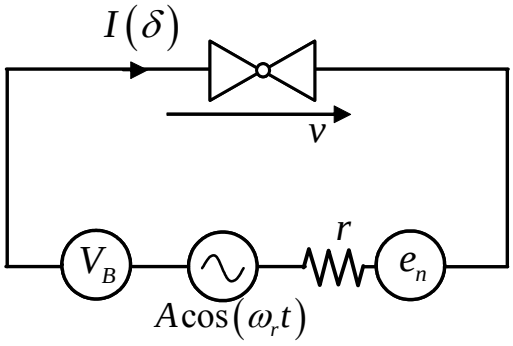

Figure 9: Atomic contact (double triangle symbol) embedded in a resistive environment and biased by both a dc voltage V_B and an oscillating voltage of amplitude A and frequency $\nu_r = \omega_r/(2\pi)$. e_n is the noise voltage source associated with the resistor r.

Using the Kirchoff's law and the second Josephson relation, the voltage across the weak link writes:

$$v = \varphi_0 \dot{\delta} = rI(\delta(t)) + e_n(t) + V_B + A\cos(\omega_r t) \tag{9}$$

The Johnson Nyquist voltage noise associated with the resistor r is Gaussian white noise characterized by $\langle e_n(t)\rangle = 0$ and $\langle e_n(t)e_n(t')\rangle = 2k_B Tr\delta(t-t')$ according to the fluctuation-dissipation theorem.

We want to describe the dynamics of the superconducting phase difference δ in the vicinity of the p/q Shapiro resonance. Right at the center of this resonance, $V = \langle v\rangle = V_B = \frac{p}{q}\varphi_0\omega_r$ because there is no net dc current flowing (see Figure 8). One can rewrite equation (9) to obtain the evolution of δ:

$$\delta(t) = \frac{p}{q}\omega_r t + \frac{A}{\omega_r\varphi_0}\sin(\omega_r t) + \gamma(t),$$

where γ represents the stochastic part of the time dependence of the superconducting phase difference around the p/q resonance. The time evolution of γ is governed by the following equation:

$$\varphi_0\dot{\gamma} = \left(V_B - \frac{p}{q}\varphi_0\omega_r\right) + e_n(t) + rI(\delta(t)) \tag{10}$$

It is possible to Fourier expand the current phase relation:

$$I\left(\delta(t)\right)=\sum_{m=1}^{\infty} I_m^{\sin}\sin\left(m\delta(t)\right)=\sum_{m\geq 1} I_m^{\sin}\sin\left[m\left(\frac{p}{q}\omega_r t+2\alpha\sin\left(\omega_r t\right)+\gamma(t)\right)\right],$$

with $\alpha=\dfrac{eA}{\hbar\omega_r}$.

Leading to:

$$I\left(\delta(t)\right)=\sum_{m\geq 1} I_m^{\sin}\left\{\sin\left[m\left(\frac{p}{q}\omega_r t+\gamma(t)\right)\right]\cos\left[2m\alpha\sin\left(\omega_r t\right)\right]\right.$$
$$\left.+\cos\left[m\left(\frac{p}{q}\omega_r t+\gamma(t)\right)\right]\sin\left[2m\alpha\sin\left(\omega_r t\right)\right]\right\}$$

And finally:

$$I\left(\delta(t)\right)=\sum_{m\geq 1} I_m^{\sin}\left\{\sin\left[m\left(\frac{p}{q}\omega_r t+\gamma(t)\right)\right]\left[J_0\left(2m\alpha\right)+2\sum_{k\geq 1}J_{2k}\left(2m\alpha\right)\cos\left(2k\omega_r t\right)\right]\right.$$
$$\left.+\cos\left[m\left(\frac{p}{q}\omega_r t+\gamma(t)\right)\right]\left[2\sum_{k\geq 0}J_{2k+1}\left(2m\alpha\right)\sin\left(\left(2k+1\right)\omega_r t\right)\right]\right\}$$

(11)

We are interested in the dynamics of γ, which is slow compared to the frequency of the microwave drive ω_r. We can therefore approximate $I\left(\delta(t)\right)$ by replacing the oscillatory terms by their time average in equation (11). This leads to:

$$I\left(\delta(t)\right)\approx 2\sum_{m\geq 1} I_m^{\sin}\sin\left(m\gamma(t)\right)\sum_{k\geq 1}J_{2k}\left(2m\alpha\right)\left\langle\cos\left(m\frac{p}{q}\omega_r t\right)\cos\left(2k\omega_r t\right)\right\rangle$$
$$-2\sum_{m\geq 1} I_m^{\sin}\sin\left(m\gamma(t)\right)\sum_{k\geq 0}J_{2k+1}\left(2m\alpha\right)\left\langle\sin\left(m\frac{p}{q}\omega_r t\right)\sin\left(\left(2k+1\right)\omega_r t\right)\right\rangle$$

(12)

Let us concentrate on the first term of equation (12):

$$\left\langle \cos\left(m\frac{p}{q}\omega_r t \right)\cos\left(2k\omega_r t\right)\right\rangle = \begin{cases} \frac{1}{2} & m\frac{p}{q} = 2k \\ 0 & \text{otherwise} \end{cases}$$

The non zero contributions to the first term arise for $m = lq,\ l \in \mathbb{N}^*$. Then $2k = lp$.

If p is even then l can be either odd or even and the first term writes:

$$\sum_{l\geq 1} I_{lq}^{\sin} J_{lp}\left(2lq\alpha\right)\left\langle \sin\left(lq\gamma\left(t\right)\right)\right\rangle$$

If p is odd then l has to be even and the first term writes:

$$\sum_{l\geq 1} I_{(2l)q}^{\sin} J_{(2l)p}\left(2\left(2l\right)q\alpha\right)\left\langle \sin\left(\left(2l\right)q\gamma\left(t\right)\right)\right\rangle$$

A similar analysis is carried out for the second term of equation (12):

$$\left\langle \sin\left(m\frac{p}{q}\omega_r t \right)\sin\left(\left(2k+1\right)\omega_r t\right)\right\rangle = \begin{cases} \frac{1}{2} & m\frac{p}{q} = 2k+1 \\ 0 & \text{otherwise} \end{cases}$$

The non zero contributions to the second term arise for $m = lq,\ l \in \mathbb{N}^*$. Then $2k+1 = lp$.

If p is even, there is no solution for l and the second term is zero.

If p is odd then l has to be odd and the second term writes:

$$\sum_{l\geq 0} I_{(2l+1)q}^{\sin} J_{(2l+1)p}\left(2\left(2l+1\right)q\alpha\right)\left\langle \sin\left(\left(2l+1\right)q\gamma\left(t\right)\right)\right\rangle$$

In all cases, we find the following approximated expression for the current:

$$I\left(\delta\left(t\right)\right) \approx \sum_{l\geq 1}\left(-1\right)^{lp} I_{lq}^{\sin} J_{lp}\left(2lq\alpha\right)\sin\left(lq\gamma\left(t\right)\right) \qquad (13)$$

We then define a new phase $\theta\left(t\right) = q\gamma\left(t\right)$. One can then combine equations (10) and (13) to obtain the time evolution of $\theta\left(t\right)$:

$$\varphi_0\dot{\theta}\left(t\right) = q\left(V_B - \frac{p}{q}\varphi_0\omega_r\right) + qe_n\left(t\right) + r\times q\sum_{l\geq 1}\left(-1\right)^{lp} I_{lq}^{\sin} J_{lp}\left(2lq\alpha\right)\sin\left(l\theta\left(t\right)\right) \qquad (14)$$

This dynamics of $\theta(t)$ around the p/q peak is thus described by a Langevin equation, similar to the one that describes the dynamics of δ giving rise to the supercurrent peak in absence of microwaves. The IV characteristic around the p/q Shapiro resonance is obtained by calculating the time average of $I(\delta(t))$, i.e. $\sum_{l\geq 1}(-1)^{lp} I_{lq}^{\sin} J_{lp}(2lq\alpha)\langle \sin(lq\gamma(t))\rangle$ as a function of V_B. For this purpose, one has to solve the Langevin equation (14) using the Ambegaokar Halperin method described in chapter 2.

However, a simple result describing the p/q resonance as a replica of the supercurrent peak with effective parameters can be established if one keeps only the $l=1$ term in equation (13). In this case, equation (14) rewrites:

$$\varphi_0\dot{\theta}(t) = q\left(V_B - \frac{p}{q}\varphi_0\omega_r\right) + qe_n(t) + r\times q(-1)^p I_q^{\sin} J_p(2q\alpha)\sin(\theta(t)) \quad (15)$$

This equation is equivalent to the equation obtained in chapter 2 for the calculation of the supercurrent peak. It only differs by a scaling and an offset of the parameters. Let us briefly recall the Ivanchenko Zil'Berman result for the supercurrent peak. In the overdamped limit and in absence of microwaves, the Langevin equation governing the phase dynamics in a Josephson tunnel junction writes (see chapter 2 and Figure 10):

$$\frac{\varphi_0}{r}\dot{\delta} + i_n(t) + I_0\sin(\delta) = I_B \quad (16)$$

Where $i_n(t)$ is the Johnson-Nyquist current noise associated to the resistor r.

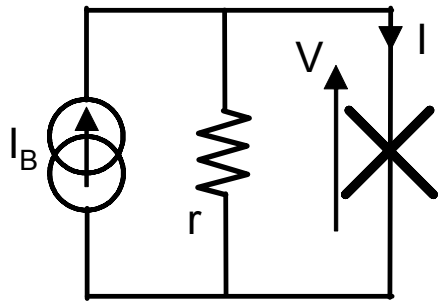

Figure 10: Electromagnetic environment of the tunnel junction (cross symbol) in the Ivanchenko Zil'berman calculation for the supercurrent peak.

Ivanchenko & Zil'Berman calculated the time average of $I(\delta)$ as a function of I_B:

$$\langle I \rangle (I_B) = I_0 \langle \sin(\delta) \rangle (I_B) = I_0 f_{IZ}\left(\frac{I_B}{I_0}, \frac{I_0 \varphi_0}{k_B T}\right),$$

where $f_{IZ}(x,y) = \mathrm{Im}\left[\frac{I_{1-ixy}(y)}{I_{-ixy}(y)}\right]$.

Equation (16) can be rewritten in the Thevenin representation, using voltage sources instead of current sources (Norton representation):

$$\varphi_0 \dot{\delta} + e_n(t) + rI_0 \sin(\delta) = V_B \tag{17}$$

with $V_B = rI_B$, and $e_n(t) = ri_n(t)$ the voltage noise of the resistor. In Thevenin's representation, the Ivanchenko Zil'Berman result rewrites:

$$\langle I \rangle (V_B) = I_0 \langle \sin(\delta) \rangle (V_B) = I_0 f_{IZ}\left(\frac{V_B}{rI_0}, \frac{I_0 \varphi_0}{k_B T}\right).$$

The analogy between equations (15) and (17) leads to an expression for the dc current around the p/q peak:

$$\langle I \rangle (V_B) = I_0^{eff} f_{IZ}\left(\frac{V_B^{eff}}{rI_0^{eff}}, \frac{I_0^{eff} \varphi_0}{k_B T^{eff}}\right),$$

with effective parameters:

$$\begin{cases} I_0^{eff} = \left| I_q^{\sin} J_p(2q\alpha) \right| \\ T^{eff} = qT \\ V_B^{eff} = V_B - \dfrac{p}{q} \varphi_0 \omega_r \end{cases}$$

Shapiro resonances are thus replica of the supercurrent peak with effective parameters. The striking result is that the effective noise temperature for a p/q resonance is qT. This explains why fractional Shapiro resonances ($q>1$) are really hard to observe experimentally: they are washed out by the fluctuations of the phase [8, 9].

Within this mapping approach, it is possible to calculate the IV characteristic of the Josephson weak link around each Shapiro resonance.
In the next section, a rigorous treatment of the phase dynamics is briefly presented. Within this formalism, it is possible to calculate the full IV in presence of microwave. Figure 12 compares the predictions of the mapping approach with the rigorous Fokker-Planck calculation for the first Shapiro resonance of a single channel ($\tau = 0.5$). Around the resonance, both approaches give the same result.

2.2.2 Rigorous treatment for the ohmic environment: Fokker-Planck equation in presence of microwaves

Let's now consider the same circuit than in the previous section but in the Norton representation. This circuit is sketched on Figure 11.

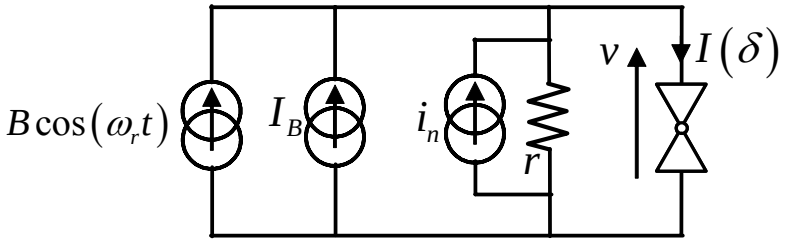

Figure 11: Atomic contact embedded in a dissipative environment. This representation is the Norton equivalent of the circuit of Figure 9 with $B = A/r$, $I_B = V_B/r$ *and* $i_n = e_n/r$.

The electrical equations (Khirchoff's law and second Josephson relation) of the circuit write:

$$\begin{cases} I_B + B\cos(\omega_r t) = \dfrac{v}{r} + i_n(t) + I(\delta) \\ v = \varphi_0 \dot{\delta} \end{cases}$$

giving rise to the following Langevin equation for the superconducting phase difference across the Josephson weak link:

$$\frac{\varphi_0}{r}\dot{\delta} = I_B + B\cos(\omega_r t) - i_n(t) - I(\delta) \qquad (18)$$

In chapter 2, we presented two methods to calculate the supercurrent peak of a Josephson weak link in absence of microwave starting from equation (18) with $B = 0$ and deriving from it a Smoluchowski equation. We recall here that a Smoluchowski equation is a specific form of Fokker-Planck equation (see chapter 2 and [10]). The first method, by Ivanchenko and Zil'berman provides us with an analytic result but only applies for a sinusoidal current phase relation $I(\delta)$. The second one, by Ambegaokar and Halperin can deal with any kind of current phase relation. R. Duprat and A. L. Yeyati have extended those two calculations to include a microwave drive $B\cos(\omega_r t)$, as in the Langevin equation (18). Their work is consistent with the results obtained earlier by D. Averin and A. Bardas [11] for a ballistic channel at zero temperature. R. Duprat and A. L. Yeyati first derive a Smoluchowski equation from the Langevin equation (18) and then calculate the mean current I and mean voltage V in terms of a matrix continued fraction (see sections II and III of [9]). A typical IV characteristic obtained within this approach is presented on Figure 12a.

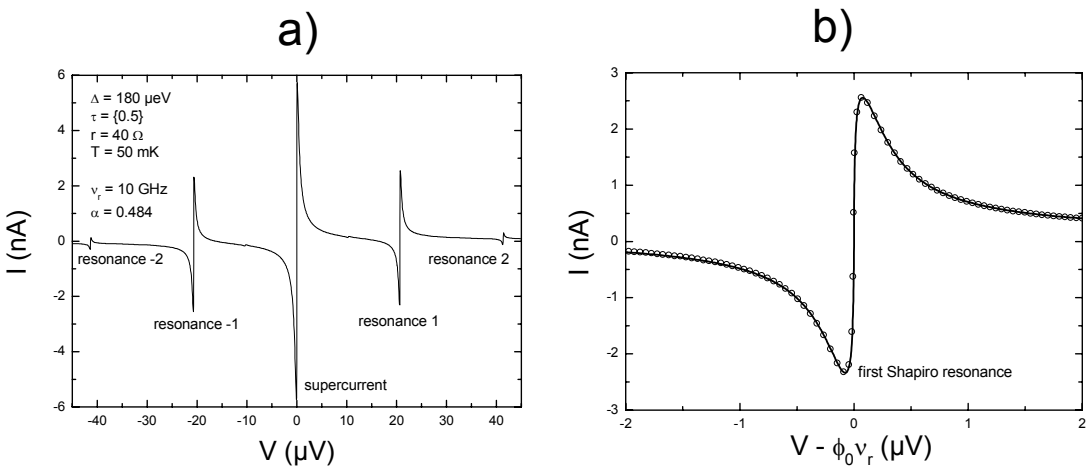

Figure 12: Calculated IV characteristic of a single channel contact ($\tau = 0.5$) in presence of microwave ($\nu_r = 10$ GHz, $\alpha = 0.484$). a): large scale IV calculated within the Fokker-Planck approach. The Shapiro resonances 1 and 2 are visible. b): Zoom on the first Shapiro resonance to compare the predictions of the mapping approach (solid line) with the predictions of the Fokker-Planck calculation (open dots). $\phi_0 = h/(2e)$ is the flux quantum.

On Figure 12b, the predictions of the Fokker-Planck calculation are compared with the result of the mapping approach for the first Shapiro resonance: both approaches give the same result.

3 Ac currents for a non adiabatic evolution of the phase

Equation (4) gives the Landau-Zener probability of ending on the upper Andreev bound state when starting on the lower one and crossing $\delta = \pi$. Once this probability starts to be sizeable, the adiabatic approximation breaks down. It is no longer true to consider that the system always follows the lower Andreev level when the phase evolves in time.

The aim of this section is to understand the modification of the Shapiro resonances and the onset of the PAMAR current when Landau-Zener transitions are taken into account.

3.1 Perfect voltage bias

As in section 2 for the adiabatic evolution of the phase, we start for simplicity by the ideal case of a perfectly voltage biased Josephson weak link with no fluctuations.

3.1.1 Empiric calculation for the Shapiro resonances

The aim of this section is to find an expression for the amplitude of the Shapiro resonances that takes into account transitions to the upper Andreev level. The way we proceed here is really similar to the strategy developed in chapter 1, where the MAR current was explained in terms of Landau-Zener transitions between the stationary Andreev levels.

Following the procedure of chapter 1, it is possible to write an empiric expression for the Josephson currents flowing in the contact:

$$I\left(t, \{\tau\}\right) \approx \sum_{i=1}^{N} \left\{ P_{LZ}\left(\tau_i\right) I_{\rightarrow}\left(\delta\left(t\right)\right) + \left[1 - P_{LZ}\left(\tau_i\right)\right] I_{-}\left(\delta\left(t\right), \tau_i\right) \right\} \qquad (19)$$

with $\delta\left(t\right) = \delta_0 + \frac{V}{\varphi_0} t + \frac{A}{\varphi_0 \omega_r} \sin\left(\omega_r t\right)$, and $P_{LZ}\left(\tau_i\right)$ is given by equation (4).

Equation (19) states that the total current is the average of two terms: the current carried by the lower Andreev level E_-, with weight $1 - P_{LZ}$; and the current carried by the ballistic level $E_{\rightarrow}$, with weight P_{LZ}. When the quantity in the exponential of equation (4) for the Landau-Zener probability goes below 1, the Landau-Zener probability becomes sizeable and transitions occur when the phase is swept through $\delta = \pi$. Therefore, the contribution to the total current from the ballistic Andreev level increases.

The total dc current at the voltage V is then:

$$\left\langle I\left(t,\{\tau\}\right)\right\rangle_V \approx \sum_{i=1}^{N}\left\{P_{LZ}\left(\tau_i\right)\left\langle I_{\rightarrow}\left(t\right)\right\rangle_V + \left[1-P_{LZ}\left(\tau_i\right)\right]\left\langle I_{-}\left(t,\tau_i\right)\right\rangle_V\right\}.$$

The quantity $\left\langle I_{-}\left(t,\tau\right)\right\rangle_V$ has been calculated in section 2.1. We now turn to the calculation of $\left\langle I_{\rightarrow}\left(t\right)\right\rangle_V$.

The current phase relation $I_{\rightarrow}\left(\delta\right) = 2\frac{e\Delta}{2\hbar}\left|\sin\left(\frac{\delta}{2}\right)\right|$, which is a periodic even function, can be expanded into a cosine Fourier series as:

$$I_{\rightarrow}\left(\delta\right) = \sum_{m=0}^{\infty} I_m^{\cos}\cos\left(m\delta\right),$$

with $I_m^{\cos} = \begin{cases} \frac{4}{\pi}\frac{e\Delta}{2\hbar} & m=0 \\ \frac{8}{\pi\left(1-4m^2\right)}\frac{e\Delta}{2\hbar} & m>0 \end{cases}$

Figure 13 displays the amplitude of these Fourier coefficients.

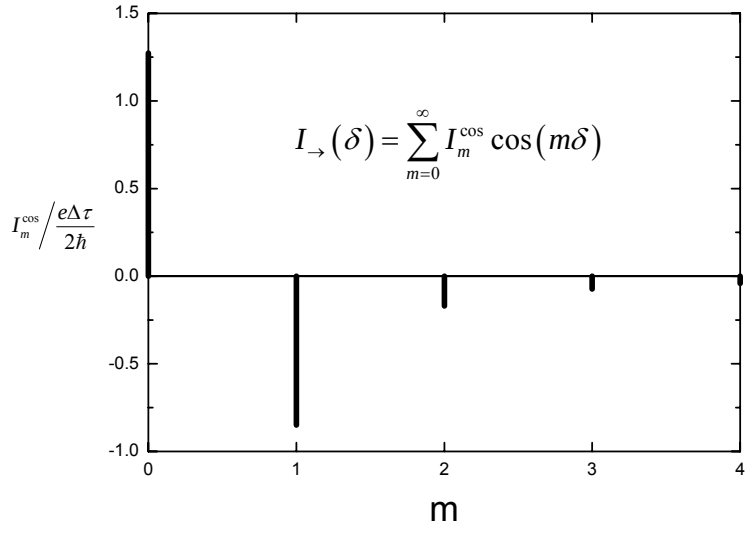

Figure 13: Fourier coefficients of the ballistic current phase relation.

The calculation of the Shapiro resonance amplitudes is performed in the same manner as for the sine Fourier decomposition. There is a noticeable fact to remark which is the existence of a dc background current $I_{m=0}^{\cos} = \frac{4}{\pi}\frac{e\Delta}{2\hbar}$ on which the resonances will superimpose. The positions and amplitudes of the resonances for a $\tau = 1$ ballistic channel are given below:

$$V = 0: \qquad \left\langle I_{\rightarrow}(t)\right\rangle_{V=0} = \sum_{m\geq 1} I_m^{\cos} J_0(2m\alpha)\cos(m\delta_0)$$

$$V = \frac{k}{m}\varphi_0\omega_r: \qquad \left\langle I_{\rightarrow}(t)\right\rangle_{V=k/m} = \sum_{n\geq 1} I_{n\times m}^{\cos} J_{n\times k}(2nm\alpha)(-1)^{n\times k}\cos(nm\delta_0)$$

$$V = -\frac{k}{m}\varphi_0\omega_r: \qquad \left\langle I_{\rightarrow}(t)\right\rangle_{V=-k/m} = \sum_{n\geq 1} I_{n\times m}^{\cos} J_{n\times k}(2nm\alpha)\cos(nm\delta_0)$$

The amplitude of the supercurrent and of the Shapiro resonances in a *N*-channel contact in presence of microwaves thus writes:

$$S_{0,\pm k/m}(\{\tau\}) = \max_{\delta_0}\left\{\sum_{i=1}^{N}\left\{P_{LZ}(\tau_i)\left\langle I_{\rightarrow}(t)\right\rangle_V + \left[1-P_{LZ}(\tau_i)\right]\left\langle I_{-}(t,\tau_i)\right\rangle_V\right\}\right\} \quad (20)$$

with $V = 0, \pm\frac{k}{m}\varphi_0\omega_r$.

In the following, we restrict the model to the case $A \ll V$ (see equation (4)). This means that transitions to the upper state due to the oscillatory dynamics of the phase are not accounted for in this model. Within this restriction, the Landau-Zener probability at the k/m resonance writes:

$$P_{LZ}(\tau) = \exp\left[-\pi\frac{m}{k}\frac{\Delta}{e\varphi_0\omega_r}(1-\tau)\right] \quad (21)$$

Figure 14 shows the predictions of this empiric calculation for the microwave power dependence of the Shapiro resonances, and a comparison with the adiabatic approximation.

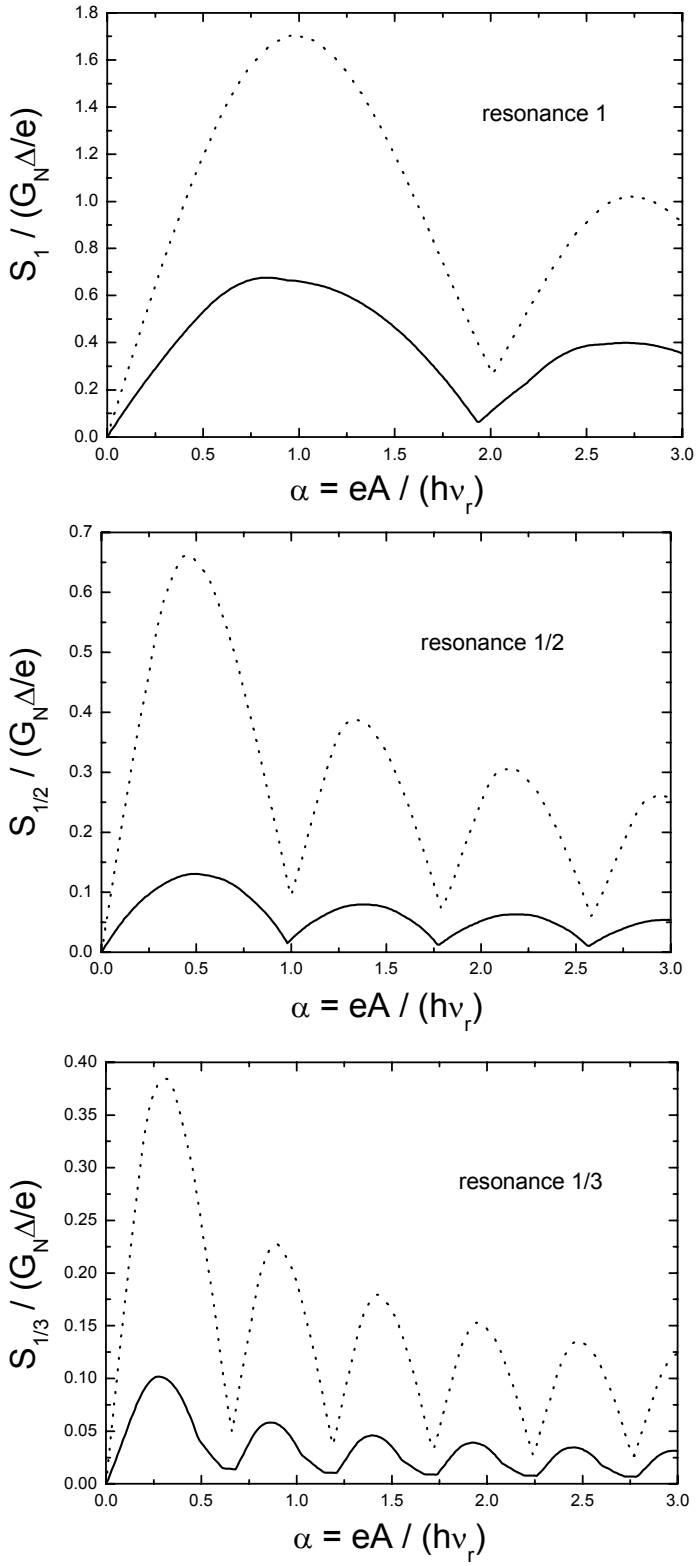

Figure 14: Microwave power dependence of the Shapiro resonance amplitudes in a single channel contact of transmission 0.995. Comparison between the adiabatic approximation (dotted line) and the empiric calculation (solid line) for a microwave frequency $\nu_r = 0.5\Delta/h$.

The empiric calculation predicts smaller Shapiro resonances than the adiabatic approximation. This striking feature can be better understood by looking at Figure 16 and Figure 17, where the predictions of the two approaches for the transmission dependence of the resonance amplitudes are plotted, and can be explained by means of qualitative arguments as follows:

The amplitude of Shapiro resonances increases with the anharmonicity of the ac Josephson currents. The comparison of Figure 5 and Figure 13 shows that the Fourier weights of the current phase relation are smaller for a ballistic channel than for a channel with $\tau = 1^-$. In the adiabatic approximation, this implies that the ac Josephson currents are more anharmonic in a channel with $\tau = 1^-$ than in a ballistic channel and thus that the amplitudes of the resonances reach their maxima for $\tau = 1^-$ (see Figure 16 and Figure 17). However, in reality, Landau-Zener transitions become frequent when the transmission of the channel approaches one. Therefore, for a transmission close to unity, the system follows almost always the ballistic Andreev level with the consequence that the Josephson currents "lose" some of their anharmonicity. The transmission τ^* maximizing the anharmonicity of the Josephson currents is not $\tau^* = 1^-$ as predicted by the adiabatic approximation, but verifies $\tau^* < 1$ in reality, as observed on Figure 16 and Figure 17. The results of Figure 14 are simply explained by these hand-waving arguments saying that for the parameters of the graphs, the transmission $\tau = 0.995 > \tau^*$.

The threshold τ^* is smaller on Figure 17 ($\nu_r = 0.5\Delta/h$) than on Figure 16 ($\nu_r = 0.1\Delta/h$). Indeed, the condition for the Landau-Zener probability given by equation (21) to remain small is:

$$\frac{m}{k}\frac{\Delta}{h\nu_r}(1-\tau) > \frac{1}{2\pi} \qquad (22)$$

Therefore, the higher the frequency, the smaller the transmission should be. For high frequencies, the Shapiro resonances appear at larger voltages on the IV characteristics, corresponding to a faster linear drift of the phase and a larger Landau-Zener probability.

For aluminum contacts ($\Delta \approx 180\ \mu\text{eV}$), with an external microwave frequency $\nu_r = 10$ GHz, the condition of equation (22) holds up to the second Shapiro resonance ($k/m = 2$) provided $\tau < 0.92$.

3.1.2 Full microscopic calculation

The empiric calculation of the last paragraph provides us with some insight on the effect of Landau-Zener transitions.

As already mentioned in section 1.2, J. C. Cuevas *et al.* [7] calculated the time dependence of the Josephson currents in a single channel of arbitrary transmission under a perfect voltage bias $v(t) = V + A\cos(\omega_r t)$. Their method is based on a tight-binding like Hamiltonian [12] that describes the charge transfer between the two superconducting electrodes. To calculate the current, they use out of equilibrium Green function techniques within the Keldysh formalism. They show that the current writes:

$$I(V,\ A,\ \omega_r,\ t) = \sum_{n,m} I_n^m(V,\ A,\ \omega_r)\, e^{i\left[n(\delta_0+\omega_0 t)+m\omega_r t\right]} \tag{23}$$

with $\omega_0 = 2eV/\hbar$ the Josephson frequency.

The dc component can be explicited as:

$$I = I_{\text{background}} + I_{\text{Shapiro}},$$

with:

$$I_{\text{background}} = I_0^0 \tag{24}$$

and:

$$I_{\text{Shapiro}} = \sum_{n,m} I_n^m(V,\ A,\ \omega_r)\, e^{in\delta_0}\,\delta\left(V - \frac{m}{n}\varphi_0\omega_r\right) \tag{25}$$

where $\delta\left(V-\frac{m}{n}\varphi_0\omega_r\right)=\begin{cases}0 & V\neq\frac{m}{n}\varphi_0\omega_r\\ 1 & V=\frac{m}{n}\varphi_0\omega_r\end{cases}$

This explicit decomposition of the current through the Josephson weak link into two parts is specific to the perfectly voltage biased case. In this ideal case, Shapiro resonances appear on the *IV* characteristic as discontinuities of the current (see Figure 15), at well defined value of the voltage. However, in practice, Shapiro resonances acquire a finite width because of the unavoidable fluctuations of the bias voltage. It is therefore no longer possible to split the contributions of the background and Shapiro currents.

The dc component in equation (23) is plotted on Figure 15. The Shapiro resonances superimpose on a background current, which is due to photon assisted multiple Andreev reflections (PAMAR). For comparison, the MAR current in absence of microwave is also shown. The background current in presence of microwaves will be thoroughly studied in section 5.

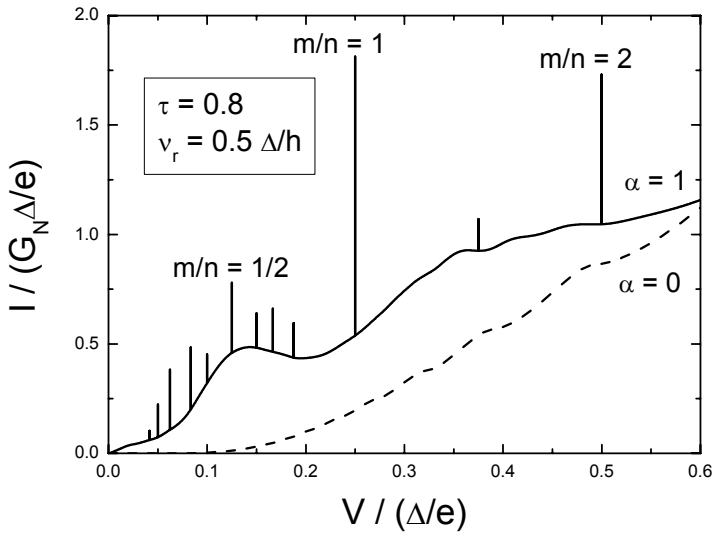

Figure 15: dc IV characteristic of a single channel contact ($\tau=0.8$). The dashed line is the IV without microwave ($\alpha=eA/(h\nu_r)=0$). The solid line is the IV with $\alpha=1$. $G_N=(2e^2/h)\tau$ is the normal state conductance of the contact (reproduced from [7]).

Figure 16 and Figure 17 show the transmission dependence of the Shapiro resonance amplitudes predicted for a single channel contact by this theory. Comparisons with the adiabatic approximation and the empiric calculation are also displayed.

- The three calculations predict the same amplitudes for low enough transmission because in this case, the system always follows adiabatically the lower Andreev level.
- At high enough transmissions, the empiric calculation and the full calculation predict the same result because the system experiences almost always Landau-Zener transitions and thus follows the ballistic level.
- For intermediate transmissions, the difference in the predictions of the full and empiric calculations can be interpreted as follows:

  At small enough microwave power (Figure 16: $\nu_r = 0.1\Delta/h$ and $\alpha = 0.25$), the Landau-Zener transitions are dominated by the linear drift of the phase and not by its oscillatory dynamics, therefore the empiric calculation, which does not take into account the oscillatory dynamics in the Landau-Zener probability and the full calculation predict almost the same results.

  At larger microwave power (Figure 17: $\nu_r = 0.5\Delta/h$ and $\alpha = 0.25$), the transitions due to the oscillatory dynamics of the phase become important, resulting in an enhanced anharmonicity of the Josephson currents. This explains that the full calculation predicts larger fractional Shapiro resonances than the empiric calculation.

Figure 18 shows the microwave power dependence of the Shapiro resonance amplitudes for a single channel contact of transmission $\tau = 0.8$. Comparisons with the adiabatic approximation and with the empiric calculation are displayed. For the parameters chosen, the empiric calculation and the adiabatic approximation predict the same results. This indicates that the linear drift of the phase doesn't induce Landau-Zener transitions for the chosen set of parameters. At low enough microwave power, the full calculation predicts the same results as the two other calculations. However, above a certain microwave power, it predicts enhanced amplitudes for the fractional Shapiro resonances, as a consequence of Landau-Zener transitions due to the oscillatory dynamics of the phase. This is coherent with the previous discussion on Figure 16 and Figure 17.

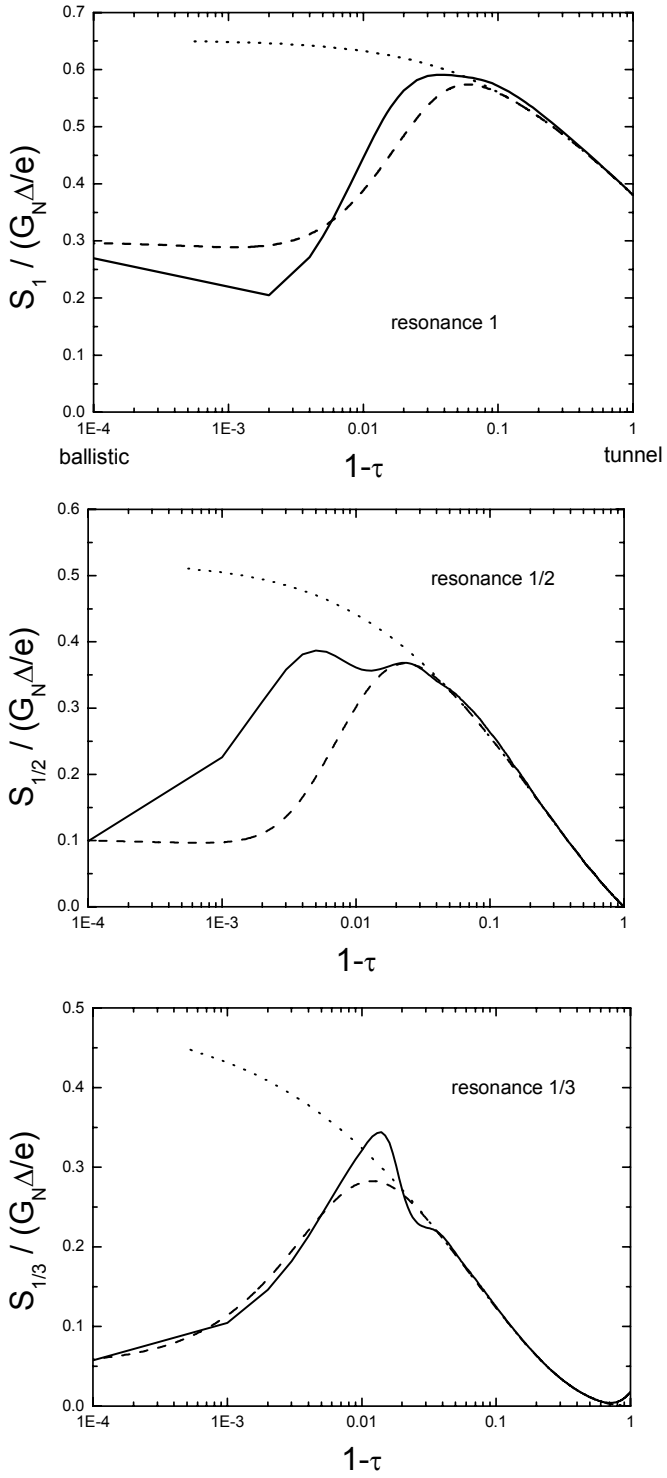

Figure 16: Amplitude of the Shapiro resonances $k/m = 1, 1/2, 1/3$ *for* $\alpha = 0.25$. *Note the horizontal axis: data are plotted as a function of the reflection coefficient* $(1-\tau)$ *on a logarithmic scale to highlight the high transmissions. The dotted lines are the predictions of the adiabatic approximation. The dashed (resp. solid) lines are the predictions of the empiric (resp. full microscopic) calculation for a microwave frequency* $\nu_r = 0.1\Delta/h$.

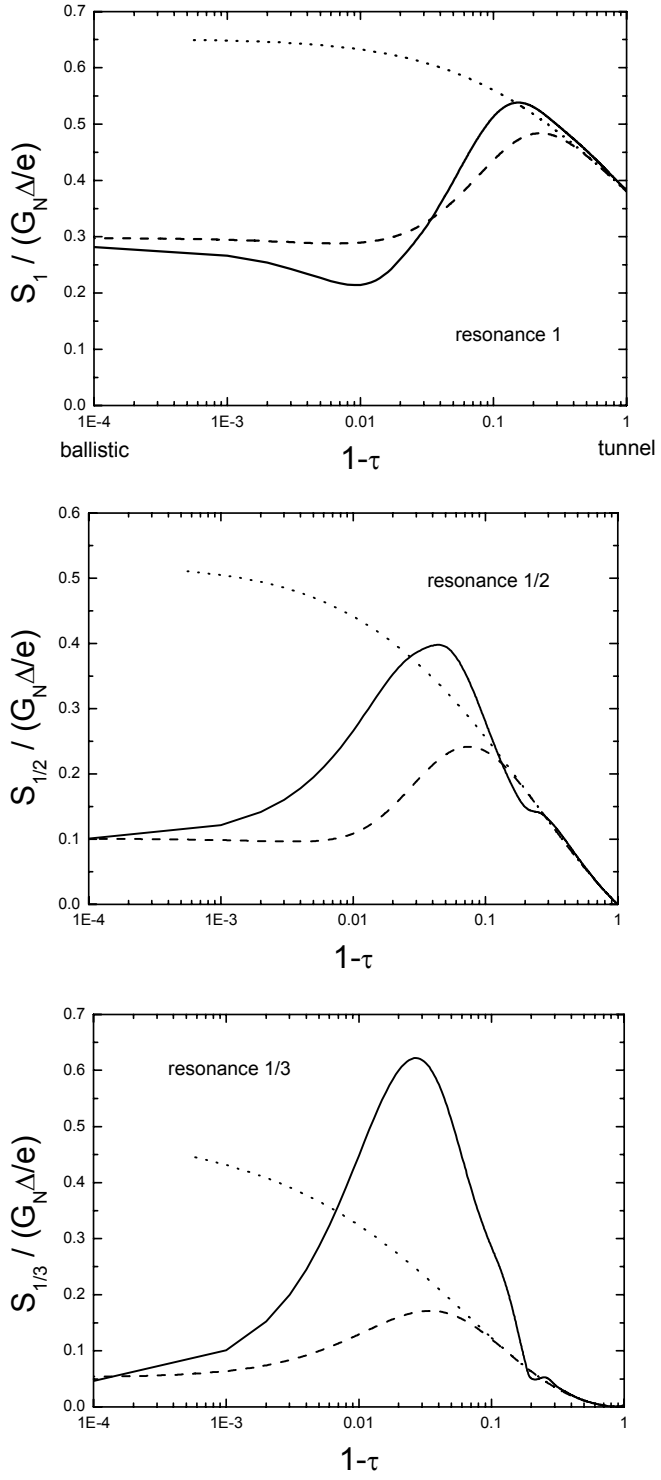

Figure 17: Amplitude of the Shapiro resonances $k/m = 1, 1/2, 1/3$ *for* $\alpha = 0.25$. *Note the horizontal axis: data are plotted as a function of the reflection coefficient* $(1-\tau)$ *on a logarithmic scale to highlight the high transmissions. The dotted lines are the predictions of the adiabatic approximation. The dashed (resp. solid) lines are the predictions of the empiric (resp. full microscopic) calculation for a microwave frequency* $\nu_r = 0.5\Delta/h$.

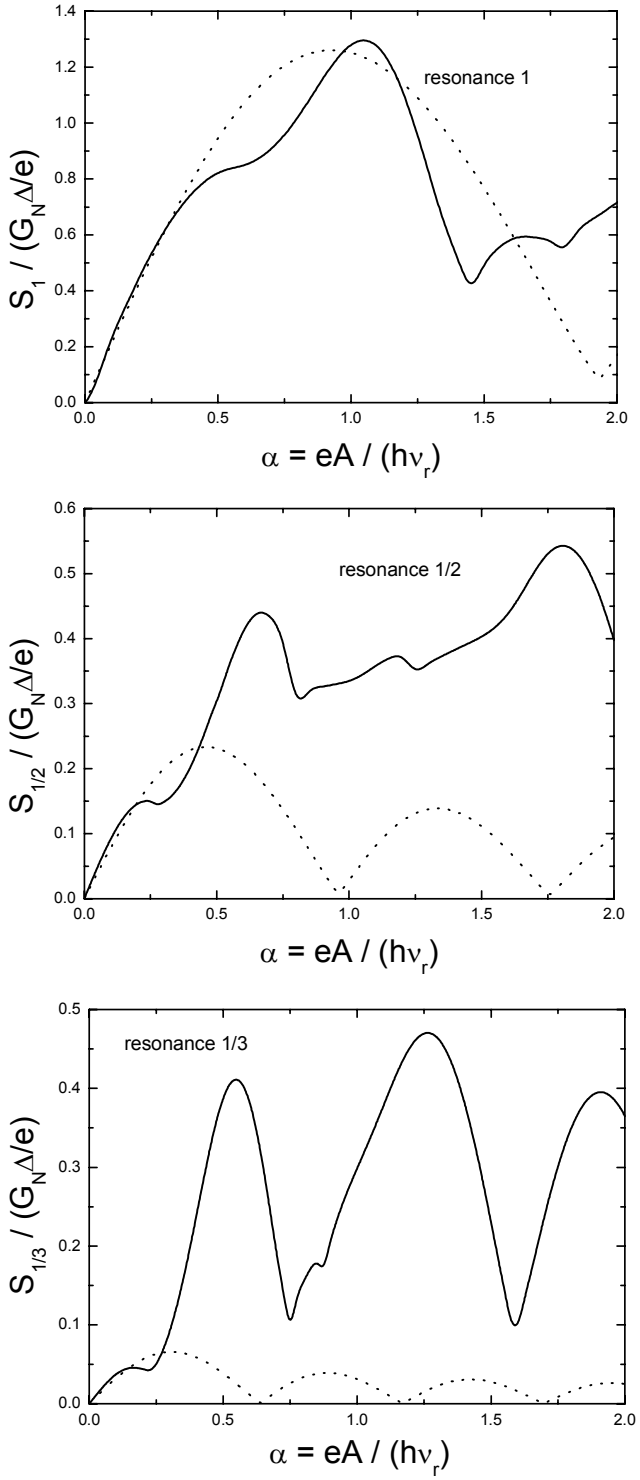

Figure 18: Amplitude of the Shapiro resonances $k/m = 1, 1/2, 1/3$ *as a function of* α *for a single channel contact of transmission* $\tau = 0.8$. *The dotted lines are the predictions of the adiabatic approximation and of the empiric calculation for a microwave frequency* $\nu_r = 0.5\Delta/h$. *For this set of parameters, both calculations give the same results. The solid lines are the predictions of the full microscopic calculation at the same frequency.*

3.2 Effect of the environment on the Shapiro resonances: imperfect voltage bias

So far, the non adiabatic evolution of the phase has been treated in an ideal case, which is the perfect voltage bias. This can never be achieved in practice since the voltage always experiences fluctuations. In this section, we present an empirical approach aiming to describe the shape of the Shapiro resonances in Josephson weak links embedded in a resistive environment including the possibility for a non adiabatic evolution of the phase.

This approach is based on the mapping approach developed in paragraph 2.2.1, where a Shapiro resonance p/q is described as a replica of the supercurrent peak with effective parameters:

$$\begin{cases} I_0^{eff} = \left| I_q J_p \left(2q\alpha \right) \right| \\ T^{eff} = qT \\ V_B^{eff} = V_B - \dfrac{p}{q} \varphi_0 \omega_r \end{cases}$$

The effective critical current I_0^{eff} appearing in the mapping approach is nothing but the maximum amplitude $S_{p/q}$ of the Shapiro resonance p/q calculated for a perfectly voltage biased contact. The effects of the fluctuations are accounted by mapping the dynamics of the phase around a Shapiro resonance to the dynamics of the phase around zero voltage in absence of microwaves.

$\left| I_q J_p \left(2q\alpha \right) \right|$ is the value of $S_{p/q}$ predicted by the adiabatic calculation. To account for the non adiabatic dynamics of the phase, we propose to take for $S_{p/q}$ the value calculated within the microscopic calculation of J. C. Cuevas *et al.* [7]. According to equation (25), $S_{p/q}$ writes in this case:

$$S_{p/q} = \max_{\delta_0} \left[\sum_{l \geq 1} I_{lq}^{lp} \left(\frac{p}{q} \varphi_0 \omega_r, A, \omega_r \right) e^{ilq\delta_0} \right] \qquad (26)$$

Another possibility for $S_{p/q}$ is the value obtained in the empiric calculation (equation (20)).

4 Experimental results on Shapiro resonances

In this section, we first describe the experimental setups that we have engineered to measure the Shapiro resonances. Then we present results on contacts with not too highly transmitting channels. These results can therefore be interpreted by the adiabatic theory developed in section 2. Finally, we present results on contacts containing an almost ballistic channel, where the results are interpreted with the theory of section 3, which takes into account the Landau-Zener transitions induced by the phase dynamics.

4.1 The two experimental setups

Like for the supercurrent peak, measuring Shapiro resonances requires to voltage bias the atomic contact. In a current bias setup, switching would occur each time the current would reach the maximum of a resonance and the resonances of smaller amplitude could be missed. For details on how to voltage bias an atomic contact, the reader is referred to chapter 5.

In the experiments we have used two different setups which essentially differ by the way the current in the contact is measured. In both setups, the break junction is placed in series with a microfabricated resistor.

The first technique to measure the current through the contact is to divert part of it by using the microfabricated resistor as a pick-up resistor, and feeding it into the input coil of a SQUID amplifier [13, 14, 15] (see Figure 19).

The second technique is to measure the voltage drop across this microfabricated resistor using high input impedance Field Effect Transistor (FET) amplifiers (see Figure 20).

4.1.1 SQUID setup

In our setup, the resistance in series with the contact must be small to allow for voltage biasing the contact (see chapter 5). It is therefore advantageous to use a SQUID amplifier because such amplifiers have a low noise level when measuring signals arising from low impedance sources.

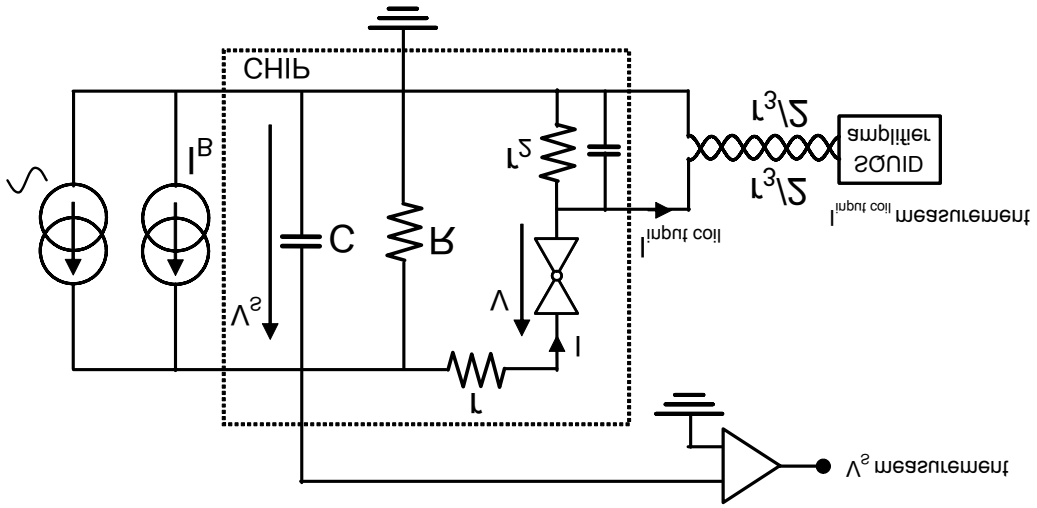

Figure 19: Experimental setup used for the measurement of Shapiro resonances using a SQUID as an ammeter.

In this setup, two quantities are measured: the voltage V_S across the bias resistor R, and the current diverted into the input coil of the SQUID amplifier, $I_{input\ coil}$ (see chapter 5 for details on the SQUID amplifier). The voltage V across the junction and the current I through the junction are calculated by:

$$\begin{cases} I = \left(1 + \frac{r_3}{r_2}\right) I_{input\ coil} \\ V = V_S - \left(r + \frac{r_2 r_3}{r_2 + r_3}\right) I \end{cases}$$

where r_3 is the dc resistance of the lossy twisted pair going from the chip to the SQUID amplifier. At low temperatures, the measured values of the various resistors are:

$R = 25.3 \pm 0.05\ \Omega$, $r = 7.4 \pm 0.05\ \Omega$, $r_2 = 6.2 \pm 0.05\ \Omega$, $r_3 = 12.8 \pm 0.05\ \Omega$. The detailed wiring of the experiment is presented in chapter 5.

4.1.2 Field Effect Transistor (FET) amplifier setup

Even though FET amplifiers are not well adapted to measure signals on small impedances, we have designed an other setup to use such an amplifier for measuring the current in the contact, because we have suspected some back-action from the SQUID amplifier. This setup is schematically represented on Figure 20.

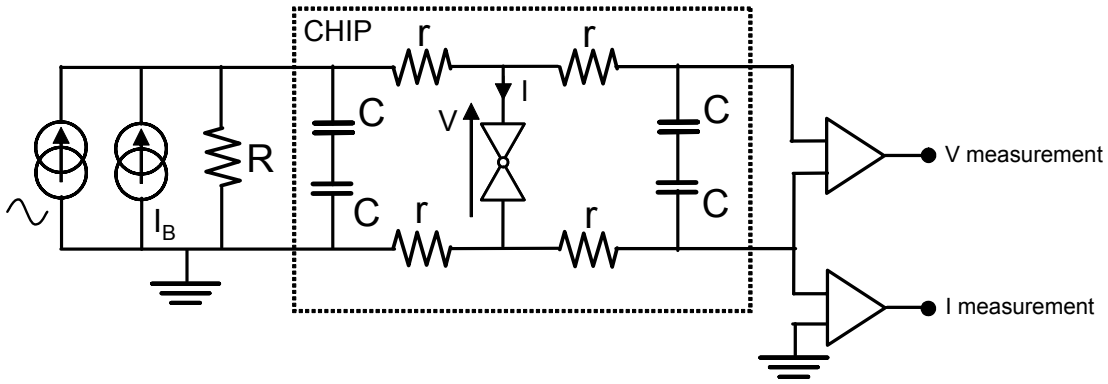

Figure 20: Experimental setup used in the experiment on Shapiro resonances and in the experiment on photon assisted multiple Andreev reflection. The current through the contact is obtained by measuring the voltage drop across one of the on-chip resistors.

In this setup, one actually obtains directly the current through the junction by measuring the voltage drop across one of the on chip resistors. Two lock-in detectors were used to measure the differential conductance of the atomic contact as a function of the dc voltage bias. The *IV* characteristics of the contact could thus either be directly measured or obtained by numerical integration of the differential conductance signal.

At low temperatures, the resistances were: $R \approx 50\ \Omega$, $r \approx 40\ \Omega$. For the detailed wiring of this setup, we refer the reader to chapter 5.

4.2 Contacts with not too high transmissions

4.2.1 Sample measured with the SQUID setup

We have measured Shapiro resonances on a contact with a mesoscopic pin code $\tau = \{0.626,\ 0.232,\ 0.033\}$. The results are presented on Figure 21.

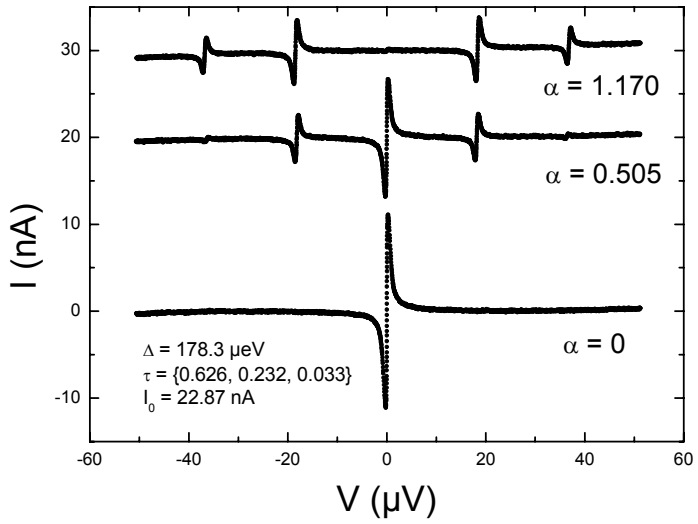

Figure 21: Measured integer Shapiro resonances. The frequency of the external radiation was $\nu_r = 9.3156$ GHz. For clarity, the two upper curves have been shifted by 20 and 30 nA respectively.

Only integer resonances are present on Figure 21 because the current phase relation of such a contact is still very close to a sine function. The voltage positions of the resonances are given by $V_n = n \times h\nu_r / (2e) \approx n \times 19.3\ \mu\text{V}$.

The non-monotonic dependence of the amplitudes of the resonances with α (already seen in sections 2 and 3) will be studied later on in greater detail.

Beforehand, it is necessary to present the procedure used to describe the effects of the environment and of the voltage fluctuations on the Shapiro resonances. This procedure corresponds to the mapping approach presented in section 2.2.1:

- First the amplitudes of the resonances are calculated at zero temperature for a perfectly voltage biased contact using the expression (6) obtained for an adiabatic evolution of the phase.
- Then the effect of the finite temperature environment is taken into account by mapping the dynamics of the phase around a Shapiro resonance to its dynamics around zero voltage, without microwave.

A Shapiro resonance is thus obtained as a replica of the supercurrent peak.

As shown in chapter 5, the electromagnetic environment seen by the junction in the electric circuit of Figure 19 can be approximated by the model environment of Figure 22. The supercurrent peak of an atomic contact embedded in such an environment was calculated in section 3 of chapter 2.

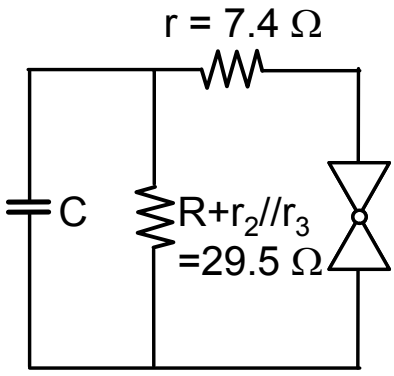

Figure 22: Simplified environment seen from the contact.

The result of the mapping approach for the first Shapiro resonance is presented on Figure 23.

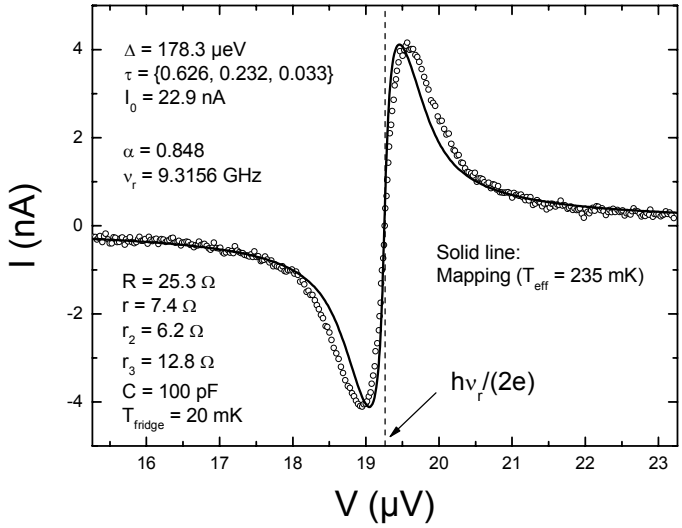

Figure 23: First integer Shapiro resonance on a contact with not too high transmission. The experimental curve is compared to a replica of the supercurrent peak as predicted by the mapping approach for an effective noise temperature of 235 mK. The experiments were carried out at the fridge base temperature (20 mK)

The width of the theoretical prediction does not reproduce the experimental data. We attribute this effect to the physical implementation of the $C = 100$ pF capacitor. This planar capacitor was obtained between a microfabricated top electrode and the metallic substrate, the dielectric being the polyimide layer. Not all of this capacitance is seen by the contact because of the stray inductance and the finite resistivity of the top electrode.

We have measured the variation of the resonance amplitudes with the microwave power. The results are shown on Figure 24.

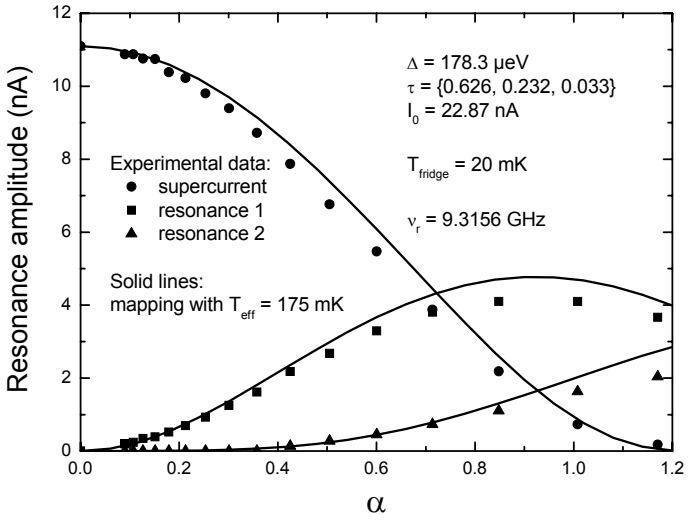

Figure 24: Variation of the resonance amplitudes with the reduced microwave power $\alpha = \frac{eA}{h\nu}$*. Dots are experimental results. Solid lines are predictions of the mapping approach for an effective noise temperature* $T_{eff} = 175$ mK*. The experiments were performed at the fridge base temperature (20 mK).*

The theoretical lines have been calculated using the mapping approach with the environment[2] of Figure 22 for an effective noise temperature $T_{eff} = 175$ mK. At large microwave amplitude, the experimental points depart from the theoretical predictions, because more microwave power is burnt in the on-chip dissipative elements and heats them up. In all cases, the effective noise temperature is well above the actual fridge temperature (20 mK) because of spurious noise on the contact.

In the following, we present the same type of measurements but performed on a different sample and using a different measurement setup (see Figure 20).

[2] We have shown that this approximate environment doesn't reproduce the width of the Shapiro resonances in a satisfactory manner (Figure 23). However we showed in section 3 of chapter 2 that the height of the supercurrent peak depends very little on the details of the environment, provided it is dissipative at all frequencies.

4.2.2 Sample measured with the FET amplifier setup

In the previous experiment, a good control of the on-chip environment was lacking. We have therefore redone the experiments using the chips designed for the supercurrent peak experiment of chapter 2 for which the environment is better known. The experimental setup and the chip are schematically represented on Figure 20. As shown in chapter 5, the on-chip electromagnetic environment seen by the junction is equivalent to the circuit sketched on Figure 25.

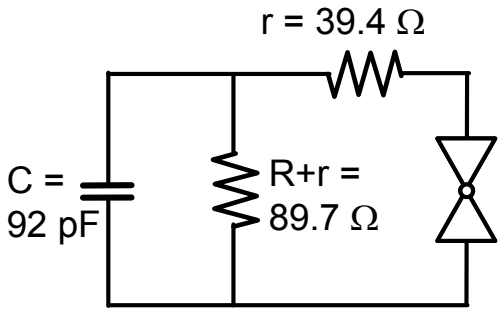

Figure 25: Electromagnetic environment of the atomic contact on the sample measured with the FET setup.

Even if this electromagnetic environment does not implement a perfectly frequency independent impedance, it is nearly equivalent, for most of the frequency range of the phase dynamics, to a single 39.4 Ω resistor. This was already pointed out in the experiments on the supercurrent peak presented in chapter 2, where we showed that the supercurrrent peaks could be perfectly fitted assuming an ohmic environment.

To confirm this, Figure 26 shows the predictions for the first Shapiro resonance of two calculations:

- The rigorous treatment of the phase dynamics in an ohmic environment based on the Fokker-Planck equation (see section 2.2.2).
- The outcome of the mapping approach. The amplitude of the resonance is first calculated at zero temperature, assuming that the contact is perfectly voltage biased. Then the effects of the environment represented on Figure 25 are taken into account by mapping the dynamics of the phase around the resonance by its dynamics around zero voltage in absence of microwaves.

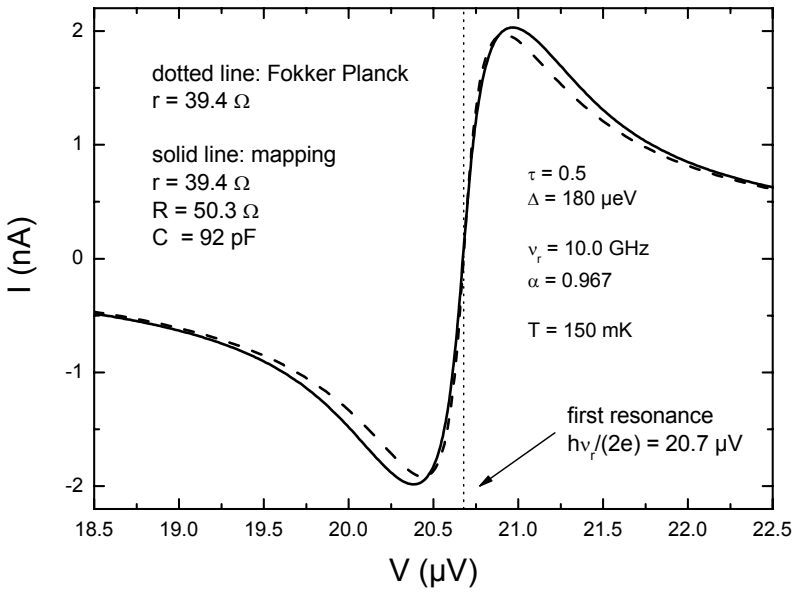

Figure 26: Comparison of two theoretical predictions for the first Shapiro resonance of a $\tau = 0.5$ single channel contact. Dashed line: predictions of the Fokker-Planck treatment of the dynamics of the phase in an ohmic environment ($r = 39.4\ \Omega$). Solid line: predictions of the mapping approach for the environment of Figure 25.

Figure 26 exhibits only small deviations between the predictions of the two calculations. This confirms the fact that, for the dynamics of the phase, the electromagnetic environment of Figure 25 is equivalent to a resistor.

On Figure 27 we present experimental results obtained on a contact with mesoscopic pin code $\tau = \{0.573, 0.233, 0.037\}$ for two different values of the microwave amplitude. The experimental results are compared to the predictions of the rigorous Fokker-Planck calculation assuming an ohmic environment. We have indeed just seen that this assumption was justified. The advantage of using the rigorous Fokker-Planck calculation is that it predicts the *IV* characteristic as a whole, and not only parts centered on the Shapiro resonances like the mapping approach.

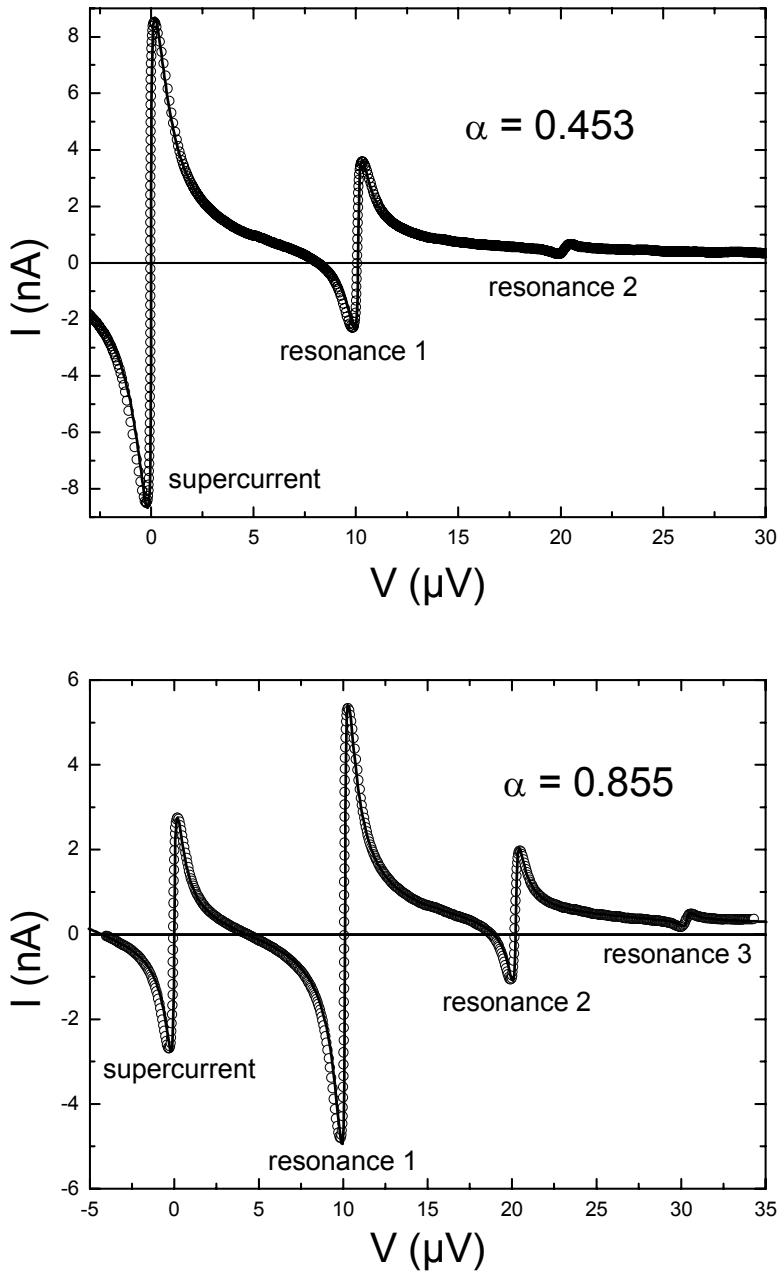

Figure 27: Shapiro resonances measured in a contact with mesoscopic pin code $\tau = \{0.573, 0.233, 0.037\}$ *at a microwave frequency* $\nu_r = 4.892$ GHz. *The superconducting gap was* $\Delta = 179.7$ μeV *and the critical current* $I_0 = 21.4$ nA. *On each graph, open dots are experimental results and the solid line is the prediction of the Fokker-Planck treatment of the dynamics of the phase in a purely ohmic environment (*$r = 39.4\ \Omega$*). The parameters of the physical environment were* $r = 39.4\ \Omega$, $R = 50.3\ \Omega$, *and* $C = 92$ pF. *The effective noise temperature entering the theory is 120 mK, well above the fridge base temperature at which the experiments were carried out (*$T_{fridge} = 20$ mK*). The upper curve corresponds to* $\alpha = 0.453$ *and the lower one to* $\alpha = 0.855$.

The agreement between the experimental data and the Fokker-Planck theory is entirely satisfactory. The effective noise temperature entering the theory is 120 mK, well above the fridge temperature (20 mK) at which the experiments were carried out.

We also have measured the amplitude of the Shapiro resonances as a function of the microwave amplitude. The results are presented on Figure 28. The effective noise temperatures entering the Fokker-Planck theory lie between 125 mK and 155 mK, depending on the microwave amplitude. At large amplitude, the effective noise temperature is larger because more microwave power is burnt in the on-chip dissipative elements.

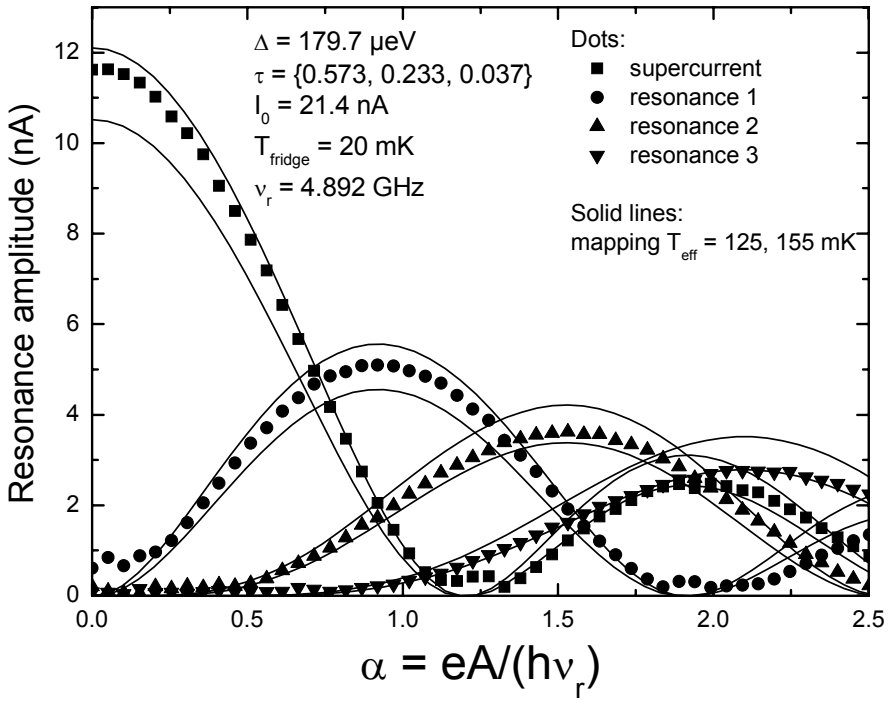

Figure 28: Dependence of the Shapiro resonance amplitudes with the microwave power. Squares: supercurrent. Circles: first resonance. Up-triangles: second resonance. Down-triangles: third resonance. The upper (resp. lower) solid lines are the theoretical predictions at 125 mK (resp. 155 mK).

The power dependence of the Shapiro resonances in contacts with not too highly transmitting channels is a benchmark result used to calibrate the microwave power on the contact.

In summary, integer Shapiro resonances are well described by the Fokker-Planck treatment of the adiabatic dynamics of the phase presented in section 2.2.2. However, in the experiments we were unable to reach effective noise temperatures smaller than 130 mK. We attribute this to spurious noise incoming on the atomic contact despite the heavy filtering.

4.3 Contacts with high transmissions

4.3.1 Sample measured with the SQUID setup

Figure 29 shows IV characteristics obtained on a contact with mesoscopic pin code $\tau = \{0.992, 0.279, 0.278\}$ for three different values of the microwave power.

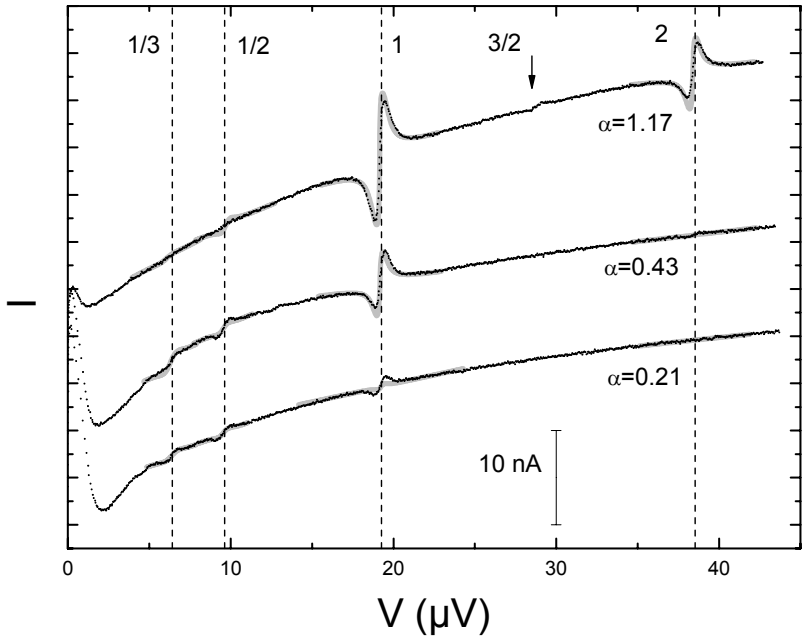

Figure 29: Shapiro resonances obtained on a $\tau = \{0.992, 0.279, 0.278\}$ *contact with a microwave of frequency* $\nu_r = 9.3156\,\mathrm{GHz}$. *The superconducting gap was* $\Delta = 177.0\,\mu\mathrm{eV}$. *The two upper curves are shifted by 10 and 30 nA respectively. Underlying gray lines are the predictions of the mapping approach for an effective noise temperature of 200 mK. The experiments were performed at the fridge base temperature (20 mK).*

For $\alpha = 0.21$ and $\alpha = 0.43$, the Shapiro resonances 1/2 and 1/3 are clearly distinguishable. For $\alpha = 1.17$, it is possible to distinguish the resonance 3/2. Fractional Shapiro resonances are the hallmark of the non sinusoidal current phase relation of contacts containing channels with transmission close to unity. (For a microwave frequency $\nu_r = 0.1\Delta / h$ with $\alpha = 0.25$, fractional Shapiro resonances become sizeable for conduction channels of transmission $\tau > 0.9$, as shown on Figure 16.)

The underlying gray lines are the predictions of the mapping approach (see section 3.2) at 200 mK even though the experiments were carried out at the fridge base temperature (20 mK), as previously pointed out.

The amplitude of each resonance is first calculated at zero temperature for a perfect voltage bias within the framework of the full microscopic theory which accounts for the non adiabatic phase dynamics. Then the effects of the environment are taken into account by mapping the dynamics of the phase around the resonance by its dynamics around zero voltage in absence of microwaves. A linear background term has also been added to take into account the background current on which the Shapiro resonances superimpose.

The agreement between the experiment and the result of the mapping approach is good on a qualitative basis. We can't expect a better agreement because the mapping approach completely ignores the structure of the microwave dependent background current on which the Shapiro resonances superimpose.

To further investigate the range of validity of this mapping approach, we have measured the amplitude of the Shapiro resonances as a function of the microwave amplitude. The results are shown on Figure 30.

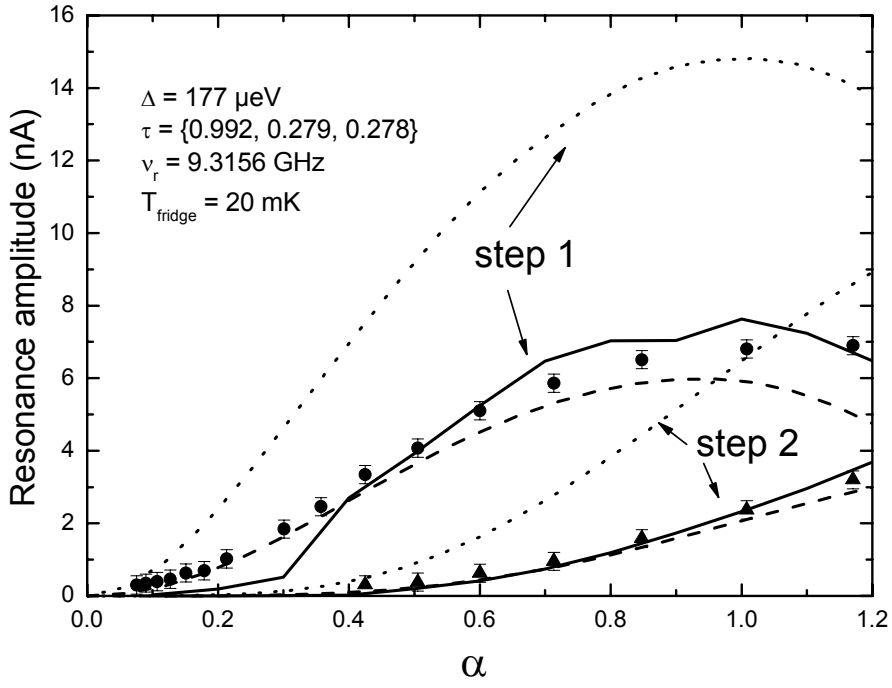

Figure 30: Power dependence of Shapiro resonances 1 and 2 for a contact containing a highly transmitting channel. Closed circles: experimental data. Dotted lines: adiabatic approximation (see section 2.1). Dashed lines: empiric calculation (see section 3.1.1). Solid lines: full microscopic calculation (see section 3.1.2.). In the three theoretical predictions, the effects of the temperature and of the environment are taken into account via the mapping approach (see section 2.2.1 & 3.2) with an effective noise temperature of 200 mK. The experiment was performed at the fridge base temperature (20 mK).

The errors bars in Figure 30 are just estimated errors which arise when a linear background term is subtracted around each resonance to extract its amplitude. As already pointed out, the structure of the background current is completely ignored with this rough technique.

Both the full microscopic calculation (section 3.1.2) and the empiric calculation (see section 3.1.1) reproduce the experimental results reasonably well. The adiabatic approximation (section 2.1) overestimates the amplitude of the Shapiro resonances. A qualitative explanation of this was given in section 3.1.2 (see Figure 16 and Figure 17). We briefly recall here the assumption behind these three calculations:

- The adiabatic approximation assumes that the systems always stays on the lower Andreev level when the phase evolves in time.

- The empiric calculation does take into account Landau-Zener transitions to the upper Andreev level, but only the transitions due to the linear drift of the phase at a velocity given by the voltage at which the resonance appears.
- The full microscopic calculation takes also into account the Landau-Zener transitions due to the oscillatory dynamics of the phase.

In the experiment presented on Figure 30, the empiric calculation and the full microscopic calculation give similar results because the microwave amplitude is small enough for Landau-Zener transitions to the upper Andreev level being mainly due to the linear drift of the phase.

4.3.2 Sample measured with the FET amplifier setup

We present fractional Shapiro resonances measured with the FET setup. Figure 31 shows the *IV* characteristics obtained on a contact with mesoscopic pin code $\tau = \{0.988,\ 0.321,\ 0.102,\ 0.061\}$ for three different values of the microwave amplitude.

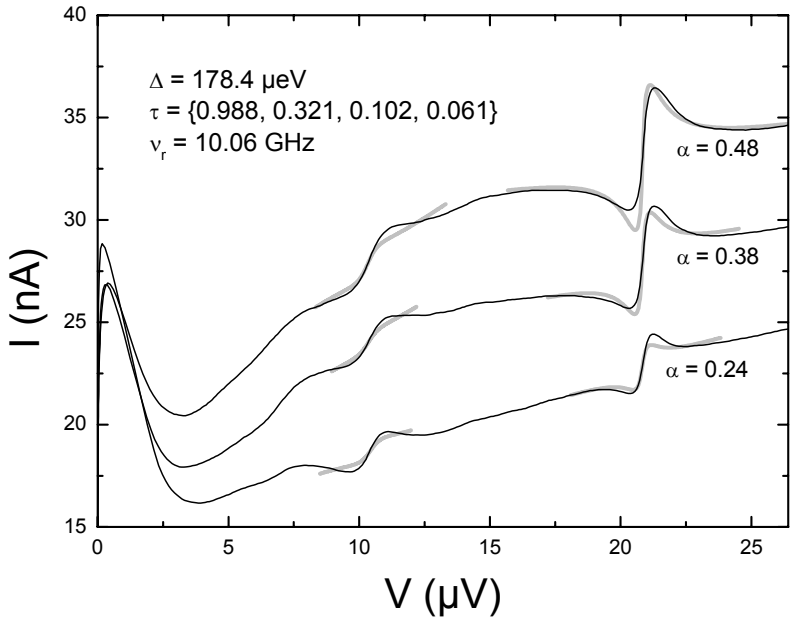

Figure 31: Shapiro resonances $1/2$ and 1. For clarity, the two upper curves have been shifted by 5 and 10 nA respectively. The solid lines are the experimental data measured at a fridge temperature of 20 mK. The underlying gray lines are the predictions of the mapping approach at 180 mK.

Once again, the presence of mainly the fractional Shapiro resonance 1/2 indicates a non sinusoidal current phase relation. The underlying gray lines are predictions of the mapping approach at $T_{eff} = 180$ mK, a temperature still well above the fridge temperature (20 mK). As before, a linear background term has been added to the prediction of the mapping approach to take into account the background current on which the Shapiro resonances superimpose.

In summary, fractional Shapiro resonances appear on the IV characteristic of contacts containing highly transmitting channels in presence of microwave. These fractional resonances are the hallmark of a non sinusoidal current phase relation. However, their amplitudes are very small because we have been unable in the experiments to lower the noise temperature below 180 mK. We have seen indeed that thermal phase fluctuations have a stronger effect on the fractional resonances than on the integer ones. If the amplitudes of the integer resonances correspond to a noise temperature of T, then for a fractional resonance p/q the effect of temperature is amplified by a factor q.
It is possible to describe the shape of the resonances using the mapping approach presented in section 3.2. However, the agreement is only qualitative because this empirical description doesn't account for the photon assisted multiple Andreev reflections (PAMAR) current on which the resonances superimpose. In the following section, the structure of this PAMAR current will be studied in detail.

5 Experimental results on photon assisted multiple Andreev reflections (PAMAR)

This section is devoted to the experimental results obtained for the interplay of an external applied microwave with the MAR current. The calculation mentioned in section 3.1.2 shows that in presence of microwaves, the MAR current is modified (see Figure 15) due to the absorption or stimulated emission of one or several photons during the charge transfer process (see Figure 32). This fundamental mechanism is called photon assisted multiple Andreev reflections.

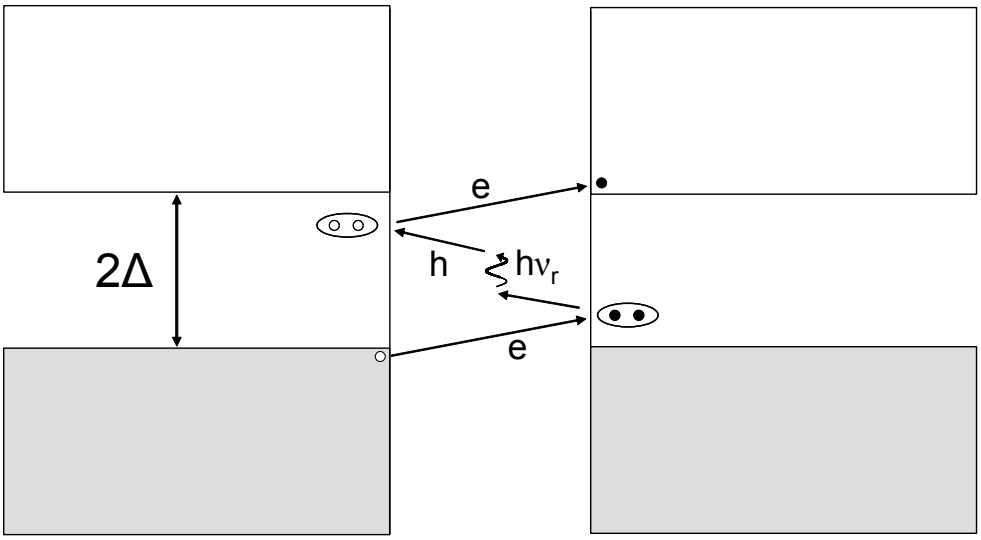

Figure 32: Schematic representation of a one-photon assisted MAR process of order three. The grayed rectangles represent the occupied states in the left and right electrodes which are biased at a constant voltage V. Empty states (white rectangles) are at a distance 2Δ *in energy from the occupied states. This particular MAR process is a three step process, involving an Andreev reflection at each electrode, which transfers all in all three electronic charges from left to right. In the case illustrated here, a photon is absorbed by the hole traveling to the left during the second step, thus lowering the voltage threshold of the full process from* $2\Delta/(3e)$ *to* $(2\Delta - h\nu)/(3e)$.

The experiments have been carried on with the FET amplifier setup. The differential conductance dI/dV was measured as a function of the voltage V across the atomic contact. The IV were obtained either by direct measurements or by numerical integration of the dI/dV.

We report measurements obtained on four different contacts obtained on the same sample.

5.1 Comparison between experiments and the full microscopic calculation

The interaction between the ac Josephson currents and an external microwave field has been reported since 1962 in various structures coupling weakly two superconductors [16, 17, 18, 19]. In 1963, P. K. Tien and J. P. Gordon [20] already came with a qualitative explanation for the effects observed by A. H. Dayem and R. J.

Martin [16] in 1962 on Al-Al_2O_3-Pb tunnel junctions in terms of photon assisted tunneling. To our knowledge, it is the first time that a semi-quantitative agreement between experiments and theory is reported (see Figure 33). Let us recall that no adjustable parameters enters the theory. The following parameters -microwave amplitude, superconducting gap and mesoscopic pin code- have been determined with independent measurements.

In this section, the measured differential conductance is compared to the predictions of the full microscopic calculation briefly presented in section 3.1.2, with no adjustable parameter.

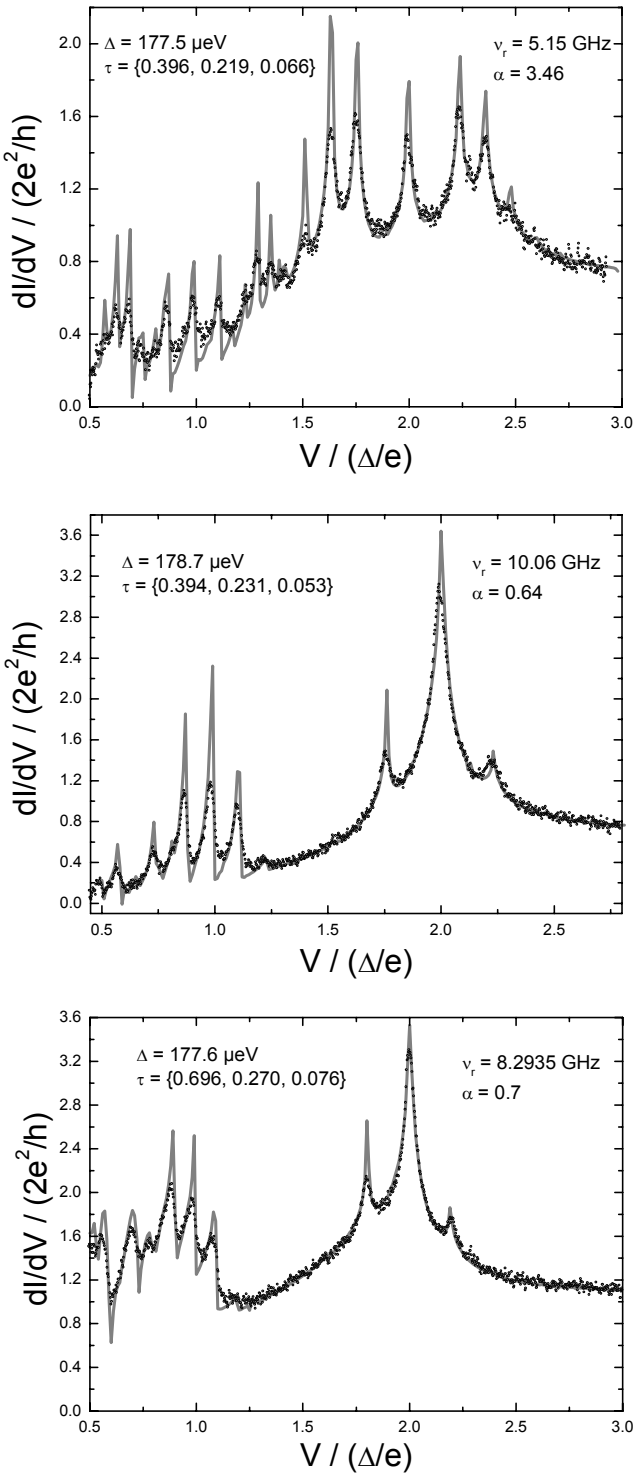

Figure 33: Differential conductance measured as a function of the voltage for three different contacts in presence of a microwave drive of frequency 5.15, 10.06 and 8.2935 GHz. Black dots are the experimental results. The underlying gray lines are the predictions of the theory of photon assisted multiple Andreev reflections (for a perfectly voltage biased contact), in which we have plugged the independently measured transmissions of the contact.

The agreement with the theory is only semi quantitative. We can attribute the rounding observed on the experimental results to both technical and physical reasons:

- The measurement: the ac excitation for the measurement of the differential conductance was $\sim 10^{-2}\,\Delta/e$. The measured dI/dV cannot resolve details of smaller width.
- The full microscopic calculation assumes a perfectly voltage biased contact. This is not achieved in reality, as seen for the Shapiro resonances. The fluctuations of the bias voltage result in a broadening of the PAMAR structure, a feature that the present state of the theory cannot account for.

In the next section we analyze in detail the features that can be observed on the three graphs of Figure 33. In particular, we focus on the peaks and side peaks (satellites) appearing around the voltage threshold of the MAR of order n given by $V_n = 2\Delta/(ne)$. The side peaks correspond to the absorption or emission of one or several photons during the charge transfer process.

5.2 General features of the PAMAR current

Figure 34 shows two IV measured on a contact with mesoscopic pin code $\tau = \{0.396, 0.219, 0.066\}$ to illustrate the effect of the microwaves on the background current. In absence of microwaves, the voltage thresholds at which the current suddenly increase are $V_n = 2\Delta/(ne)$. They correspond to the onset of a MAR process of order n. In presence of microwaves, the MAR current is modified as shown on Figure 34. Figure 35, Figure 36 and Figure 37 show the differential conductance as a function of the voltage. The voltage thresholds appear as a peak on the dI/dV. In presence of microwave, they are replicated.

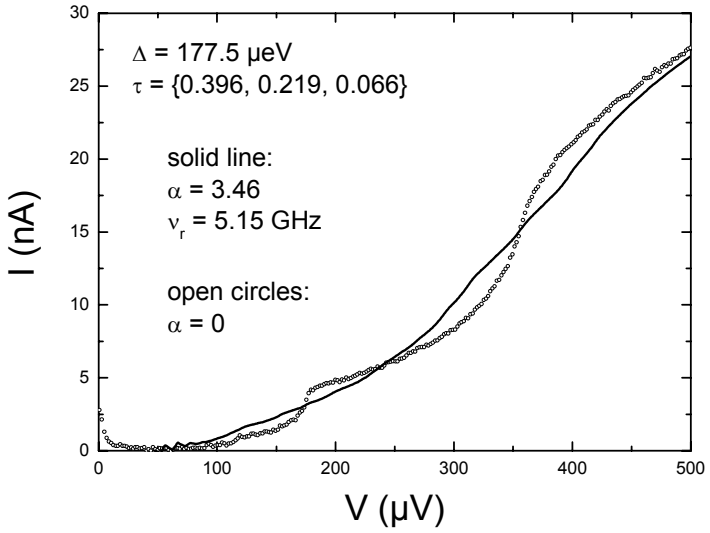

Figure 34: Experimental comparison of the MAR current (open dots) with the PAMAR current (solid line) when microwaves are switched on.

The condition for a PAMAR process of order n involving m photons to occur is:

$$eV = \frac{2\Delta}{n} \pm \frac{mh\nu_r}{n}$$

The minus (resp. plus) sign correspond to the absorption (resp. stimulated emission) of m photons, each of energy $h\nu_r$ during the charge transfer process. On the IV characteristic, the distance between the center peaks and its satellites is given by the quantity

$$\frac{mh\nu_r}{ne} \tag{27}$$

where m is the number of photons absorbed or emitted and n is the order of the MAR process (i. e. the total number of electronic charges transferred, see e.g. Figure 32). In the next subsections, this is illustrated for PAMAR of order 1, 2 and 3.

5.2.1 PAMAR of order 1

Figure 35 shows the side peaks around $V_1 = 2\Delta/e$. The case $n = 1$ is specific since it doesn't involve any Andreev reflection in the coupling structure. It corresponds to the tunneling of a single electron from an occupied state at energy $-\Delta$ to an empty state at energy $+\Delta$. Processes of assisted tunneling with one ($m = 1$) and two ($m = 2$) photons are visible. The solid line on Figure 35 is the theoretical prediction of the calculation presented in section 3.1.2. Note the normalization factor $h\nu_r/e$ on the horizontal axis in order to clearly exhibit the fractions m/n of expression (27).

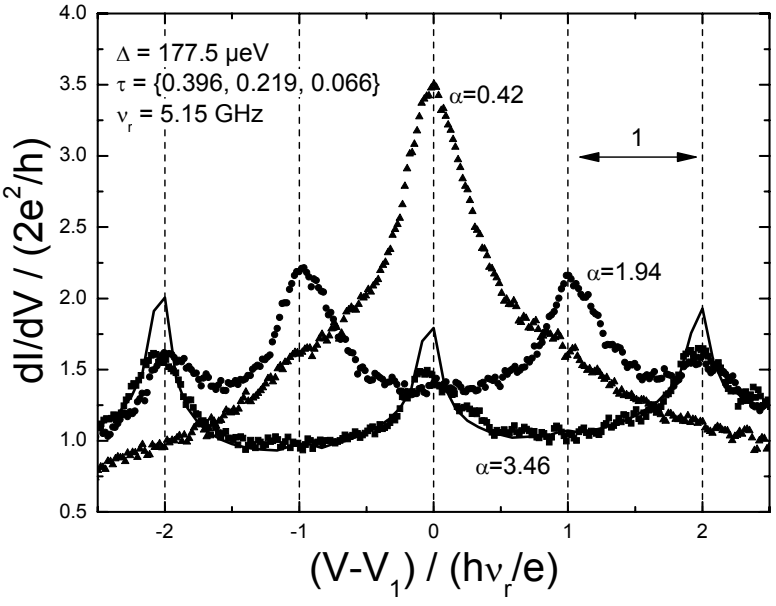

Figure 35: Dots: measured differential conductance around $V_1 = 2\Delta/e$ of an atomic contact for three different values of the microwave power. Solid line: theory for $\alpha = 3.46$. The satellite peaks correspond to photon assisted tunneling of a single electron.

5.2.2 PAMAR of order 2

Figure 36 shows the side peaks around around $V_2 = 2\Delta/(2e)$. The processes involve one Andreev reflection during the charge transfer. The distances to the MAR

threshold voltage[3] in absence of microwaves are $mh\nu_r/2$. PAMAR involving one, two and three photons are visible.

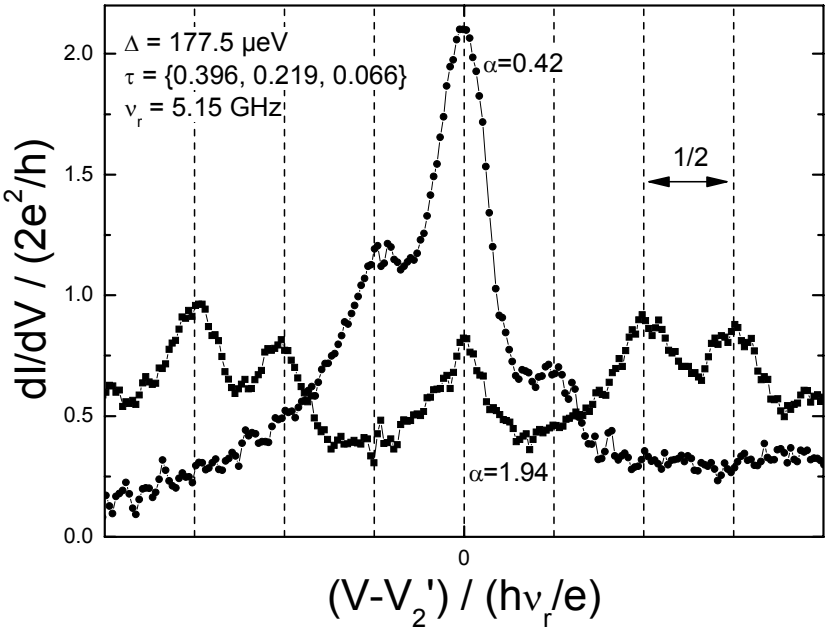

Figure 36: Measured differential conductance around $V_2' = 0.98 \times 2\Delta/(2e)$ of an atomic contact for two different values of the microwave power. The satellite peaks correspond to a single Andreev reflection assisted by one, two or three photon(s).

5.2.3 PAMAR of order 3

The next results correspond to processes involving two Andreev reflections. The satellite peaks appearing when the microwave is switched on are photon assisted processes involving a single photon. The offset voltage V_3' is close to the MAR threshold voltage $V_3 = 2\Delta/(3e)$: $V_3' = 0.98 \times V_3$ (see footnote 3).

---

[3] On Figure 36 the curves have been shifted by an offset V_2' close but different from the MAR threshold voltage $V_2 = 2\Delta/(2e)$. The reason is that the local maximum of the dI/dV without microwave occurs at a voltage $V_2' = 0.98 \times V_2$.

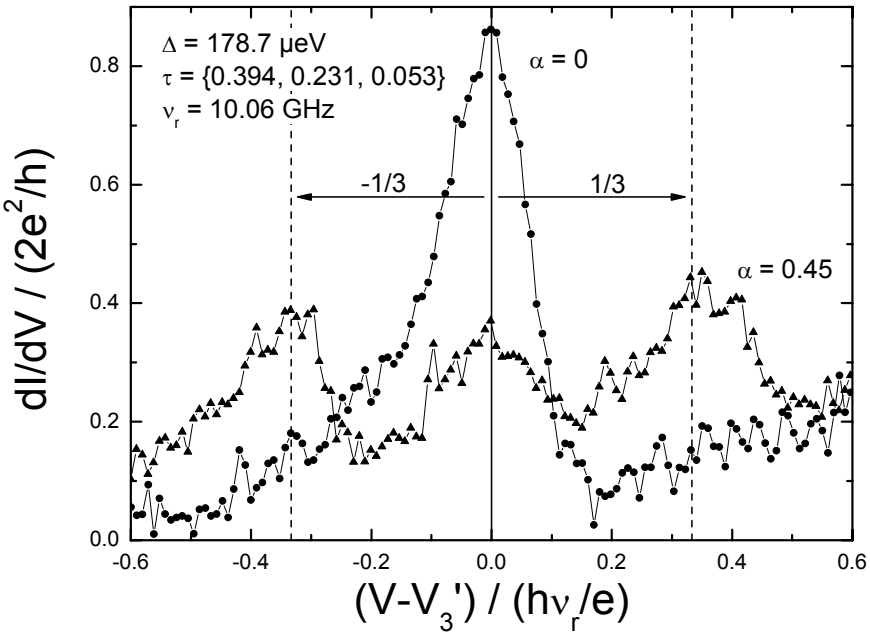

Figure 37: Measured differential conductance around $V_3' = 0.98 \times 2\Delta/(3e)$ of an atomic contact for two different values of the microwave power. The satellite peaks correspond to a charge transfer process involving two Andreev reflections, each one assisted by a single photon.

5.3 Frequency dependence of the satellite positions

We have checked that the distance between the center peak and the satellite peaks scales linearly with the frequency. This experiment is performed for the charge transfer process involving a single Andreev reflection. The satellite peaks on Figure 38 correspond to the absorption (left) or stimulated emission (right) of a single photon.

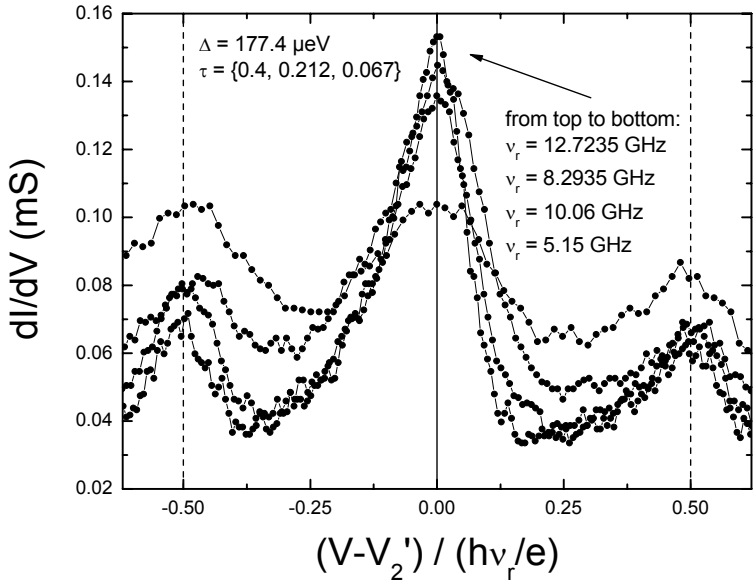

Figure 38: Differential conductance of an atomic contact around $V_2' = 0.98 \times 2\Delta/(2e)$ *at different microwave frequencies. The distance of the first satellite to the center peak scales linearly with the radiation frequency* ν_r*. The normalization factor* $h\nu_r/e$ *of the horizontal axis is different for each one of the four curves.*

Figure 39 shows a linear fit of the distance in voltage between the satellites and the center peak. The distance between the center peak and the first satellite for the charge transfer process involving a single Andreev reflection is $\Delta V = \frac{h\nu_r}{2e}$. The experimental result is in good agreement with this prediction.

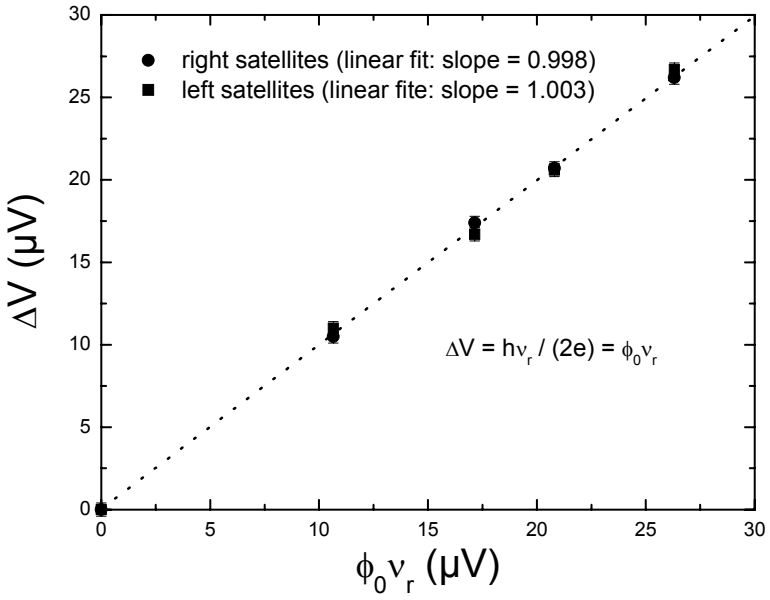

Figure 39: Linear fits of the distance between the satellites and the center peak for a charge transfer process, in presence of microwaves at the frequency ν_r, involving a single Andreev reflection.

6 Outlook

There is a lack of theory to describe the interplay between a microwave and the ac Josephson currents in contacts containing highly transmitting channels for the realistic case of an imperfect voltage bias.

As the transmissions go close to one, the Shapiro resonances superimpose on the PAMAR current. Because of the environment in which the contact is embedded, the Shapiro resonances acquire a finite width. Therefore, the separation of the current into a Shapiro resonance current and a PAMAR current is no longer possible like in the perfectly voltage biased case, since both contributions completely mix one with each other.

This effect was already pointed out in chapter 2 concerning the supercurrent peak of highly transmitting channels. At low voltages, the MAR and supercurrent contributions to the total dc current are indistinguishable.

A. L. Yeyati carried out a calculation showing the smooth transition from supercurrent into MAR current for an atomic contact embedded in an ohmic environment at finite temperature (chapter 2 section 2.3). The input of this self-consistent calculation were the current components (see equation (3)) obtained from a microscopic approach [12] for a perfectly voltage biased contact.

A similar calculation should be possible to account for the Shapiro resonances and the PAMAR current, when a microwave field is applied on the contact. The main difference is the set of current components used for the input of the self-consistent calculation. Instead of taking the current components calculated for a constant voltage bias, one should consider the current components, when in addition to the dc voltage bias, a microwave voltage is superimposed. These current components (see equation (23)) were already calculated by J. C. Cuevas *et al.* [7] in 2002. However the numerical evaluation of these current components is a time consuming task that prevented us from carrying out the self-consistent calculation. Such a calculation should predict the full IV characteristics of an atomic contact embedded in an ohmic environment and in presence of an external microwave.

References of chapter 3

[1] I. K. Yanson, V. M. Svistunov, and I. M. Dmitrenko, Zh. Eksp. Teor. Fiz. **48**, 976 (1965) translated in Sov. Phys. JETP **21**, 650 (1965).

[2] I. Giaever, Phys. Rev. Lett. **14**, 904 (1965).

[3] D. N. Langenberg et al., Phys. Rev. Lett. **15**, 294 (1965).

[4] D. N. Langenberg et al., Phys. Rev. Lett. **15**, 842 (1965).

[5] S. Shapiro, Phys. Rev. Lett. **11**, 80 (1963).

[6] L. D. Landau, Phys. Z. Sow. **2**, 46 (1932); C. Zener, Proc. R. Soc. London, Ser A **137**, 696 (1932).

[7] J. C. Cuevas *et al.*, Phys. Rev. Lett. **88**, 157001 (2002).

[8] E. Ben-Jacob and D. J. Bergman, Phys. Rev. A **29**, 2021 (1984).

[9] R. Duprat and A. L. Yeyati, Phys. Rev. B **71**, 54510 (2005).

[10] H. Risken, The Fokker-Planck Equation (Springer-Verlag, Berlin, 1989).

[11] D. Averin and A. Bardas, Phys. Rev. B **53**, R1705 (1996).

[12] J. C. Cuevas, A. Martín-Rodero, and A. Levy Yeyati, Phys. Rev. B **54**, 7366 (1996).

[13] R. P. Welty and J. M. Martinis, IEEE Trans. Magn. **27**, 2924 (1991).

[14] M. E. Huber *et al.*, Appl. Supercond. **5**, 425 (1998).

[15] A. Steinbach *et al.*, Phys. Rev. Lett. **87**, 137003 (2001).

[16] A. H. Dayem and R. J. Martin, Phys. Rev. Lett. **8**, 246 (1962).

[17] Ivar Giaever, Phys. Rev. Lett. **14**, 904 (1965).

[18] P. E. Gregers-Hansen *et al*., Phys. Rev. Lett. **31**, 524 (1973).

[19] O. H. Soerensen *et al.* Phys. Rev. B **9**, 3746 (1974).

[20] P. K. Tien and J. P. Gordon, Phys. Rev. **129**, 647 (1963).

Chapter 4: Direct measurements of the current-phase relation of a Josephson weak link

1 Introduction

We have seen in chapters 2 and 3 that the supercurrent and the Shapiro resonances do not give full access to the current phase relation of a Josephson weak link.

The aim of this chapter is to present two methods for investigating more directly the current phase relation of superconducting atomic size contacts.

As shown in chapter 1, in a single channel Josephson weak link, the supercurrent is carried by two Andreev bound states with phase dependent energies E_+ and E_-. These two bound states carry opposite currents:

$$I_{\pm}(\delta, \tau) = \frac{1}{\varphi_0}\frac{\partial E_{\pm}(\delta, \tau)}{\partial \delta} = \mp\frac{e\Delta}{2\hbar}\frac{\tau \sin(\delta)}{\sqrt{1-\tau \sin^2\left(\frac{\delta}{2}\right)}}.$$

Figure 1 shows the current carried by the ground Andreev bound state E_- as a function of the superconducting phase difference δ across the weak link. For channels with a transmission close to one, the current phase relation deviates from the well know sine function of the Josephson tunnel junction.

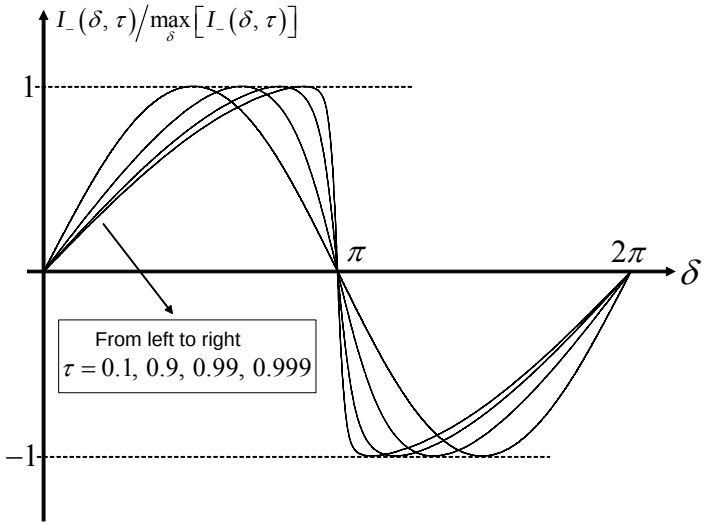

Figure 1: Current carried by the ground Andreev bound state E_- for different values of the channel transmission. For transmission close to one, the current phase relation deviates from the well known sine function of the Josephson tunnel junction. Each curve has been normalized by its respective critical current, $\max_\delta\left[I_-(\delta,\tau)\right]$.

For an arbitrary multichannel Josephson weak link characterized by its mesoscopic pin code $\{\tau\} = \{\tau_1, \tau_2, ..., \tau_N\}$, the current phase relationship is given, by:

$$I(\delta,\{\tau\}) = \sum_{i=1}^{N}\left[n_+^i I_+(\delta,\tau_i) + n_-^i I_-(\delta,\tau_i)\right] \qquad (1)$$

where n_+^i and n_-^i are the occupation numbers of the upper and lower Andreev bound state in the *i*-th channel respectively. n_+^i and n_-^i can take either the values 0 or 1 (see chapter 2, paragraph 1). At thermal equilibrium, $n_+^i = \overline{n_+^i}$ and $n_-^i = \overline{n_-^i}$, and the thermal equilibrium current phase relation is then:

$$\overline{I(\delta,\{\tau\},T)} = \sum_{i=1}^{N}\left[\overline{n_+^i} I_+(\delta,\tau_i) + \overline{n_-^i} I_-(\delta,\tau_i)\right]$$

The expression of $\overline{n_\pm^i}$ is given in the paragraph 1 of chapter 2.

For the sake of clarity and simplicity, we adopt the following notations to refer to the different expressions of the current phase relation that will be used throughout this chapter:

$$I_c(\delta) = \overline{I(\delta, \{\tau\}, T)} \tag{2}$$

$$I_c^-(\delta) = \sum_{i=1}^{N} I_-(\delta, \tau_i) \tag{3}$$

Equation (2) is the thermal average of the contribution of the Andreev states of each channel to the total current. Equation (3) assumes that only the lower Andreev bound state of each channel is occupied.

In the previous experiments presented throughout this thesis, the atomic contact was either voltage biased or current biased. However, in order to measure a current phase relation one should phase bias the atomic contact and measure the current flowing through it.
This was already performed in an experiment by M. C. Koops *et al.* [1], where they inserted an atomic contact in a superconducting ring. However, in their setup, the set of transmissions of the contact could not be measured, which prevented a comparison with equation (1).

To measure, for a given contact, both the current phase relationship and the transmissions, the challenge is to find a setup that enables the contact to be reversibly phase biased or voltage biased. The latter situation allows to extract the mesoscopic pin code of the contact from the measurement of its IV characteristic.

The solution that we propose is to place the atomic contact in parallel with a large Josephson tunnel junction which will act like a reversible superconducting switch. This is largely inspired from the Quantronium QUBIT setup [2]. We thus form an unbalanced SQUID, as represented on Figure 2. The tunnel junction is designed so that its critical current I_t^0 is one order of magnitude larger than the critical current of a typical aluminum atomic contact I_c^0.

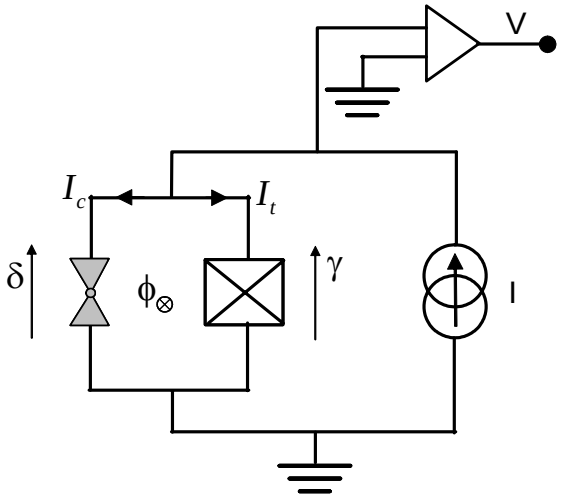

Figure 2: The atomic contact (double triangle symbol) is placed in parallel with a large Josephson tunnel junction (crossed box). δ and γ are the superconducting phase differences across the atomic contact and the Josephson tunnel junction respectively. ϕ is the magnetic flux enclosed by the SQUID.

As long as the current I_t in the Josephson tunnel junction is smaller than its critical current, it is possible to phase bias the atomic contact by applying a magnetic flux through the loop of the SQUID. Once the current exceeds its critical current, the tunnel junction switches to a finite voltage state, which enables us to measure the IV characteristic of the SQUID. We can then obtain the IV characteristic of the contact by subtracting the contribution of the tunnel junction, which can be accurately calibrated by fully opening the contact.

In the following sections, we present the two methods that we have used to investigate the current phase relation of atomic contacts with this SQUID device. We first start by presenting the method we have used to measure the mesoscopic pin code of the atomic contact shunted by the large Josephson tunnel junction.

2 Determination of the mesoscopic pin code of the contact

The *IV* characteristic of the tunnel junction alone is first measured after opening completely the contact. It is presented on Figure 3.

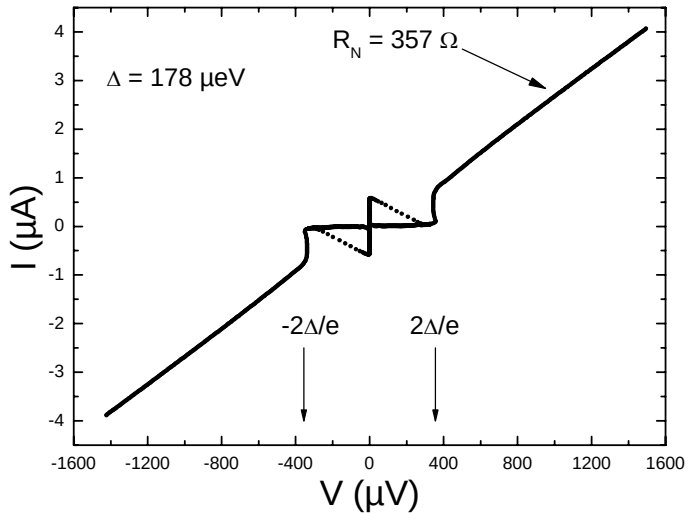

Figure 3: IV characteristic of the tunnel junction alone measured at 26 mK. Note the supercurrent branch at zero voltage.

The critical current of the junction can be determined by the Ambegaokar Baratoff relation (see chapter 2) using the value of the superconducting gap determined on Figure 3:

$$I_t^0(T) = \frac{\pi\Delta(T)}{2eR_N}\tanh\left(\frac{\Delta(T)}{2k_BT}\right), \qquad (4)$$

where R_N is the normal state resistance of the tunnel junction, and $\Delta(T)$ the superconducting gap[1] [3]. This value is consistent with the switching measurements of

[1] Throughout all this chapter, the reduction of the superconducting gap with temperature is taken into account because experiments at temperatures of the order of half the critical temperature of aluminum ($\Delta(T=0) = 178\ \mu\text{eV}$, $T_{critical} = 1.17\ \text{K}$) are carried out.

the tunnel junction alone, from which we extracted [4, 5] a critical current $I_t^0(T=0)$ of 750 nA. We attribute this discrepancy to non-thermal spurious noise which was not included in the model used to extract $I_t^0(T=0)$ from the switching measurements. Throughout this chapter, the finite temperature critical current $I_t^0(T)$ of the Josephson tunnel junction is calculated with the Ambegaokar Baratoff relation, taking $I_t^0(T=0)=750$ nA .

Figure 4 shows an IV characteristic of the SQUID formed by the tunnel junction and a one atom contact. It looks very similar to the IV of the tunnel junction alone because the current flowing in the contact is much smaller than the current in the junction. The IV characteristic of the contact is then obtained by subtracting from the one of the SQUID the contribution of the tunnel junction.

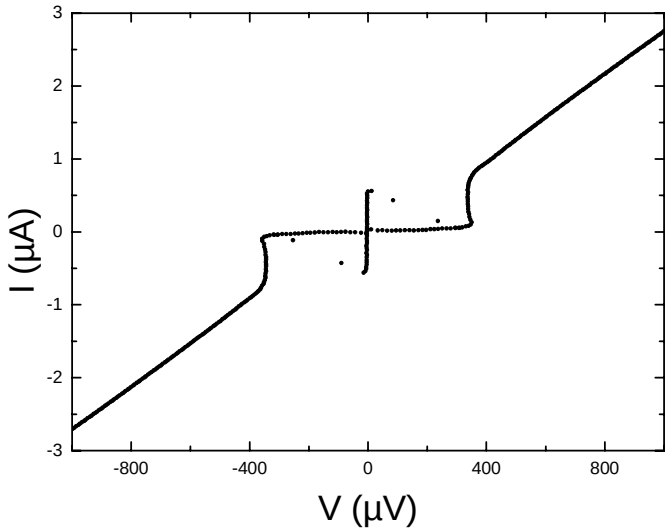

Figure 4: IV characteristic of an atomic contact SQUID.

After subtracting the contribution of the tunnel junction from the IV characteristic of the SQUID, one is left with the IV characteristic of the contact, shown on Figure 5.

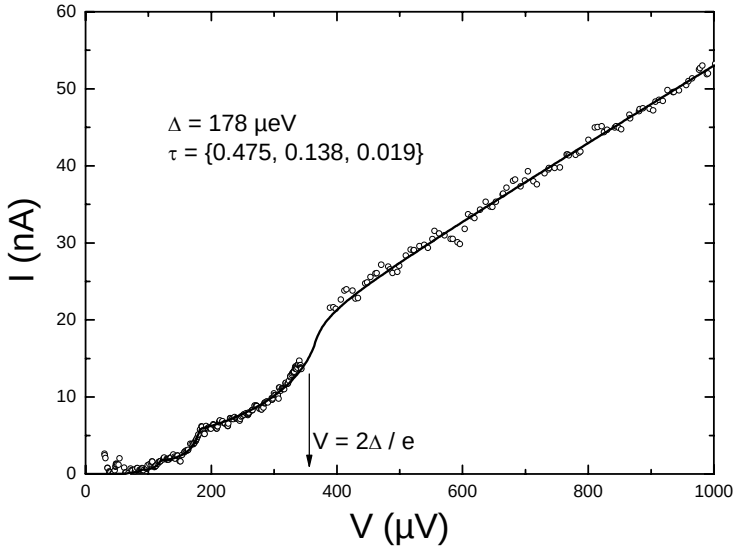

Figure 5: IV characteristic of the atomic contact after subtracting the contribution of the tunnel junction to the total current in the SQUID. The solid line is the fit with the MAR theory. The arrow pointing to $V = 2\Delta/e$ indicates the voltage around which experimental points had to be removed before performing the fit of the transmissions (see text).

A few experimental points around $2\Delta/e$ (see arrow on Figure 5) had to be removed to perform the fit because of the particular shape of the *IV* characteristic of the tunnel junction at the gap discontinuity. We attribute this peculiar non-monotonous behavior to heating effects that lower the value of the gap as the current is increased.

The *IV* characteristic of the contact is then fitted using the procedure described in chapter 5 to obtain the mesoscopic pin code of the contact. Because of the noise on the *IV* characteristic of the junction, the fit is less accurate that what was achieved in the experiments described in chapters 2 and 3, where the current through the contact was directly measured.

3 Two methods of investigation of the current-phase relation

The first method provides directly the current-phase relation, and is based on the measurement of the SQUID switching current as a function of the external magnetic flux threading it.

The second method is a measurement of the Josephson inductance of the contact, a quantity simply inversely proportional to the phase derivative of the current-phase relation. This measurement involves a small microwave excitation of the phase across the contact, and the measurement of the signal reflected by the SQUID.

3.1 Switching method

A schematic representation of the experimental setup is presented on Figure 6. In the experiments, a current ramp I is applied through the SQUID with the current source. After amplification, the voltage across the SQUID is fed into a timer which is triggered above a threshold value. The timer measures the elapsed time between the beginning of the ramp and the onset of the voltage across the SQUID, which gives access to the switching current. Thousands of switching events are recorded for each value of the magnetic flux ϕ to have enough statistics on the switching process and determine the mean switching current with a good accuracy. The detailed wiring can be found in section 6. For more details on the operation of the timers, we refer the reader to chapter 2. The bias tee represented on Figure 6 (ac and dc inputs) isolates galvanically the resistor R from the SQUID, which is therefore not shunted at dc, a basic requirement to measure switching. However, at finite frequencies, and especially at its plasma frequency, the SQUID sees a dissipation fixed by the combination of r and R, that ensures an overdamped dynamics of the phase. We recall that the small resistor r represents the on-chip dissipation.

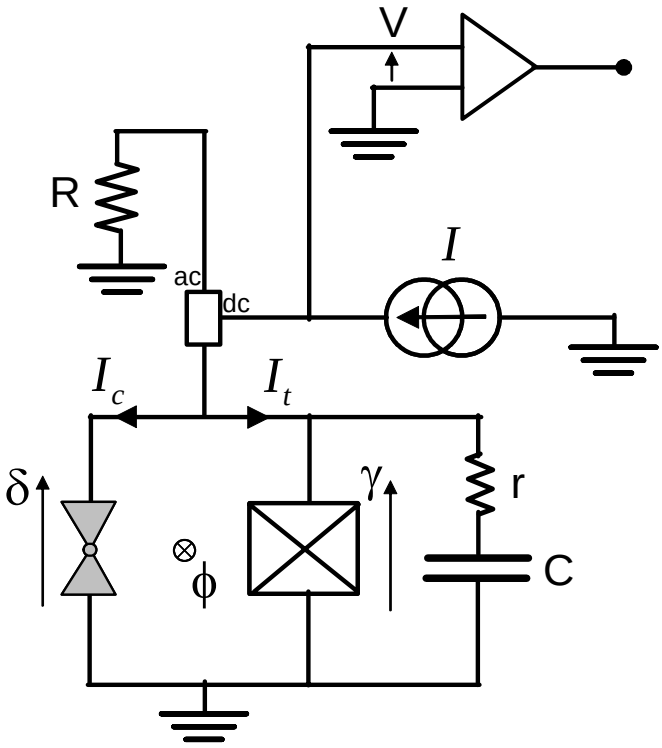

Figure 6: Schematic representation of the circuit used to measure the switching current of the atomic SQUID. The atomic contact (double triangle symbol) is placed in parallel with a large Josephson tunnel junction (crossed box). δ and γ are the superconducting phase differences across the atomic contact and the Josephson tunnel junction respectively. ϕ is the magnetic flux enclosed by the SQUID. The SQUID is shunted on-chip by a large capacitor. The bias tee (rectangle with dc and ac inputs) isolates galvanically the resistor R from the SQUID, so that it is not shunted at dc. However, at finite frequency the SQUID sees a dissipation fixed by the combination of r and R. The small resistor r represents the on-chip dissipation.

The total dc current through the SQUID is the sum of the current in the tunnel junction and the current in the atomic contact:

$$I = I_t + I_c = I_t^0 \sin(\gamma) + I_c^-(\delta) \tag{5}$$

where I_t^0 is the critical current of the Josephson tunnel junction and $I_c^-(\delta)$ the current phase relation of the atomic contact that one wishes to measure, assuming that only the lower Andreev levels are occupied.

The superconducting phase differences γ and δ are related by the quantization of the magnetic flux in the superconducting loop formed by the SQUID:

$$2\pi\frac{\phi}{\phi_0} = \delta - \gamma \pmod{2\pi} \tag{6}$$

where ϕ is the magnetic flux enclosed in the superconducting ring[2], and $\phi_0 = h/(2e)$ is the flux quantum. Therefore, equation (5) rewrites:

$$I = I_t + I_c = I_t^0 \sin(\gamma) + I_c^- (2\pi\phi/\phi_0 + \gamma) \tag{7}$$

The critical current I^0 of the SQUID is the largest value of the bias current I for which equation (7) has a solution. Because the critical current of the Josephson tunnel junction is one order of magnitude larger than the critical current of the atomic contact, the critical current of the SQUID is reached for a value of the phase γ_S lower but very close to $\pi/2$. The critical current of the SQUID therefore writes:

$$I^0(\phi) \approx I_t^0 + I_c^- (2\pi\phi/\phi_0 + \pi/2)$$

The magnetic flux ϕ modulates the SQUID critical current I^0 around the critical current of the tunnel junction, I_t^0. This modulation writes $\delta I^0(\phi) = I^0(\phi) - I_t^0$.

---

[2] ϕ differs from the external applied flux ϕ_a by the screening flux of the superconducting loop. However, the geometric inductance of the $3\times 3\ (\mu\text{m})^2$ superconducting loop is very small ($L \approx 30$ pH). Assuming this geometric inductance to be equally distributed on the two arms of the SQUID, an upper bound for the screening flux is $L/2\left(I_c^0 + I_t^0\right) \approx 0.6\%\ \phi_0$, taking $I_c^0 = 50$ nA and $I_t^0 = 750$ nA. Therefore $\phi \approx \phi_a$.

The current-phase relation $I_c(\delta)$ of the atomic contact can therefore be obtained from $\delta I^0(\phi)$ using the following identities:

$$\begin{cases} I_c^-(\delta) = \delta I^0(\phi) \\ \delta(\phi) \approx 2\pi\phi/\phi_0 + \pi/2 \end{cases}$$

This analysis assumes that there are no fluctuations (thermal or quantum) in the system. However, experiments are performed at finite temperature, in which case the critical current of the SQUID is never reached. The quantity amenable to measurement in the experiments is actually the switching current of the SQUID.

The switching of the SQUID is a stochastic process whose rate increases when the ratio I/I^0 gets closer to unity. The switching current is always smaller than the critical current. Only at zero temperature, in absence of any fluctuations, the switching current equals the critical current.

The quantity deduced from the experiments is therefore not $\delta I^0(\phi)$ but rather $\delta I^S(\phi)$, the modulation of the SQUID switching current with the magnetic flux ϕ. Because of the fluctuations, the amplitude of the modulation $\delta I^S(\phi)$ is smaller than the critical current of the atomic contact. Figure 7 shows the comparison between the zero temperature current-phase relation for two contacts, as calculated from their pin code, and the measured modulations $\delta I^S(\phi)$.

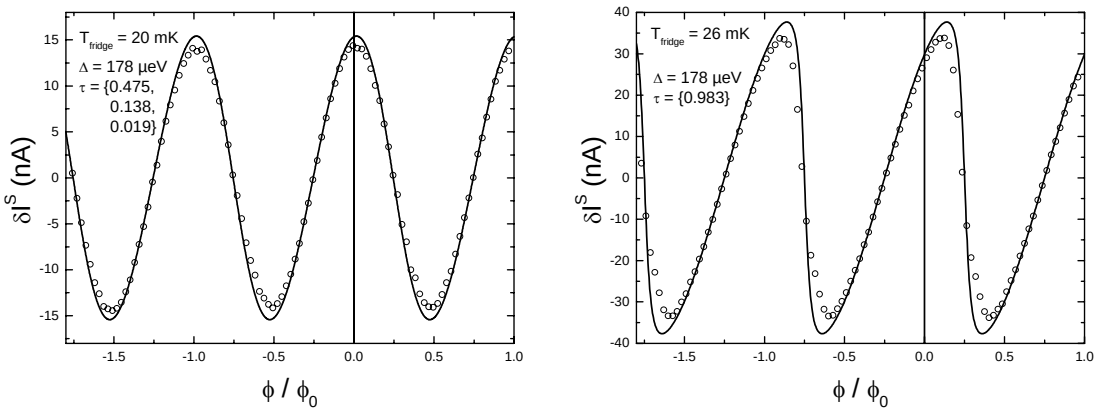

Figure 7: Open circles: measured modulation of the switching current of the SQUID due to the atomic contact. The solid line is the zero temperature current phase relation calculated with the mesoscopic pin code fitted from the IV of the contact.

On the left panel of Figure 7, the measured modulation is nearly sinusoidal because the contact doesn't contain channels with high transmission. On the right panel of Figure 7, the modulation is clearly anharmonic. This particular contact contains indeed a single conduction channel of transmission close to one. The amplitude of the modulations are smaller than the critical currents of the atomic contacts, due to fluctuations of the phase across the contacts.

In section 4, we present a theory taking into account the thermal fluctuations which predicts the variations of the switching current of the SQUID both as a function of magnetic flux and of temperature.

3.2 Microwave reflectometry

The second experimental strategy that we have implemented is based on the measurement of the Josephson inductance of the SQUID device. As shown in chapter 1 and 2, any Josephson weak link behaves as a non-linear inductor. In a conduction channel of transmission τ, each Andreev bound state is characterized by an inductance given by:

$$L_{\pm}(\delta,\tau)=\frac{\varphi_0}{dI_{\pm}(\delta,\tau)/d\delta}=\frac{{\varphi_0}^2}{d^2E_{\pm}(\delta,\tau)/d\delta^2},$$

Here, L_+ (respectively L_-) is the inductance of the system when it is in the upper (respectively lower) Andreev bound state of energy E_+ (respectively E_-). In a contact containing N channels, the contributions to the total admittance simply add up to build up the inverse inductance of the contact, according to:

$$L^{-1}(\delta,\{\tau\})=\sum_{i=1}^{N}\left[n_+^i L_+^{-1}(\delta,\tau_i)+n_-^i L_-^{-1}(\delta,\tau_i)\right]$$

It is convenient to deal with admittances since a Josephson weak link is a parallel combination of independent conduction channels.

Like for the current phase relation at finite temperature T, the thermal equilibrium value of the inductance is given by:

$$\overline{L^{-1}(\delta,\{\tau\},T)}=\sum_{i=1}^{N}\left[\overline{n_+^i}L_+^{-1}(\delta,\tau_i)+\overline{n_-^i}L_-^{-1}(\delta,\tau_i)\right],$$

The expression of $\overline{n_\pm^i}$ is given in section 1 of chapter 2.

Like for the current phase relation, we simplify the notations that we use throughout this chapter to refer to the Josephson inductance of the contact:

$$L_c^{-1}(\delta)=\overline{L^{-1}(\delta,\{\tau\},T)} \tag{8}$$

$$L_c^{--1}(\delta)=\sum_{i=1}^{N}L_-^{-1}(\delta,\tau_i) \tag{9}$$

$L_c^{-1}(\delta)$ given by Equation (8) is the inverse of the thermal averaged inductance of an atomic contact at temperature T. $L_c^{--1}(\delta)$ given by Equation (9) is the inverse of the

atomic contact inductance, assuming that in each channel, only the lower Andreev level is occupied.

The microwave reflectometry experiment probes the Josephson inductance of the contact. The key idea of this method is to form a microwave resonator between the Josephson tunnel junction and an on chip fabricated capacitor (see Figure 8). The atomic contact, in parallel with the tunnel junction, modulates the effective inductance of the resonator when a magnetic flux is applied through the superconducting loop. The reflection properties of the resonator are probed around its bare resonance frequency ν_r, defined as the resonance (or plasma) frequency of the *LC*-oscillator formed just by the tunnel junction and the capacitor, i.e. when the atomic contact is fully open and with no applied bias current I. The bare plasma frequency is given by:

$$\nu_r = \frac{1}{2\pi}\sqrt{\frac{I_t^0}{\varphi_0 C}}$$

The capacitor was designed for ν_r to be between 1 and 2 GHz, in the bandwidth of the available cryogenic microwave elements (bias-tee, directional coupler, circulators, amplifiers, … See section 6). The two parameters are $I_t^0 = 750$ nA and $C = 34$ pF, leading to a resonance frequency $\nu_r = 1.28$ GHz at $T = 0$. The value of the capacitor has been estimated from the surface of the pads, the thickness of the insulating polyimide layer and its dielectric constant (see chapter 5).

What is actually measured is the reflection coefficient R_ν of the resonator at the frequency ν as a function of the magnetic flux[3] ϕ and of the bias current I. Equation (7) shows that in the limit $I_t^0 \gg I_c^0$, the dc bias current I essentially changes the inductance of the Josephson tunnel junction whereas the magnetic flux essentially modifies the inductance of the atomic contact. To measure R_ν, a microwave signal of

[3] We recall that the magnetic flux enclosed by the superconducting loop ϕ is almost identical to the externally applied magnetic flux ϕ_a when the geometric inductance of the loop is negligible.

frequency $\nu \approx \nu_r$ is sent on the resonator and the reflected signal is monitored by a network analyzer.

The experimental setup that we have used for measuring the reflection coefficient R_ν is largely inspired from [6], and is presented on Figure 8. The detailed wiring can be found in section 6 (Figure 23). The microwave source of a vector network analyzer (internal impedance $50\ \Omega$) delivers an harmonic signal $V = V_0 \cos(2\pi\nu t)$ which is fed into a microwave directional coupler. The role of the directional coupler is to separate the signal reflected by the resonator from the incident signal. The incident microwave excitation is then fed into the ac input of a bias-tee whose output is connected to the resonator. The bias-tee fully isolates the dc and ac lines, and it is therefore possible to drive a dc current through the SQUID. The signal reflected by the resonator travels all the way back to the directional coupler, which directs it into the measurement port of the vector network analyzer. The vector network analyzer measures the reflection coefficient (modulus and phase):

$$R_\nu = \frac{V_r(\nu)}{V_i(\nu)} = \frac{V_r(\nu)}{V_0/2}.$$

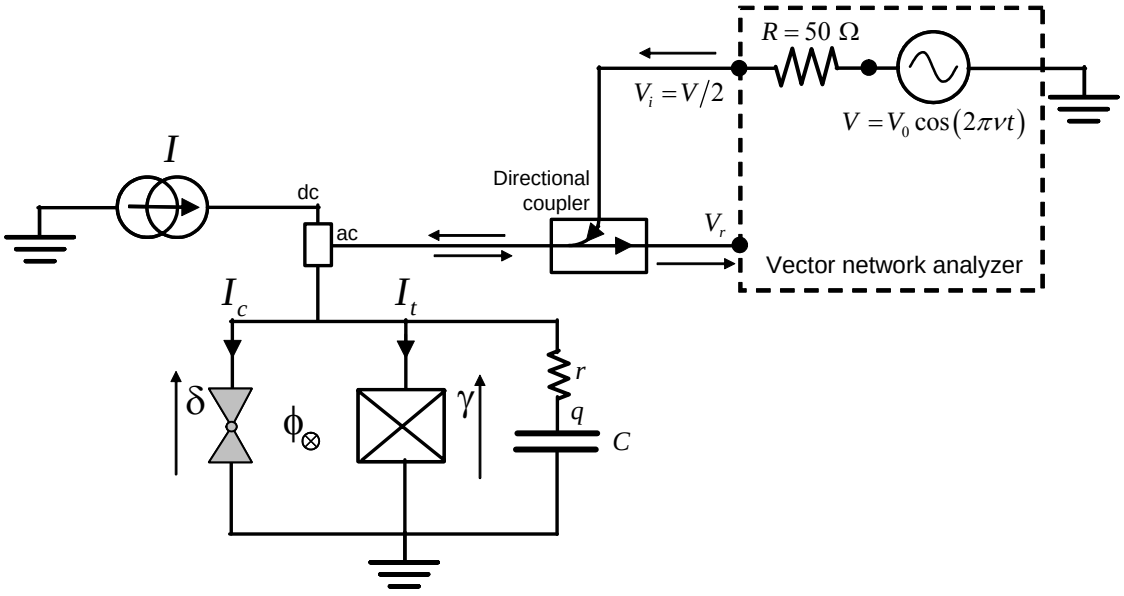

Figure 8: Schematic representation of the experimental setup used to measure the reflection coefficient of the resonator formed by the SQUID and the capacitor.

In the linear approximation, the reflection coefficient R_ν is simply given by:

$$R_\nu = \frac{Z_\nu - Z_0}{Z_\nu + Z_0} \tag{10}$$

with Z_0 the characteristic impedance of the microwave line connecting the sample ($Z_0 = 50\ \Omega$) to the source and the measurement apparatus, and Z_ν the impedance of the resonator given by:

$$\frac{1}{Z_\nu} = \frac{1}{jL_{tot}^{-}2\pi\nu} + \frac{jC2\pi\nu}{1 + jrC2\pi\nu} \tag{11}$$

where $L_{tot}^{-\,-1} = L_t^{-1} + L_c^{-1}$.

The Josephson inductance of the tunnel junction writes:

$$L_t(\gamma) = \frac{\varphi_0}{I_t^0 \cos(\gamma)} = \frac{\varphi_0}{I_t^0 \sqrt{1 - \left(\frac{I_t(\gamma)}{I_t^0}\right)^2}} \tag{12}$$

And the inductance of the contact, $L_c^{-}(\delta)$, is given by equation (9). Here we assume that only the lower Andreev level is occupied in each channel. Therefore, the effective inductance of the resonator is given, as a function of the two control parameters ϕ and I, by:

$$L_{tot}^{-\,-1}(\phi, I) = \frac{I_t^0}{\varphi_0}\sqrt{1 - \left(\frac{I - I_c^{-}(\delta(\phi, I))}{I_t^0}\right)^2} + \frac{1}{\varphi_0}\frac{\partial I_c^{-}}{\partial \delta}\bigg|_{\delta(\phi, I)} \tag{13}$$

where $\delta(\phi, I)$ is solution of the equation:

$$\delta = 2\pi\frac{\phi}{\phi_0} + \arcsin\left(\frac{I - I_c^{-}(\delta)}{I_t^0}\right) \tag{14}$$

As a zero order approximation one can neglect the current flowing in the contact branch. The phase across the contact then writes:

$$\delta(\phi, I) \approx 2\pi \frac{\phi}{\phi_0} + \arcsin\left(I/I_t^0\right) \tag{15}$$

This leads to a simplified expression for the effective inductance:

$$L_{tot}^{-1}(\phi, I) = \frac{I_t^0}{\varphi_0}\sqrt{1-\left(\frac{I}{I_t^0}\right)^2} + \frac{1}{\varphi_0}\frac{\partial I_c^-}{\partial \delta}\bigg|_{\delta = 2\pi\phi/\phi_0 + \arcsin\left(I/I_t^0\right)} \tag{16}$$

We now present results obtained on two different contacts for the modulus of the reflection coefficient as a function of the external magnetic flux and of the dc bias current (Figure 9 and Figure 10). In the setup shown on Figure 8, the bias tee (ac and dc inputs) isolates completely the ac and dc lines and enables us to drive a dc current through the SQUID while measuring the reflection properties of the resonator. The frequency of the microwave signal was $\nu = 1.24$ GHz for the two contacts we have investigated.

The full lines on Figure 9 and Figure 10 are the zero temperature theoretical predictions of equation (10). For the superconducting gap, we have taken $\Delta(T=0) = 178$ μeV. The only adjustable parameters were the values of the resistor $r = 0.57\ \Omega$ and of the capacitor $C = 33.7$ pF, in good agreement with the value expected from the geometry of the capacitor (34 pF). In the expression of the effective inductance of the resonator, we have taken for $\delta(\phi, I)$ the expression given by equation (15) but we have checked that it was almost identical to the solution of equation (14).

The absolute value of the measured reflection coefficient is calibrated by measuring it when the SQUID has switched and can therefore be characterized by its normal state resistance.

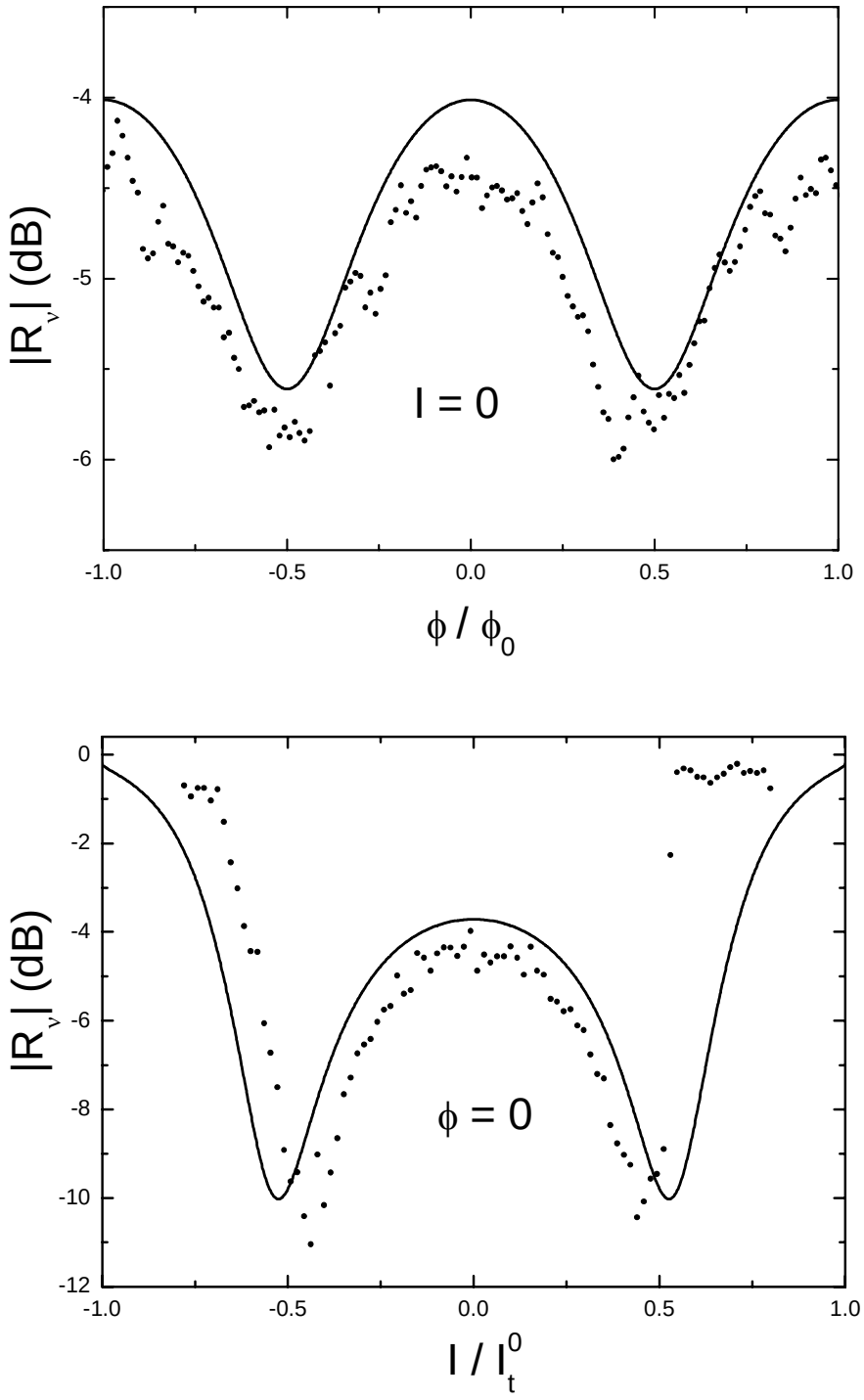

Figure 9: Modulus of the reflection coefficient R_ν for a contact with mesoscopic pin code $\tau = \{0.475, 0.138, 0.019\}$. The fridge temperature was 20 mK. Lower graph: modulus as a function of the dc bias current I at $\phi = 0$. Upper graph: modulus as a function of the external magnetic flux ϕ threading the loop at $I = 0$. Dots: experimental data. The full lines are the zero temperature theoretical predictions of equation (10).

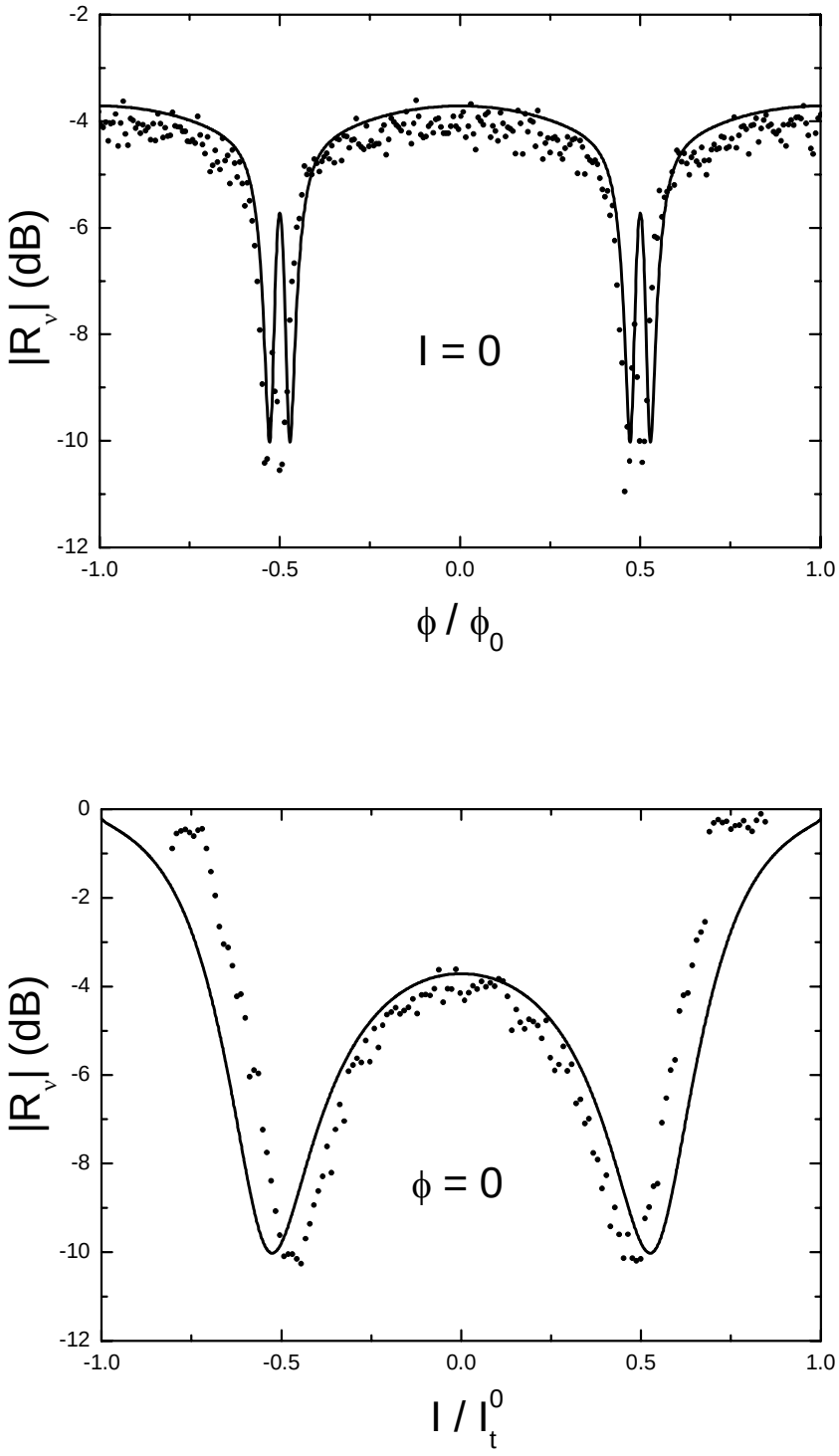

Figure 10: Modulus of the reflection coefficient for a contact with mesoscopic pin code $\tau = \{0.983\}$. *The fridge temperature was 26 mK. Lower graph: modulus as a function of the dc bias current* I *at* $\phi = 0$. *Upper graph: modulus as a function of the external magnetic flux* ϕ *threading the loop at* $I = 0$. *Dots: experimental data. The full lines are the zero temperature theoretical predictions of equation (10).*

The experimental results obtained at the base temperature of the fridge can be semi-quantitatively explained by the simple model we have just presented. We attribute the discrepancies to the anharmonicity of the oscillations of the phase, to thermal fluctuations and to transitions within each pair of Andreev levels. These three effects are studied in more details in section 5.

4 Switching at finite temperature

As seen in section 3.1, the thermal fluctuations of the phase reduce the modulation of the SQUID switching current. The goal of this section is to calculate the mean switching current of the SQUID as a function of the external magnetic flux, taking into account the thermal fluctuations of the phase across the contact.

4.1 Calculation of the SQUID mean switching current

As shown in chapter 2, the dynamics of the phase δ is equivalent to the motion of a particle in the so-called tilted washboard potential $U_{-}(\delta, I, \phi)$:

$$U_{-}(\delta, I, \phi) = \sum_{i=1}^{N} E_{-}(\delta, \tau_i) - \varphi_0 \left[I_t^0 \cos(\delta - 2\pi\phi/\phi_0) + I\delta \right]$$

The subscript "-" in $U_{-}(\delta, I, \phi)$ indicates that in each of the N channels of the atomic contact, only the lower Andreev bound state is occupied.

The SQUID is characterized by two degrees of freedom. However, because the geometric inductance of the loop can be neglected (see footnote 2), the two phases δ and γ are rigidly linked by equation (6) and the potential remains unidimensional, like in chapter 2 where only a single Josephson element was considered. On Figure 11, the potential $U_{-}(\delta, I = 0.4I_t^0, \phi = 0)$ is plotted for a SQUID with a single channel contact

of transmission 0.7. We have taken $I_t^0 = 750$ nA and $\Delta = 178$ μeV, which are the zero temperature values.

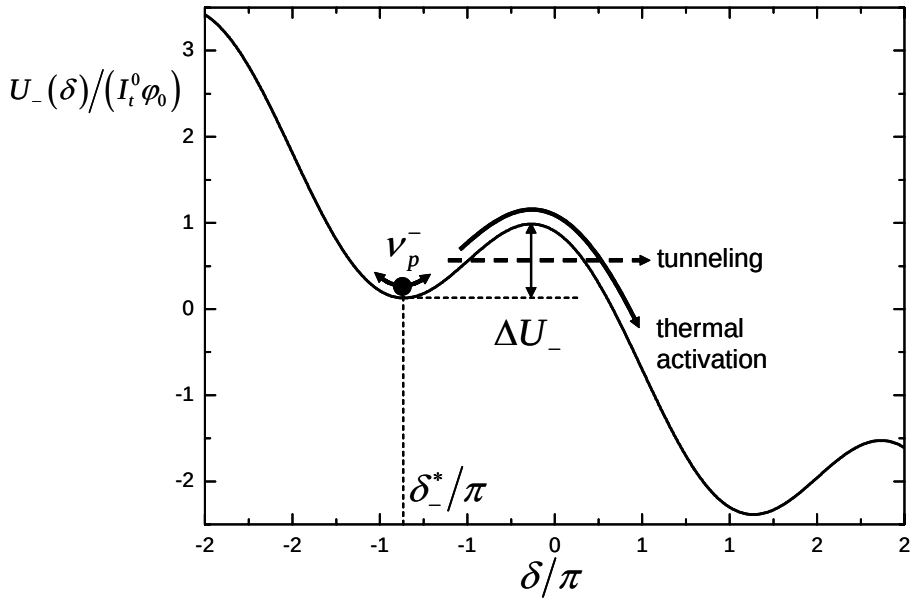

Figure 11: Tilted washboard potential of the SQUID assuming that only the lower Andreev bound state is populated.

The switching to a voltage state occurs when the fictitious particle escapes from the potential well and starts to runaway. In addition to thermal activation, escape from the well can also occur by quantum tunneling through the barrier. Tunneling is a process with no classical analog and has a rate which is temperature independent. Therefore, tunneling becomes predominant at low temperatures. In the low damping regime ($Q = \frac{R}{\sqrt{L_{tot}^-/C}} > 1$), it can be shown [4] that the crossover temperature from quantum to classical escape is $T_{co} = \hbar\omega_p^-/(2\pi k_B)$. In our experiments, $Q > 1$ and $T > T_{co}$. Therefore the predominant process is thermal activation out of the potential well. The rate of this process is given by:

$$\Gamma_-(I,\phi) = a_t \frac{\omega_p^-(I,\phi)}{2\pi} \exp\left(-\frac{\Delta U_-(I,\phi)}{k_B T}\right),$$

where $\Delta U_-(I,\phi)$ is the barrier height, and $\omega_p^-(I,\phi)/(2\pi)$ is the frequency of the plasma oscillations in the potential well. Both quantities are calculated numerically. The

plasma frequency is obtained from $\omega_p^-(I,\phi) = 1/\sqrt{L_{tot}^- C}$ with $L_{tot}^-(I,\phi) = \dfrac{{\varphi_0}^2}{\left.\dfrac{d^2U_-}{d\delta^2}\right|_{\delta=\delta_-^*}}$.

The prefactor a_t can be calculated exactly [7] and turns out to be of order unity. For simplicity, in the following, we will take $a_t = 1$.

The switching rate depends exponentially on the ratio of the barrier height to the thermal excitation energy. The barrier height ΔU_- depends on the bias current and on the external magnetic flux.

The probability W of switching during the time interval dt is $W = \Gamma_- dt$. In the experiment a current ramp $I(t) = \alpha t$ is applied through the SQUID starting at $t = 0$. In this configuration, we want to calculate the switching current I^S of the SQUID as a function of the external magnetic flux ϕ and temperature T.

The mean switching current I^S of the SQUID writes:

$$I^S = \int_0^\infty I \times e^{-\int_0^I \frac{\Gamma_-(I',\phi)}{\alpha} dI'} \times \frac{\Gamma_-(I,\phi)}{\alpha} dI ,$$

where $e^{-\int_0^I \frac{\Gamma_-(I',\phi)}{\alpha} dI'}$ is the probability that the SQUID has not switched in the current interval $[0, I]$, and $\dfrac{\Gamma_-(I,\phi)}{\alpha} dI$ the probability that it switches between I and $I + dI$.

4.2 Experimental results

We present experimental results obtained on two contacts with different mesoscopic pin codes and at different temperatures and compare with the theoretical predictions of section 4.1. The zero temperature critical current of the Josephson tunnel junction is $I_t^0 = 750$ nA and the zero temperature superconducting gap is $\Delta = 178$ μeV. In the theoretical predictions, the reduction of the gap with the temperature is taken into

account [3], as well as the temperature dependence of the tunnel junction critical current (see equation (4)).

Figure 12 and Figure 13 show, rather than the SQUID switching current itself I^S, the flux modulation of the SQUID switching current $\delta I^S(\phi) = I^S(\phi) - \overline{I^S}$, where $\overline{I^S}$ is the mean value of $I^S(\phi)$ taken over the magnetic flux. Because the SQUID is highly asymmetric ($I_t^0 \gg I_c^0$), its mean switching current $\overline{I^S}$ is very close to the switching current of the Josephson tunnel junction by itself I_t^S.

Figure 12 shows the modulation of the SQUID switching current when an atomic contact with mesoscopic pin code $\tau = \{0.475, 0.138, 0.019\}$ was formed.

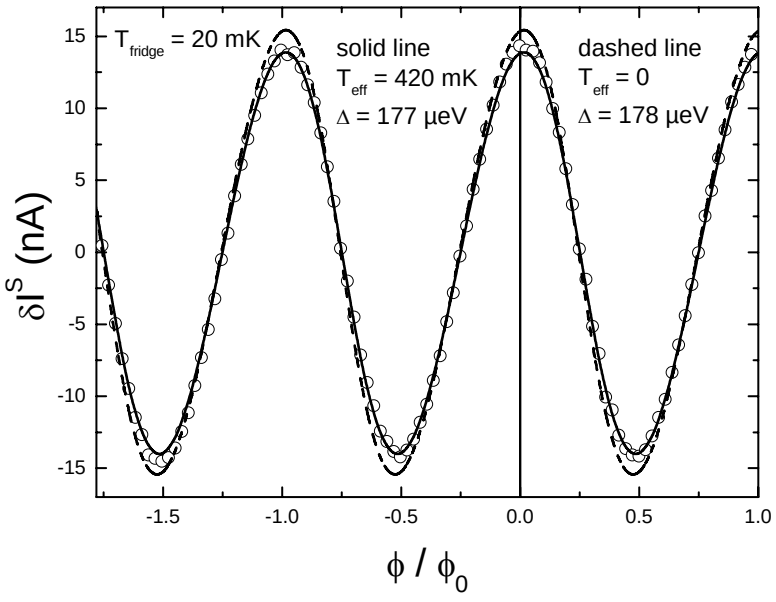

Figure 12: Modulation of the SQUID switching current as a function of the reduced magnetic flux threading the loop. The mesoscopic pin code of the atomic contact is $\tau = \{0.475, 0.138, 0.019\}$. Open circles: experimental results, the fridge temperature was 20 mK. Solid line: prediction of the theory presented in section 4.1 at an effective temperature of 420 mK. Dashed line: prediction of the zero temperature theory (presented in section 3.1).

The modulation of the SQUID switching current is sinusoidal because the atomic contact doesn't contain channels with high transmission. The data obtained in the experiments can be described by the theory of the switching presented in section 4.1 provided the effective noise temperature entering the theory is assumed to be 420 mK, well above the fridge temperature at which the experiments were carried out (20 mK).

Figure 13a shows the modulation of the SQUID switching current measured at different temperatures for an atomic contact with mesoscopic pin code $\tau = \{0.983\}$. As already mentioned, the modulation is not sinusoidal because of the high transmission of the channel (see Figure 1). As expected, the amplitude of modulation decreases with the temperature. Figure 13b, Figure 13c and Figure 13d present the experimental data with the predictions of the theory for each value of the temperature.

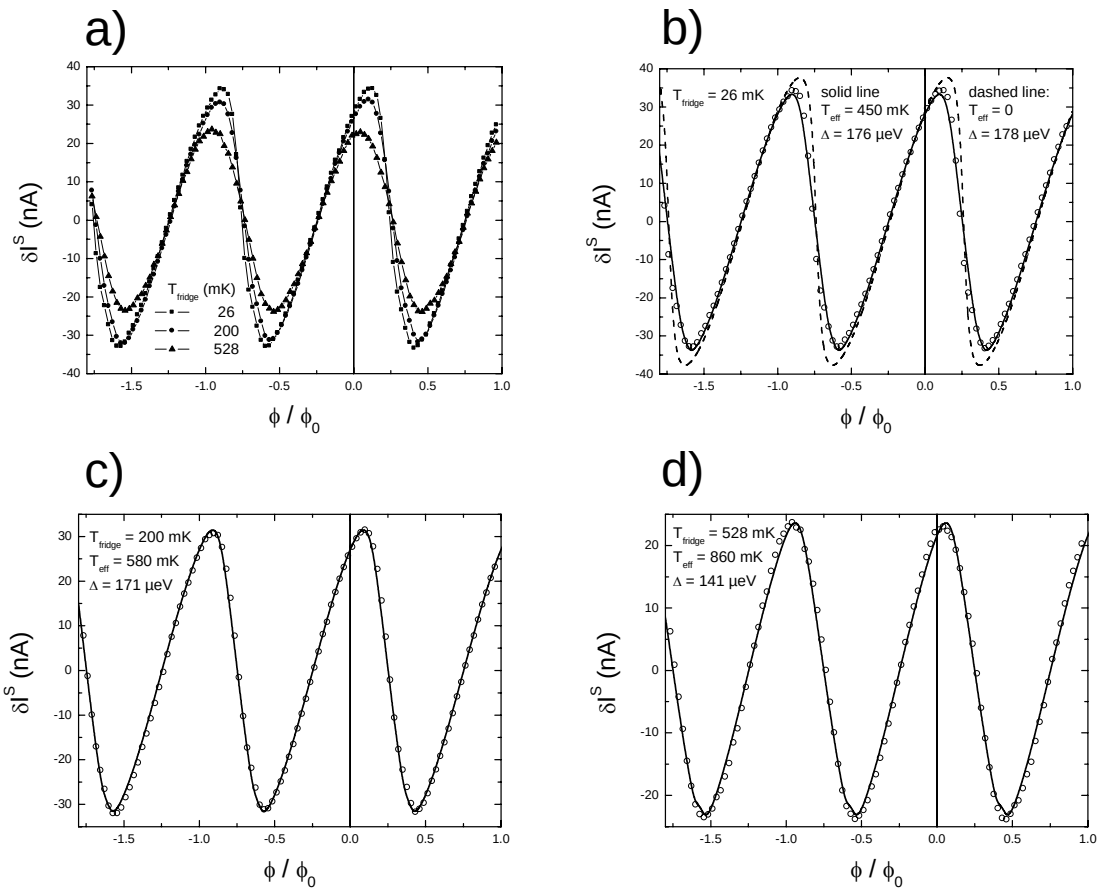

Figure 13: Contact with mesoscopic pin code $\tau = \{0.983\}$. *Symbols are experimental points. a) Measured modulation of the SQUID switching current for three different values of the fridge temperature (26, 200, 528 mK). b) Comparison of the experimental results at T = 26 mK with both the predictions of the zero temperature theory of section 3.1 (dashed line) and the predictions at 450 mK of the theory of section 4.1. (solid line). c) (resp. d)) Comparison of the experimental results at 200 mK (resp. 528 mK) with the predictions of the theory of section 4.1 at 580 mK (resp. 860 mK).*

Once again, the theory describes qualitatively the experimental data, but the temperatures entering the theory are well above the fridge temperature at which the experiments were performed. In fact, transitions between the lower and upper Andreev levels could play a major role on the measured mean switching current. In the following, we present a model aiming to account for the effect of these transitions.

4.3 Population of the Andreev levels in the atomic contact

If the system always stays in the lower Andreev bound state, its contribution to the total current through the Josephson tunnel junction is a smooth function of the phase difference across it. However, if there is a sudden transition to the upper Andreev level, the current in the Josephson tunnel junction changes abruptly, resulting in a drastic change of the switching rate.
This effect is completely ignored in the previous theoretical description.

The goal of this section is to extend the last model to take into account transitions to the upper Andreev level. Instead of describing the system by a single potential $U_-(\delta, I, \phi)$, assuming that the atomic contact stays in the lower Andreev level, the system is now described by a potential $U(n_+, n_-, \delta, I, \phi)$ which depends on the occupation numbers n_+ and n_- of the upper and lower Andreev levels respectively ($n_\pm = 0, 1$). Here we assume a single channel contact. The expressions of this potential is then:

$$U(n_+, n_-, \delta, I, \phi) = (n_+ - n_-)\Delta\sqrt{1-\tau\sin^2(\delta/2)} - \varphi_0 I_t^0 \cos(\delta - 2\pi\phi/\phi_0) - \varphi_0 I\delta \quad (17)$$

On Figure 14, we have represented the three following potentials for a single channel contact of transmission $\tau = 0.9$ for $I = 0.9I_t^0$ and $\phi = 0.1\phi_0$. For simplicity, we have adopted the following notations:

$$U_-(\delta, I, \phi) = U(n_+ = 0, n_- = 1, \delta, I, \phi)$$
$$U_+(\delta, I, \phi) = U(n_+ = 1, n_- = 0, \delta, I, \phi)$$
$$U_0(\delta, I, \phi) = U(n_+ = 0, n_- = 0, \delta, I, \phi) = U(n_+ = 1, n_- = 1, \delta, I, \phi)$$

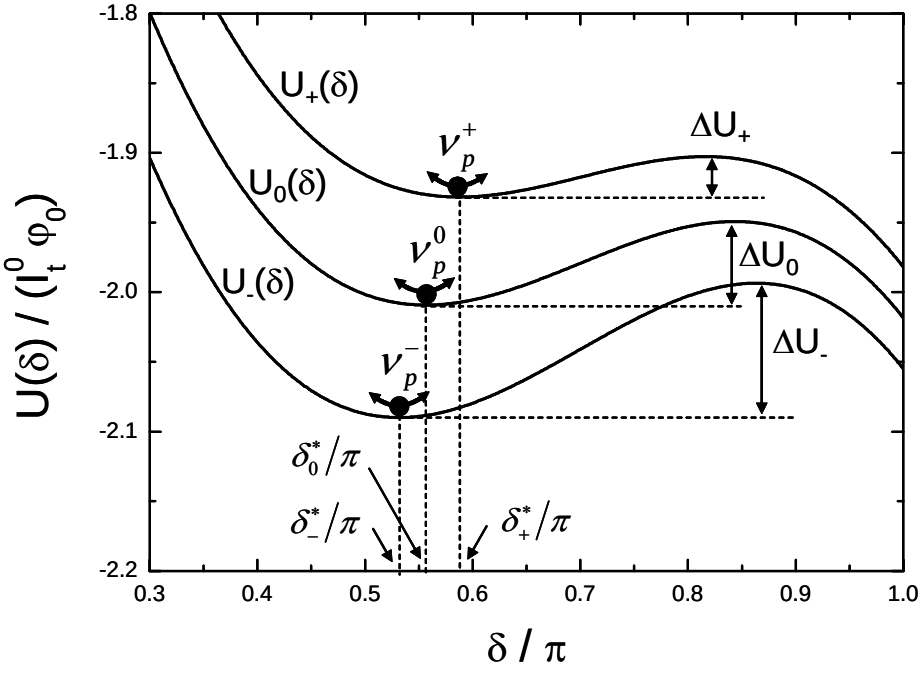

Figure 14: The three tilted washboard potentials $U_{\pm}\left(\delta,\, I = 0.9I_t^0,\, \phi = 0.1\phi_0\right)$ *and* $U_0\left(\delta,\, I = 0.9I_t^0,\, \phi = 0.1\phi_0\right)$.

The switching rate including these transitions between levels can then empirically be written as:

$$\Gamma\left(I,\,\phi\right) = \frac{1}{\Xi}\left(e^{-\beta U_-\left(\delta_-^*(I,\,\phi),\,I,\,\phi\right)}\Gamma_- + e^{-\beta U_+\left(\delta_+^*(I,\,\phi),\,I,\,\phi\right)}\Gamma_+ + 2e^{-\beta U_0\left(\delta_0^*(I,\,\phi),\,I,\,\phi\right)}\Gamma_0\right),$$

with the partition function $\Xi = \sum_{n_\pm = 0,\,1} e^{-\beta U\left(n_+,\,n_-,\,\delta^*(n_+,\,n_-,\,I,\,\phi),\,I,\,\phi\right)}$, where $\delta^*\left(n_+,\,n_-,\,I,\,\phi\right)$ is the value of the phase δ across the atomic contact which minimizes the total energy $U\left(n_+,\,n_-,\,\delta,\,I,\,\phi\right)$. For simplicity we have adopted the following notations (Figure 14):

$$\delta_-^*(I,\phi)=\delta^*(n_+=0,n_-=1,I,\phi)$$
$$\delta_+^*(I,\phi)=\delta^*(n_+=1,n_-=0,I,\phi)$$
$$\delta_0^*(I,\phi)=\delta^*(n_+=0,n_-=0,I,\phi)=\delta^*(n_+=1,n_-=1,I,\phi)=\arcsin\left(I/I_t^0\right)+2\pi\phi/\phi_0$$

Note that when no current is flowing through the atomic contact ($n_\pm=0$ or $n_\pm=1$), the expression of the phase difference $\delta^*(n_+,n_-,I,\phi)$ is analytical.

Γ_- (resp. Γ_+, Γ_0) is the switching rate of the SQUID when its total energy is given by U_- (resp. U_+, U_0). To be valid, this empiric formula requires the transitions between the Andreev levels to occur at rate faster than the frequency of the current ramp used to record the switching events (~ 1 kHz typically).

The expressions for the rates Γ_+, Γ_-, and Γ_0, as a function of the magnetic flux ϕ threading the loop and of the bias current I write:

$$\Gamma_j(I,\phi)=\frac{\omega_p^j(I,\phi)}{2\pi}\exp\left(-\frac{\Delta U_j(I,\phi)}{k_BT}\right),\ j=\pm,0.$$

As can be seen on Figure 14, the barrier heights ΔU_j may differ by a sizeable factor. For the set of parameters chosen on Figure 14, the rate Γ_+ will therefore be much larger than the rate Γ_-.

The plasma frequencies are obtained from $\omega_p^j(I,\phi)=1/\sqrt{L_{tot}^jC}$ with $L_{tot}^j(I,\phi)=\dfrac{{\varphi_0}^2}{\left.\dfrac{d^2U_j}{d\delta^2}\right|_{\delta=\delta_j^*}}$.

Both ω_p^j and ΔU_j are calculated numerically. On Figure 15, the predictions of this model are compared with the experimental data obtained at different temperatures, on the contact with mesoscopic pin code $\tau=\{0.983\}$. In the theory, the reduction of the

gap with temperature is taken into account [3], as well as the temperature dependence of the tunnel junction critical current (see equation (4)).

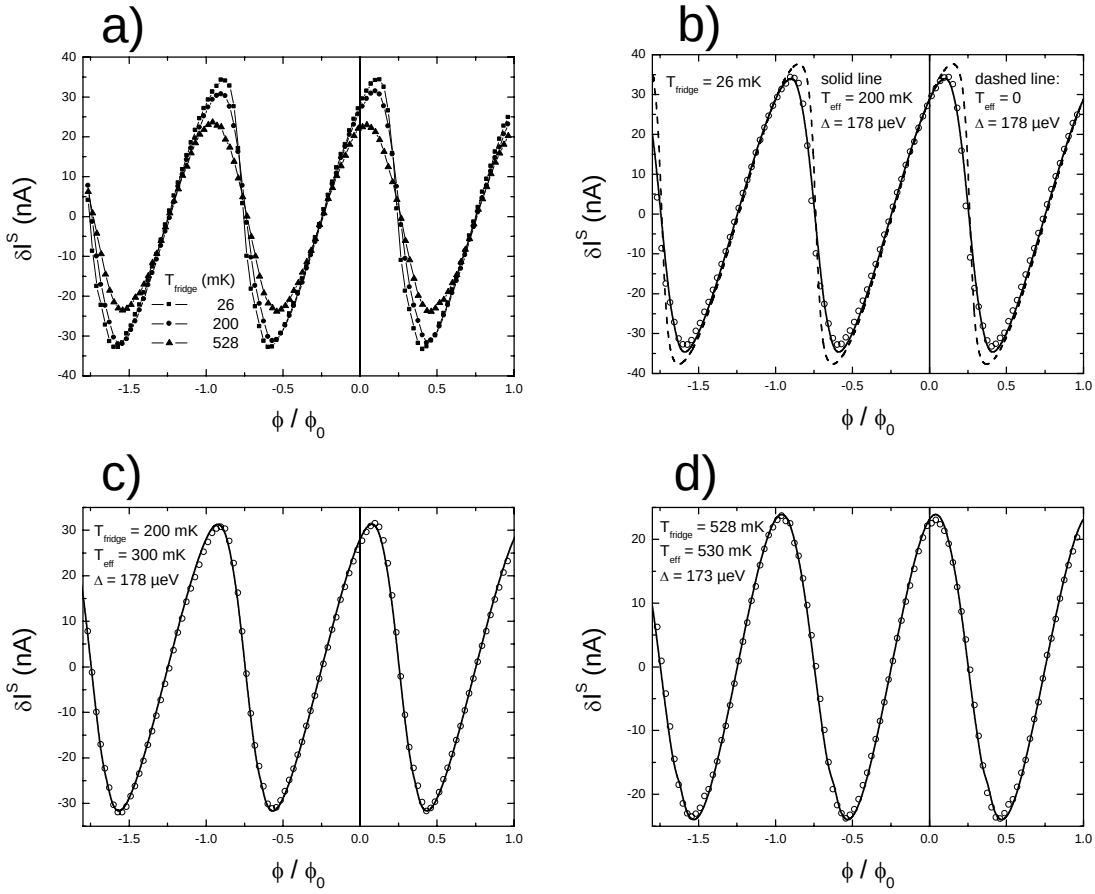

Figure 15: Contact with mesoscopic pin code $\tau = \{0.983\}$. *Symbols are experimental points. a) Measured modulation of the SQUID switching current for three different values of the fridge temperature (26, 200, 528 mK). b) Comparison of the experimental results at 26 mK with both the predictions of the zero temperature theory of section 3.1 (dashed line) and the predictions at 200 mK of the above theory including transitions between the Andreev states (solid line). c) (resp. d)) Comparison of the experimental results at 200 mK (resp. 528 mK) with the above theory (solid line) at 300 mK (resp. 530 mK).*

At the highest temperature, the effective temperature entering the theory is consistent with the measured fridge temperature. However, the effective temperature saturates at 200 mK for the lowest fridge temperature. We think that despite heavy filtering and attenuation of the lines some spurious electromagnetic noise still reaches the SQUID, in

particular through the microwave measurement line (the circulators provide only limited protection outside their working bandwidth).

The effective temperatures found within the two theoretical approaches are summarized on Table 1.

T_{fridge} (mK)	T_{eff} (mK) System in ground Andreev level (section 4.1 & 4.2)	T_{eff} (mK) Thermal equilibrium population of Andreev levels (section 4.3)
26	450	200
200	580	300
528	860	530

Table 1: Summary of the effective switching temperatures found within the two theoretical approaches. In the approach assuming the system in the ground Andreev level, the effective temperatures entering the theory are well above the fridge temperatures. In the theory accounting for the population of the upper Andreev level, the effective temperature is consistent with the fridge temperature at the highest temperature investigated. However, the effective temperature saturates at 200 mK for the lowest fridge temperature, probably due to spurious electromagnetic noise incoming on the SQUID.

Another possible approach to account for the population of the upper Andreev level is to calculate a switching rate for an effective potential, in which the contribution of the two Andreev bound states energies enters by their thermal average. For a single channel contact, this effective potential writes:

$$U_{eff}(\delta, I, \phi) = -\varphi_0\left[I_t^0 \cos(\delta - 2\pi\phi/\phi_0) + I\delta\right] + \frac{1}{\Xi}\left(e^{-\beta U_-\left(\delta_-^*(I,\phi), I, \phi\right)} E_-(\delta) + e^{-\beta U_+\left(\delta_+^*(I,\phi), I, \phi\right)} E_+(\delta)\right),$$

with the partition function $\Xi = \sum_{n_\pm = 0, 1} e^{-\beta U\left(n_+, n_-, \delta^*(n_+, n_-, I, \phi), I, \phi\right)}$.

However, to be valid, this approximation requires that transitions between the Andreev levels occur at a frequency larger than the frequency of the plasma oscillations of the phase (~ 1 GHz). We have checked (results not shown) that the predictions of this

approximation[4] display strong distortions of the modulation of the SQUID switching current, indicating that the effective potential approximation is not justified.

As a conclusion, the switching of the SQUID is indeed a direct way of tracking the current phase relation of the superconducting atomic size contact placed in parallel with the Josephson tunnel junction. However, the thermal fluctuations of the phase reduce the modulation amplitude, which can never reach the critical current of the atomic contact. The theory of the switching process that we have presented in section 4.3 quantitatively describes the experimental results. However the effective noise temperatures are well above the fridge temperature, for the lowest temperatures at which the experiments were performed. This could partly be attributed to spurious noise incoming on the SQUID, but we cannot exclude that an ingredient is missing in this theoretical description of the switching process.

5 Microwave reflectometry

In this section, we present a reflection coefficient calculation that goes one step beyond the approximation of section 3.2 where the reflection coefficient was calculated as $R_\nu = \frac{Z_\nu - Z_0}{Z_\nu + Z_0}$, by treating the Josephson elements as simple linear inductors. This calculation is based on the full resolution of the dynamics of the superconducting phase difference across the SQUID in presence of the external microwave drive. Moreover, the Johnson Nyquist Gaussian white noise sources associated with the two resistors of the circuit are included.

In presence of the microwave voltage drive $V = V_0 \cos(2\pi\nu t)$, the superconducting phase difference will acquire a time dependence given, in the steady state, by:

[4] As usual, the reduction of the gap with temperature is taken into account [3] in the theory, as well as the temperature dependence of the tunnel junction critical current (see equation (4)).

$\delta(t) = \overline{\delta} + \tilde{\delta}(t)$, where $\overline{\delta}$ is the mean value of the phase around which it oscillates. The two phases δ and γ are rigidly linked by the magnetic flux bias ϕ according to equation (6). Therefore the time dependence of γ writes $\gamma(t) = \overline{\delta} - 2\pi\phi/\phi_0 + \tilde{\delta}(t)$. The linear regime is simply defined by $\tilde{\delta}(t) \ll 1$. In this limit, the Josephson elements can be considered as linear inductors and the treatment presented in section 3.2 is valid. However, as soon as the amplitude of $\tilde{\delta}(t)$ starts to be sizeable, the Josephson elements are not linear any longer and the treatment of section 3.2 breaks down.

It is clear that in the experiment, the ac modulation $\tilde{\delta}(t)$ can be reduced to remain in the linear regime by reducing the microwave amplitude V_0. However, there is a threshold level below which the reflected signal is completely buried in the noise. In practice the experiments have been performed with $V_0 = 0.084 \times RI_t^0$, where $R = 50\ \Omega$ and $I_t^0 = 750$ nA.

The calculation of the reflection coefficient is carried out in the equivalent circuit schematically represented in Figure 16. The bias tee is simply represented by the capacitor C' on its ac input. All the dc current I is forced to flow in the two arms of the SQUID.

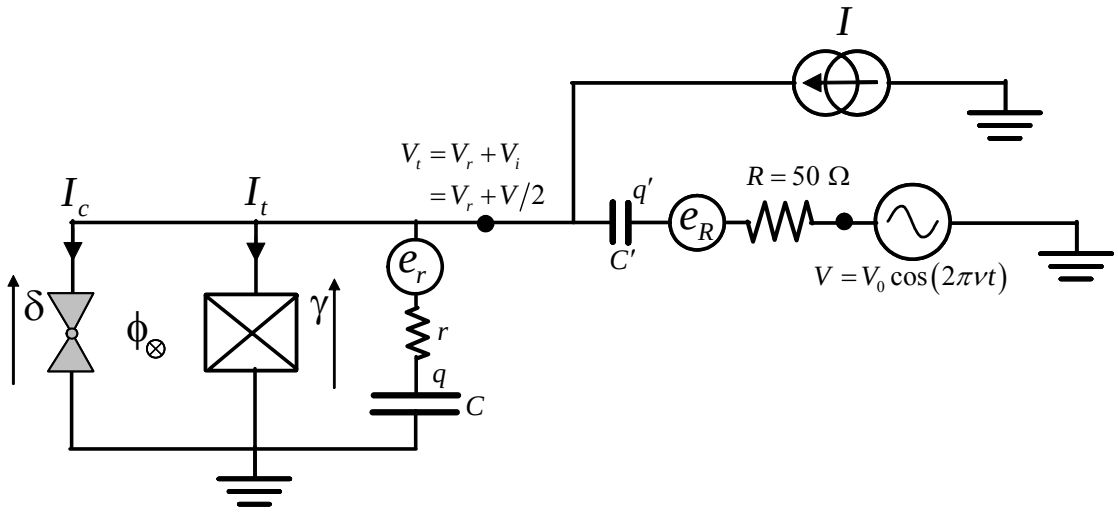

Figure 16: Discrete element circuit for the calculation of the reflection coefficient R_ν. This circuit can be described by the three following independent variables: the charge q on the on-chip capacitor C, the charge q' on the capacitor C' of the bias tee, and the superconducting phase difference δ across the contact. The total voltage V_t across the resonator can be decomposed in the sum of two terms: the voltage V_r corresponding to the signal reflected by the resonator, and the voltage $V_i = V/2$ delivered by the $50\ \Omega$ internal impedance source of the vector network analyzer.

Using the second Josephson relation, the three electrical equations for the variables q, q', and δ (see Figure 16) of the circuit write:

$$\begin{cases} V_0 \cos(2\pi\nu t) = \varphi_0\dot{\delta} + q'/C' + R\dot{q}' + e_R(t) \\ \varphi_0\dot{\delta} = q/C + r\dot{q} + e_r(t) \\ I + \dot{q}' = I_c^-(\delta) + I_t(\delta - 2\pi\phi/\phi_0) + \dot{q} \end{cases}$$

where $e_r(t)$ and $e_R(t)$ are the random Johnson Nyquist voltage noise sources associated with the resistors r and R respectively. This set of equation can be rewritten as follows:

$$\begin{cases} V_t = \varphi_0 \dot{\delta} \\ = \dfrac{1}{(R+r)}\left\{ r\left[V_0 \cos(2\pi\nu t) - e_R(t) - q'/C' + R\left(I - I_c^-(\delta) - I_t(\delta - 2\pi\phi/\phi_0) \right) \right] + Rq/C \right\} + e_r(t) \\ \dot{q} = \dfrac{1}{R+r}\left[V_0 \cos(2\pi\nu t) - e_R(t) - e_r(t) - q'/C' - q/C + R\left(I - I_c^-(\delta) - I_t(\delta - 2\pi\phi/\phi_0) \right) \right] \\ \dot{q}' = \dfrac{1}{R+r}\left[V_0 \cos(2\pi\nu t) - e_R(t) - e_r(t) - q'/C' - q/C - r\left(I - I_c^-(\delta) - I_t(\delta - 2\pi\phi/\phi_0) \right) \right] \end{cases}$$

It is possible to simplify the last set of equations if one assumes the capacitor C' of the bias tee being infinitely large. In this limit, the capacitor C' behaves as a perfect voltage source. Therefore the variable q' drops out of the equations:

$$\begin{cases} V_t = \varphi_0 \dot{\delta} \\ = \dfrac{1}{(R+r)}\left\{ r\left[V_0 \cos(2\pi\nu t) - e_R(t) + R\left(I - I_c^-(\delta) - I_t(\delta - 2\pi\phi/\phi_0) \right) \right] + Rq/C \right\} + e_r(t) \\ \dot{q} = \dfrac{1}{R+r}\left[V_0 \cos(2\pi\nu t) - e_R(t) - e_r(t) - q/C + R\left(I - I_c^-(\delta) - I_t(\delta - 2\pi\phi/\phi_0) \right) \right] \end{cases}$$

These two first order coupled differential equations can be solved numerically in order to obtain the reflection coefficient R_ν. The modulus of the reflection coefficient is simply given by:

$$|R_\nu| = \left| \frac{V_r(\nu)}{V_i(\nu)} \right| = \frac{|V_r(\nu)|}{V_0/2} = \frac{|V_t(\nu) - V_0/2|}{V_0/2},$$

where $V_t(\nu)$ is the Fourier weight of the voltage $V_t(t)$ across the resonator in steady state ($t \to \infty$).

In the two following sections, the predictions of this model are compared with the experimental results, to understand the non linear effects and the effect of thermal phase fluctuations.

5.1 Non linearity of the Josephson inductors

In this section, the zero temperature predictions of the above theoretical model are compared with the experimental data (measured at the fridge base temperature, i.e. 20 mK) and with the zero temperature linear approximation of section 3.2. Figure 17 shows the comparison for the contact with mesoscopic pin code $\tau = \{0.475, 0.138, 0.019\}$. Figure 18 shows the comparison for the contact with a single, highly transmitting channel $\tau = \{0.983\}$.

In the theoretical predictions presented on Figure 17 and Figure 18, we have taken $\Delta(T=0) = 178\ \mu\text{eV}$ for the superconducting gap. The only adjustable parameters were the values of the resistor $r = 0.57\ \Omega$ and of the capacitor $C = 33.7\ \text{pF}$, in good agreement with the value expected from the geometry of the capacitor ($34\ \text{pF}$). The frequency of the microwave signal was $\nu = 1.24\ \text{GHz}$ for the two contacts we have investigated. The absolute value of the measured reflection coefficient was calibrated when the SQUID had switched and behaved as a resistor corresponding to its normal state resistance.

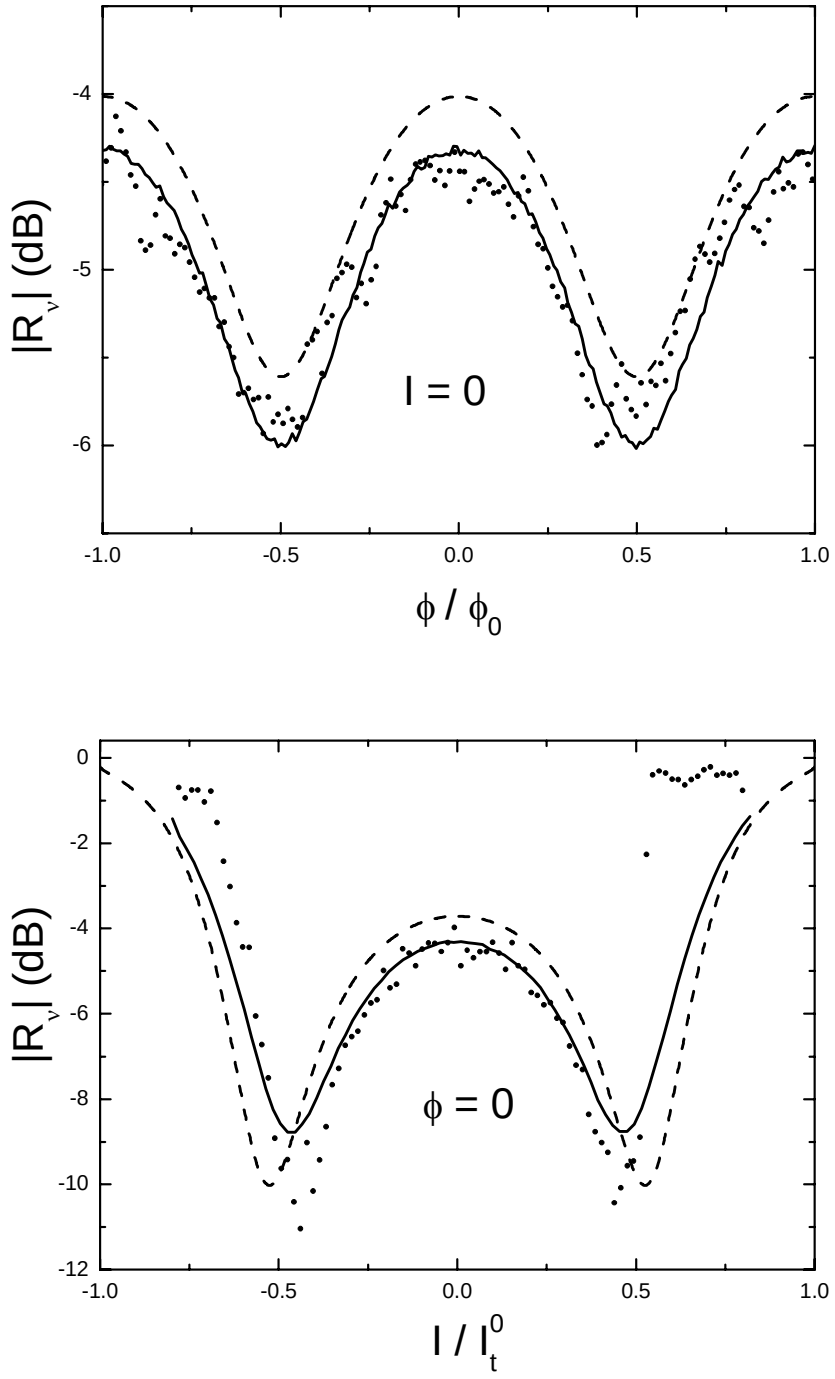

Figure 17: Modulus of the reflection coefficient R_ν for a contact with mesoscopic pin code $\tau = \{0.475, 0.138, 0.019\}$. The fridge temperature was 20 mK. Lower graph: modulus as a function of the dc bias current I at $\phi = 0$. Upper graph: modulus as a function of the external magnetic flux ϕ threading the loop at $I = 0$. Dots: experimental results. Dashed lines: zero temperature prediction of the linear approximation presented in section 3.2. Solid lines: zero temperature prediction of the numerical simulation of the phase dynamics.

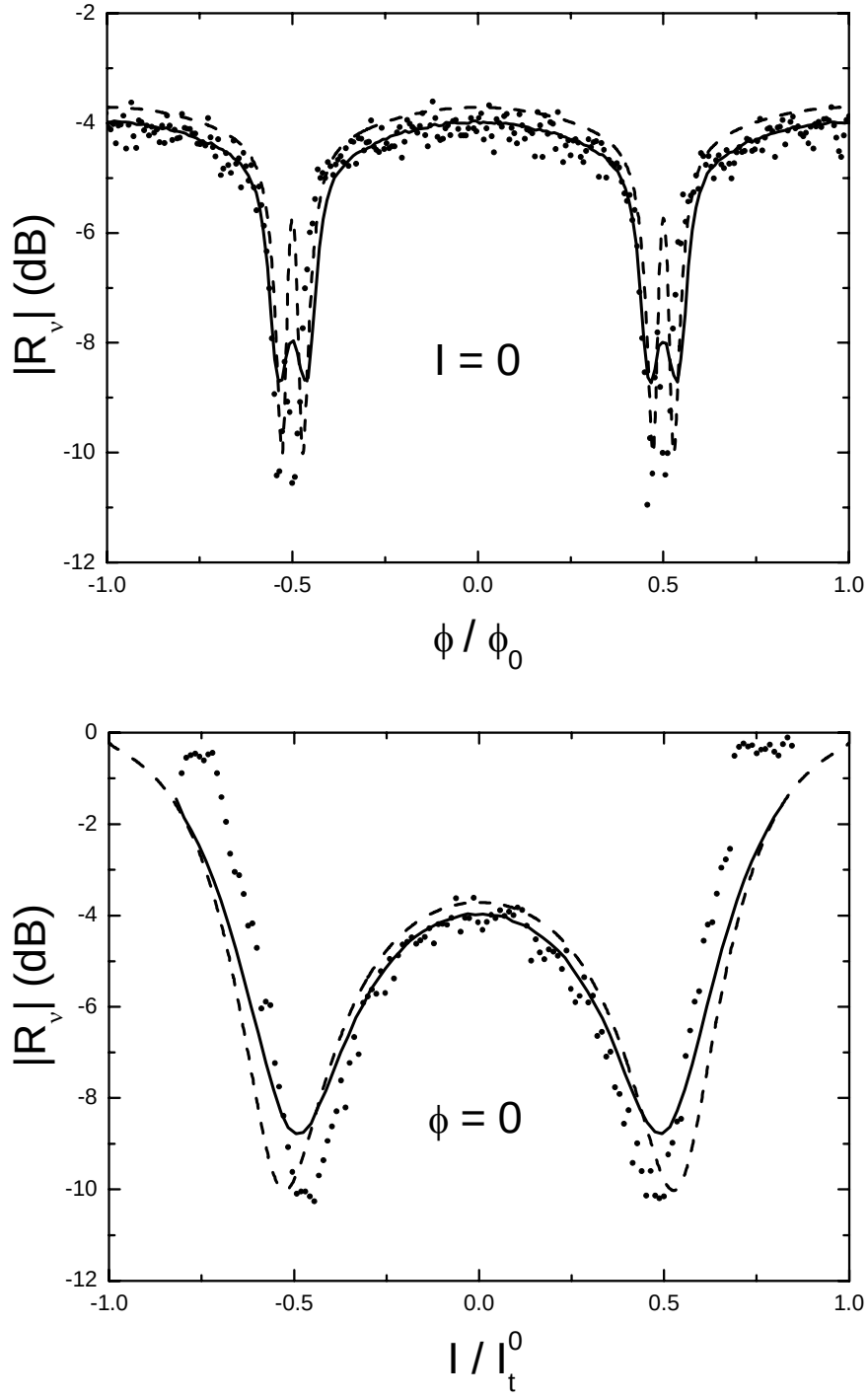

Figure 18: Modulus of the reflection coefficient for a contact with mesoscopic pin code $\tau = \{0.983\}$. *The fridge temperature was 26 mK. Lower graph: modulus as a function of the dc bias current* I *at* $\phi = 0$. *Upper graph: modulus as a function of the external magnetic flux* ϕ *threading the loop at* $I = 0$. *Dots: experimental results. Dashed lines: zero temperature prediction of the linear approximation presented in section 3.2. Solid lines: zero temperature prediction of the numerical simulation of the phase dynamics.*

The predictions of the simulation of the non-linear phase dynamics for the reflection coefficient describe the experimental data slightly better than the linear approximation, the main improvement being essentially on the absolute value of the reflection coefficient. We conclude that the amplitude of the microwave excitation that we have used in the experiments was therefore slightly too large to remain in the regime where the Josephson elements can be described as linear inductors.

The twofold effect of the temperature (population of the Andreev levels and thermal phase fluctuations) is described in the next section.

5.2 Effect of the temperature - population of the Andreev levels and thermal phase fluctuations

The effect of temperature on the modulus of the measured reflection coefficient is shown on Figure 19 for the contact with mesoscopic pin code $\tau = \{0.983\}$. The main features are the following:

- A reduction of the modulation amplitude of the reflection coefficient, both as a function of the magnetic flux (Figure 19, left panel) and of the dc bias current (Figure 19, right panel),
- A reduction of the mean value of the reflection coefficient.

There is almost no difference between the data at 26 mK and 200 mK, meaning that the system does not cool below 200 mK, as already suggested by the switching experiments.

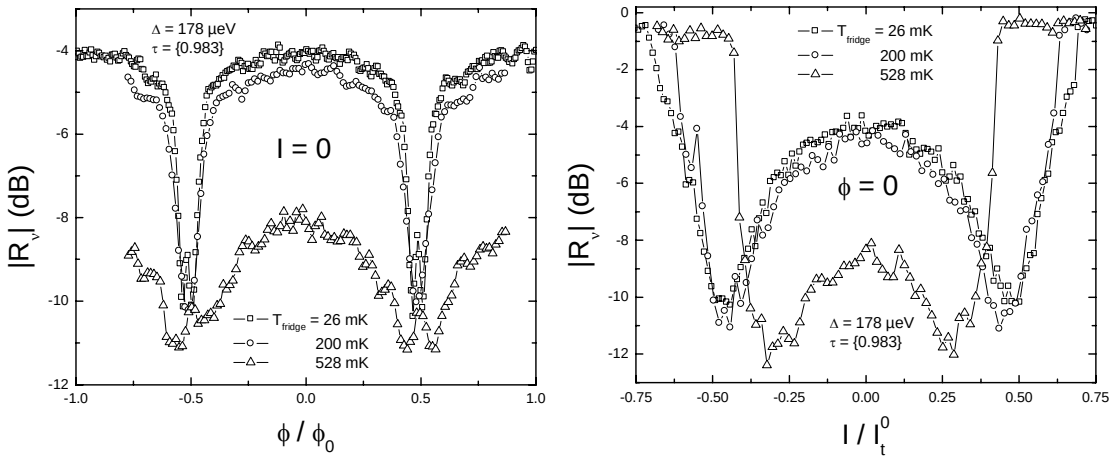

Figure 19: Measured modulus of the reflection coefficient (at the frequency $\nu = 1.24$ GHz*) for the atomic contact with mesoscopic pin code* $\tau = \{0.983\}$ *at three different temperatures (26 mK, 200 mK, 528 mK). Right panel: modulus as a function of the dc bias current* I *at* $\phi = 0$*. Left panel: modulus as a function of the external magnetic flux* ϕ *threading the loop at* $I = 0$*.*

The previous calculations of the reflection coefficient (section 3.2 and section 5) were based on an adiabatic approximation assuming that in each channel only the lower Andreev level is occupied. In the following, we present two approaches aiming to describe the effect of the population imbalance of the two Andreev states on the reflection coefficient (see Figure 19). For simplicity, only the case of a single channel contact is presented.

The first approach consists in calculating the reflection coefficient according to equation (10), where in the expression of the resonator impedance Z_ν, we take the thermally averaged inductance $L_{tot}(I, \phi)$ of the SQUID. The inductance of the SQUID is related to the curvature of the potential $U(n_+, n_-, \delta, I, \phi)$ given by equation (17) as follows:

$$L_{tot}(n_+, n_-, \delta, I, \phi) = \frac{{\varphi_0}^2}{\partial^2 U(n_+, n_-, \delta, I, \phi)/\partial \delta^2}$$

The thermally averaged inductance $L_{tot}(I, \phi)$ corresponding to the oscillations around a minimum of the potential $U(n_+, n_-, \delta, I, \phi)$ therefore writes:

$$L_{tot}(I, \phi) = \frac{1}{\Xi}\left[e^{-\beta U_-\left(\delta_-^*(I, \phi), I, \phi\right)} L_{tot-}\left(\delta_-^*(I, \phi), I, \phi\right) + e^{-\beta U_+\left(\delta_+^*(I, \phi), I, \phi\right)} L_{tot+}\left(\delta_+^*(I, \phi), I, \phi\right) \right.$$
$$\left. + 2e^{-\beta U_0\left(\delta_0^*(I, \phi), I, \phi\right)} L_t\left(\arcsin\left(I/I_t^0\right)\right) \right] ,$$

where

$$L_{tot+}(\delta, I, \phi) = L_{tot}(n_+ = 1, n_- = 0, \delta, I, \phi)$$
$$L_{tot-}(\delta, I, \phi) = L_{tot}(n_+ = 0, n_- = 1, \delta, I, \phi)$$
$$L_t\left(\arcsin\left(I/I_t^0\right)\right) = L_{tot}(n_+ = 0, n_- = 0, \delta, I, \phi)$$
$$= L_{tot}(n_+ = 1, n_- = 1, \delta, I, \phi)$$

$L_t(\gamma)$ is the inductance of the tunnel junction alone and is given by equation (12). Indeed, when no current is flowing in the atomic contact ($n_\pm = 0$ or $n_\pm = 1$), it is equivalent to an infinite impedance and the total inductance of the SQUID reduces to the one of the tunnel junction alone. All the other notations have already been defined in section 4.3.

The second approach consists in calculating the reflection coefficients R_ν^- (resp. R_ν^+, R_ν^0) corresponding to the four occupation configurations of the Andreev level ($n_\pm = 0, 1$) and taking their thermal average to obtain the mean reflection coefficient as:

$$R_\nu = \frac{1}{\Xi}\left(e^{-\beta U_-\left(\delta_-^*(I, \phi), I, \phi\right)} R_\nu^- + e^{-\beta U_+\left(\delta_+^*(I, \phi), I, \phi\right)} R_\nu^+ + 2e^{-\beta U_0\left(\delta_0^*(I, \phi), I, \phi\right)} R_\nu^0 \right).$$

These two different approaches for averaging, as well as their range of validity have already been mentioned in section 4.3 when discussing the effect on the switching of thermally populating the excited Andreev level.

On Figure 20, the experimental results at 528 mK are compared with the predictions of the two linear approaches described above.

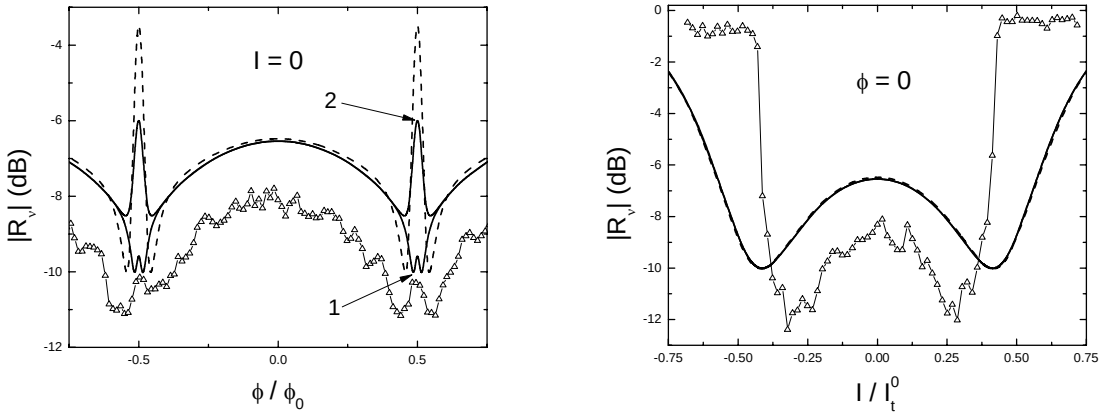

Figure 20: Modulus of the reflection coefficient (at the frequency $\nu = 1.24$ GHz) for an atomic contact of mesoscopic pin code $\tau = \{0.983\}$. Open triangles: experimental results at 528 mK. Lines: theoretical predictions for the reflection coefficient at 528 mK (the reduction of the gap has been taken into account: $\Delta(T = 528\ \mathrm{mK}) = 173\ \mu\mathrm{eV}$). Solid line 1 (resp. 2): linear approach based on the thermal average of the inductance (resp. reflection coefficient). Dashed line: linear approach based on the adiabatic approximation (see section 3.2). Left panel: $|R_\nu|$ as a function of the external magnetic flux ϕ at $I = 0$. Right panel: $|R_\nu|$ as a function of the dc bias current I at $\phi = 0$. The three lines are superposed on the right panel.

These two linear approaches taking into account the population of the upper Andreev level do not describe quantitatively the experimental results obtained at 528 mK. However, they show a better agreement with the experiment than the predictions of the linear approach of section 3.2 which assumes than only the lower Andreev bound level is occupied. Note that two ingredients are missing in these three approaches: the non-linearity of the Josephson inductors and the thermal fluctuations of the phase.

To try to explain the experimental results obtained at 528 mK, we have used the finite temperature simulations of the phase dynamics presented in section 5. These simulations include the two missing ingredients mentioned above. However, they disregard the occupation of the upper Andreev level. The predictions of these

simulations are presented on Figure 21: they qualitatively agree with the experimental results of Figure 19. Namely, the simulations show that the overall level of the reflected signal decreases with the temperature. However, as shown on Figure 22, the predictions of the phase dynamics simulation at 528 mK better agree with the data measured at 200 mK than with the data measured at 528 mK. At this stage, the effect of temperature on the measured reflection coefficient is still not well understood.

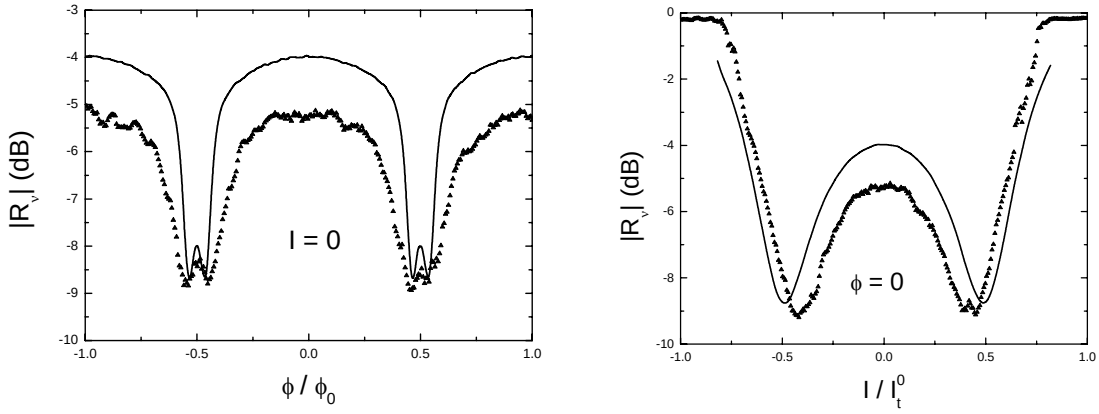

Figure 21: Predictions of the phase dynamics simulation for the modulus of the reflection coefficient R_ν (at the frequency $\nu = 1.24$ GHz) for an atomic contact of mesoscopic pin code $\tau = \{0.983\}$. Left panel: $|R_\nu|$ as a function of the external magnetic flux ϕ at $I = 0$. Right panel: $|R_\nu|$ as a function of the dc bias current I at $\phi = 0$. The solid lines are the predictions at zero temperature. Closed triangles are the predictions at 528 mK, where the reduction of the gap has been taken into account ($\Delta(T = 528\ \text{mK}) = 173\ \mu\text{eV}$). In the numerical simulations, the adiabatic current phase relation of the contact, $I_c^-(\delta)$, was used (see equation (3)).

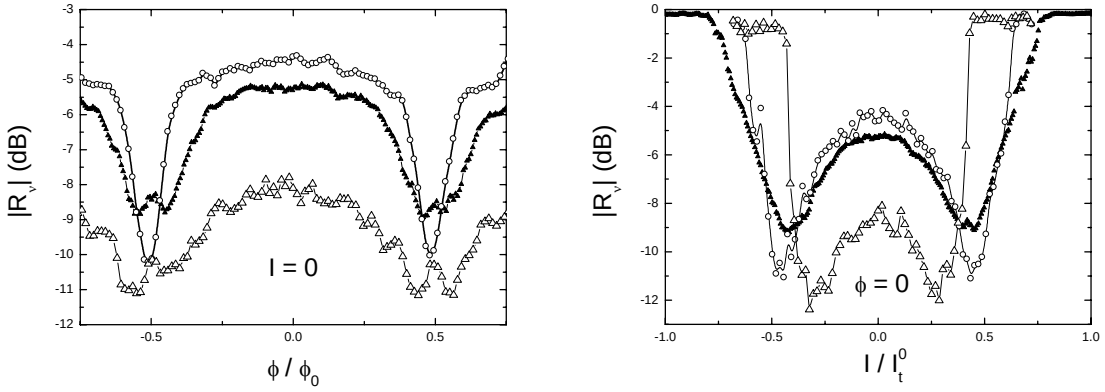

Figure 22: Closed triangles: predictions of the phase dynamics simulation (528 mK) for the modulus of the reflection coefficient R_ν (at the frequency $\nu = 1.24$ GHz). In the simulation, the adiabatic current phase relation of the contact, $I_c^-(\delta)$, was used (see equation (3)) and the reduction of the gap was taken into account ($\Delta(T = 528\text{ mK}) = 173\ \mu\text{eV}$). Open dots: experimental results at 200 mK. Open triangles: experimental results at 528 mK. The mesoscopic pin code of the contact is $\tau = \{0.983\}$. Left panel: $|R_\nu|$ as a function of the external magnetic flux ϕ at $I = 0$. Right panel: $|R_\nu|$ as a function of the dc bias current I at $\phi = 0$.

As a conclusion, the reflection coefficient on the resonator formed by the parallel combination of the two Josephson elements and the capacitor carries all the information on the Josephson inductance of the contact and thus on its current-phase relation. The experimental data compare quite well with the predictions of the theory for the reflection coefficient R_ν at low temperature. However, the data at high temperatures couldn't be explained by our simple models. A perspective for the future would be to include transitions between Andreev levels in the numerical simulation of section 5.

6 Wiring of the experiment

The detailed wiring of the two experiments of chapter 4 is schematically represented on Figure 23. Six lines of the cryostat were used to perform this set of experiments: four dc lines (on the left on Figure 23) and two microwave lines (on the right on Figure 23).

- microwave lines:

Although the two microwave lines were used only in the reflectometry measurements, they were always connected to the sample. The internal microwave source of the vector network analyzer injects a signal through the first line. Attenuators and filters are placed along this microwave biasing line to reduce the noise level on the on-chip resonator. The reflected signal is fed into the second microwave line by the directional coupler. No attenuator is placed on this measurement line in order not to reduce the magnitude of the signal one wishes to measure. As a compromise, circulators are used instead, which provide good isolation, although only in the their working bandwidth(1.3 – 1.8 GHz). The reflected signal is almost perfectly transmitted by the circulators, whereas the noise coming from the hotter parts of the cryostat is directed into the $50\ \Omega$ resistors and dissipated (see arrows on the circulators represented on Figure 23). The ensemble of these elements results in a narrow bandwidth for the experiment (1.3 – 2 GHz). The reflected signal is amplified at room temperature (+ 80 dB) before entering the network vector analyzer. Care is taken to thermally anchor all the elements (filters, attenuators, circulators, directional coupler) and the lines at the different stages of the cryostat.

- dc lines:

Two of the four dc lines have been used in the two experiments to thread a magnetic flux through the loop of the SQUID, and to apply a dc bias current through the SQUID. The two measurement lines have been used in the switching experiment only. The total dc current in the SQUID is monitored by measuring the voltage drop across a $400\ \Omega$ resistor. The dc lines are completely isolated from the microwave lines by a bias tee. It is therefore possible to both apply a dc current through the SQUID while probing the reflection properties of the resonator with a microwave signal. The current through the coil is obtained from a dc voltage source in series with a $5\ \text{k}\Omega$ biasing resistor.

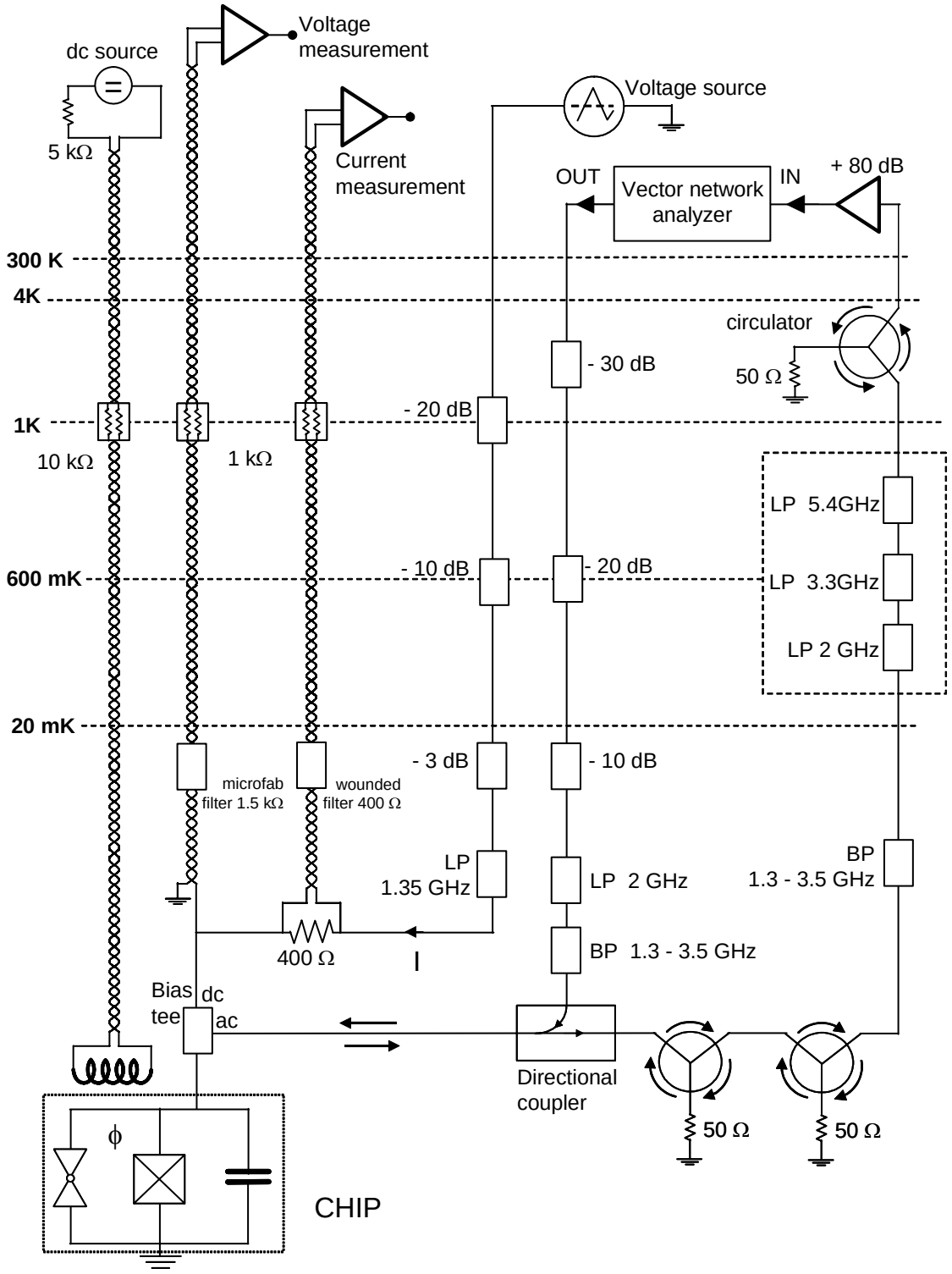

Figure 23: Detailed wiring of the experimental setup used for the two experiments of chapter 4 (switching and microwave reflectometry).

References of chapter 4

[1] M. C. Koops, G. V. van Duyneveldt, and R. de Bruyn Ouboter, Phys. Rev. Lett. **77**, 2542 (1996).

[2] D. Vion, A. Aassime, A. Cottet, P. Joyez, H. Pothier, C. Urbina, D. Esteve, and M. H. Devoret, Science **296**, 286 (2002).

[3] M. Tinkham, *Introduction to superconductivity Second Edition*, Dover Publications, New York (2004).

[4] Macroscopic Quantum Mechanics of the Current-Biased Josephson Junction, M. H. Devoret, D. Esteve, C. Urbina, J. Martinis, A. Cleland and J. Clarke, in *Exploring the Quantum/Classical Frontier: Recent Advances in Macroscopic Quantum Phenomena*, Jonathan Friedman and Siyuan Han (eds.) Nova Science Publishers, Inc., New York, 2003, pp. 1-34.

[5] Michel H. Devoret, John M. Martinis, and John Clarke, Phys. Rev. Lett. **55**, 1908 (1985).

[6] I. Siddiqi, R. Vijay, F. Pierre, C. M. Wilson, M. Metcalfe, C. Rigetti, L. Frunzio, and M. H. Devoret, Phys. Rev. Lett. **93**, 207002 (2004).

[7] P. Hänggi, P. Talkner, and M. Borkovec, Rev. Mod. Phys. **62**, 251 (1990).

Chapter 5: Experimental techniques

Section 1 and appendix 1 of this chapter are inspired from R. Cron's Ph.D. thesis [1].

In this chapter, we describe the techniques that were used to perform the three experiments presented throughout this thesis. These techniques were dictated by a series of basic requirements.

First, the measurements that are carried out on a given atomic contact usually last for several hours or even several days. It is therefore crucial to form mechanically stable atomic contacts. Secondly, as the Josephson coupling established through an atom between the superconducting electrodes is small (~ 1 K for a typical aluminum single atom contact), the experiments must be performed at low temperature (20 mK), i.e. in a dilution refrigerator. Third, it is necessary to impose stable bias conditions and to be able to measure small voltages and small currents. The experimental setup had thus to be shielded from the ambient electromagnetic noise. Finally, in order to control the evolution of the superconducting phase difference, it is necessary to provide a well defined electromagnetic environment to the contact, over a broad range of frequencies going from dc up to the plasma frequency (typically in the tens of gigahertz range).

We first show how to obtain stable and clean atomic contacts using microfabricated mechanically controllable break junctions (MCBJ).

Then we discuss how to voltage bias or phase bias atomic contacts, by embedding them in specific on-chip environments.

We then detail the techniques used in our experiments to perform low-noise measurements at low temperatures.

Finally, we explain how to measure the mesoscopic PIN code of superconducting atomic size contacts, the crucial feature that makes them fully characterized coherent conductors.

The more specific fabrication recipes, the operation of the SQUID amplifier used to measure the current in the contact, and the wiring of the cryostat are presented in the appendices at the end of the chapter.

1 Obtaining atomic size contacts with the nanofabricated mechanically controllable break junction technique

The first experiments on small metallic contacts were performed by bringing a needle into contact with a metallic surface. This technique, first used by I. K Yanson in

1974 [2] and developed later on by A. G. M. Jansen [3], allowed to obtain contacts with a diameter of a few tens of nanometers. The ultimate size of these contacts was limited by the poor mechanical stability of the needle with respect to the surface. Later on, stable contacts with dimensions down to the atomic scale were obtained. Ultimately, the technical progresses of the field lead to the invention of the scanning tunneling microscope (STM) by G. Binnig and H. Rohrer in 1981 [4]. Since then, a variety of STM related techniques have been used to achieve reproducibly atomic size contacts [5, 6].

Atomic contacts formed using the break-junction technique were first obtained in the group of J. M. van Ruitenbeek at Leiden, at the beginning of the 1990's [7]. In conventional MCBJ, a metallic wire of a few tens of microns in diameter is glued with two droplets of epoxy on an elastic substrate and notched in its center with a knife. Then, the substrate is bent in order to break the wire at its weak point. By releasing the strain on the substrate, the electrodes formed by the two pieces of wire are brought back together, until forming a single atom contact. The stability reached within this technique allowed to carry out a wide range of experiments [6]. Recently, a variant of the conventional MCBJ technique incorporating a force sensor based on a piezoelectric quartz tuning fork enabled the simultaneous measurement of electrical conductance and force gradient between two sharp gold tips [8]. The high resolution measurements enabled a quantitative study of the interaction between the electrodes.

In our experiments, we have used the nanofabricated mechanically controllable break junction technique to obtain highly stable atomic size contacts [9]. Appendix 1 presents in detail the electron-beam lithography steps necessary to obtain the narrow metallic bridge, suspended over a few microns on a flexible substrate, shown in Figure 1. The central constriction is initially ~ 100 nm in diameter, and corresponds thus to a contact of several million atoms between the two sides.

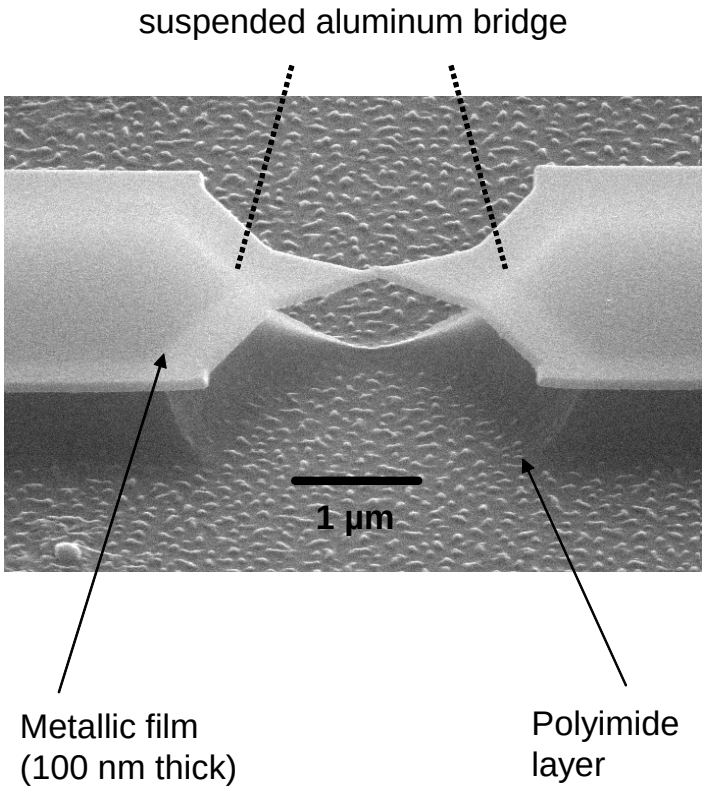

Figure 1: Scanning electron microscope (SEM) micrograph of a nanofabricated metallic bridge after etching of the polyimide layer.

The substrate is then placed on a three point bending bench (see Figure 2 and Figure 3), thermally anchored to the mixing chamber of a dilution refrigerator and sitting in cryogenic vacuum. The axes of the two counter-supports are a distance $L = 14$ mm apart. A differential screw, with a 100 µm pitch, controls the relative translation between the pushing rod and the counter-supports. The sample is mounted with the bridge centered with respect to the pushing rod. Initially, the distance between the two anchors of the bridge is $u_0 \approx 3$ µm. The substrate (thickness $t \approx 0.3$ mm) is then bent by pushing in its center with the pushing rod. The strain imposed on the metallic layer is geometrically concentrated at the constriction. The distance u between the two anchors is increased until the metallic layer breaks at the constriction. The two resulting electrodes are then brought back into contact by pulling the pushing rod backwards. Assuming an elastic uniform deformation of the substrate, one finds that a longitudinal displacement δx of the pushing rod results in a change in the inter-electrode distance $\delta D = r\delta x$, where the reduction ratio $r = 6u_0 t / L^2 \approx 9\times10^{-5}$ [9]. As the rotation of the

differential screw can be controlled with a precision better than 1°, δx can be adjusted with submicron accuracy. The intrinsic leverage of the system allows then to control the contact between the electrodes at the atomic level.

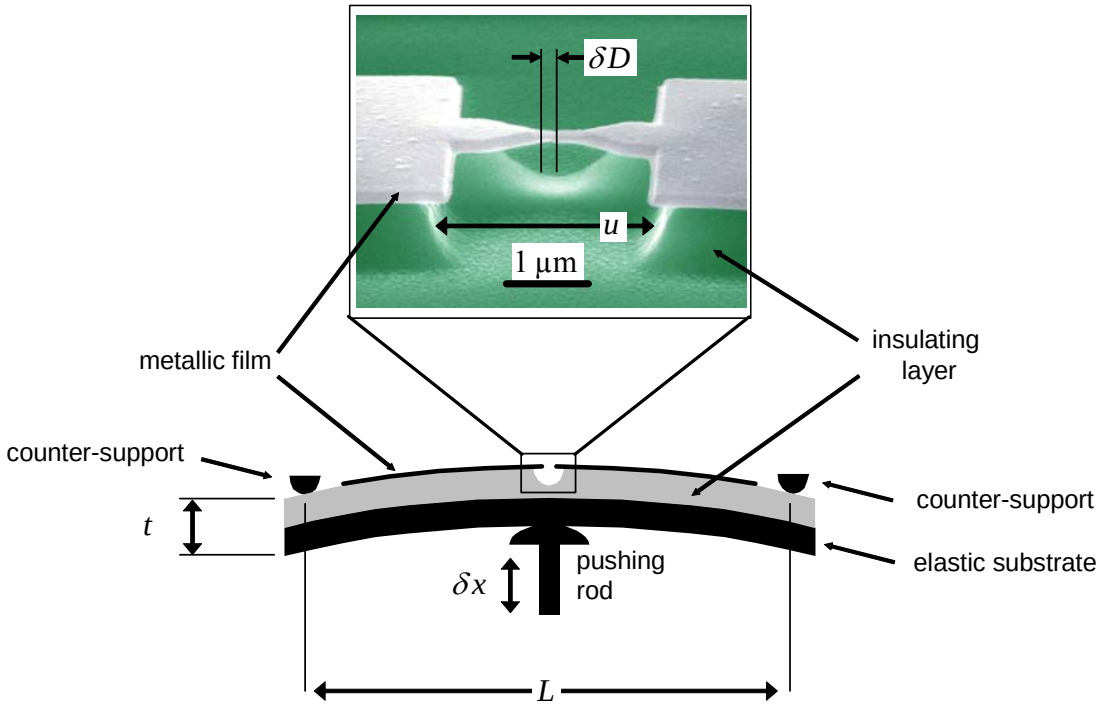

Figure 2: Bending mechanism used to form an atomic contact with the suspended nanofabricated bridge.

These techniques, developed within the Quantronics Group at Saclay [9], lead to a greatly improved mechanical stability of contacts as compared with the standard MCBJ technique. Indeed, in the latter the smaller achievable distance between the anchor pads (epoxy droplets in this case) is typically $u_0 \approx 0.5$ mm, thus limiting the reduction ratio to $r \approx 10^{-2}$.

Besides the increased stability of the nanofabricated MCBJ technique, another great advantage is the possibility of embedding the contact in an on-chip electromagnetic environment (see section 2). This is done by designing a specific pattern for the electron beam exposure, according to the electrical circuit one wishes to implement around the junction. The fabrication procedures of the different electromagnetic environments that we have used in the experiments are presented in appendix 1.

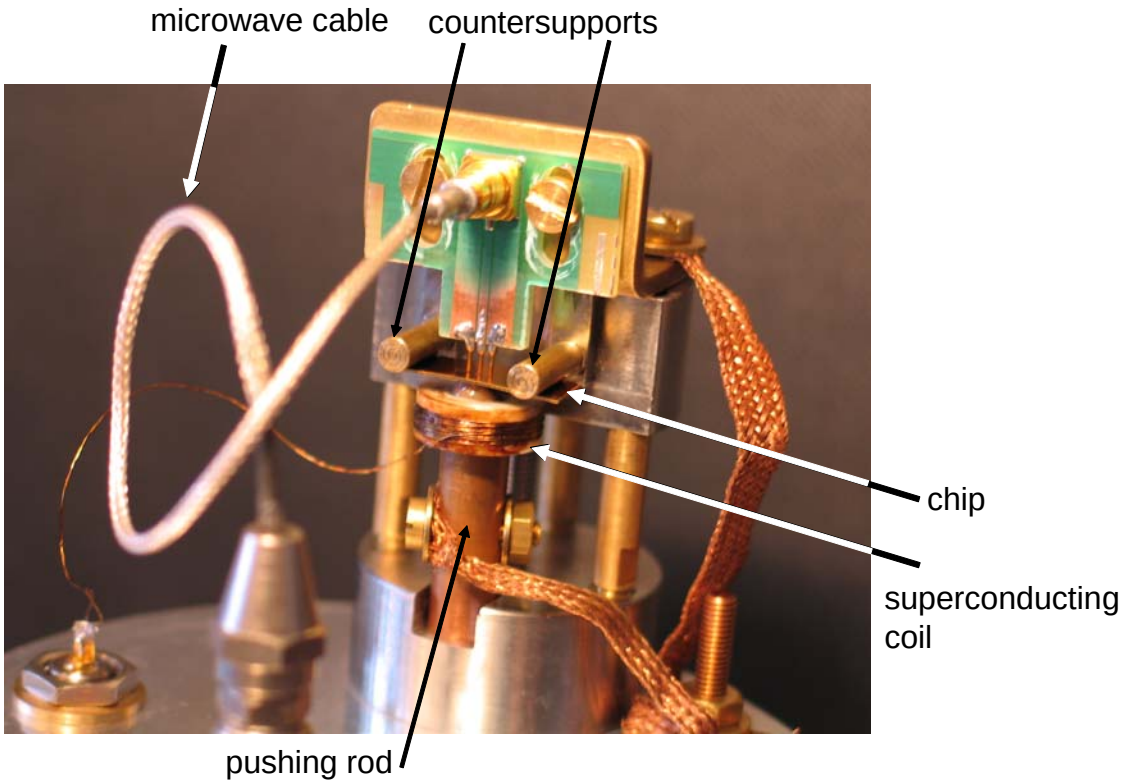

Figure 3: Photograph of the bending mechanism. The chip is placed between two counter-supports (small horizontal cylinders, 14 mm apart from each other) and a pushing-rod. Spring probes pressed on millimetric pads on the chip connect the sample through a 50 Ω *line to the external signals. A small superconducting coil (400 turns of niobium wire of 0.2 mm in diameter) has been added on the pushing rod to apply a magnetic field on the sample.*

2 Observing the Josephson effects in atomic contacts

The experiments performed throughout this thesis demanded the design of specific electromagnetic environments for the atomic contact, fulfilling the following inter-related and sometimes contradictory requirements:

- Provide, at low frequencies, either a voltage, current or phase bias.
- Damp, at all frequencies up to the plasma frequency, the fluctuations of the superconducting phase difference across the contact.

- Keep the electrons in the dissipative elements cold enough to reduce the Johnson Nyquist noise incoming on the contact.
- Measure the current flowing through the contact (with sub-nanoampere precision) and the voltage across it (with sub-microvolt precision).

2.1 The two experimental setups

We present here the two experimental setups that we have implemented to voltage bias the contacts, and establish the necessary conditions on the different elements of the environment to ensure that the full current-voltage is amenable to measurement.
Figure 4 presents a scheme of principle for a basic IV measurement setup imposing a voltage bias.

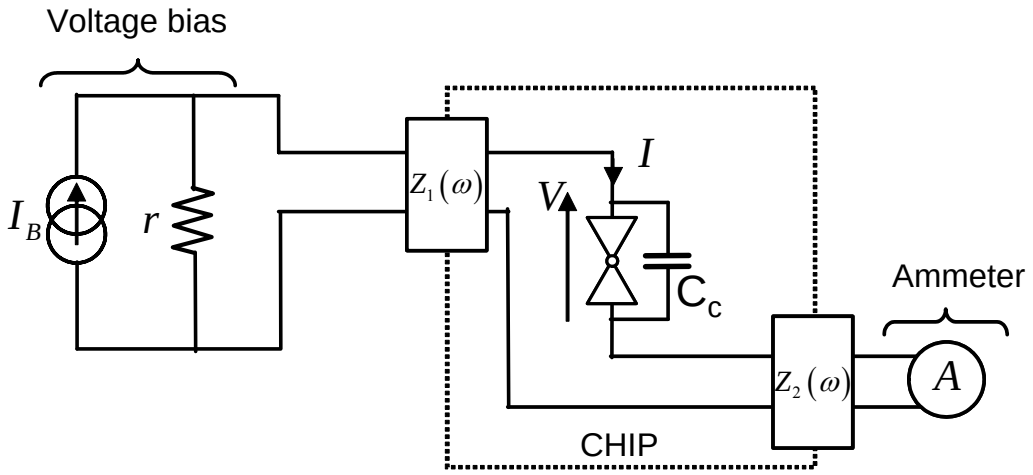

Figure 4: Basic setup to measure the current-voltage characteristic of atomic contacts. The two impedances $Z_1(\omega)$ and $Z_2(\omega)$ represent the electric lines connecting the chip to the voltage source and the ammeter. C_c is the capacitance between the two electrodes forming the contact.

In this setup an ideal current source I_B shunted by a resistor of small enough resistance r provides a voltage bias for the contact and an ideal ammeter measures the current in the contact without disturbing the voltage bias. The resistor has to behave as such at all frequencies up to the plasma frequency, as it also provides the necessary dissipation for damping the high-frequency fluctuations of the phase.

However, in practice it is difficult to implement along these lines a setup that fulfills the requirements listed above. The main difficulty is that the line connecting the chip to the source, typically shunts the resistor r at high frequency and the phase fluctuations are not damped as desired. A solution would be to microfabricate the resistor r on chip, very close to the contact, to avoid the stray capacitance. However, the volume of such a resistor would be too small for the electrons to thermalize at the temperature of the phonon bath (assumed to be equal to the fridge temperature) when submitted to the Joule heating of the dc bias. On the ammeter side the requirements are less stringent. The total impedance as seen from the chip has to be small enough at all frequencies, so that the voltage bias is not perturbed.

A known solution [16] to the problem just mentioned is to split the biasing resistor in two (see Figure 5). In this configuration, the dissipation associated to the dc voltage bias takes place in a macroscopic resistor R (placed either on-chip or off-chip). The ac dissipation takes place in a microfabricated on-chip resistor r, placed as close as possible to the junction to avoid any stray inductance and capacitance. The large on-chip capacitor provides at high frequencies a short that makes the contact insensitive to the impedance of the lines connecting it to the source.

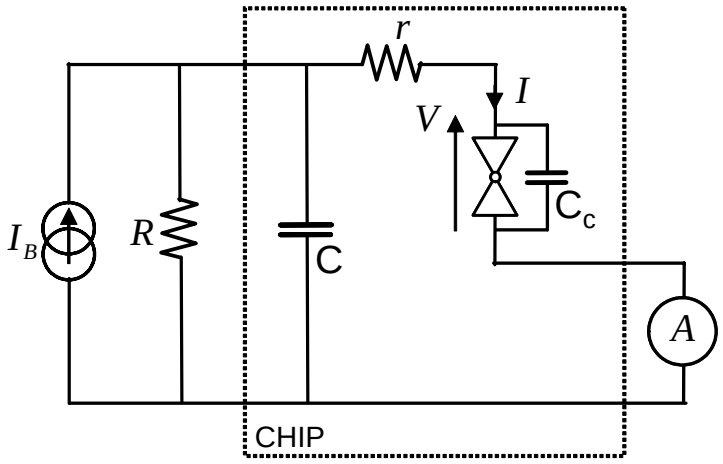

Figure 5: Schematic representation of a generic setup fulfilling the requirements for the measurement of the supercurrent peak. The large capacitor is at high frequencies a short that isolates the on-chip circuitry from the rest of the setup. The dc shunt resistor R has been represented off chip.

With appropriate values for the three elements of this setup it is possible to voltage bias the contact, damp the phase fluctuations at all frequencies and keep the electrons cold, an important requirement to investigate physics involving energies of the order of the

Josephson coupling in atomic contacts. Essentially, the capacitance *C* has to be as large as possible (an infinite capacitor provides a perfect voltage source). The small microfabricated resistor *r* has to be small enough for the dynamics of the phase across the contact to be classical and overdamped. The first requirement is fulfilled for $r \ll R_Q \approx 26\ \mathrm{k\Omega}$. Assuming $C \to \infty$, the second criterion imposes $r \ll Z_c$, where $Z_c = \sqrt{L_c/C_c} = \sqrt{\varphi_0/(C_c I_0)}$ is the impedance of the Josephson weak link. For typical values of the intrinsic capacitance of the contact C_c (a few fF) and of the Josephson inductance L_c (a few nH) this leads to $r \ll 1\ \mathrm{k\Omega}$. However as the external capacitor is finite (typically not much larger than 100 pF with the simple technology used here), it is also a necessary condition (assuming $C_c \to 0$) to obey $r \gg \sqrt{L_c/C} = \sqrt{\varphi_0/(CI_0)} \sim 10\ \Omega$. The overall criterion is therefore $10\ \Omega \ll r \ll 1\ \mathrm{k\Omega}$.

Of course, from the point of view of Joule dissipation it is favorable to have the smallest possible resistance within this range.

Finally, the resistor *R* plays a role mainly in determining the low frequency stability of the *IV* measurement. The precise conditions imposed on its value will be discussed later on.

In practice, we have tried to implement this idea of a split circuit in two different setups that differ essentially in the exact configuration of the on-chip ac dissipation and by the technique used to measure the current flowing through the contact. They are presented in the next subsections.

2.1.1 SQUID amplifier setup

Figure 6 presents a setup in which the current through the contact was measured using a SQUID array amplifier [14, 15] provided by Prof. Martin E. Huber of the University of Colorado at Denver. This setup was used in the experiment on the Shapiro resonances described in chapter 3. A SQUID amplifier[1] is very well adapted to measure small signals on low impedance sources, and has been used already to measure the supercurrent peak in planar tunnel junctions [16]. The dc voltage bias is provided by the

[1] Details on the operation of the SQUID amplifier can be found in appendix 2.

current source I_B shunted by the resistor R. In this setup, R is a surface mounted component placed on the chip (see Figure 6). The ac dissipation is ensured by the resistor r, microfabricated close to the contact, and the large capacitor C formed by a very large on-chip contact pad and the ground plane of the substrate.

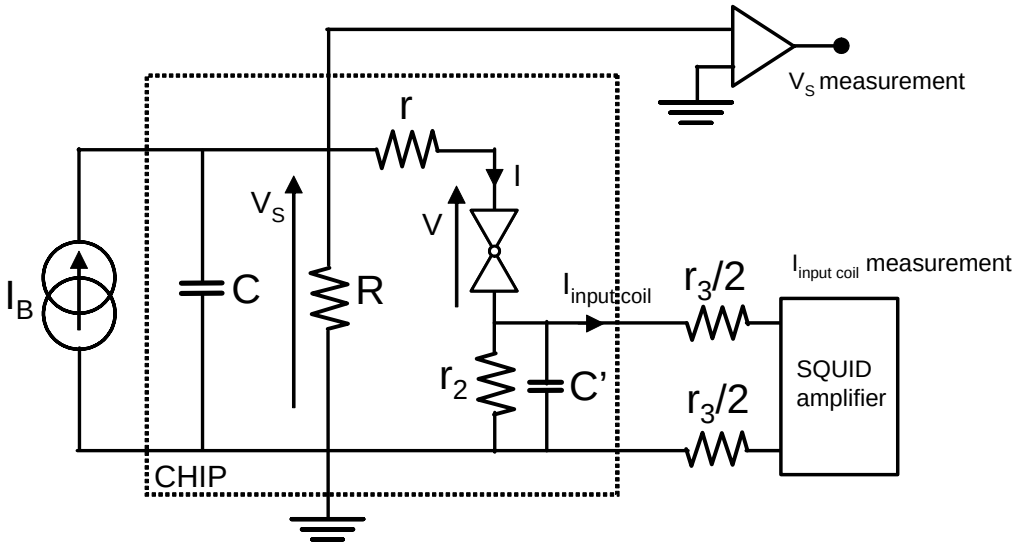

Figure 6: Electric circuit in which the atomic contact is embedded for the measurement of the current with the SQUID amplifier.

The role of the resistor r_2 is to pick-up a fraction of the current in the contact and feed it in the input coil of the SQUID to measure it. As depicted on Figure 6, the lossy twisted pair line connecting the chip to the SQUID superconducting input coil, can be represented essentially by two resistors, the same on each wire, shunted by the capacitance C' of a second smaller connecting pad. Therefore, a fraction $r_2/(r_2+r_3)$ of the dc current in the contact is fed into the input coil of the SQUID.

To establish the conditions on the values of the different resistors (R, r, r_2, r_3) to voltage bias the contact, we can model the electromagnetic environment of Figure 6 by a simplified version of it, respecting both the dc and high frequency limits for the dissipation seen by the junction, as sketched in Figure 7. It corresponds to the circuit of chapter 2, section 3, for which the full form of the supercurrent peak can be calculated.

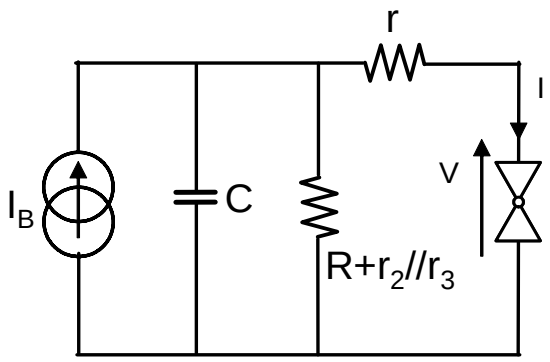

Figure 7: Simplified version of the electromagnetic environment seen by the junction in the circuit of Figure 6.

The on-chip physical realization of this experimental setup is presented on Figure 8.

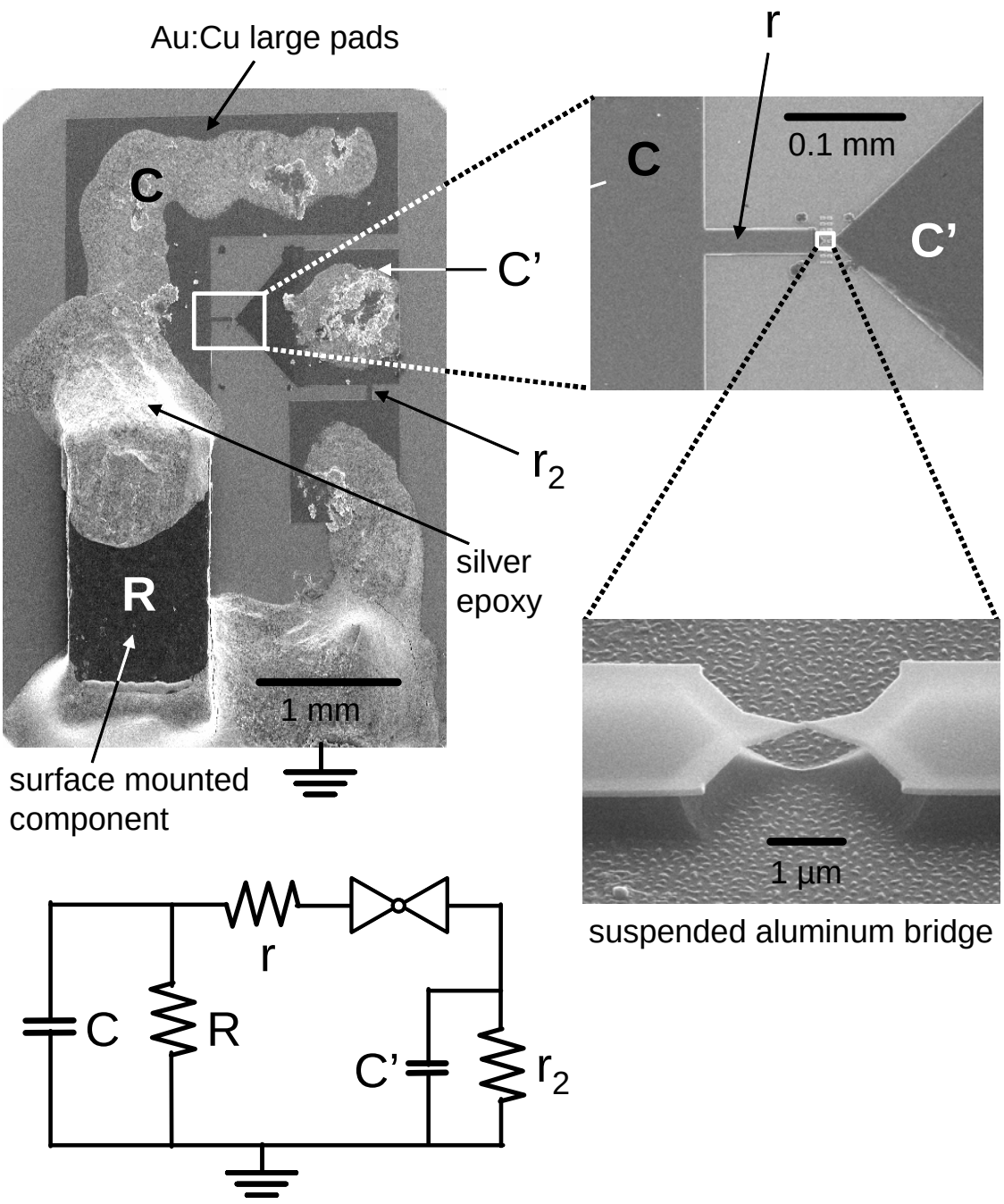

Figure 8: SEM micrographs (3 successive zooms) and on-chip finite elements circuit scheme of one of the samples in which the current through the contact is measured using a SQUID amplifier. The biasing resistor R is a commercial component mounted on the chip with silver epoxy. The two microfabricated resistors r and r2 are carved in a 60 nm thick Au:Cu alloy layer. The two capacitors are formed between the contact pads and the metallic substrate, the dielectric being a 1.6 µm thick polyimide layer. Typical values are $R \sim 50\ \Omega$, $r \sim 7\ \Omega$, $r_2 \sim 6\ \Omega$, $C \sim 100$ pF, and $C' \sim 30$ pF.

Let's comment here on the expected electronic temperature of the resistors. The electrons heat up because of the power P dissipated by the current traversing the resistor. If they cool down just by relaxing their energy into the phonon bath (assumed at temperature T_{ph}), the temperature T_{el} at which the electrons thermalize is limited to [10]:

$$T_{el} = \left(\frac{P}{\Sigma V} + T_{ph}^5 \right)^{1/5},$$

where V is the volume and Σ depends on the material considered. A typical value for the metals and alloys considered here is $2\ \mathrm{nW.K^{-5}.(\mu m)^{-3}}$.

For a macroscopic resistor the volume is large enough for the electrons to completely thermalize with the phonon bath. On the contrary, the volume of the microfabricated resistors r and r_2 is only of the order of $V \sim 100\ \mu\mathrm{m}^3$. In a typical experiment aiming to measure the supercurrent peak of an atomic contact with a critical current $I_0 = 50$ nA, the maximum dc power dissipated is $P = rI_0^2 \sim 20$ fW. If one assumes the phonon bath to be thermalized at the cryostat temperature (i.e. $T_{ph} = 20$ mK), the electronic temperature is then expected to saturate at $T_{el} \approx 100$ mK. In fact, this is a worse case estimation as we haven't taken into account the possibility for the hot electrons to diffuse away from the resistor into one of the attached large pads. The actual temperature of the electrons in the resistors is thus expected to be lower than this estimation.

2.1.2 FET amplifier setup

In practice, as discussed in chapter 3, the electromagnetic environment of the contact in the previous setup was not as good as required. We could attribute this to the physical implementation of the large capacitor C. The "L" shape of this structure and its rather large dimensions made in fact its stray inductance and parasitic resistance not negligible. As a result, this large pad did not behave as a simple large capacitor at the highest frequencies. Moreover, as we suspected the SQUID to be the source of at least part of the spurious noise we observed in the experiments, we decided to implement a different current monitoring scheme.

Figure 9a presents a second setup used in the experiments on the supercurrent peak and on the ac Josephson currents aiming to a better control of the environment seen by the atomic contact. It is essentially a four-point measurement setup. The voltage bias is ensured by the current source shunted by the off-chip resistor R. The ac currents are damped locally on the small loops formed by the four on-chip microfabricated resistors r (see Figure 11), and the shorting capacitors. In this setup, the current through the contact is obtained by measuring the voltage drop across one of the on-chip resistors r with a room temperature low-noise JFET amplifier.

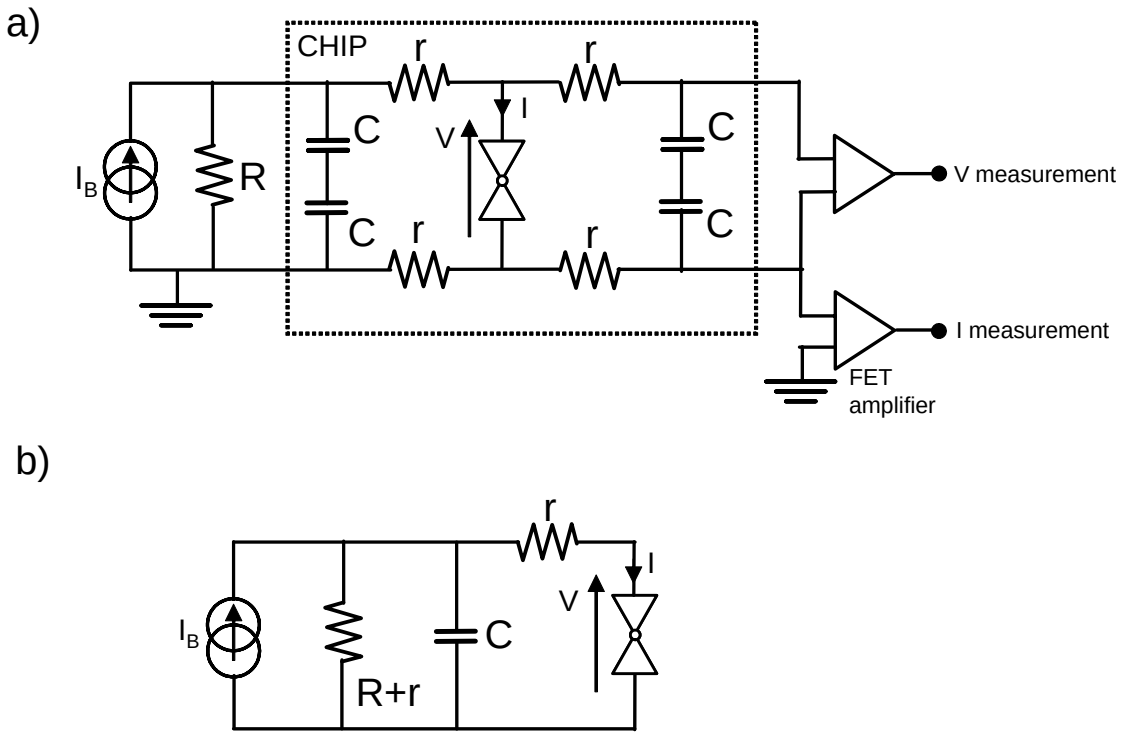

Figure 9: Actual (a) and simplified (b) electromagnetic environments of the atomic contact (double triangle symbol). The current in the contact is obtained by directly measuring the voltage drop across one of the on-chip resistors r.

Figure 9b shows an almost equivalent circuit for the electromagnetic environment as seen by the junction in the circuit of Figure 9a. The impedances Z_a and Z_b seen by the contact in both situations are compared on Figure 10, where their real and imaginary parts are plotted versus frequency. The values chosen for the graph are $R = 50\ \Omega$, $r = 40\ \Omega$ and $C = 100$ pF, very close to those implemented in practice.

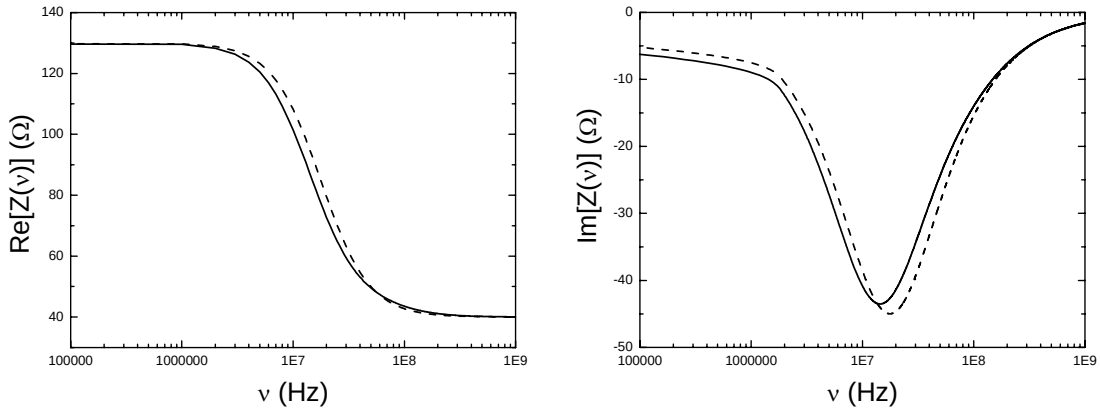

Figure 10: Comparison of the impedances Z_a (solid line) and Z_b (dashed line) seen by the contact in the actual and simplified electromagnetic environments of Figure 9.

The simplified environment of Figure 9b, reproduces almost perfectly the real environment of Figure 9a at all frequencies. The on-chip realization of this experimental setup is presented on Figure 11.

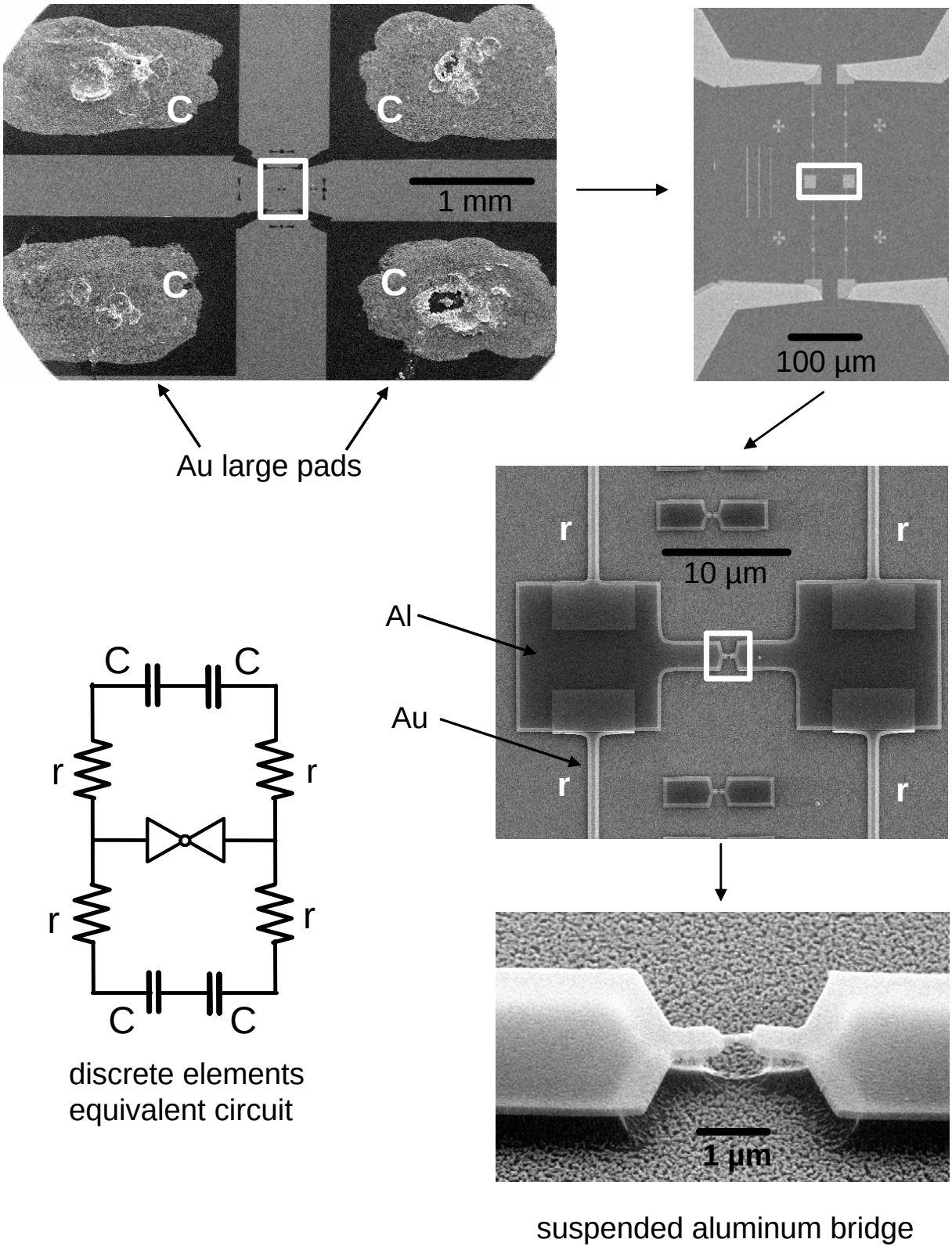

Figure 11: SEM micrographs (4 successive zooms) and on-chip finite elements circuit scheme of a sample in which the IV characteristic are monitored using a four point measurement technique. The resistors are 500 nm wide, 70 µm long wires carved in a 30 nm thick pure gold layer. The four capacitors are formed between the very large gold contact pads and the metallic substrate, the dielectric being a 1.6 µm thick polyimide layer.

As the volume of the resistors r is in this case very small ($V \sim 1\,\mu m^3$), the electronic temperature is expected to saturate slightly below $T_{el} \approx 140$ mK, the latter value corresponding to the case where the only cooling mechanism is the electron-phonon coupling.

2.2 Dc voltage biasing the atomic contact

When measuring the IV characteristic of an electrical dipole presenting regions of negative differential resistance, like the sharp supercurrent peak in our atomic contacts, one has to make sure to provide a source with a quite small impedance. If not, some parts of the IV characteristic will become unstable and therefore won't be amenable to measurement. The choice of the source impedance value is therefore dictated by two contradictory conditions. One the one hand it cannot be to small to avoid excessive overheating. On the other hand it has to be kept as small as possible in order to provide the contact with a voltage V not too dependent on the current I flowing through it. Of course, for a perfect voltage bias the resistance has to be vanishing small. But this requirement is not strictly necessary to guarantee the stability of the measurement of the IV. It is sufficient that the load line $I(V) = \frac{X}{X+r} I_B - \frac{V}{X+r}$ imposed by the current source I_B is steeper than the $I(V)$ characteristic of the contact in the regions of negative differential resistance (see Figure 12). In the setup presented in section 2.1.1 $X = R + r_2 // r_3 + r$, and $X = R + r$ in the setup of section 2.1.2. Depending on the slope of the loadline, the system admits different solutions.

If the load line is not steep enough, there can be three solutions for a given value of the bias current. The solution M is only metastable, and the system eventually switches to the stable point S, because of the thermal fluctuations in the resistors. The solution U is unstable because at that point the IV characteristic is steeper than the loadline.

On the contrary, for a steep load line the system has only one stable solution S for a given value of I_B, i.e. a good voltage bias is achieved. Therefore, on regions of negative slope on the $I(V)$ characteristic, the following condition has to be satisfied:

$$-\frac{1}{X+r} < -\frac{\partial I(V)}{\partial V} \Leftrightarrow X < \frac{1}{-\frac{\partial I(V)}{\partial V}} - r$$

This inequality defines an upper bound R^* for the value R of the dc shunt resistor This value differs between the two setups.

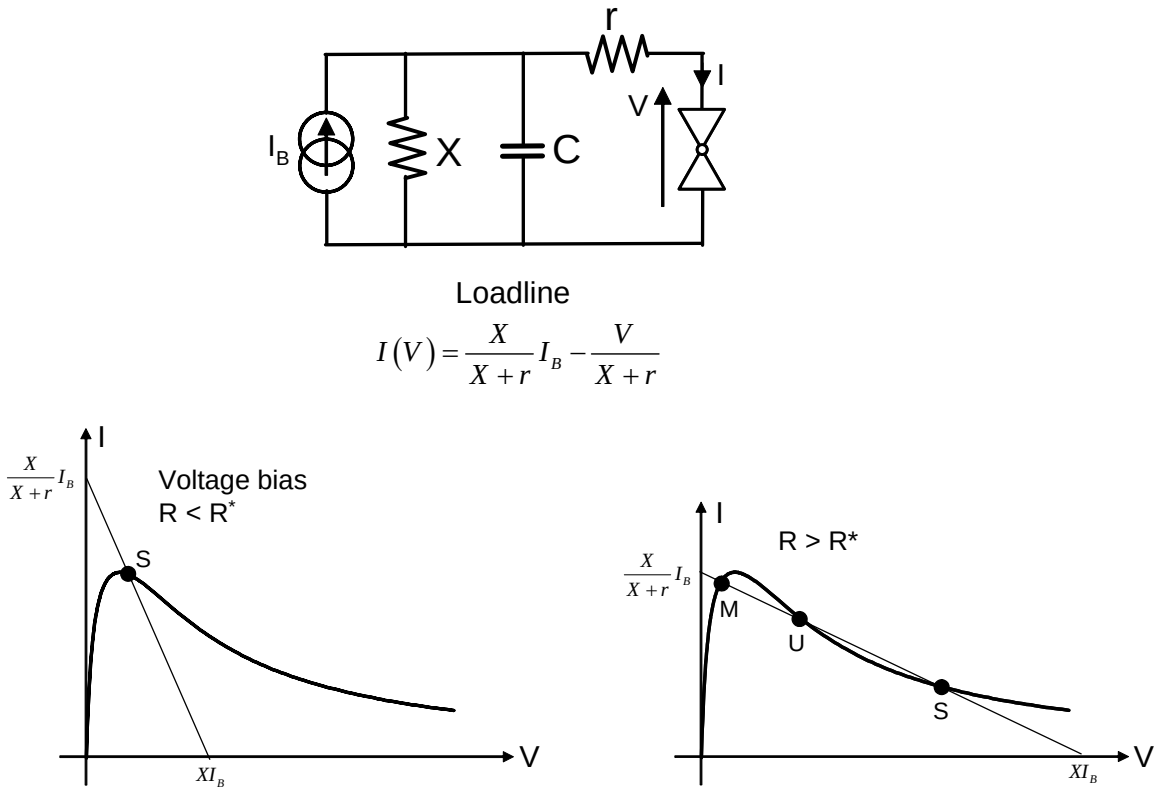

Figure 12: Simplified circuit in which the atomic contact is embedded (upper panel). If the loadline defined by the biasing circuit is steeper than the negative differential resistance regions of the IV a single stable solution exists and the full curve can be swept continuously (left bottom panel). If not (right bottom panel), for a given bias current there can be three solutions: a stable one (S) at large voltages, an unstable one (U) at intermediate voltages, and a metastable one (M) in the phase diffusion branch, from which the system eventually switches to (S).

For the SQUID setup (Figure 6) the upper bound R^* for the value of the dc shunt resistor is:

$$R^* = \frac{1}{-\left(\frac{\partial I(V)}{\partial V}\right)_{\min}} - r_2 // r_3 - 2r = \left(\rho - 2 - \frac{r_2 r_3}{r(r_2 + r_3)}\right) r ,$$

where

$$\rho = \frac{1}{-r\left(\frac{\partial I(V)}{\partial V}\right)_{\min}} .$$

and $I(V)$ is the current-voltage characteristic of the contact calculated for the simplified environment of Figure 7.

Similarly, for the FET setup (Figure 9), the upper bound R^* for R is:

$$R^* = \frac{1}{-\left(\frac{\partial I(V)}{\partial V}\right)_{\min}} - 2r = (\rho - 2) r ,$$

In general, the determination of R^* is a complicated task because the IV characteristic of the junction itself depends on the electromagnetic environment in which it is embedded, i.e. ρ depends on the three parameters R, r, and C (for the FET setup). Nevertheless, as shown in chapter 3, if the capacitor C shunting R is large enough, the shape of the IV is essentially determined by the resistor r. We have therefore calculated ρ for a Josephson tunnel junction embedded in a purely ohmic environment r, using the analytical Ivanchenko-Zil'berman result of chapter 2 (see Figure 13).

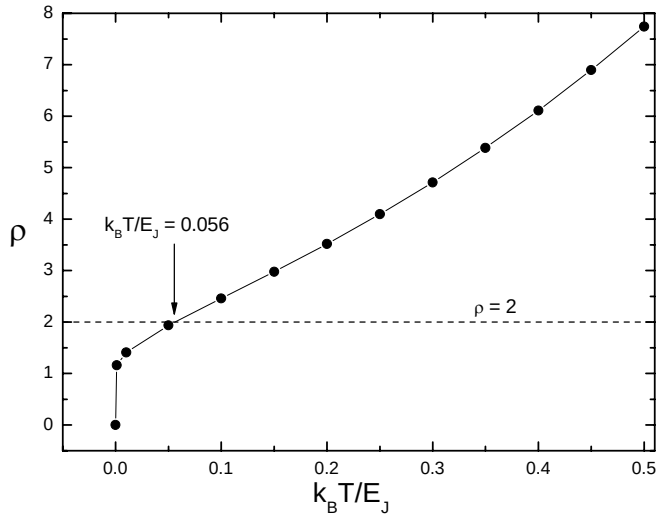

Figure 13: ρ as a function of the reduced temperature. The calculation of ρ has been carried out using the Ivanchenko-Zil'berman result for a Josephson tunnel junction.

It is clear that ρ is an increasing function of $\frac{k_B T}{E_J}$ since the IV becomes smoother as the ratio $\frac{k_B T}{E_J}$ increases. For the FET setup (Figure 9), there is a threshold value $\frac{k_B T}{E_J} = 0.056$, reached when $\rho = 2$, below which the supercurrent peak becomes too sharp, making thus impossible to really voltage bias the contact with this setup. A similar threshold exists for the SQUID setup, but its exact value depends on the resistors r_2 and r_3 used to probe the current. Even though ρ is calculated for a Josephson tunnel junction, the result can be safely applied to the case of contacts with sizeable transmissions. Indeed we have seen in chapter 2 that the shape of the supercurrent doesn't depend too much on the value of the transmission. It is only for contacts with transmission close to unity, that a detailed analysis has to be performed because the shape of the IV 's at low voltages highly depends on the exact transmissions.

Moreover, as was shown in chapter 2, the effect of the finite capacitance C is to stretch the IV of the contact on the voltage axis. It therefore tends to reduce the steepness of the IV. Therefore the value of R^* obtained in the large capacitance limit will always be beyond the actual threshold value when finite capacitance effects comes into play.

At the end, one is forced to adopt a reasonable compromise within all the constraints mentioned above. For example, in the experiments on the supercurrent peak with the FET setup, the values chosen for the resistors were $R \approx 50\ \Omega$, and $r \approx 40\ \Omega$. The condition $R < (\rho - 2) r$ rewrites $\rho > 2 + \frac{R}{r}$. In the experiments this leads to $\rho > 3.25$ which is equivalent to $\frac{k_B T}{E_J} > 0.1747$ from the $\rho\left(\frac{k_B T}{E_J}\right)$ plot. Therefore, contacts with critical current above 30 nA displayed some switching at the lowest electronic temperatures ($\sim 125\,\mathrm{mK}$) reached in the experiments.

Of course by choosing a large enough shunt resistor it is always possible to current bias the contacts. Switching measurements performed on current biased contacts are reported in chapter 2.

2.3 Phase biasing atomic contacts

Chapter 4 presents experiments aiming at the direct measurement of the current phase relation of an atomic contact for which the mesoscopic pin code is known. To measure, for a given contact, both the current phase relationship and the transmissions, the challenge is to find a setup that enables the contact to be reversibly phase biased or voltage biased, the latter situation allowing to extract the mesoscopic pin code of the contact from the measurement of its IV characteristic.

The solution that we propose is to place the atomic contact in parallel with a large Josephson tunnel junction which acts like a reversible superconducting switch. The physical implementation of the on-chip circuit is presented on Figure 14.

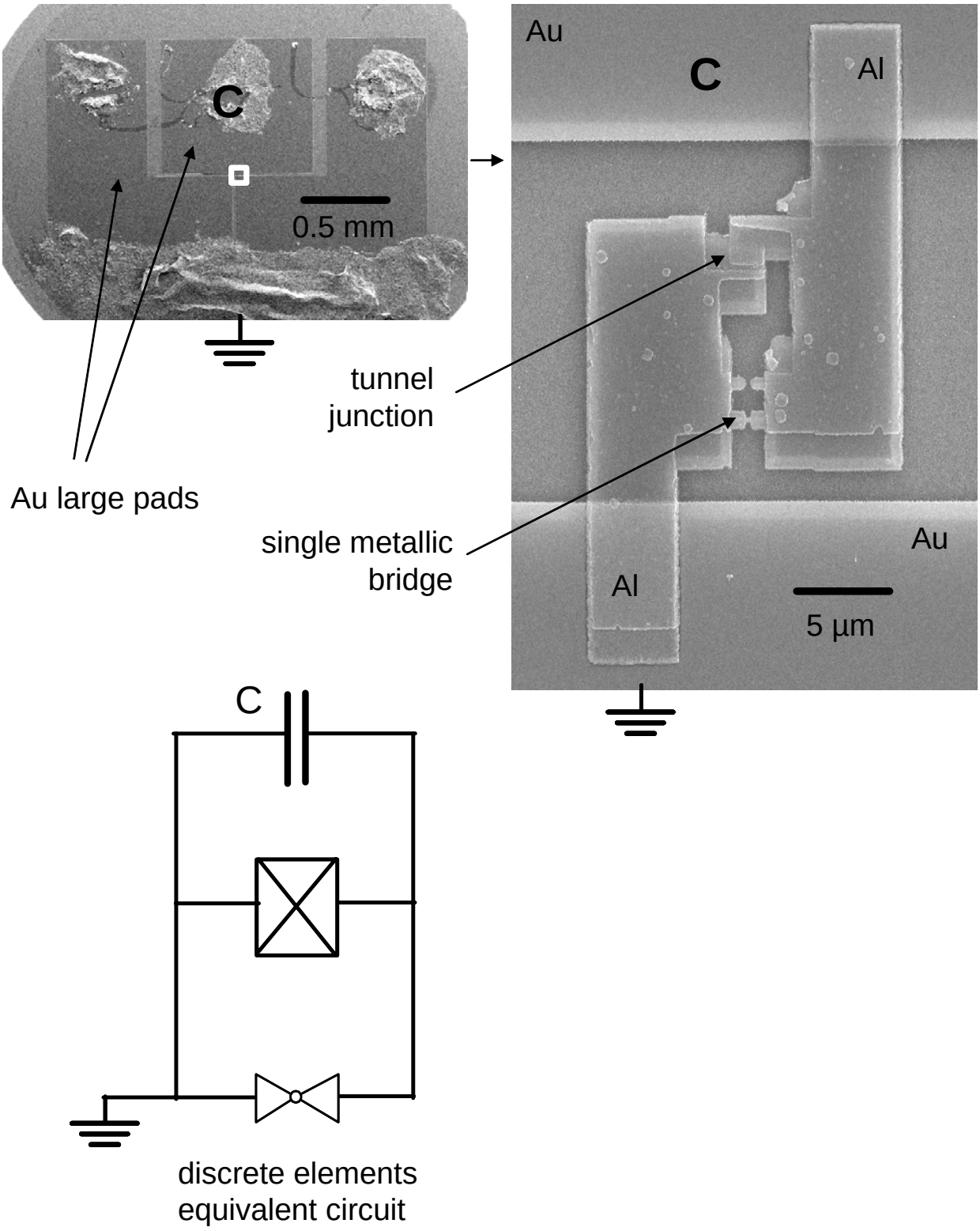

Figure 14: SEM micrographs (2 successive zooms) and equivalent circuit of the sample used in the current-phase relation experiment (chapter 4). In the discrete elements equivalent circuit, the cross box symbol represents the large Josephson tunnel junction and the double triangle symbol the atomic contact.

3 Measurements at low temperature, example of the FET amplifier setup

The Josephson coupling energy for a weak link of critical current I_0 is $E_J = I_0\varphi_0$. For a typical value of the critical current - $I_0 = 40$ nA -, this energy is $E_J = 0.953$ k_BK. Experiments must therefore be performed at temperatures well below 1 K. Measurements were carried out in a Oxford ^{3}He/^{4}He dilution refrigerator, with a base temperature of 17 mK. The metallic substrate is thermalized through the pushing rod and the two countersupports of the bending mechanism. The full bending mechanism is enclosed in a shield consisting of 2 boxes, the outermost one in copper and the inner one in aluminum, to screen the magnetic flux and the electromagnetic noise. The whole setup is attached to the mixing chamber of the cryostat. Before entering the shields all the wires necessary to bias and measure the sample are filtered. The detailed wiring of the cryostat can be found in appendix 3.

The experimental setup presented here was used to measure the *IV* characteristics of voltage biased contacts. With this setup, it was therefore possible to go beyond the experiments performed by M. F. Goffman *et al.* [11] by measuring the full supercurrent peak and not only the diffusion branch, the only part of the supercurrent peak amenable to measurement for a current biased contact.

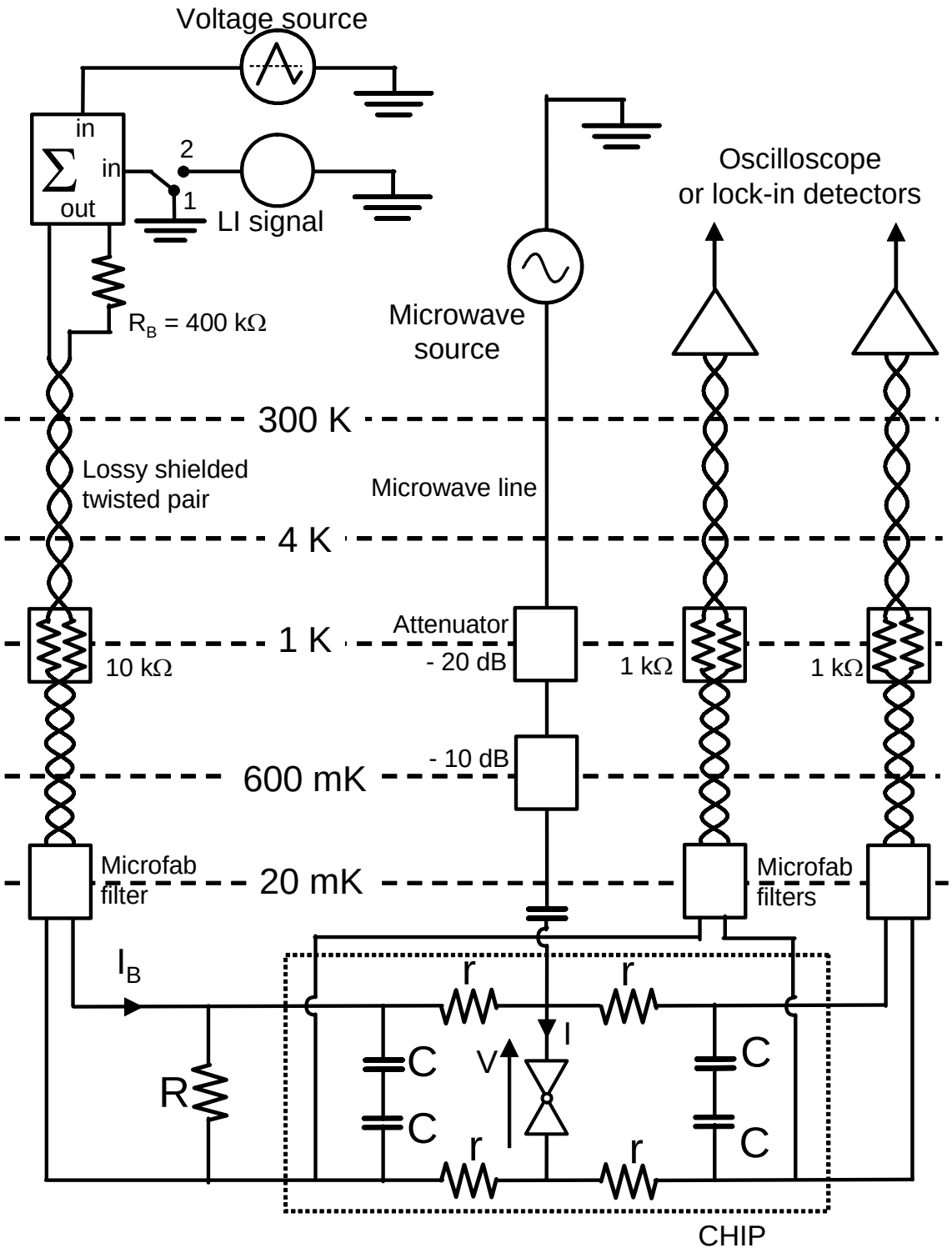

Figure 15: Detailed wiring of the experimental setup for measuring IV characteristics both in the supercurrent peak and in the ac Josephson currents experiments with a FET amplifier to measure the current. The box Σ represents a bipolar summing amplifier.

The voltage bias V across the atomic contact is obtained by using a voltage division between a large bias resistor $R_B = 400\ \text{k}\Omega$ and a small shunt resistor $R = 50\ \Omega$. This setup enabled both to measure the IV characteristic of the contact and also its differential conductance. The voltage source (Agilent 33250A) was used as a ramp generator in the experiments. To measure the IV characteristic, the switch is placed in position 1. Measurements were performed at frequencies within the bandwidth of the lines, at around 1 kHz.
To measure the differential conductance, the switch is placed in position 2. The summing amplifier (box Σ) adds up the two signals: the dc voltage provided by the voltage source and the ac excitation provided by the lock-in source (Stanford SR 830).

The dc current I through the contact is obtained by measuring the voltage drop across one of the on chip resistors r. The dc voltage V across the contact is directly measured. Both signals are measured using low-noise battery powered differential FET-preamplifiers of fixed gain $\times 100$ (NF LI-75A) followed by an amplifier of selectable gain (Stanford SR 560). The signals were then digitized by a Nicolet Pro44 oscilloscope (for an IV characteristic measurement) or by the Stanford SR 830 lock-in detectors (for measuring the differential conductance) and transferred to a PC for treatment.

It is necessary to know the value of the resistor r for the measurement of the dc current I. Therefore, the two resistors R and r were precisely measured. One measures the resistor R by fully opening the atomic contact. In this configuration, all the bias current flows through the resistor R, whose value is then obtained by measuring the voltage drop across it. Once the value of R is known, the bridge is closed as much as possible so as to have a large critical current. r is determined by measuring the voltage drop across it, knowing that only a fraction $R/(R+2r)$ of the bias current flows through it (provided the contact stays on its supercurrent branch at $V = 0$). In the experiments, the typical values were $R = 50\ \Omega$ and $r = 40\ \Omega$.

In the experiments on the ac Josephson currents (chapter 3), the microwaves were applied on the contact through a 20 GHz bandwidth line along which attenuators have been placed at different stages of the cryostat to reduce the noise reaching the contact.

In this setup the microwave is coupled to the contact through an antenna placed 2 mm away from the contact region.

4 Determination of the mesoscopic pin code of the contact

In chapter 1, we showed that the IV characteristics of Josephson weak links were highly non linear in the voltage range $|V| < 2\Delta/e$, where the processes responsible for carrying the current are multiple Andreev reflections. The onset of these processes occurs at well defined values of the voltage, leading to a rich structure on the IV. Since atomic contacts accommodate only a small number of channels, their IV characteristics contain enough information to extract their mesoscopic pin code. In this section, we review the standard procedure used throughout this Ph.D. work to determine the transmissions of the atomic contacts.

The determination of the pin code is done by decomposing the IV characteristic into the contribution of a few independent conduction channels:

$$I(V) = \sum_{i=1}^{N} I(V, \tau_i, \Delta),$$

where N is the total number of channels in the contact and Δ the superconducting gap.

The procedure used to extract the mesoscopic pin code $\{\tau\} = \{\tau_1, ..., \tau_N\}$ is a least-square fit based on a Monte-Carlo algorithm. The code has been developed by G. R. Bollinger at UAM [12]. The theoretical elementary IV's have been calculated using a code developed by J. C. Cuevas *et al.* [13].

In a first step, the number of channels and the value of the superconducting gap are determined. For aluminum contacts, the actual value of the gap is searched for in the interval from 175 to 185 μeV by steps of 0.1 μeV. The number of channels is first set to ten which corresponds to contacts larger than the largest contacts we have actually measured.

The fitting procedure is then started. For each value of the gap, the Monte-Carlo fit of the transmissions is ran. As this step is only intended to determine the value of the superconducting gap and the number of channels but not their transmissions, the number of Monte-Carlo iterations is limited to 100000 for each gap value. Moreover, the transmissions are allowed to explore a broad range around their current value to ensure a sufficient convergence within the allowed number of iterations. The chi-squared is calculated for each value of the gap scanned. The actual value of the gap is the one that minimizes the chi-squared. Once the gap is determined, its value is kept constant throughout the rest of the fitting procedure and the number of channels is reset to the number of channels with a transmission different from zero. Limiting the number of channels to its actual value speeds up the second step of the fitting procedure.

The second step is intended to determine the transmission of each channel accurately. The Monte-Carlo fitting procedure is no longer limited by the number of iterations. We leave it running as long as necessary to reach a steady situation where the transmissions no longer change. Throughout the second step of the Monte-Carlo fit, the allowed noise on the channel transmissions is progressively reduced to obtain a fit with the best accuracy.

On Figure 16, *IV* characteristics of two contacts with different mesoscopic pin code and their corresponding fits are plotted. The two contacts presented here have nearly the same normal state conductance but completely different mesoscopic pin codes. The value of the gap differs on the two curves of Figure 16, even if they have been measured on the same sample. The dilution fridge had to be opened and put at atmospheric pressure between the two measurements, resulting in a possible contamination of the aluminum electrodes.

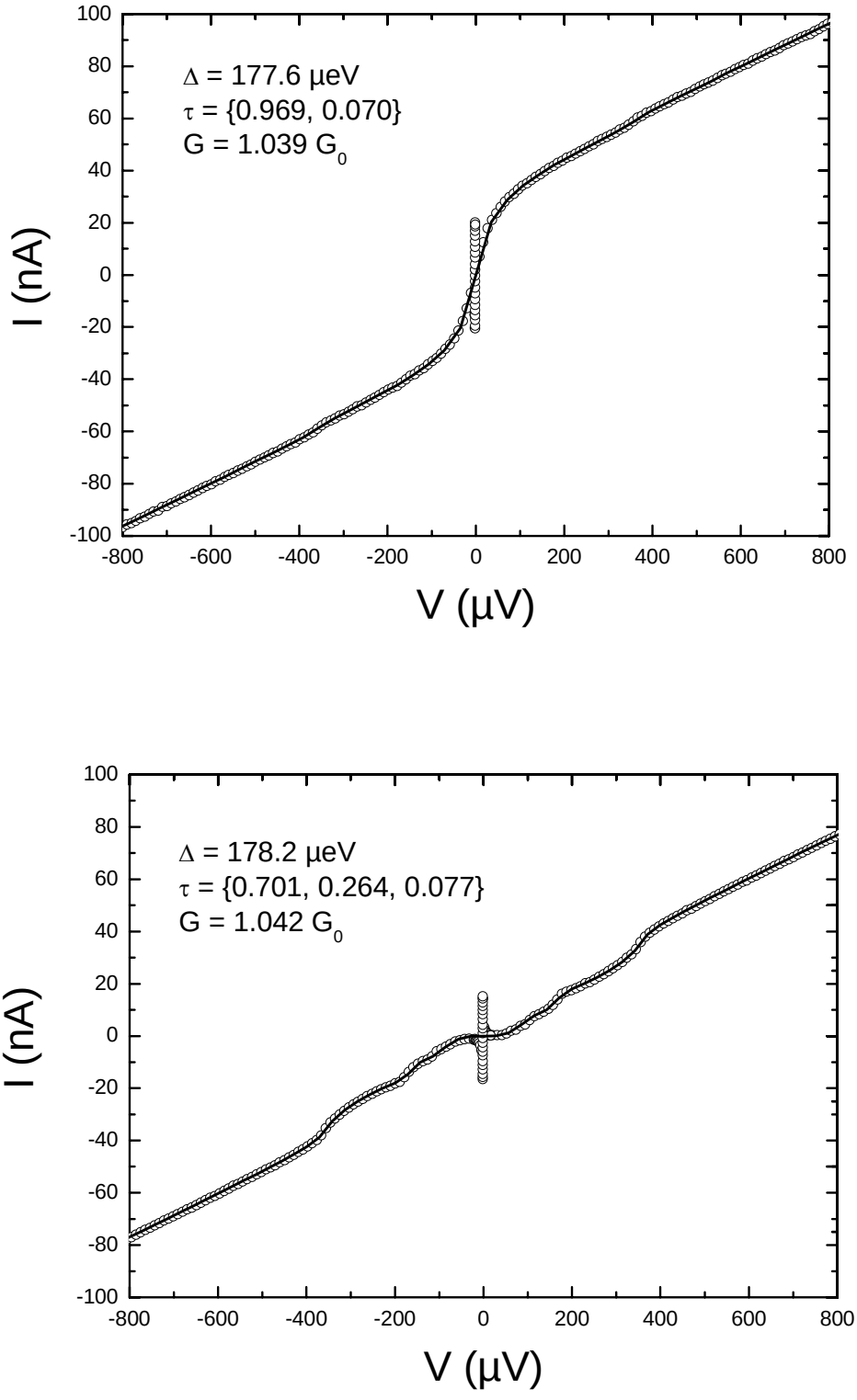

Figure 16: Two IV characteristics of aluminum single atom contacts. The two contacts have nearly the same normal state conductance but correspond in fact to different mesoscopic pin codes.

It is interesting to discuss the contribution to the current of channels with $\tau \ll 1$, $\tau \sim 1$ and channels of intermediate transmissions:

- The current through a channel with $\tau \ll 1$ is vanishingly small for $|V| \ll 2\Delta/e$. It only becomes sizeable above this threshold. Moreover, it doesn't carry any excess current[2] at large enough voltages. Therefore the information on the channels with $\tau \ll 1$ lies in the slope of the IV at large voltages.
- On the contrary, highly transmitting channels give a large contribution to the current at low voltages and they also carry some excess current. Therefore, the information on the highly transmitting channels lies both at low voltages and high voltages on the IV characteristic of a contact.
- The information on channels with intermediate transmission lies in the non-linearities on the IV in the voltage range $|V| < 2\Delta/e$.

For details on the accuracy of the fit of the transmissions, we refer the reader to R. Cron's Ph.D. thesis [1].

[2] The excess current is defined as $\lim_{V' \to \infty} \left[I(V') - V' \times \left(\frac{\partial I(V)}{\partial V} \right)_{V=V'} \right]$

Appendix 1: Sample fabrication

This appendix presents the nanofabrication steps involved to obtain a narrow metallic bridge suspended over a few microns on a flexible substrate (see Figure 1). In the experiments, the metallic bridge is broken by bending the substrate under cryogenic vacuum to obtain the atomic contact. The on-chip environment in which the contact is embedded is also fabricated at the same time.

First, an insulating polyimide layer is deposited on the flexible metallic substrate and topped with an electrosensitive resist. Then, the resist is exposed to the electron beam of a scanning electron microscope. During the development, the exposed parts of the resist are dissolved and a mask is obtained on top of the polyimide. Metal is then deposited through the mask on the polyimide. During the lift-off, the remaining resist is dissolved and only regions corresponding to the openings of the mask are left with a metallic layer. This procedure is repeated two times: first to fabricate the on-chip dissipative environment (made out of Au or Au:Cu alloy) and then to fabricate the metallic bridge (aluminum). The different steps of the fabrication of a sample are now presented in more detail.

1 Wafer preparation

Polishing of the wafer

The substrates are 0.3 mm thick and 3 inches in diameter bronze wafers. The wafers are first roughly polished using abrasive disks and water as lubricating agent to remove the larger scratches. In a second step, soft disks loaded with diamond paste with particles of 9, 6, 3 and 1 μm are used successively to obtain a residual roughness of about 1 μm. During this step, oil is used to lubricate the disks. The wafer is carefully rinsed between each diamond paste step to avoid contamination by larger particles. During the whole process, the spin speed of the rotating polishing machine is kept low, at about 30 rpm. Each polishing step lasts for about 30 min.

The wafer is then processed in a clean room. It is first cleaned in an ultrasonic bath with isopropanol and acetone. It is rinsed with isopropanol and blow dried with nitrogen.

Polyimide layer deposition

First an adhesion promoter (Ultradel A600) is spun at 2000 rpm for 30 s. Then the wafer is dried on a hot plate at 100°C for 1 min. It is cooled down afterwards with a nitrogen blow. A solution of PI2611 in N-methyl-2-pyrrolidone (30 g (HD Microsystems PI2611[3]) + 30 mL (N-methyl-2-pyrrolidone)) is spun at 2000 rpm for 1 min. Then it is baked in an oven for one hour, starting from room temperature, up to 180°C to remove the solvent and get a uniform thickness over the wafer thanks to surface tension. Finally, the polyimide is annealed at 350°C for 1 hour in a vacuum chamber under a residual pressure of 10^{-6} mbar. This last step ensures that the polyimide film will keep its elastic properties at low temperatures. The final thickness of the polyimide is 1.6 µm. It is measured by laser interferometry, knowing the refractive index provided by HD Microsystems ($n = 1.90$).

The polyimide layer planarizes the surface of the substrate. It also insulates the nanocircuit from the substrate. The capacitors of the on-chip environment can be designed using the metallic substrate as a ground plane and the polyimide layer as a dielectric. The polyimide can also be etched to fabricate the suspended bridge that we break to form the atomic contact.

Electrosensitive resist deposition.

To realize the suspended masks through which the metallic thin films will be evaporated, a bilayer of electrosensitive resists is used. The bottom layer (MMA/MAA 8.5 EL10) is spun on the polyimide at 2500 rpm for 1 min. Then the solvent is evaporated on a hot plate at 160°C. This layer has a thickness of about 500 nm. The top

[3] The PI 2611 solution of HD Microsystems contains 13.5% in weight of polymer. The solvent is N-methyl-2-pyrrolidone.

layer (PMMA 950 A3) is spun at 4800 rpm for 1 min. The thickness of this layer is around 100 nm. The bilayer is then baked for 25 min on a hot plate at 160°C.

Using this electrosensitive bilayer is a convenient way to obtain a suspended mask by electron beam lithography. The bottom layer, which has a greater electron sensitivity, sustains the suspended mask through which metals are deposited. The two main advantages of having a suspended mask are the following:

- It is possible to deposit the metallic layers at an angle, a useful technique to fabricate tunnel junctions,
- The lift-off is easier.

Cutting of the substrate into chips

Then the substrate is cut into chips that will be processed individually later on. The chips are rectangles of size 16 mm by 6 mm.

2 Electron beam lithography and metal deposition

The successive steps described in this section are summarized on Figure 17.

Electron beam exposure

The lithography is performed in a scanning electron microscope (SEM) whose beam is driven by a computer according to a pattern defined in the Elphy Quantum software.
The exposure dose of the bilayer is 180 $\mu C/cm^2$ with a 25 keV electron beam. The SEM has different beam currents and magnifications which are chosen depending on the sizes of the structures to pattern. The currents range from 15 pA to 100 nA. The smaller the pattern, the smaller the current and the greater the magnification.

The electrons penetrate the bilayer and lose their energy in the resist. In irradiated regions, the polymers chains are broken into small pieces.

The MMA/MAA layer is affected by the electron beam in a broader region because it has a greater sensitivity. Moreover it is closer from the metallic substrate and experiences more backscattered electrons than the PMMA layer. This undercut can be enhanced locally by an additional low dose affecting only the bottom layer.

Development

The chips are placed in a solvent (MIBK 1vol : isopropanol 3vol) for 35 sec at 20°C. The irradiated parts of the resist are completely removed whereas the non-exposed regions remain unaffected. The mask is then rinsed for 20 s in isopropanol and blow dried with nitrogen.

Metallic thin film deposition

The metallic thin films are deposited using an electron gun evaporator or a Joule evaporator. The metals are deposited at a typical rate of 1nm/s and at a pressure 2×10^{-6} mbar. The typical thickness of the films deposited is 100 nm. The sample is fixed on a tiltable sample holder enabling evaporation at different angles.

Lift off

After the evaporation, the chips are immersed in acetone at 65°C for 10 min. The mask and the metal on top of it are completely removed. The sample is rinsed with isopropanol and blow dried with nitrogen. Care is taken so that the sample doesn't dry between the lift-off and the rinsing. After lift-off, the sample is left with the desired metallic structure at the position of the openings in the suspended mask.

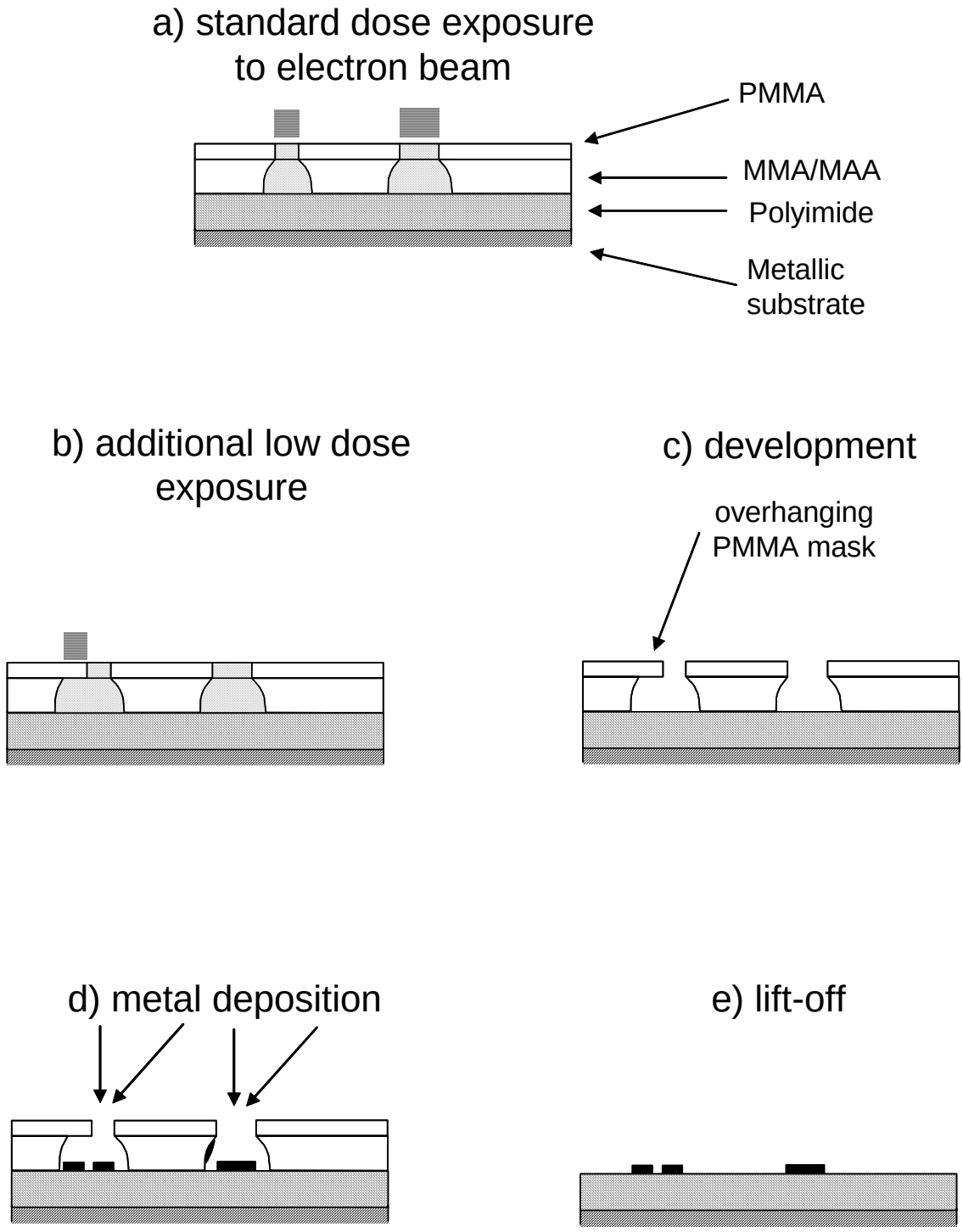

Figure 17: Successive steps in the lithography process. On panel d), some metal is deposited on the wall of the MMA/MAA bottom layer where no additional low dose exposure has taken place. This metal is removed during the lift off.

3 Reactive ion etching of the polyimide layer

To obtain the suspended bridge the polyimide is isotropically dried etched in a reactive ion etcher. To ensure the isotropic etching, the sample is maintained at 200°C during the etching.

The plasma conditions were the following:

A flow of 50 sccm O_2 and 5 sccm SF_6 at a total pressure of 0.3 mbar and an auto-polarization voltage of 25 V.

The vertical etching depth is monitored by means of a laser interferometer. Etching 1 μm vertically is sufficient to free the metallic bridge from the surface (see Figure 1).

4 Embedding the break junction in an on-chip electromagnetic environment

One of the great advantages of the nanofabricated mechanically controllable break junction technique is the possibility of embedding the junction in an on-chip electromagnetic environment. This is done by designing a specific pattern for the electron beam exposure, according to the electrical circuit one wishes to implement around the junction. The detailed fabrication procedures, very similar from one kind of chip to the other, are presented in the next subsections.

4.1 Samples measured with the SQUID amplifier setup

Resistors were made out of Au:Cu alloy (3:1 in weight) and capacitors were formed between the Au:Cu large pads and the metallic substrate, the dielectric being the polyimide layer. The chips were obtained with two lithography steps, with an intermediate alignment procedure. In the first step, the large pads, the resistors and alignment crosses were deposited in a Joule evaporator (1 nm Ti @ 0.1 nm/s, 60 nm Au:Cu @ 1nm/s). A few atomic layers of titanium are deposited before the Au:Cu alloy to increase its adhesion. After lift-off, a new bilayer is deposited on the single chip and

another lithography cycle is performed to obtain the aluminum bridge and the connections to the Au:Cu structures. It is possible to align the second lithography pattern on the Au:Cu structures because the bilayer is almost transparent to electrons, which allows for tracking the alignment crosses. Before depositing aluminum (100 nm @ 1 nm/s) in an electron gun evaporator, the Au:Cu structures are cleaned with an ion-milling procedure to ensure good electric contact between the two layers. The ion-milling is performed with ionized argon at an energy of 500 eV with a current density of ~ 1 mA.cm^{-2} during 2 seconds. The next step is the etching of the polyimide layer. At last, a surface mounted component (resistor $R = 25.3\ \Omega$) is glued with silver epoxy on the substrate.

The resistance per square of the 60 nm thick Au:Cu layer is $1.48\ \Omega\square$ at 300 K and $1.26\ \Omega\square$ at 4.2 K.

The measured resistances at 20 mK were $r_2 = 6.2\ \Omega$ and $r = 7.4\ \Omega$.

The relative dielectric constant of the polyimide has been measured at 300 K and at low frequency (1 kHz) was 3.2 (in good agreement with the value provided by HD Microsystems: 2.9). The expected capacitances were thus $C = 100$ pF and $C' = 30$ pF according to the surface of the pads and the thickness of the polyimide.

4.2 Samples measured with the FET amplifier setup

Instead of depositing a Au:Cu alloy in a Joule evaporator, Au (99.999% purity) was deposited in an electron gun evaporator in two different lithography steps. In the first step, a thin layer of gold was evaporated (1 nm Ti @ 0.1 nm/s, 30 nm Au @ 1 nm/s) to fabricate the resistors. Then a thicker layer of gold was deposited (200 nm Au @ 1 nm/s) to form the large pads. Because the sample had to be processed in air between the two layers of gold, an ion-milling cleaning was performed before depositing the second gold layer. We use a thicker layer for the connecting pads because the connecting spring probes would damage the thin layer used to obtain the desired value of the resistors. Also, this thick gold layer provides extra volume for the electrons in the resistors to thermalize with the phonon bath.

At 20 mK, the resistance per square of the 30 nm thick Au layer is $0.27\ \Omega\square$.
The resistors r were 500 nm wide, 70 µm long, leading to a resistance of $\sim 40\ \Omega$.

According to their surface and to the polyimide thickness and dielectric constant, the expected capacitance C of each large pad to the metallic substrate is 92 pF.

4.3 Samples measured in the current phase relation experiment

Gold was deposited (1 nm Ti @ 0.1 nm/s, 100 nm Au @ 1 nm/s) in an electron gun evaporator to fabricate the large pad forming the capacitor with the metallic substrate. In the second lithography step, aluminum was deposited at two different angles (0° and 55°) with an intermediate oxidation procedure. First, the metallic bridge and the first electrode of the tunnel junction are evaporated (100 nm Al @ 1 nm/s) perpendicularly to the substrate. Then the aluminum layer is oxidized under a total pressure of 8 mbar (15% O_2, 85% Ar (mol)) for 10 minutes. Then the sample is tilted to 55° and a second layer of aluminum (250 nm @ 1 nm/s) is deposited to form the top electrode of the tunnel junction. Because the width of the mask opening at the bridge constriction is 100 nm, equal to the thickness of the PMMA layer, the second image of the bridge consists of two disconnected electrodes. At the end, we are thus left with only one metallic bridge.

Appendix 2: SQUID amplifier as an ammeter

In section 2.1, two ways of measuring the current in the contact were presented: either using a SQUID amplifier setup or using a FET amplifier setup. To measure small signals on small impedances, a SQUID amplifier [14, 15, 16] is better suited. The experimental setup using a FET amplifier was presented in detail in section 3. We now present the experimental setup in which the SQUID amplifier was used.

1 Presentation of the experimental setup

The experimental setup depicted on Figure 18 was used in the Shapiro resonance experiment to measure IV characteristics of atomic contacts in presence of microwaves. As in the experimental setup presented in section 3, the requirement is to voltage bias the contact. The voltage bias is produced by feeding a current into the shunt resistor R in nearly the same way as in the setup depicted on Figure 15. The difference is the wiring: instead of using a twisted pair, a coaxial line was used to bias the sample, with a lossy part from 4 K to 20 mK and a microfabricated filter was placed at 4 K to prevent noise from reaching the contact. We had to use a coaxial line because all the lossy twisted pair lines from 300 K to 1K were used (3 for the SQUID amplifier and one for the measuring the voltage V_S (see Figure 18).

Instead of measuring the voltage drop across a resistor in series with the atomic contact, a fraction $I_{input\ coil}$ of the current in the atomic contact is diverted into the input coil of a SQUID amplifier and measured. In this setup, the other measured quantity is not the voltage across the contact directly, but rather the voltage V_S across the shunt resistor R. The voltage V across the junction and the current I through the junction are then deduced using:

$$\begin{cases} I = \left(1 + \dfrac{r_3}{r_2}\right) I_{\text{input coil}} \\ V = V_S - \left(r + \dfrac{r_2 r_3}{r_2 + r_3}\right) I \end{cases}$$

The values of the three resistors r, r_2 and r_3 have to be known with precision to deduce the IV characteristic of the contact. Before turning to the principle of operation of the SQUID amplifier, we present the measurement procedure of these resistors.

The resistance r_3 of the twisted pair line going from the sample to the input coil of the SQUID amplifier was measured independently at low temperature.

The resistor R is a surface mounted component that can be calibrated in situ by fully opening the contact. In this configuration, all the bias current flows in the resistor R and the voltage drop is measured across it.

The resistors r and r_2 can be measured in the supercurrent branch of a contact with large critical current. As long as the contact stays on its supercurrent branch ($V = 0$), $V_S = \left(R // \left(r + r_2 // r_3\right)\right) I_B$. We can therefore obtain the value of the $\left(r + r_2 // r_3\right)$ resistor combination. Then r_2 is deduced from the following equality:

$$\frac{R}{R + \left(r + r_2 // r_3\right)} I_B = \left(1 + \frac{r_3}{r_2}\right) I_{input\ coil}.$$

The left hand side is the current I expressed as the division of the bias current I_B into two branches.

At last, r is deduced from the value of the $\left(r + r_2 // r_3\right)$ combination, using r_2 and r_3 previously measured.

At low temperatures, the measured values of the various resistors are: $R = 25.3\ \Omega$, $r = 7.4\ \Omega$, $r_2 = 6.2\ \Omega$, $r_3 = 12.8\ \Omega$.

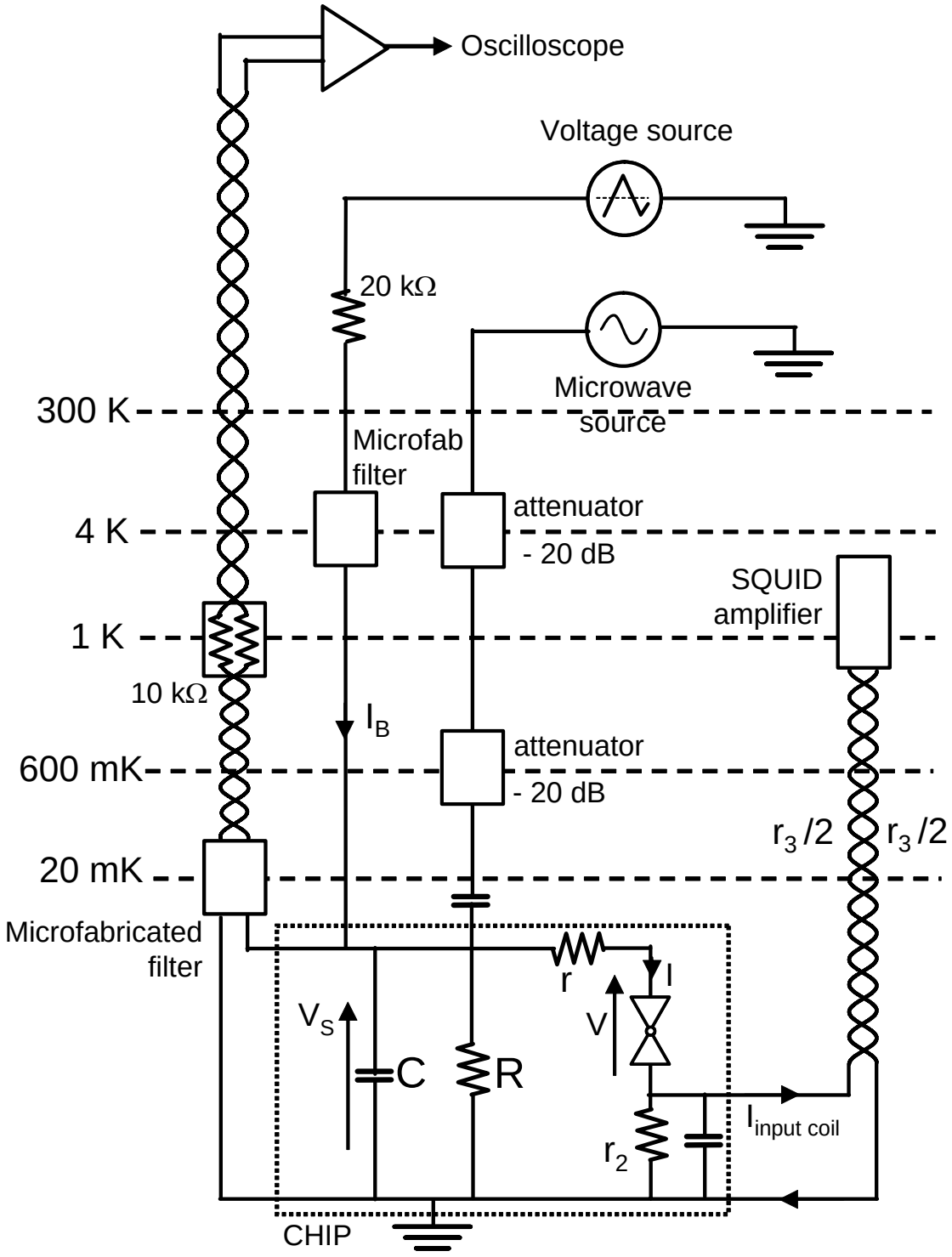

Figure 18: Experimental setup used for the measurement of Shapiro resonances with a SQUID as an ammeter. For biasing the sample, a coaxial line with a lossy part between 4 K and 20 mK is used. A microfabricated filter (dc resistance $\sim 1\ \mathrm{k}\Omega$ *) has been placed at 4 K, a refrigerator stage with sufficient cooling power to absorb the heat produced by Joule effect. The voltage* V_S *is measured with a lossy shielded twisted pair line to avoid thermoelectric voltages.*

2 Principle of operation of the SQUID amplifier

A SQUID amplifier is well suited to measure small signals on small impedances. Indeed, the key figures of such an amplifier is the current noise - typically 1 pA/$\sqrt{\text{Hz}}$ referred to input -, and the extremely low voltage noise in the standard conditions of operation.

The principle of operation of this amplifier is the following. The SQUID array (100 SQUID's in series) is biased by a constant current I. The current one wishes to measure is fed into the input coil and produces a flux, coupled to the squid array with the constant $M_{IN}^{-1} = 21.06\ \mu\text{A}/\phi_0$ ($\phi_0 = h/(2e)$). When the current changes in the input coil, a feedback electronics maintains the voltage across the SQUID array at a constant value by driving a current in the feedback coil to cancel the flux produced by the input coil. This feedback coil is coupled to the SQUID array with a constant $M_{FB}^{-1} = 221.1\ \mu\text{A}/\phi_0$.

The difference in the mutual inductances is essentially due to the difference in the number of turns of each coil. Each mutual can easily be calibrated.

Therefore, the current in the feedback coil, which is easy to measure, is an image of the input coil current, which is what we are actually interested in.

The IV of the array of $N = 100$ SQUID's is shown on Figure 19. Each squid is dc shunted by a small resistor of the order of $1\ \Omega$ to avoid hysteresis on the IV characteristic of the array. The tunnel junctions are in niobium which has a superconducting gap $\Delta = 1.4$ meV. The advantage of taking 100 SQUID's and not only one is that the voltage on which the feedback is performed is hundred times larger.

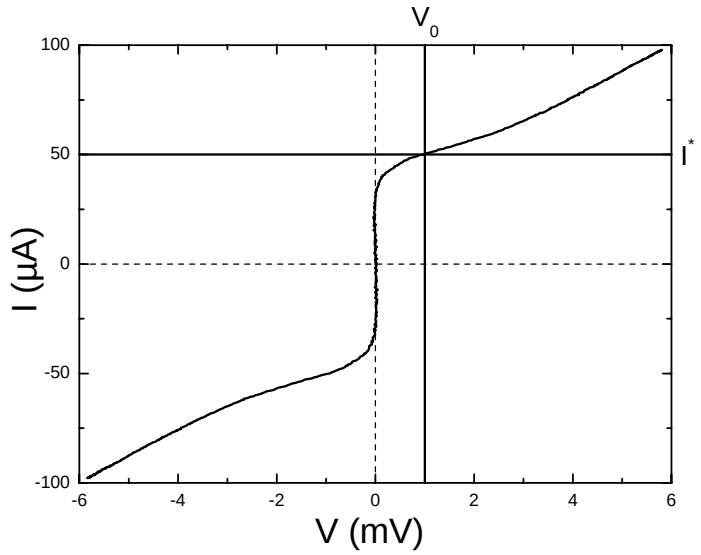

Figure 19: IV characteristic of the array of 100 SQUID's at zero flux. I^* is the bias current that maximizes the voltage modulation by the magnetic flux. This current I^* corresponds to a voltage V_0 on the SQUID's IV characteristic.

To operate the amplifier at its maximum of sensitivity, one has to set it in a configuration of maximum $\gamma = \frac{\partial V}{\partial \phi}$. To maximize γ one first has to find the value I^* of the bias current I that maximizes the voltage modulation with respect to the flux. The modulation curve is shown on Figure 20. Then, the feedback setpoint V_{SP} on the voltage across the array has to be chosen at the maximum slope of the $V(\phi)$ (see Figure 20). A typical value for γ is 4 mV/ϕ_0.

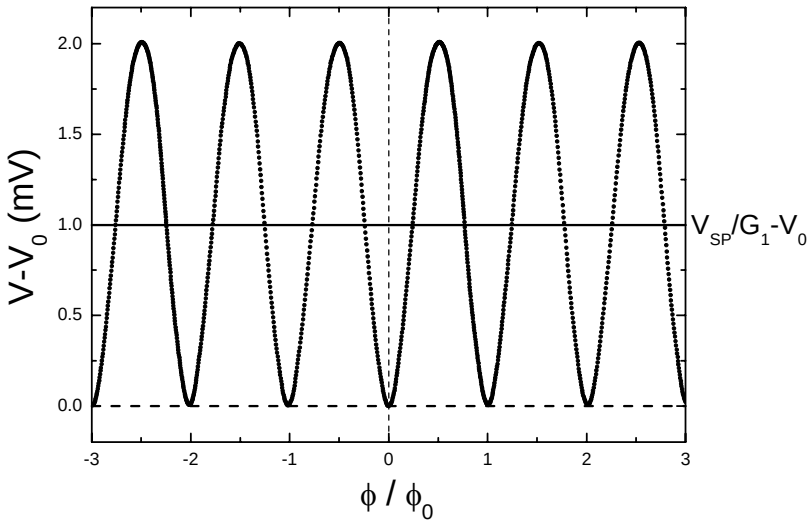

Figure 20: Modulation of the voltage across the SQUID array as a function of the flux threading each of the 100 SQUID's. V_0 is the voltage corresponding to the biasing current I^* at zero flux (see Figure 19). The feedback is performed on the voltage across the SQUID array after amplification by a gain G_1 (see Figure 21).

3 Feedback electronics

When the amplifier is operating, i.e. in feedback mode, the monitored quantity is the voltage on the bias resistor R_{FB} of the feedback coil. This voltage is proportional to the current in the input coil. This section is devoted to the analysis of the frequency response of the feedback electronics, whose schematic representation is shown on Figure 21. We use the standard formalism of the Laplace transforms to describe the gain of the different elements in the frequency domain.

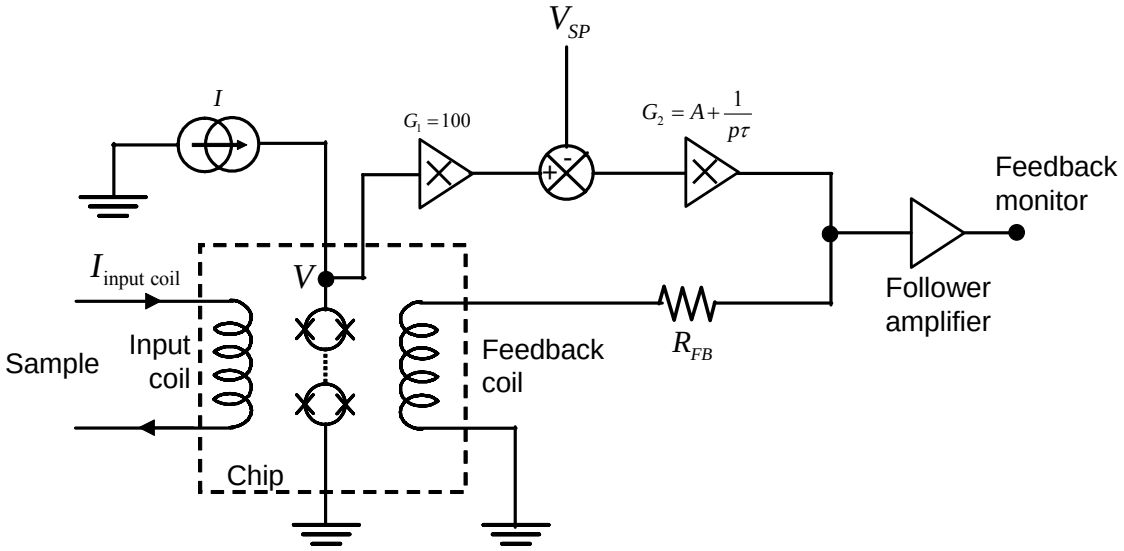

Figure 21: Schematic representation of the feedback electronics. The gain of the amplifiers are given within the Laplace transform formalism.

The feedback is performed on the voltage across the SQUID array after amplification by a gain G_1. The setpoint of the feedback is V_{SP}. The integrator amplifier, characterized by its gain $G_2(p) = A + \frac{1}{p\tau}$ in the frequency domain, tries to maintain the difference $G_1 V - V_{SP}$ close to zero. τ is the time constant of the integrator amplifier.

In feedback mode, when the flux produced by the input coil changes, the electronics changes the current in the feedback coil to compensate for the flux variation, according to:

$$\delta\phi_{FB} = G\left(\delta\phi_{FB} + \delta\phi_{IN}\right),$$

where $G(p)$ is the transfer function with the feedback loop open.

$$G(p) = \gamma G_1 G_2(p) \frac{1}{R_{FB}} M_{FB} = K\left(A + \frac{1}{p\tau}\right) \text{ with } K = \gamma G_1 \frac{1}{R_{FB}} M_{FB}$$

The parameters entering in $G(p)$ are self-explained on Figure 21. The transfer function with the feedback loop closed thus writes:

$$F(p) = \frac{\delta\phi_{FB}}{\delta\phi_{IN}} = \frac{G(p)}{1-G(p)}.$$

$\lim_{p\to 0} F(p) = -1$: At low frequency ($p \to 0$), the feedback electronics can follow perfectly the variations of the flux of the input coil; $\delta\phi_{FB} = -\delta\phi_{IN}$.

$\lim_{p\to\infty} F(p) = \frac{KA}{1-KA}$: At too high frequency ($p \to \infty$), the feedback loop cannot follow the variations of the flux of the input coil any longer; $\delta\phi_{FB} = \frac{KA}{1-KA}\delta\phi_{IN}$.

The cut-off frequency f_c is given by $p/2\pi$ with p satisfying $|G(p)| = 1$.

$$f_c = \frac{K}{2\pi\tau\sqrt{1-A^2K^2}}.$$

Typical values of the parameter are:

$K \approx 1.8$ (with $R_{FB} = 1\ \text{k}\Omega$)

$A \approx 0.047$

$\tau \approx 0.94\times10^{-6}$ s

Therefore: $f_c \approx 0.3$ MHz

In practice, the amplifier has been used at much lower frequencies (~ 1 kHz) because of the heavy filtering that was placed on the lines of the amplifier.

4 Wiring of the amplifier

In the experiment, the SQUID amplifier was placed at the 1K pot in the cryostat. The wiring of the amplifier is sketched on Figure 22. The four lines connected to the amplifier are lossy shielded twisted pairs. The inner conductors of the twisted pair going from the sample to the input coil are polyimide coated 0.2 mm diameter manganin wires

(15 Ω/m , 7 Ω per wire) inside a stainless steel capillary shield ($\phi_{int} = 0.7$ mm and $\phi_{ext} = 1$ mm).

The amplifier of gain $G_1 \simeq 100$ (see Figure 21 and Figure 22) is a low noise battery powered differential preamplifier (NF LI-75A). The amplifier used to monitor the feedback signal is a low noise battery powered differential amplifier of variable gain (Stanford SR560) (see Figure 22). In the experiments, the feedback monitor signal (see Figure 21 and Figure 22) is digitized by a Nicolet Pro 44 oscilloscope and transfer to a PC for treatment.

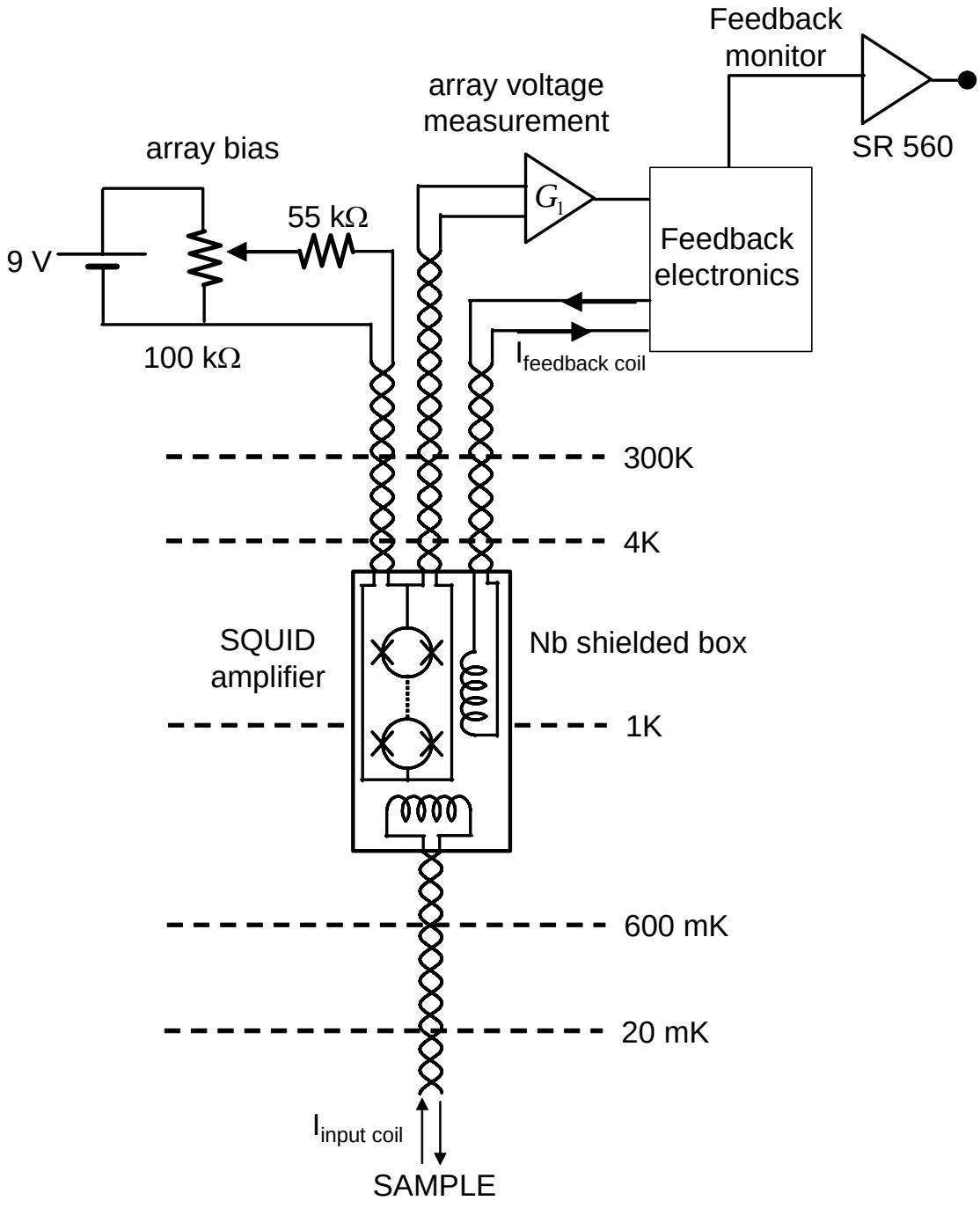

Figure 22: Wiring of the SQUID amplifier thermally anchored at the 1 K pot of the dilution refrigerator. The SQUID array is placed in a Nb shielded box to screen the external flux. All the lines arriving on the SQUID array and the two coils are lossy shielded twisted pairs.

Appendix 3: Wiring of the cryostat

The cryostat is equipped with 4 shielded twisted pairs and 3 coaxial lines.

- Shielded twisted pairs

The inner conductors of three twisted pairs going from 300 K to 1K are polyimide coated 0.1 mm diameter manganin wires ($60\ \Omega/\mathrm{m}$, $70\ \Omega$ per wire at room temperature) inside a stainless steel capillary shield ($\phi_{\mathrm{int}} = 0.4$ mm and $\phi_{\mathrm{ext}} = 1.0$ mm). The inner conductors of those going from 1 K to 20 mK are 0.05 mm diameter manganin wires ($240\ \Omega/\mathrm{m}$, $130\ \Omega$ per wire) inside a $\phi_{\mathrm{int}} = 0.2$ mm, $\phi_{\mathrm{ext}} = 0.7$ mm shield. The resistivity of the manganin doesn't change much with temperature: $\frac{\rho(300\ \mathrm{K})}{\rho(4.2\ \mathrm{K})} = 1.1$.

The inner conductors of the fourth twisted pair going from 300 K to 1K are polyimide coated 0.18 mm diameter manganin wires ($18.5\ \Omega/\mathrm{m}$, $20\ \Omega$ per wire) inside a Cu-Ni capillary shield ($\phi_{\mathrm{int}} = 0.7$ mm and $\phi_{\mathrm{ext}} = 1.0$ mm).

- Coaxial lines

All coaxial lines lines from 300 K to 4 K are microwave lines. They are characterized by low losses and a $50\ \Omega$ characteristic impedance. From 4 K to 20 mK, there are two microwave lines and one lossy coaxial line. The inner conductor is polyimide coated 0.05 mm diameter manganin wire ($240\ \Omega/\mathrm{m}$, $130\ \Omega$ per wire) inside a stainless steel capillary shield ($\phi_{\mathrm{int}} = 0.2$ mm, $\phi_{\mathrm{ext}} = 0.7$ mm).

The lossy lines (shielded twisted pair and coaxial) are used to transmit low frequency signals. The microwave lines have a bandwidth of 20 GHz.
All the lines have been designed to minimize the heat flow into the coldest part of the cryostat and are carefully thermally anchored at the different stages of the cryostat.
To minimize the electromagnetic noise reaching the contact, filters and attenuators are placed along the lines.

The lossy lines act as distributed RC filters (100 pF/m to the ground for each of the inner conductors) and prevent high frequency noise from reaching the sample. With the 1 kΩ (resp. 10 kΩ) resistors placed at 1K (see Figure 15), they form RC filters with a cut-off frequency of 10 MHz (resp. 1 MHz).

Microfabricated distributed RC filters [17] (cut-off frequency: 50 kHz) shaped as meander lines are inserted in the lossy lines. They have a dc resistance of the order of 1 kΩ on each wire of the pair.

References of chapter 5

[1] R. Cron, *Atomic Contacts: a Test-Bed for Mesoscopic Physics*, Ph.D. thesis, Université Paris 6 (2001);
http://www-drecam.cea.fr/drecam/spec/Pres/Quantro/Qsite/archives/theses/RCronThesis.pdf.

[2] I. K. Yanson, Zh. Eksp. Teor. Fiz. **66**, 1035 (1974) translated in Sov. Phys. JETP **39**, 506 (1974).

[3] A. G. M. Jansen, A. P. van Gelder, and P. Wyder, J. Phys. C: Solid St. Phys. **13**, 6073 (1980).

[4] G. Binnig, H. Rohrer, C. Gerber, and E. Weibl, Appl. Phys. Lett. **40**, 178 (1982).

[5] D. M. Eigler, C. P. Lutz, and W. E. Rudge, Nature **352**, 600 (1991).

[6] J. M. van Ruitenbeek, in *Mesoscopic Electron Transport*, edited by L. L. Sohn, L. P. Kouwenhoven, and G. Schön (Kluwer, Dordrecht, 1997).

[7] C. J. Muller, J. M. van Ruitenbeek, and L. J. de Jongh, Physica C **191**, 485 (1992).

[8] G. Rubio-Bollinger, P. Joyez, and N. Agraït, Phys. Rev. Lett. **93**, 116803 (2004).

[9] J. M. van Ruitenbeek *et al.*, Rev. Sci. Instrum. **67**, 108 (1996).

[10] F. C. Wellstood, C. Urbina, and John Clarke, Phys. Rev. B **49** 5942 (1994).

[11] M. F. Goffman *et al.*, Phys. Rev. Lett. **85**, 170 (2000).

[12] J. J. Riquelme, L. de la Vega, A. Levy Yeyati, N. Agraït, A. Martin-Rodero and G. Rubio-Bollinger, Europhys. Lett. **70** (5), 663 (2005).

[13] J. C. Cuevas, A. Martín-Rodero, and A. Levy Yeyati, Phys. Rev. B **54**, 7366 (1996).

[14] R. P. Welty and J. M. Martinis, IEEE Trans. Magn. **27**, 2924 (1991).

[15] M. E. Huber *et al.*, Appl. Supercond. **5**, 425 (1998).

[16] A. Steinbach *et al.*, Phys. Rev. Lett. **87**, 137003 (2001).

[17] D. Vion *et al.*, J. Appl. Phys. **77**, 2519 (1995).